

Development of Tunable Optical Filters For Interrogation of White-Light Interferometric Sensors

Bing Yu

Dissertation submitted to the Faculty of the
Virginia Polytechnic Institute and State University
in partial fulfillment of the requirements for the degree of

Doctor of Philosophy
in
Electrical Engineering

Dr. Anbo Wang, Chair
Dr. Robert W Hendricks
Dr. Yilu Liu
Dr. Ting Chung Poon
Dr. William B Spillman, Jr.
Dr. Roger H Stolen

April 28, 2005
Blacksburg, Virginia

Keywords: Tunable Optical Filter, White-Light Interferometry, Optical Fiber Sensor

©Copyright 2005, Bing Yu

Development of Tunable Optical Filters For Interrogation of White-Light Interferometric Sensors

Bing Yu

(ABSTRACT)

Interferometric fiber optic sensors have been extensively used to measure a large variety of physical, chemical and biomedical parameters due to their superior performance. At the Center for Photonics Technology of Virginia Tech, a variety of interferometric fiber optic sensors have been developed in recent years, for efficient oil recovery, partial discharge detection in high voltage transformers, pressure sensing in gas turbine engines, and temperature measurements in gasifiers and boilers. However, interrogating an interferometric sensor involves accurate recovery of a measurand from the phase-modulated lightwaves, and has been a challenge for high performance, high speed, and low-cost, to current white-light interferometry (WLI) techniques, such as the widely used scanning WLI (S-WLI) and spectral-domain WLI (SD-WLI). The performance of a white-light interferometric sensing system depends not only on the design of the probes, but also, to a great extent, on the interrogation strategy to be used.

In this Ph.D. research, a tunable optical filter based WLI (TOF-WLI) is proposed and validated as a low cost, yet high performance, solution to the interrogation of various types of interferometric sensors. In addition to the capability of linear/quadrature demodulation, TOF-WLI retains all the features of WLI, is compatible with the SD-WLI, and can be tailored for both static and wideband signals. It also has great potential in surface metrology and biomedical imaging as well as optical spectroscopy. The key, to the success of this new approach in competition with the other available WLI techniques, is that the tunable optical filter (TOF) must be specially designed for sensing and extremely low cost. Therefore, two novel TOFs, a diffraction grating tunable filter (DG-TOF) and an extrinsic Fabry-Perot tunable filter (EFP-TF), are proposed and demonstrated. Laboratory and field test results on using the DG-TOF WLI for partial discharge and thermal fault detection in high voltage power transformers, and the EFP-TF WLI in temperature sensor systems and a turbine engine monitoring system will also be presented to demonstrate the feasibility for efficient sensor interrogation.

ACKNOWLEDGEMENT

First of all, I gratefully acknowledge my advisor, Dr. Anbo Wang. Thank you for your professional guidance, advices, enormous encouragements, and continuous support technically and financially, without which my research progress in this tough subject and this dissertation would not have been possible. For me you have not only been an advisor, but also a leader, an example, a collaborator, and a friend.

I would like to extend my gratitude to my other wonderful committee members, from teaching and learning, Dr. Yilu Liu, Dr. Robert W Hendricks, Dr. Ting Chung Poon, Dr. Roger H Stolen and Dr. William B Spillman. Thank you for sharing with me your knowledge, and thank you for your time, cooperation, and confidence. You have helped make this an unforgettable and productive experience.

Very special thanks goes to Dr. Gary Pickrell, Associate Director of the Center for Photonics Technology, for sharing with us his expertise in material science, his help in our technical writing, excellent project management and guidance. It has been an honor to work with you in these past five years.

I wish to acknowledge Dr. Jiangdong Deng, a former graduate student at CPT. I really enjoyed the years working with you. Thank you for your assistance and friendship. I would also like to express my appreciation to Debbie Collins, William Cockey, and all staff and students at CPT for making CPT a great place for study and research.

The work described in this dissertation has been supported by the Electrical Power Research Institute (EPRI), the National Science Foundation (NSF), and the Department of Energy (DOE).

Dedicated to my wife, Xuerong, and my daughter, Ruthie.

List of Related Publications, Presentations, and Patents

Journal & Magazine Publications

- 1) **B. Yu**, A. Wang, and G. Pickrell, "Tunable Optical Filter Based White Light Interferometry for Sensing," *Optics Letters*, vol. **30**, no. **12**, June 15, 2005. (in press)
- 2) **Bing Yu**, Gary Pickrell, and Anbo Wang, "Spectral Filter Is Cheap, Tunable and Accurate," *Photonics Spectra*, Sept. 2004, pp. 26-28. (Reported by Editor Breck Hitz)
- 3) **B. Yu**, A. Wang, and G. Pickrell, "Analysis of Fiber Fabry-Perot Interferometric Sensors Using Low-Coherence Light Sources," submitted to *J Lightwave Technol* (March 2004).
- 4) **Bing Yu**, Gary Pickrell, and Anbo Wang, "Thermally Tunable Extrinsic Fabry-Perot Filter," *IEEE Photon. Technol. Lett.*, vol. **16**, no. **10**, pp. 2296-98, Oct. 2004.
- 5) **Bing Yu** and Anbo Wang, "Grating-assisted Demodulation of Interferometric Optical Sensors", *Applied Optics*, vol. **42**, no. **34**, Dec. 2003, pp. 6824-29.
- 6) **Bing Yu**, Dae Woong Kim, Jiangdong, Den, Hai Xiao, and Anbo Wang, "Fiber Fabry-Perot Sensors for Partial Discharge Detection in Power Transformers", *Applied Optics*, vol. **42**, no. **16**, pp. 3241-3250, 2003.
- 7) **Bing Yu**, Dae Woong Kim, Jiangdong, Den, Hai Xiao, and Anbo Wang, "Partial discharge detection uses optical fiber sensors," *Photonics Spectra*, Sept. 2003, pp. 40-42. (Magazine, reported by Editor Brent D. Johnson)

Conference Publications and Presentations

- 1) X. Wang, J. Xu, Y. Zhu, **B. Yu**, M. Han, K. L. Cooper, G. Pickrell, and A. Wang, "An Optical Fiber Tip Sensor for Medical Applications," accepted for presentation by *CLEO/QELS 2005*, Baltimore, MD.
- 2) **B. Yu** and A. Wang, "Tunable Extrinsic Fabry-Perot Filter for Sensing Applications", *2004 Optics in the Southeast*, SE04-A2, November 4 - 5, 2004, Charlotte, North Carolina.
- 3) X. Wang, J. Xu, Y. Zhu, **B. Yu**, M. Han, K. L. Cooper, G. Pickrell, and A. Wang, "An Optical Fiber Tip Sensor for Pressure Measurement in High Temperature Environment", *2004 Optics in the Southeast*, November 4 - 5, 2004, Charlotte, North Carolina.
- 4) **B. Yu**, G. Pickrell, and A. Wang, "Thermally tunable extrinsic Fabry-Perot filter for white-light interferometry", *Frontiers in Optics, the 88th Annual Meeting of OSA*, Oct. 10-14, 2004.

- 5) **B. Yu**, A. Wang, G. Pickrell, “Analysis of White-light Fiber Fabry-Perot Interferometric Sensors”, *Proc. of SPIE, Fiber Optic Sensor Technology and Applications III*, Edited by Michael A. Marcus, Brian Culshaw, John P. Dakin, vol. **5589**, 2004.
- 6) J. Xu, G. R. Pickrell, **B. Yu**, M. Han, Y. Zhu, X. Wang, K. L. Cooper, A. Wang, “Epoxy-free high temperature fiber optic pressure sensors for gas turbine engine applications,” *Proc. of SPIE, Sensors for Harsh Environments*, Edited by Anbo Wang, vol. **5590**, 2004.
- 7) Y. Zhu, G. R. Pickrell, X. Wang, J. Xu, **B. Yu**, M. Han, K. L. Cooper, A. Wang, A. Ringshia, W. Ng, “Miniature fiber-optic pressure sensor for turbine engine,” *Proc. of SPIE, Sensors for Harsh Environments*, Edited by Anbo Wang, vol. **5590**, 2004.
- 8) D. W. Kim, **B. Yu**, Y. Song, A. Wang, Y. Liu, A. Shahsiah, R. Degeneff, B. Ward, “Discharge and Thermal Gassing Monitoring using Fiber Acoustic Sensors,” *EPRI Substation Equipment Diagnostics Conference XII*, February 15-18, 2004, New Orleans, Louisiana.
- 9) X. Chen, **B. Yu**, Y. Zhu, A. Wang, “Deep wet etching of fused silica material for fiber optic sensor fabrication,” *Proc. of the SPIE*, vol. **5342**, pp. 128-136, 2004.
- 10) **Bing Yu**, Gary R. Pickrell and Anbo Wang, “Grating-assisted Operation-Point Tuning for Fiber-Optic Fabry-Perot Interferometric Sensors,” *Proc. of the SPIE*, vol. **5272**, pp. 41-48, 2004.
- 11) (Presentation Author) – G. R. Pickrell, R. Stolen, and D. Kominsky, “Random hole optical fibers,” *Proc. of SPIE*, vol. **5272**, pp. 207-215, 2004.
- 12) **B. Yu**, D.W. Kim, J. Deng, B. Ward, W. Cockey, Y. Liu, and A. Wang, “Fiber Optic Sensors for Partial Discharge Monitoring in Power Transformers,” *19th Annual Virginia Tech GSA Research Symposium*, Virginia Tech, Blacksburg, March 2003. (Poster presentation)
- 13) **B. Yu** and A. Wang, “Grating-assisted operating-point tuning for fiber-optic interferometric sensors,” *19th Annual Virginia Tech GSA Research Symposium*, Virginia Tech, Blacksburg, March 2003. (Poster presentation)
- 14) **B. Yu**, D.-W. Kim, J. Deng, B. Ward, W. Cockey, Y. Liu and A. Wang, “Fiber Optic Sensors for Partial Discharge Monitoring in Power Transformers”, *2003 EPRI Substation Equipment Diagnostics Conference*, Feb. 23-26, 2003, New Orleans, Louisiana.

- 15) Steven Tsai, **Bing Yu**, Ling Chen, Anbo Wang, Yilu Liu, Barry Ward, “Analysis of on-site transformer partial discharge measurement from fiber optic acoustic sensors”, *2003 EPRI Substation Equipment Diagnostics Conference*, Feb. 23-26, 2003, New Orleans, Louisiana.
- 16) Ling Chen, Steven Tsai, Bin Qiu, Yilu Liu, **Bing Yu**, Anbo Wang, Barry Ward, “Finite Element Simulation and Theoretical Analysis of the Partial Discharge Acoustic Wave Propagation inside Power Transformers”, *2003 EPRI Substation Equipment Diagnostics Conference*, Feb. 23-26, 2003, New Orleans, Louisiana.

Patents and Patent Disclosures

- 1) **Bing Yu** and Anbo Wang, “Q-point Stabilization for Linear Interferometric Sensors Using Tunable Diffraction Grating,” (US patent application No. 10/670,457).
- 2) **Bing Yu**, and Anbo Wang, “Thermally Tunable Fiber Fabry-Perot Filters”, Virginia Tech Intellectual Properties, Inc., VTIP No. **03-098**, July 2003.
- 3) **Bing Yu**, Anbo Wang, “Bi-directionally Tunable Optical Filters”, Virginia Tech Intellectual Properties, Inc., VTIP No. **03-081**, May 2003.
- 4) **Bing Yu**, Anbo Wang, “Grating-assisted Operating-Point Tuning for Fiber-Optic Fabry-Perot Interferometric Sensors”, Virginia Tech Intellectual Properties, Inc., VTIP No. **03-012**, Jan. 2003. (Exclusively Licensed to Prime Photonics, L.C., Blacksburg, VA)
- 5) **Bing Yu**, Anbo Wang, “Diaphragm-based Fabry-Perot Tunable Filter”, Virginia Tech Intellectual Properties, Inc., VTIP No. **02-127**, Dec. 2002.

Table of Contents

ABSTRACT.....	ii
ACKNOWLEDGEMENT.....	iii
Dedication.....	iv
List of Related Publications, Presentations and Patents.....	v
Table of Contents.....	viii
List of Figures.....	xii
List of Tables	xvii
Chapter 1 Introduction	1
1.1 Motivation.....	1
1.2 Outline of Dissertation.....	5
Chapter 2 White Light Interferometry for Interrogation of Interferometric Sensors.....	8
2.1 Scanning white-light interferometry (S-WLI).....	10
2.2 Spectrum-domain white-light interferometry (SD-WLI).....	13
2.3 Tunable-laser-based wavelength-tuning interferometry (TL-WLI).....	15
2.4 Tunable-Optical-Filter-Based White-light Interferometry (TOF-WLI).....	16
2.4.1 Scan mode.....	18
2.4.2 Linear mode.....	18
2.4.3 Advantages of TOF-WLI.....	23
2.5 Summary.....	24
Chapter 3 Theoretical Analysis of Interferometric Sensors Interrogated by a TOF-WLI.....	26
3.1 Transfer function of a reflective fiber Fabry-Perot interferometer.....	27
3.1.1 Sensitivity.....	29
3.1.2 Fringe contrast.....	31
3.1.3 Dynamic range.....	32
3.2 Numerical analysis results.....	32
3.2.1 Guided FFPI model with symmetric mirrors without filter.....	33

3.2.2	Filter effects.....	37
3.3	Summary.....	39
Chapter 4	Tunable Optical Filters: A Review.....	40
4.1	TOF specifications.....	40
4.2	Current tunable optical filters.....	42
4.2.1	Fabry-Perot type tunable filters.....	43
4.2.2	Tunable filters based on mode coupling.....	52
4.2.3	Grating filters.....	53
4.2.4	Other tunable filters.....	54
4.3	Summary.....	55
Chapter 5	Diffraction Gratings Tunable Optical Filter (DG-TOF).....	56
5.1	Principle of a DG-TOF.....	57
5.2	Filter fabrication.....	60
5.3	Filter characterization.....	62
5.4	Summary.....	65
Chapter 6	Extrinsic Fabry-Perot Tunable Filter (EFP-TF).....	68
6.1	Principle of operation.....	68
6.2	Filter preparation.....	70
6.3	Filter characterization.....	75
6.4	Summary.....	81
Chapter 7	Fiber Fabry-Perot Interferometric Sensors.....	82
7.1	EFPI temperature sensor.....	82
7.1.1	Principle of operation.....	83
7.1.2	Sensor fabrication and characterization.....	84
7.2	DFPI sensors.....	86
7.2.1	Principle of operation.....	87
7.2.2	Diaphragm design considerations.....	89
7.2.3	DFPI Sensor fabrication.....	92
7.2.4	DFPI sensor packsging.....	97

7.3	Summary.....	98
Chapter 8 Low Noise Analog Optical Receiver.....99		
8.1	Introduction.....	99
8.2	Noise resources.....	100
8.2.1	Intrinsic noise.....	101
8.2.2	External noise.....	102
8.3	Noise reduction strategies.....	103
8.4	Optical receiver for the EFP-TF WLI system.....	111
8.5	Optical receiver for the DG-TOF WLI system.....	112
8.6	Summary.....	114
Chapter 9 DFPI-PD Sensors for PD Detection Using DG-TOF WLI.....115		
9.1	Introduction.....	115
9.2	Instrumentation.....	118
9.2.1	System design.....	118
9.2.2	Instrument.....	119
9.3	Laboratory experiments.....	122
9.4	Field demonstrations without DG-TOF WLI.....	126
9.4.1	Sensor selection.....	126
9.4.2	Sensor installation.....	128
9.4.3	Test results.....	132
9.5	Field tests with DG-TOF WLI.....	135
9.5.1	Corona and thermal fault generation system.....	135
9.5.2	Sensor installation and equipment setup.....	137
9.5.3	Test results.....	139
9.6	Summary.....	146
Chapter 10 EFP-TF WLI for EFPI and DFPI Sensor Interrogation.....148		
10.1	Instrumentation.....	148
10.1.1	Light source.....	149
10.1.2	Electronics.....	150

10.1.3 EFP-TF controller and computer interface.....	151
10.1.4 Instrument.....	154
10.2 Low-finesse EFPI temperature sensor.....	155
10.3 High-finesse EFPI temperature sensor.....	157
10.4 DFPI-Engine Sensors.....	158
10.5 Summary.....	164
Chapter 11 Conclusions.....	165
11.1 Conclusions.....	165
11.2 Summary of contributions.....	167
11.3 Suggestions for future research.....	168
Appendix A Matlab codes for the calculation of fringe sensitivity, contrast and linear range...	169
Appendix B Labview programs for the EFP-TF WLI system.....	175
Bibliography.....	183
Vita.....	199

List of Figures

Fig. 2.1 Typical interference fringes generated by a F-P interferometer of low-finesse (two-beam interferometer) and medium-finesse (multiple-beam interferometer).....	9
Fig. 2.2 Principle diagram of a typical scanning white-light interferometric sensing system.....	11
Fig. 2.3 Interference fringes of a scanning WLI sensing system.....	11
Fig. 2.4 Component blocks of an OCT system.....	12
Fig. 2.5 The principle diagram of a SD-WLI sensing system.....	13
Fig. 2.6 General configuration of a TOF-WLI measurement system.....	17
Fig. 2.7 Linear region of an interferometric sensor.....	19
Fig. 2.8 Generalized homodyne and heterodyne detection system for a Mach-Zehnder interferometer.....	20
Fig. 3.1 Fiber F-P interferometer models. (a) Guided FFPI model; (b) Unguided FFPI model....	27
Fig. 3.2 Interference fringes and sensitivity as a function of optical path length of a typical low-finesse FFPI sensor.....	30
Fig. 3.3 Performances of a guided FFPI model with symmetric mirrors at different finesse. (a) Peak sensitivity; (b) Fringe contrast; (c) Dynamic range.....	34
Fig. 3.4 Performance degradation of the guided FFPI model with symmetric mirrors caused by angular misalignment. (a) Peak sensitivity; (b) Fringe contrast; (c) Dynamic range....	36
Fig. 3.5 Performance improvements due to an optical bandpass filter. (a) Peak sensitivity; (b) Fringe contrast; (c) Dynamic range.....	38
Fig. 4.1 A Fabry-Perot filter. (a) Principle diagram; (b) Transmission bands.....	44
Fig. 4.2 Fiber Fabry-Perot tunable filter configuration.....	47
Fig. 4.3 Hysteresis curves of an open-loop piezo actuator for various peak voltages. The hysteresis is related to the distance moved.....	47
Fig. 4.4 MEMS-TFs. (a) Structure of MEMS Fabry-Perot etalon; (b) Schematic structure of a micromachined vertical cavity filter with thermal strain control.....	49
Fig. 4.5 Schematic of a typical thin film tunable interferometer.....	51
Fig. 4.6 Tunable filter based on mode coupling.....	52
Fig. 5.1 Diffraction of a plane reflective holographic grating.....	57
Fig. 5.2 Schematic of a DG-TOF.....	58

Fig. 5.3 Wavelength dependence of the tuning angle and the DG-TOF bandwidth ($\Delta\lambda$).....	60
Fig. 5.4 Efficiency curves of the plane holographic grating (Thermal RGL, Richardson Grating Laboratory, 53004BK01-175H).....	61
Fig. 5.5 A top view of the DG-TOF.....	62
Fig. 5.6 Bandpass characteristics of the DG-TOF with a 200/230 μm MMF at different stage positions. (a) Original spectrum; (b) Normalized spectrum.....	63
Fig.5.7 Bandpass characteristics of the DG-TOF with a 100/140 μm MMF at different stage positions. (a) Original spectrum; (b) Normalized spectrum.....	64
Fig. 5.8 Bandwidth of the DG-TOF passband.....	65
Fig. 5.9 Modal Noise.....	67
Fig. 6.1 Principle diagram of an EFPI filter.....	69
Fig. 6.2 Experimental setup for cleaved endface quality inspection.....	70
Fig. 6.3 Reflectivity of the dielectric mirrors.....	71
Fig. 6.4 Photograph of the sensor fabrication stage system.....	72
Fig. 6.5 Schematic diagram of the cavity length monitoring system.....	72
Fig. 6.6 Optical micrograph of a bonded point.....	73
Fig. 6.7 Optical micrograph of an EFPI filter.....	74
Fig. 6.8 Recorded spectrum of the prototype EFPI the bonding at ambient temperature.....	74
Fig. 6.9 Photo of a packaged prototype EFP-TF.....	75
Fig. 6.10 Schematic diagram of the HTC-3000 from Wavelength Electronics.....	76
Fig. 6.11 Experimental setup for filter characterization.....	76
Fig. 6.12 Normalized spectrum at $T=10.11^\circ\text{C}$	77
Fig. 6.13 Tuning curves of the prototype EFP-TF.....	78
Fig. 6.14 Hysteresis of the prototype EFP-TF.....	79
Fig. 6.15 Fig. 6.16 Temperature sensitivity and linearity. (a) Linear fit; (b) 3 rd -order polynomial fit.....	80
Fig. 6.16 Filter's temperature sensitivity and linearity.....	80
Fig. 7.1 Principle diagram of an EFPI sensor head.....	83
Fig. 7.2 Principle diagram of a low-finesse EFPI sensor fabrication monitoring system.....	85
Fig. 7.3 Reflection spectrum of the low-finesse reflection-type EFPI sensor.....	85
Fig. 7.4 Transmission spectrum of the high-finesse transmission-type EFPI temperature	

sensor at T=20°C.....	86
Fig. 7.5 Principle diagram of an DFPI-PD sensor.....	88
Fig. 7.6 Diaphragm sensitivity and frequency response.....	90
Fig. 7.7 Support system for the inter-media layer bonding method.....	93
Fig. 7.8 Photo of the DFPI sensor bonding setup.....	94
Fig. 7.9 Heating process during the thermal-bonding.....	94
Fig. 7.10 Photo of the airgap length and interference fringe monitoring system.....	95
Fig. 7.11 Typical interferogram of a medium-finesse DFPI-PD sensor.....	95
Fig. 7.12 Photograph of two DFPI-PD sensors.....	96
Fig. 7.13 DFPI-PD sensor holder. (a) Side view of the holder, (b) DFPI-PD sensors mounted on the tube.....	97
Fig. 7.14 A packaged DFPI-Engine sensor.....	98
Fig. 8.1 Schematic of a basic transimpedance amplifier.....	99
Fig. 8.2 Noise analysis model of the basic transimpedance amplifier.....	100
Fig. 8.3 Electrostatic noise coupling through mutual capacitances.....	103
Fig. 8.4 Magnetic and RFI noise coupling through a mutual inductance.....	103
Fig. 8.5 Noise coupling from power-supply.....	104
Fig. 8.6 Noise from the light source. (a) without optical input; (b) with 2.5 μ W optical input...	105
Fig. 8.7 Noise measurement setup.....	105
Fig. 8.8 Noise reduction using a low pass filter. (a) a second order low pass filter; (c) frequency response of the preamp with the low pass filter.....	106
Fig. 8.9 Experimental results with a low pass filter. (a) Noise spectrum before the low-pass filter; (b) Noise spectrum after the low-pass filter (Gain =2).....	107
Fig. 8.10 Power-supply isolation.....	108
Fig. 8.11 Power-supply filtering. (a) Circuits; (b) Noise spectrum at Point A; (c) Noise spectrum at Point B.....	109
Fig. 8.12 Shielding, grounding and cabling. (a) Layout; (b) Noise w/o shielding and grounding; (c) Noise with shielding and grounding.....	110
Fig. 8.13 Schematics of the optical receiver for the EFP-TF WLI system.....	111
Fig. 8.14 Gain linearity.....	112
Fig. 8.15 Schematics of the optical receiver for the DG-TOF WLI system.....	113

Fig. 8.16 Frequency response of the optical receiver for PD detection.....	114
Fig. 9.1 Principle diagram of a FFPI sensor system based on DG-TOF.....	118
Fig. 9.2 Schematic of the DG-TOF WLI interrogation system for PD detection.....	120
Fig. 9.3 Spontaneous emission spectrum of the SLED1300D20A.....	121
Fig. 9.4 Photograph of the DFPI-PD sensor interrogation system.....	122
Fig. 9.5 Acoustic wave test setup for PD sensor evaluation.....	123
Fig. 9.6 Scan output of a DFPI-PD sensor in atmospheric pressure.....	123
Fig. 9.7 Normalized outputs of the sensor in atmospheric pressure and under 50cm water.....	124
Fig. 9.8 Scanning the DG-TOF for Q-points of the DFPI-PD sensor.....	125
Fig.9.9 Acoustic wave outputs without and with a DG-TOF at different operation-points.....	125
Fig. 9.10 Laboratory simulation of acoustic wave detection. (a) h=1.0m. (b) h=2.0m.....	127
Fig. 9.11 Static-pressure sensitivity test results in the laboratory.....	127
Fig. 9.12 Typical acoustic signals recorded by a DFPI-PD sensor and a PZT sensor in the Lab.....	128
Fig. 9.13 The NGC SGT3A 400KV/275KV transformer.....	128
Fig. 9.14 Layout of the drain valves and sensor positions.....	129
Fig. 9.15 Illustration of PD sensors installed inside the transformer tank through a drain valve.....	130
Fig. 9.16 Packaged DFPI-PD sensors in a sensor holder.....	130
Fig. 9.17 Picture of the Group 1 sensors inside the tank.....	131
Fig. 9.18 Test equipment setup in the control cabin.....	132
Fig. 9.19 A sample of measured signal from DFPI-PD sensor FB-1 and FT-3.....	133
Fig. 9.20 Original signals and denoised signals of FB1.....	135
Fig. 9.21 Schematic of the corona and thermal fault generation system.....	136
Fig. 9.22 Schematic of the corona generator.....	137
Fig. 9.23 Test setup and PD sensor installation. (a) DFPI-PD sensors for electrical faults (corona, PD and breakdown); (b) DFPI-PD sensors for thermal faults.....	138
Fig. 9.24 Signal conditioner and data recording system.....	139
Fig. 9.25 Signal conditioner for the PZT sensors and the DC and AC high-voltage sources....	139
Fig. 9.26 Oscillogram of the 1 st DC test.....	141
Fig. 9.27 Oscillogram of the 2 st DC test.....	142

Fig. 9.28 Oscillogram of the 1 st AC test.....	143
Fig. 9.29 Oscillogram of the 2 nd AC test.....	144
Fig. 9.30 DFPI-PD sensors installed for thermal tests.....	145
Fig. 9.31 The thermal test results.....	145
Fig. 10.1 Layout schematic of the EFP-TF WLI interrogation system.....	148
Fig. 10.2 Output spectrum of the SLED at 180 mA and 20 °C.....	150
Fig. 10.3 Interrogation system on a single PCB board.....	151
Fig. 10.4 Flow chart of the Labview programs for EFP-TF control and data acquisition.....	153
Fig. 10.5 The front panel of the Labview programs.....	154
Fig. 10.6 Photo of the 1550nm EFP-TF WLI interrogation system.....	155
Fig. 10.7 A top view of the main box.....	155
Fig. 10.8 Low-finesse EFPI temperature sensor. (a) Q-point searching, (b) Lock-mode.....	156
Fig. 10.9 High-finesse EFPI sensor. (a) Scan outputs; (b) Temperature-voltage curve.....	158
Fig. 10.10 Gas turbine engine under test.....	159
Fig. 10.11 Test equipment setup in the control room.....	160
Fig. 10.12 Typical test results from DFPI-Engine sensors and the reference sensor. (a) Time-domain signals; (b) Frequency-domain signals.....	161
Fig. 10.13 Frequency-domain dynamic pressure signals recorded by the miniature sensors and the Kulite reference sensor. (a) Type I miniature fiber optic sensor; (b) Type II miniature fiber optic sensor.....	163

List of Tables

Table 10.1 Main frequencies measured by the Kulite and the DFPI-Engine sensor.....	162
--	-----

Chapter 1 Introduction

This dissertation investigates the efficient interrogation of interferometric optical sensors by the use of a tunable-optical-filter-based white-light interferometry (TOF-WLI). High cost and system complexity of current sensor interrogation systems are the two of the major limiting factors that have been hindering the widespread use of fiber optical sensors in industry. White-light interferometry (WLI) is an extremely powerful tool in optical sensing, surface profiling, biomedical imaging, non-destructive testing (NDT), and optical component and waveguide test. The investigation focuses on the theoretical study of the performance of a TOF-WLI, the development of low-cost tunable optical filters (TOF), and the feasibility of TOF-WLI for the interrogation of optical fiber sensors at low cost.

1.1 Motivation

Fiber optic sensors may be defined as a means through which a measurand interacts with light guided in an optical fiber (an intrinsic sensor) or guided to (and returned from) an interaction region (an extrinsic sensor) by an optical fiber to produce an optical signal related to the parameter of interest [1]. During its over 30 years of history, fiber optic sensor technology has been successfully applied by laboratories and industries worldwide in the detection of a large number of mechanical, thermal, electromagnetic, radiation, chemical, flow and turbulence of fluids, and biomedical parameters. The driving forces behind this work are the advantages, provided by fiber optic sensors over conventional electronic sensors, of survivability in harsh environments, immunity to EMI, light weight, small size, compatibility with optical fiber communication systems, high sensitivity to many measurands, and good potential of multiplexing [2]. In general, the transducers used in these fiber optic sensor systems are either an intensity-modulator or a phase-modulator. Optical interferometers, such as Mach-Zehnder, Michelson, Sagnac and Fabry-Perot interferometers, have become widely accepted as a phase-modulator in optical fiber sensors for the ultimate sensitivity to a range of weak signals [3]. The distribution chart of papers presented at the 15th Optical Fiber Sensor Conference according to technologies [4] shows that interferometers are involved in about 25.9% presented papers, second only to fiber gratings (44.2%) which may be considered as a stack of Fabry-Perot interferometers. According to the light source being used, the interferometric sensors can be

simply classified as either a coherence interferometric sensor if the interferometer is interrogated by a coherent light source, such as a laser or a monochromatic light, or a low-coherence interferometric sensor when a broadband source, for example, a light emitting diode (LED) or a superluminescent diode (SLD), is used.

White-light interferometry (WLI), also called low-coherence interferometry (LCI), was first described by Delisle and Cielo, in a paper published in 1975, in an experiment where two Michelson interferometers were used with a white-light source for possible use in optical communication systems [5]. In their experiment, the first interferometer was illuminated by white-light and had a path difference much larger than the coherence length of the light source ($l_c = \lambda^2 / \Delta\lambda$). The output was then sent to the second interferometer, which acted as a spectrum selective component of the otherwise invisible modification of the spectrum. The first sensing application of WLI was reported by Al-Chalabi, et al in 1983 [6]. The first fully developed WLI sensing system for displacement measurement achieved a range to resolution ratio better than $10^4:1$ with a conventional lamp source [7]. This excellent work shows that the WLI technique could also be used to measure any parameters that can be converted into a displacement with high accuracy [8]. The white-light or low-coherent interferometry was well described by Born and Wolf in classic optics [9]. Since then, low-coherence interferometers have been extensively developed as fiber-optic sensors for the measurements of a wide variety of measurands, such as displacement [10], temperature [11], strain and temperature [12], [13], pressure [14] [15], vibration [16], [17], acoustic wave [18], electric field (voltage) [19], wind [20], velocity [21], humidity [22], and multiparameters [23], etc. Several detail reviews of fiber optic LCI were given by Lefevre in 1990 [24], Grattan Meggit in 1995 [25], and Rao and Jackson in 1996 [8].

More recently, WLI has also found an increasing research interest in chemical sensing [26], and biomedical sensing [27]-[29]. Multiplexing [30], [31] or distributed sensing [32] employing a LCI to reduce the cost per sensor is another hot topic under study.

In addition to sensing applications, optical coherence domain reflectometry (OCDR) or optical low-coherence reflectometry (OLCR) based on low-coherence interferometry has been developed to detect and localize weakly reflecting regularities in optical waveguides [33], and is a powerful tool for micrometer-scale imaging in objects including miniature devices [34] and recently biological tissues [29]. LCI is also a powerful tool in optical component characterization [35] [36], and surface profiling [37], etc.

The fact that WLI has attracted more attention recently over its counterpart, laser interferometry, can be attributed to the following reasons [11], [38]-[40]:

- 1) The capability to make absolute and unambiguous measurements over a wide range, which allows the sensors to be used for quasi-static measurands such as temperature or pressure.
- 2) Sensor systems can be operated such that the effects of wavelength instabilities are greatly reduced.
- 3) Higher achievable spatial density of sensors in a multiplexing array than using a light source of long coherence.
- 4) Sensors can be fabricated with very short F-P cavities, which tends to greatly reduce the effects of measurand cross sensitivity. With a short cavity, simple demodulation techniques, such as intensity-based demodulation, may be used to recover the phase change, and therefore, no local reference interferometer (LRI) is necessary.
- 5) Reduced spurious interference and Rayleigh backscattering induced excess noise in interferometric sensors because of the shorter coherence length.
- 6) Insensitivity to strong optical feedback so no optical isolator is necessary.

To take good use of the advantages provided by WLI in a fiber optic sensing system, efficient signal-processing or signal demodulation is essential to accurately recover the phase change of the interferometer, and thus the measurand related. The system performance of a WLI sensing system not only depends on the interferometer itself, but also highly relies on the demodulation strategy to be used. Early WLI sensing systems generally employed interferometers of optical path difference (OPD) on the order of millimeters, such as a Mach-Zehnder interferometer or a Michelson interferometer, for the absence of a precise control of the OPD. It is very common for these systems to use a scanning white-light signal-processing, in which a low-coherence light source is used to interrogate the sensing interferometer, and a second interferometer, which is termed local reference interferometer (LRI), has to be employed to recover the OPD from the phase modulated signal [41], [42]. This configuration is generally bulky and requires the LRI to scan a large OPD using a moveable part, which results in reliability issues. High signal-to-noise ratio (SNR) and sophisticated signal-processing are generally required to recover the phase information from the central interference fringe. A variation of the S-WLI is widely used in the time-domain optical coherence tomography (OCT)

[35], surface metrology [43] and some Mach-Zehnder or Michelson sensors, in which the optical length of the reference arm is directly scanned. The major advantage of this configuration is that only one interferometer is required. However, it is hard, if not impossible, to be applied to Fabry-Perot and Sagnac type interferometers due to the difficulty to access the reference beam. Another issue is that the two arms may experience different environmental fluctuations.

The Spectrum-Domain demodulation technique developed later replaces the LRI with a spectrum analysis component, such as a grating or a Fizeau interferometer, and replaces the single photodiode with a CCD array [44]. Once the output spectrum is obtained, fringe counting, fringe tracking or Fourier transform may be used to recover the OPD of the interferometer. SD-WLI is applicable to all types of interferometer, insensitive to source fluctuations, very accurate, reliable, and requires no mechanical scanning. Speed and price are two major issues with SD-WLI. Commercial spectrometers which in general are slow and expensive, especially in the 1.0–1.7 μm wavelength range.

When very small OPD changes or dynamic perturbations are to be measured, linear or quadrature operation has to be considered for the highest sensitivity and largest signal bandwidth provided by the linear region (a small region on an interference fringe near its quadrature point, or Q-point). Linear (or Quadrature) demodulation is an important tool in laser interferometry. The biggest challenge is that Q-points drift due to fabrication tolerances and random environmental fluctuations. In laser interferometry, linear demodulation using a homodyne or heterodyne detection has achieved great success in overcoming both the ambiguity and fading problems in the demodulation of Mach-Zehnder interferometers [45], but it is generally not applicable in other interferometric sensors, such as F-P and Sagnac type sensors. A quadrature-shifted demodulation approach [46] or its variation employed two sensing interferometers of $\pi/2$ phase shift has been applied to solve the ambiguity and fading in fiber optic Fabry-Perot sensors. The disadvantage is the need of twin sensors at each test point, and it is no simpler to maintain the $\pi/2$ phase shift than to stabilize the sensor itself. Tunable lasers have sometimes been used for this purpose [47], though it retains all the drawbacks of a coherent sensing system. A most important common disadvantage of all these approaches is the high cost per sensor, which makes fiber-optic interferometric sensors less competitive in the sensing market. Attributing to the advances, since early 1990s, in sensor fabrication technologies, especially the fiber Fabry-Perot (FFP) sensor technology [15], [17], [39] [48], [49] and MEMS sensor fabrication technology

[50], miniature interferometers with an OPD on the order of tens of micrometers are readily obtainable. This small OPD is even smaller than the coherence of most broadband light sources, such as SLED, LED, or multimode lasers, so that intensity-based direct detection may also be used as an alternative signal-processing approach. Therefore, no LRIs or spectrum analysis components are necessary, significantly simplifying the system design and reducing the cost per system [39]. However, linear operation has not usually been provided by current WLI techniques due to poor fringe contrast and lack of Q-point stabilization.

In this dissertation, a tunable-optical-filter-based white-light interferometry (TOF-WLI) will be introduced as a universally efficient solution for the demodulation of various types of interferometric sensors at low cost. In addition to the capability for quadrature demodulation, TOF-WLI, retains all the features of traditional WLI, is compatible with the SD-WLI, can be used for various types of interferometer, and can be tailored for both static and dynamic signals. TOF-WLI also has great potential in other areas beyond sensors, such as surface metrology and biomedical imaging. The key, to the success of this new approach in competition with current white-light demodulation approaches and its coherence counterparts, is that the tunable optical filter must be specially designed for sensing applications and extremely low cost. Therefore, two novel tunable optical filters, a diffraction grating tunable filter (DG-TOF) and an extrinsic Fabry-Perot tunable filter (EFP-TF), suitable for sensing, will be described in detail. Experimental and field test results on using DG-TOFs for partial discharge and thermal fault detection in high voltage transformers and cable networks and using the EFP-TF for temperature sensors and engine pressure sensors will also be presented to demonstrate the feasibility for sensor interrogation.

1.2 Outline of Dissertation

Pursuant to this introduction, Chapter 2 reviews in detail the up-to-date sensor interrogation techniques which have been widely used in the low-coherence signal recovery of interferometric fiber-optic sensors, including the scanning white-light interferometry (S-WLI), the spectral-domain white-light interferometry (SD-WLI), and the tunable-laser-based wavelength-tuning interferometry (TL-WTI). Then I discuss the concept of using TOF-WLI for the interrogation of interferometric optical sensors and its advantages over conventional approaches.

In Chapter 3, a theoretical treatment of interferometric fiber-optic sensors using a broadband light source is given. A numerical analysis based on the theoretical treatment manifests how a white-light interferometric sensor is sensitive to its design parameters and environment changes as well as how a TOF may significantly improve the performance of the sensors.

The principles and performances of various available TOF techniques, including Fabry-Perot type tunable filters, mode coupling type tunable filters and grating tunable filters, are reviewed in detail and their drawbacks for sensing applications are identified and summarized in Chapter 4.

Chapter 5 describes the operating principle, the design, the fabrication and the characterization of a newly developed TOF, which is named a diffraction grating based tunable optical filter (DG-TOF).

The design of an alternative TOF, which is named an extrinsic Fabry-Perot tunable filter (EFP-TF), is introduced in Chapter 6 with its operation principle, fabrication processes, filter packaging, and characterizations.

Chapter 7 describes the principles and the fabrication techniques of extrinsic Fabry-Perot interferometric (EFPI) temperature sensors and diaphragm-based Fary-Perot interferometric (DFPI) sensors which will be used as examples in the later chapters for interferometric sensor demodulation with the TOF-WLI.

After an introduction of the research background of partial discharge (PD) detection and location in high voltage power transformers, Chapter 8 provides a detail description of a 1300nm DG-TOF based white-light interrogation system designed for PD detection and location, and experimentally investigates the feasibility of using the system for the demodulation of DFPI PD sensors, both in the lab and in fields.

Chapter 9 focuses on the interrogation of EFPI temperature sensors and DFPI engine pressure sensors, respectively, by using the EFP-TF based WLI. Section 9.1 deals with the instrumentation of a 1550nm White-light Interrogation System with an EFP-TF, emphasizing on the design of the broadband light source, the low-noise optical receiver, and the computer interfaces and the programming for EFP-TF control and data acquisition. Section 9.2 investigates the demodulation of a low-finesse EFPI temperature sensor in a linear operation mode, while Section 9.3 focuses on demodulation of a high-finesse EFPI temperature sensor using a peak tracking approach. In Section 9.4, I describe the field test of a DFPI turbine engine sensor supported by the White-light Interrogation System.

The dissertation ends with a list of major contributions and some suggestions for future improvement of the performance of a TOF-WLI system, given in the last chapter.

Chapter 2 White-light Interferometry For Interrogation of Interferometric Sensors

The basic idea of the demodulation of an interferometric sensor is to accurately recover the optical path difference (*OPD*) with minimum uncertainty, no matter the sensor is a Michelson, a Mach-Zehnder, a Sagnac or a Fabry-Perot interferometer [51]. In any interferometric sensor, the *OPD* can be generally expressed as nL , where n is the refractive index of the medium comprising the interferometer, and L is the physical path length difference between the path of the sensing light beam and that of the reference light beam (L is length of a round-trip in the case of a reflective Fabry-Perot sensor). Any measurand change can be represented by the *OPD* change of the transducer. The recovery of *OPD* starts from the measurement of the phase angle, ϕ . For an interferometric sensor interrogated with a monochromatic source of wavelength λ , ϕ is given by

$$\phi = 2\pi \cdot OPD / \lambda = 2\pi nL / \lambda \quad (2-1)$$

A perturbation of a measurand causes a change in the length L , or the refractive index n , or both, resulting in a phase shift defined by the following equation

$$\phi + \Delta\phi = \frac{2\pi}{\lambda} \cdot OPD + \frac{2\pi}{\lambda} \cdot \Delta(OPD) = \frac{2\pi}{\lambda} \cdot nL + \frac{2\pi}{\lambda} \cdot (n \cdot \Delta L + L \cdot \Delta n) \quad (2-2)$$

Unfortunately, the phase angle and the shift cannot be measured directly by any instruments. Therefore, the demodulation is somehow related to the detection of the intensity or the intensity distribution of the optical power received by a detector. Of course, it is much more sensitive than the intensity-based detection.

In the cases of two-beam interference, which is the case for all interferometers mentioned before except a Fabry-Perot interferometer, the optical intensity arrives at the photodiode is [9]

$$I(l, \lambda) = (I_1 + I_2) / 2 + \sqrt{I_1 I_2} \cos \phi \quad (2-3)$$

where I_1 and I_2 are the optical intensity from the reference beam and the sensing beam, respectively. Assuming $I_1 = I_2 = I_0$, Eq.(2-3) can be simplified as

$$I(l, \lambda) = I_0(1 + \cos \phi) \quad (2-4)$$

For a F-P sensor, multiple-beam interference has to be considered. Assuming symmetric mirrors and lossless cavity, the reflection can be expressed as [52]

$$I(l, \lambda) = 2RI_0 \cdot \frac{1 + \cos \phi}{1 + R^2 + 2R \cos \phi} \quad (2-5)$$

where R is the reflectivity of the mirrors. In the limit of small R (low-finesse), Eq. (2-5) can be rewritten as

$$I(l, \lambda) = 2RI_0(1 + \cos \phi) \quad (2-6)$$

Eq. (2-6) is similar to Eq. (2-5) and the difference is only a constant factor $2R$. This implies the two-beam interferometers may be represented by a low-finesse F-P interferometer. For this reason, both theoretical and experimental work through this proposed research focus on a Fabry-Perot type interferometric sensor unless otherwise specified. White-light interferometric sensors based on Mach-Zehnder, Michelson or Sagnac interferometers can be studied similarly as a low-finesse F-P sensor. Fig. 2.1 shows typical interference fringes of a F-P interferometer of low-finesse and medium-finesse.

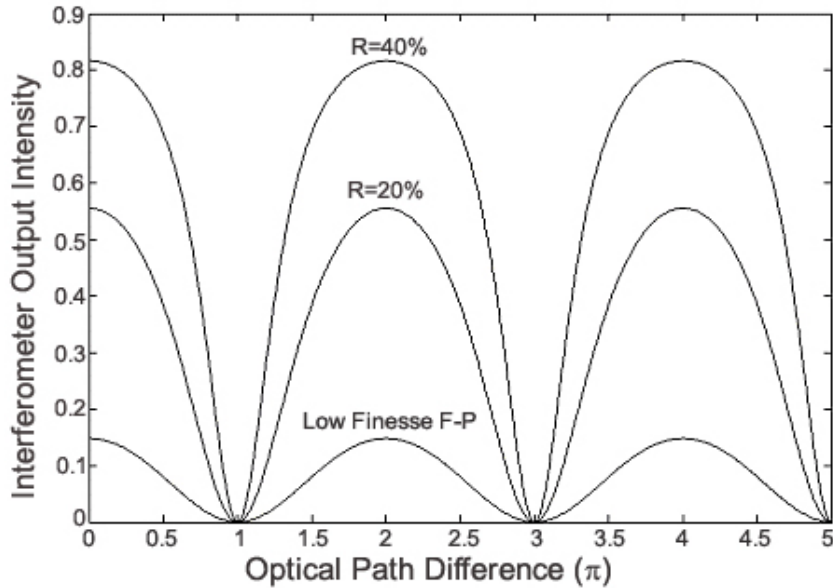


Fig. 2.1 Typical interference fringes generated by a F-P interferometer of low-finesse (two-beam interferometer) and medium-finesse (multiple-beam interferometer).

As indicated by Eqs. (2-1) – (2-6) and Fig. 2.1, demodulation of an interferometric sensor is not a trivial task because of the non-linear and periodical feature of the interference fringes (the transfer function), and what is worse is that the presence of low frequency random temperature, strain and pressure fluctuations which causes the changes in the amplitude of the detected signal (signal fading) and the distortion of the signal (frequency up-conversion) [53]. When a low-coherence light (or white-light) source is employed to interrogate an interferometric sensor, the spectral distribution of the source has to be considered ($I_o(\lambda)$), and the total output intensity of a sensor is an integration of the contribution of all the wavelength components that reach the detector. More detailed analysis of a white-light Fabry-Perot interferometric sensor will be given in Chapter 3 and in Ref. [54]. Signal recovery becomes more complicated and demodulation schemes that are different from those for the coherence interferometric sensors have to be employed.

With the increased interest in the research of white-light interferometry (WLI) in the last three decades, various white-light techniques have been proposed for the interrogation of various types of interferometric sensors. These techniques can be simply classified into three major categories: Scanning white-light interferometry, Spectrum-Domain white-light interferometry and tunable-laser-based wavelength-tuning interferometry. In the following sections, each of these techniques is reviewed in detail. Then I propose an alternative WLI, which is named a TOF-WLI, as an effective solution for various types of interferometric sensors.

2.1 Scanning White-light Interferometry (S-WLI)

A basic conventional scanning white-light interferometric sensor system is generally composed of a sensing interferometer located inside the measurand field and a LRI placed in a controlled environment far from the field, as essential components [8], shown in Fig. 2.2. The former usually has an OPD larger than the coherence length of the light source such that interferometric fringes cannot be observed and is used to convert the measurand perturbations into a phase modulation of the lightwaves through the variations of the OPD. Through optical fiber links, the phase-modulated lightwaves are delivered to the LRI. In order to recover the OPD of the sensing interferometer, the OPD of the LRI is required to be scanned, creating an interference fringe pattern. Either a reflective or transmissive type interferometer can be used as

a LRI. When the OPDs of the two interferometers are the same, the LRI has the maximum fringe peak, which is termed the central interference fringe or centroid. Fig. 2.3 shows an example of the interference fringe pattern from such a system. The shift of the central fringe position is usually used to determine the absolute OPD change of the sensing interferometer. A theoretical treatment of a scanning WLI can be found in [8].

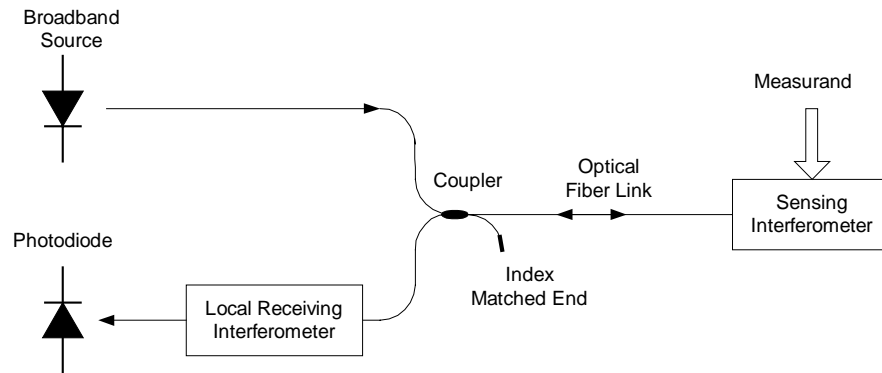


Fig. 2.2 Principle diagram of a typical scanning white-light interferometric sensing system.

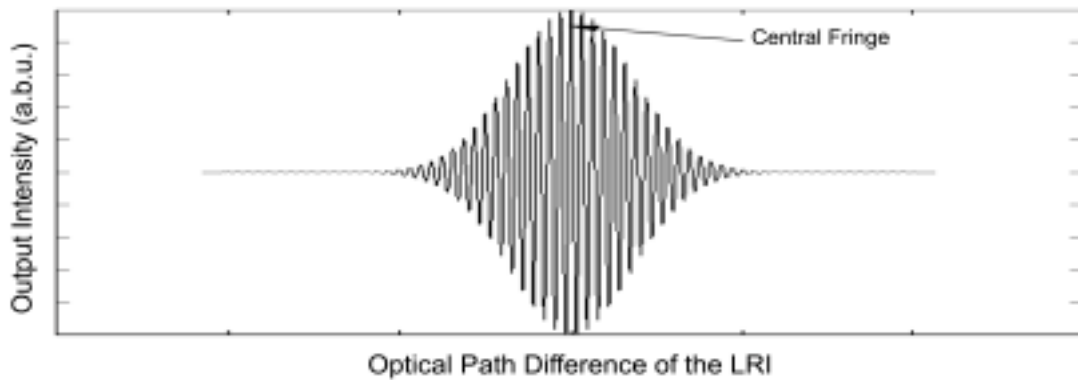


Fig. 2.3 Interference fringes of a scanning WLI sensing system

The scanning of the receiving interferometer may be achieved using different methods, such as a mechanical scanning interferometer using a piezoelectric linear stage [41], a mobile mirror [55], an electronically scanned WLI using a CCD [42] [55] [56], and a Fizeau interferometer with a linear photodiode array [57]. The accuracy of any scanning WLI sensing system is determined by the degree to which the central fringe can be accurately identified [56]. Various algorithms have been used for the identification of a central fringe in the past three decades. The

simplest method is to directly measure the position of the maximal fringe by comparing the output amplitude [57]. Apparently, a SNR above 50dB is essential for high measurement accuracy in this method and source drift may cause excess errors. However, it is possible that the intensity difference between the central fringe and its adjacent fringes is too small to be distinguished because of the existence of noise in the system. In order to reduce the required SNR, centroid algorithms based on a synthesized source [58] [59] or adaptive filtering [60] [61] have been developed. The achievable accuracy for central fringe identification is less than one-tenth of a fringe width.

Generally speaking, scanning white-light interferometric sensors are “down-lead insensitive” because external perturbations are common-mode to the recombined waves, and immune to the drift of the light source because the measurement is achieved by the comparison of the OPDs of the two interferometers [56]. The dynamic range of a S-WLI sensing system is the largest compared with other demodulation schemes attributing to the large scanning range of available LRIs. The obvious disadvantages of the scanning WLI are, in addition to the low resolution, a large system size, low mechanical stability and poor signal-to-noise ratio [62].

A variation of the S-WLI with double-interferometers is widely used in the time-domain OCT [29], surface metrology [43], and some Mach-Zehnder or Michelson sensors, in which the optical length of the reference arm is directly scanned. Fig. 2.4 shows component blocks of a general time-domain OCT system, in which the reference mirror is required to be scanned. The photo-detector has the maximum output when the optical length of the reference arm matches that of the sensing arm.

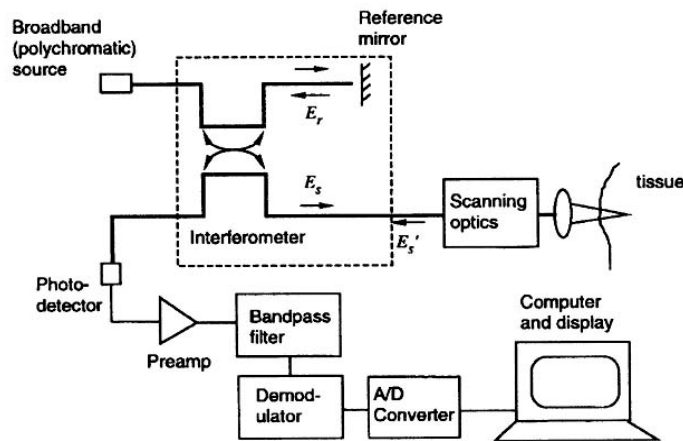


Fig. 2.4 Component blocks of an OCT system [29].

The major advantage of this configuration is that only one interferometer is required. However, it is hard, if not impossible, to be applied to Fabry-Perot and Sagnac interferometers due to the difficulty to access the reference beam. Another issue is that the two arms may experience different environmental fluctuations.

2.2 Spectrum-Domain White-light Interferometry (SD-WLI)

The SD-WLI technique is based on the detection of the output spectrum of the sensing interferometer. The spectrum of the signal from the sensor is usually obtained by means of a spectrometer with a CCD or a photodetector array, shown in Fig. 2.5. This technique eliminates the need of any moving parts or reference interferometer, and provides a combination of the high sensitivity of an interferometric sensor with absolute accuracy and reliability of spectrum encoding. It can also provide non-incremental absolute measurements of the OPD and correspondingly the external physical measurand [44]. SD-WLI has been widely used, in the past 10 years, in the detection of static or quasi-static parameters, such as micro-displacement, temperature, pressure, and strain [44] [15]. Recently, SD-WLI also becomes a powerful tool in biomedical sensing and imaging [63]-[65].

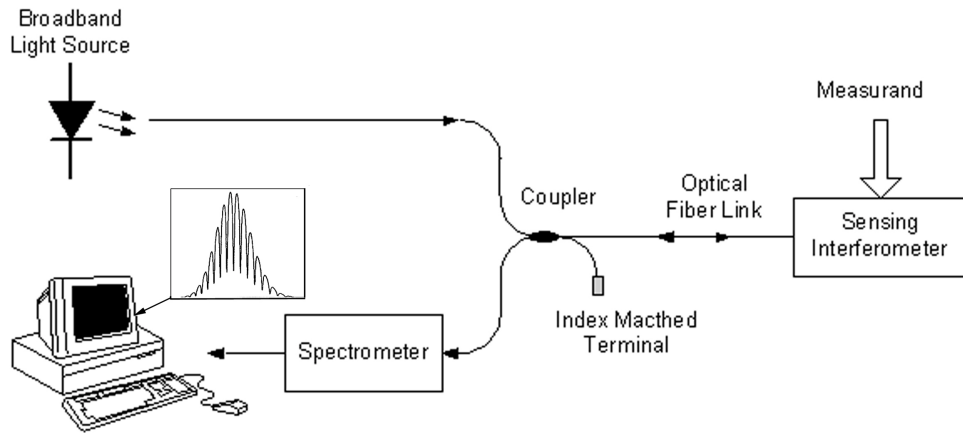


Fig. 2.5 The principle diagram of a SD-WLI sensing system.

Once the output spectrum of a WLI sensor has been obtained, *OPD* may be recovered by using various algorithms. The simplest way to compute the *OPD* is a direct interference fringe counting [66]. The fringe counting is based on the fact that when the optical phase runs, in the

wavelength domain, through a number of 2π , maxima and minima occur in the output, and the number of fringes counted m can be directly converted to the actual OPD using the following equation

$$OPD = m \cdot \frac{\lambda_1 \lambda_2}{\lambda_1 - \lambda_2} \quad (2-7)$$

where $m=0, 1, 2, \dots$, is the interference fringe order number, and λ_1 and λ_2 are the upper and lower boundary of the spectrum range used for the fringe counting. Fringe counting generally limits the sensor's resolution to, at best, a small fraction of the wavelength, depending on the particular interferometer [67].

A more accurate algorithm recovers the OPD by tracking the spectral position of one of the interference fringes [68] [12] or the wavelengths of two adjacent fringes [15] [69]. When only one peak is tracked, the OPD change can be expressed as, provided that the original OPD is known,

$$\Delta(OPD)/OPD = \Delta\lambda/\lambda \quad (2-8)$$

where $\Delta\lambda$ is the shift of the fringe peak from the original wavelength λ . When two peaks are tracked,

$$OPD = \frac{\lambda_1 \lambda_2}{\lambda_1 - \lambda_2} \quad (2-9)$$

Apparently, the precision of this fringe tracking approach highly depends on how accurately the position of a peak can be located. System noise is the major source of errors, and therefore, low-pass filtering or averaging of the acquired OPD calculated by using more than one pair of peaks may be used to improve the measurement accuracy.

Another efficient processing method is based on the analysis of the output spectrum in the domain of Fourier images [70]. In this method, the first harmonic corresponding to the interferometric signal was separated from the whole Fourier image of the output signal and then the phase difference as a function of the optical frequency was obtained. It provides the absolute and accurate value of the OPD in sensing interferometer and is insensitive to the power and spectral fluctuation of the source. However, the use of only the first harmonic makes the method susceptible to the influence of parasitic interferometers which are common in Fabry-Perot

interferometric sensors. The processing of several harmonics leads to the reduction of the disturbing influence of parasitic interferometers and results in higher accuracy and reliability of the sensor [71]. Other spectrum processing methods, such as the discrete Fourier transform used by Yun *et al* [63] and the one used by Mercado *et al* [72], have also been used for the recovery of measurands from the output spectrum of a WLI sensor.

SD-WLI is applicable to all types of interferometer, insensitive to source fluctuations, and very accurate and reliable, and requires no mechanical scanning. The SD-WLI is also applicable to WLI-based sensors with a wide range of OPD, depending on the resolution of the spectrometer and the available source bandwidth. For example, if a spectrometer of 0.5 nm resolution at 1550 nm band is used, theoretically, an OPD up to 4.8 mm may be recoverable, and an OPD as small as that generating only a few interference fringes can be resolved with good accuracy if a suitable algorithm is used.

Two major issues of the current spectral domain techniques are the slow response, which limits them to the measurement of static or quasi-static signals, such as temperature, displacement, strain and pressure, and the requirements of expensive spectrum processing components, such as diffraction gratings and detector arrays, especially those operating in the 1.0~1.7 μm band. For example, a spectrometer at the visible band may cost more than \$2,000, while one at 1.55 μm may cost ten times higher.

2.3 Tunable-Laser-Based Wavelength-Tuning Interferometry (TL-WTI)

Tunable laser is a laser in which the frequency of the emitted radiation can be changed across some range in the UV, visible, and IR regions of the electromagnetic spectrum. A tunable laser consists of an optical gain medium, a pumping process for stimulating the medium, and frequency-selective optical feedback [73]. As a wavelength-tunable laser is capable of covering a broad wavelength range, a single tunable laser has the potential to replace tens or even hundreds of single-wavelength lasers [74]. For years, however, the tunable laser remained confined to the laboratory as a spectroscopist's tool to investigate the spectral characteristics of atoms and molecules, due to the expensive and large organic liquid-dye laser [75]. Attributing to the commercialization of the extrinsic-cavity diode laser (ECDL), tunable lasers fit in the palm of a hand, extremely robust and cost a fraction of previous tunable lasers are commercially available,

and are finding increasing use in biomedical diagnose, environmental monitoring, surface profiling, testing in optical components and telecommunication systems, and optical sensor interrogation [73].

The use of tunable lasers has recently attracted a lot attention in optical sensing and biomedical imaging. The probably most important applications are for the interrogation of Fiber-Bragg-Grating sensors and EFPI sensors for health monitoring of bridges, buildings and aircrafts. Actually, several systems of this type are already commercially available, such as the Intune Technologies's AltoWave5500TM sensor interrogator [75], Blue Road Research's fiber optic sensor readout systems [76], and the Micron Optics's optical sensing analyzers [77]. Most of these systems monitor the measurand-induced wavelength-shifts by scanning a tunable laser. In some other applications, tunable lasers were used in the linear demodulation of interferometric sensors to dynamically stabilize the operation-point of the sensors, which, otherwise, may drift out of the linear region due to random environment fluctuations [17] [47] [78]. Linear demodulation of an interferometric sensor will be discussed in detail in Section 2.4.

Another important use of tunable lasers is the wavelength-tuning interferometry (TL-WTI). TL-WTI recently becomes a powerful tool to replace the S-WLI or the SD-WLI [79]-[82]. In the TL-WTI, the phase information of the sensing interferometer is recovered by scanning the wavelength of the tunable laser and by applying a Fourier transform algorithm. In a TL-WTI, no LRI or spectrometer is required and, therefore, the system is very simple, robust and reliable. Unfortunately, a current TL-WTI interrogation system has the same order of scanning speed (typically from a few Hz up to several hundred Hz) as and costs moderately higher than a SD-WLI system (\$20k~50k) of similar performances. Another drawback of tunable lasers is their small tuning range, which is generally around 50 nm. This small scan range limits the dynamic range and the measurement accuracy of TL-WTI system in spectral-domain operation mode due to the insufficient fringe numbers at very small OPD.

2.4 Tunable-Optical-Filter-Based White-light Interferometry (TOF-WLI)

TOFs are now key components for wavelength or channel selection in optical communication systems using wavelength division multiplexing (WDM) techniques and fiber optic video broadcast and select networks. TOFs have also been used in fiber-optic sensing applications in a

few specific cases [68] [83] [84]. However, the roles a TOF can play in a fiber-optic sensor system, especially in WLI, have not been systematically investigated and few TOFs have been developed particularly for these applications.

Based on the fact that the phase of an interferometer, and therefore its output intensity, are a function of the interrogation optical wavelength, as indicated in Eqs. (2-1)-(2-6), a TOF may play an important role in the interrogation or demodulation of interferometric optical sensors. Actually the receiving interferometer in the scanning white-light interferometry may be considered as a very coarse TOF. The major difference is that a LRI generally has a much larger OPD and a much wider transmission band than a normal TOF, and it is used to match the OPD of sensing interferometer, instead of scanning the wavelength.

In this dissertation, I describe an alternative WLI technique, which is termed tunable-optical-filter-based WLI (TOF-WLI). By introducing a tunable optical filter into a WLI system, one can interrogate an interferometer in the similar ways as the TL-WTI described in Section 2.3. Fig. 2.6 shows the general configuration of a TOF-WLI measurement system. It consists of a broadband light source, a circulator, a sensing interferometer, a tunable optical filter, receiving electronics, a computer and optical fibers to connect all the optical parts. The TOF-WLI may operate either in a scan mode (or spectrum acquisition mode) or a locked-mode (or linear operation mode). First demonstration of using an acousto-optic tunable filter (AOTF) for the interrogation of interferometric sensors in both scan mode and fringe-tracking mode was reported by Xu *et al.* [68].

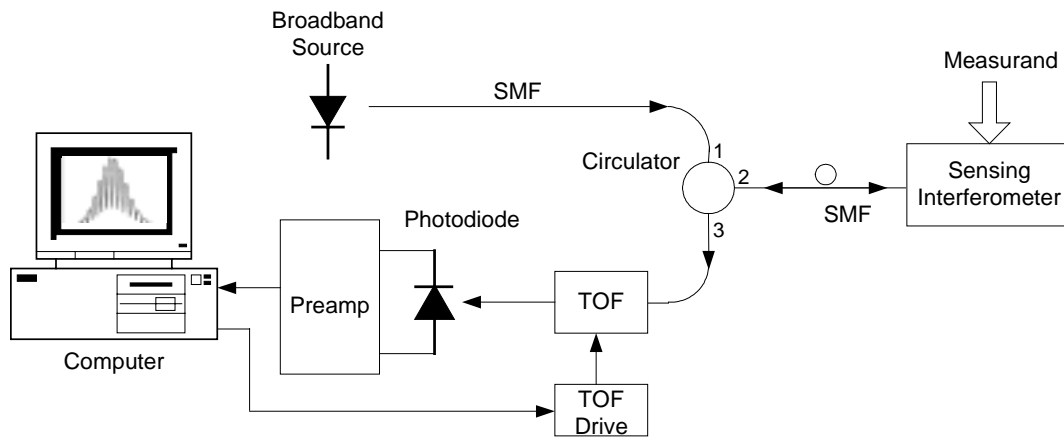


Fig. 2.6 General configuration of a TOF-WLI measurement system.

2.4.1 Scan mode

Obviously, the output spectrum of the sensing interferometer is readily obtainable by scanning the TOF, and the system can work similarly to an SD-WLI, and most of the developed signal-processing algorithms for SD-WLI, such as fringe peak tracking and Fourier transform, can be directly applied. In order to be applicable for interferometric sensors of a large OPD range with high resolution and large signal-to-noise ratio (*SNR*), a scan range above 100 nm and a filter bandwidth of 0.5~2 nm are usually preferred. A larger scan range challenges the TOF technology, while a smaller filter bandwidth requires a significant increase of the source output power. Both may remarkably increase the cost of a system. For static measurands, such as temperature or strain, the tuning speed of the TOF is not critical. When quasi-static measurements are necessary, a scanning rate several times higher than the signal frequency is a must. However, linear operation has to be used for dynamic signals, such as acoustic waves and vibrations. Linear operation will be discussed in detail in Section 2.4.2.

In addition to interferometric sensors, TOF-WLI operating in a scan mode may also be used in the demodulation of FBG sensor arrays [84] [85], in chemical and biomedical sensing as a spectrometer [86], in surface profiling, and in the spectral-domain biomedical imaging.

2.4.2 Linear operation mode

When very small OPD changes or dynamic perturbations are to be measured, linear or quadrature operation has to be considered for the highest sensitivity and largest signal bandwidth provided by the linear region. A linear region is defined as a small region on one side of an interference fringe near the point where sensitivity is the maximum, as illustrated by Fig. 2.7. Compared with other sensor demodulation techniques, sensors operating in the linear region have the advantages of linear transfer function, ultra-high frequency response, no fringe direction ambiguity, simple signal-processing and highest sensitivity at the Q-point. They are, therefore, suitable for the detection of small variations, such as acoustic wave [17] [87], ultrasound [78] [47], vibration [17], magnetic field [88], partial discharge [18], and pressure and temperature [39], etc.

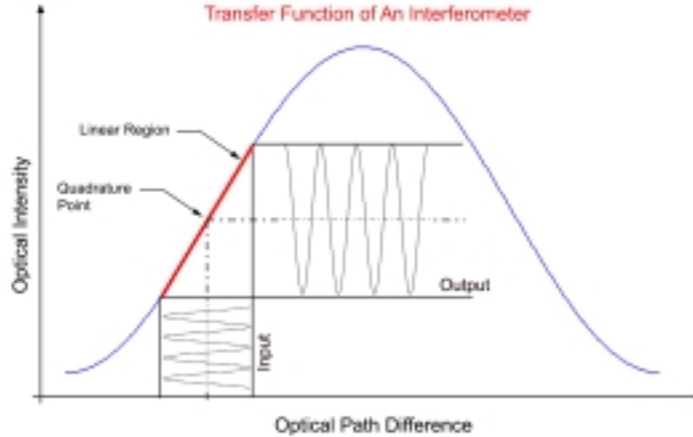


Fig. 2.7 Linear region of an interferometric sensor.

However, confining the operation to the linear region places difficult manufacturing constraints on the sensor head by requiring the initial cavity length to be positioned at the Q-point or sometimes one end of a linear region of the transfer function [89]. They also suffer from signal fading caused by random environment fluctuations, such as temperature changes, which may drive the sensors out of the linear region. The drifts are even more critical for Fabry-Perot sensors with medium or high-finesse F-P cavities often necessary for higher measurement sensitivity, because of their steeper fringe slopes. Therefore, poor control of the operation point has been one of the major factors that limit the practical application of interferometric optical sensors.

In the absence of an efficient operating-point stabilization method, a “trial and fail” strategy was used during the sensor fabrication to select sensors that had an operating-point close to its quadrature point in a specific system [78]. Apparently, the yield is extremely low considering the nanometer accuracy required for the quadrature point control and the operation of the sensor may still suffer from environment drifts unless it is made really insensitive to any environmental disturbance. To solve this problem, various schemes have been demonstrated in the past, such as using a bias, homodyne or heterodyne demodulation, and quadrature-shifted demodulation. Each of these techniques will be reviewed briefly below.

A. Using a Bias

A straightforward way to adjust the operating-point is to apply a bias on the sensing interferometer. In the demonstration of acoustic wave detection using a fiber-optic Fabry-Perot

interferometer (FFPI) by Yoshino et al, an acoustic wave bias was applied to the FFPI which was controlled by a servo system to maintain the operating-point against the temperature-induced phase shift [87]. In another experiment for partial discharge detection with a diaphragm-based Fabry-Perot sensor by Yu *et al*, static water pressure was used to manually adjust the operating-point for the compensation of fabrication errors and temperature-induced phase shift [18]. Unfortunately, Q-point stabilization using a bias is a very application specific approach and not a universal solution for all applications. It is also not an efficient approach because of the complexity.

B. Homodyne and Heterodyne Detection

One or two phase shifters generated by stretching sections of fibers wound on piezoelectric transducers have been widely used in the demodulation of Mach-Zehnder interferometers with high accuracy [45] [90] [91]. A generalized form of this configuration is shown in Fig. 2.8. Depending on the type of the detection system used, either the phase shifter A controlled by a feedback circuit to maintain the interferometer at its quadrature point, or the phase shifter B driven by a piezoelectric element with an oscillator, or both can be used. The detection systems of this kind can be categorized, according to their configuration, into five classes: passive homodyne (HOM), homodyne with dc phase tacking (PTDC), homodyne with ac phase tacking (PTAC), true heterodyne (HET), and synthetic heterodyne (SHET). A complete review of these schemes can be found in reference [45].

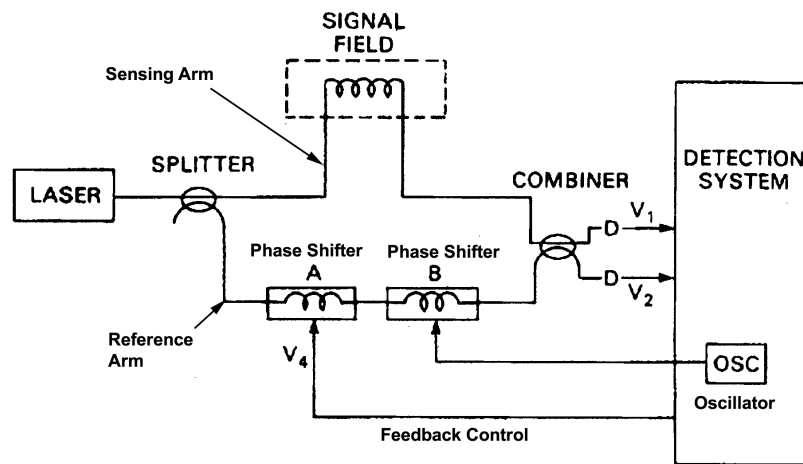


Fig. 2.8 Generalized homodyne and heterodyne detection system for a Mach-Zehnder interferometer [45].

Although both homodyne and heterodyne detection have achieved great success in the demodulation of Mach-Zehnder interferometers with extremely high resolution, good linearity and low harmonic distortion, they are generally not applicable in other interferometric sensors, such as Fabry-Perot and Sagnac type sensors, because of the difficulties to apply a phase shifter in the reference arm. In order to achieve the high level of performance, homodyne and heterodyne require relatively large size of phase modulators, which increase the sensor size and decrease reliability, and fast reset circuitry, which adds additional noise [53]. A recently published paper demonstrated a new synthetic-heterodyne demodulator for an optical fiber Fabry-Perot interferometer of large cavity length using low-coherence light source [92], but PZT stacks, which increase the size of the system and limit the carrier frequency, and an expensive lock-in amplifier, have to be used to extract the phase shift.

C. Quadrature-shifted demodulation

Quadrature-shifted demodulation is another important linear demodulation scheme, in which two or three interferometric sensor outputs with a $\pi/2$ phase shift one from the other are used to recover the measurand without signal fading or direction-ambiguity. Quadrature-shifted outputs can be obtained by using a passive quadrature demodulator (PQD) which is an output coupler matrix comprising of four fiber-optic directional couplers with precisely controlled path-lengths between them [93], two phased-shifted sensors [46], a two-wavelength passive quadrature demodulator [94], or a three-wavelength digital phase demodulation system [95].

The PQD with a coupler matrix was demonstrated in interferometric sensors using a fiber-optic Mach-Zehnder configuration. The matrix created two interferometers which are identical except for an additional ΔL path-length introduced into one of them by the output coupler matrix. In the case of using two sensors, the sensors were fabricated with a path-length imbalance ΔL . In order to obtain a quadrature-shift, the phase difference $\Delta\phi$ at the operating wavelength λ between the two interferometers must satisfy

$$\Delta\phi = \frac{2\pi n \cdot \Delta L}{\lambda} = (2N + 1)\pi/2 \quad (2-10)$$

where n is the refractive index and N is integer.

If two- or three-wavelength demodulation is used, a single sensing interferometer is generally sufficient. The phase-shift $\Delta\phi_{i,i+1}$ between two adjacent wavelengths λ_i and λ_{i+1} , should satisfy

$$\Delta\phi_{i,i+1} = \frac{2\pi nL}{\lambda_i \lambda_{i+1}} \cdot \Delta\lambda = (2N + 1)\pi/2 \quad (2-11)$$

where L is the physical path difference of the interferometer. Once quadrature-shifted outputs are obtained, the measurand can be recovered unambiguously using available phase calculation algorithms.

The quadrature-shifted demodulation eliminates the bulk phase shifter and feedback control required by homodyne and heterodyne detection. It is very efficient for unambiguous fringe demodulation and stabilization of the operating point. However, maintaining a $\pi/2$ phase shift is not an easy task. The random phase shift caused by environmental changes may not be identical for the twin sensors, and Eq. (2-11) may not be valid when L changes unless one of the two wavelengths is tunable. Either case results in a deviation from the quadrature condition and reduced accuracy. The use of either twin sensors or multiple wavelengths also makes the system undesirably complex.

As the TL-WTI, the TOF-WLI operating in a linear mode can also be used to search, set and track the quadrature point of an interferometric sensor. The optical phase difference between the sensing and the reference beams is given by Eq. (2-1). In the TOF-WLI system given in Fig. 2.6, a wavelength-tuning of

$$\Delta\lambda = [\Delta(OPD)/OPD] \cdot \lambda \quad (2-12)$$

is required to compensate for the phase change $\Delta\phi$ caused by an environmentally induced drift of magnitude $\Delta(OPD)$. Since most interferometers have an initial $OPD \gg \Delta(OPD)$, only a small wavelength tuning may be required to compensate for a large OPD fluctuation. In the TL-WTI approach, tunable lasers have sometimes been used for this purpose. However, linear operation has not been provided by current WLI techniques due to a poor fringe contrast and the lack of Q-point stabilization. A unique feature of the TOF-WLI is that it does provide this capability with a reasonably good fringe contrast and potentially low cost.

The optical intensity arriving at the photodiode, with a TOF central wavelength λ_0 , can be expressed as

$$I(OPD, \lambda_0) = \alpha_0 I_0 \cdot \int_0^{+\infty} f_s(\lambda) \cdot f_{TOF}(\lambda, \lambda_0) \cdot X(\phi) \cdot d\lambda \quad (2-13)$$

where, I_0 is the total output intensity of the broadband light source, α_0 describes the total loss of all optical parts and fibers in the signal path, $f_s(\lambda)$ is the spectral distribution of the source, $f_{TOF}(\lambda, \lambda_0)$ is transmission spectrum of the TOF at λ_0 , and $X(\phi)$ is the transfer function of the interferometer at wavelength λ . In a scan mode, the OPD can be treated as a constant, while in a linear mode, the TOF wavelength λ_0 is fixed. Eq. (2-13) is the starting point for the calculation of the system sensitivity, fringe contrast and linear range. A theoretical analysis of TOF-WLI will be given in detail in Chapter 3.

As mentioned in Chapter 1, due to the considerable improvement of sensor fabrication, sensing interferometers with an OPD smaller than the coherence of most broadband light sources are readily obtainable. We will see in Chapter 3 that smaller OPD means better fringe contrast and higher sensitivity. Small OPD also means a TOF-WLI system can have a good fringe contrast even with a relatively wide TOF passband. Depending on the source power density, a TOF bandwidth of 5~8 nm is generally required for both a good *SNR* and a good fringe contrast in a linear mode TOF-WLI. A smaller TOF bandwidth has definite advantages of a better fringe contrast and a higher tuning resolution as well as a larger OPD range if a high power broadband light source is used.

2.4.3 Advantages of TOF-WLI

Compared to the other white-light interferometry techniques, such as the S-WLI, the SD-WLI and the TL-WTI, TOF-WLI has many advantages for the interrogation of interferometric sensors. A TOF-WLI measurement system:

- 1) Retains all the advantages of white-light interferometry.
- 2) is a universally effective method for most interferometric sensors, including Mach-Zehnder, Michelson, Sagnac, F-P, and even FBG sensors.
- 3) Can readily be tailored for both static and dynamic signals.
- 4) May significantly improve the sensors' sensitivity and fringe visibility.

- 5) Is compatible with most available signal-processing approaches, such as fringe counting, fringe tracking, spectral processing, quadrature point stabilization, and systems using a tunable source.
- 6) May drastically reduce the cost of each sensor system to a fraction of current system cost, provided that a low cost TOF can be developed, which is one of the major objectives of this dissertation.

2.5 Summary

In this chapter, the fundamentals of interferometric optical sensor demodulation were briefly described. The challenges in sensor interrogation include the non-linear and periodical feature of the interference fringes which requires sophisticated sensor demodulation strategies, the presence of low frequency random environment fluctuations which causes the changes in the amplitude of the detected signal (signal fading) and the distortion of the signal (frequency up-conversion), and the spectral distribution of a low-coherence source which makes it important to consider the contribution of all the wavelength components that reach the detector.

A scanning white-light interferometry (S-WLI) requires a scan of the OPD of a local receiving interferometer (LRI) or optical length of the reference arm of the sensing interferometer. The dynamic range of a S-WLI sensing system is the largest compared with other demodulation schemes. However, due to the small amplitude difference between two adjacent interference fringes, the achievable accuracy for central fringe identification is less than one-tenth of a fringe width. In general, the two-interferometer configuration requires large scan range and has low mechanical stability, while scanning the reference arm is hard, if not impossible, to be applied to Fabry-Perot and Sagnac interferometers due to the difficulty to access the reference beam.

The spectral-domain white-light interferometry (SD-WLI) is based on the detection of the output spectrum of the sensing interferometer with a spectrometer. Various algorithms, such as fringe peak tracking and Fourier transform, have been developed to recover the OPD of the sensor from the output spectrum. SD-WLI requires no mechanical scanning, is applicable to various types of interferometer, insensitive to source fluctuations, and very accurate and reliable.

Speed and price are two major issues with spectral-domain WLI.

Tunable-laser-based Wavelength-Tuning Interferometry (TL-WTI) represents the latest technology in interferometry. It can deliver the highest optical power density to a sensor, and therefore, extremely high SNR can be expected. Both the functions of a SD-WLI and linear demodulation can be effectively realized by using a tunable laser. The factors retarding the widespread use of TL-WTI in sensing are the comparatively high cost and slow scan rate. However, with continuous reduction of the price and increase of scan speed of tunable lasers, TL-WTI may be widely accepted in the sensing industry as in the optical communications.

The author proposed a tunable-optical-filter-based white-light interferometry (TOF-WLI) as an alternative solution to the aforementioned approaches. By introducing a tunable optical filter into a WLI system, one can interrogate an interferometer in the similar ways as using the TL-WTI, but at considerably low cost, provided that a cheap TOF can be designed specifically for sensing applications.

Chapter 3 Theoretical Analysis of Interferometric Sensors Interrogated by a TOF-WLI

In this chapter, a theoretic study of the performances of a white-light interferometric sensor is presented. The system configuration used for this study is that shown in Fig. 2.6. We consider two cases, interrogating the sensor without and with a tunable optical filter. The former configuration (without a filter) has attracted more and more attention recently because OPD smaller than the coherence of the light source can be obtained with new fabrication techniques, such as micromachining and microfabrication, and intensity-based direct detection can be used to recover the measurand through fringe counting in the physical path length domain, similar to that is used in coherence demodulation [96] [97], or linear demodulation [39] [18]. However, the direct detection suffers from direction ambiguity due to the nonlinear transfer function and signal fading caused by environment change-induced drifts, encountered by coherence interrogation. In addition to these drawbacks, the measurement accuracy may be limited by the fringe contrast reduction due to the short source coherence or high F-P finesse. This study provides some insight understanding of the performance of white-light interferometric sensors using direct intensity detection, such as the sensitivity, the fringe contrast and the linear operation range, and the susceptibility factors that exist, as well as how a TOF-WLI may improve these performance parameters.

The sensing interferometer that can be interrogated by a TOF-WLI can be a Mach-Zehnder, a Michelson, a Sagnac, or a Fabry-Perot interferometer, among which, the last one is the most complicated one and others may be represented by a low-finesse Fabry-Perot interferometer in the two-beam interference approximation. Therefore, in this study, only white-light fiber Fabry-Perot interferometers (WL-FFPI) will be used and the others can be treated similarly.

The position of the TOF in Fig. 2.6 can be either in the return path between the coupler and the photodiode or just after the broadband source. Although it can also be located between the sensor and the coupler, double insertion loss is resulted. In this chapter, we treat the TOF as a fixed filter, and its function as a spectrum-scanning tool and an operating-point controller is given in Chapter 2.

3.1 Transfer Function of a Reflective Fiber Fabry-Perot Interferometer

Two fiber Fabry-Perot interferometer (FFPI) models, which have been named the guided FFPI model, shown in Fig. 3.1(a), and the unguided FFPI model, shown in Fig. 3.1(b), respectively, are to be used as a sensing interferometer in this analysis. The guided FFPI model consists of a single-mode fiber with two internal mirrors, which is a good representation of most IFPI type sensors [48] [98]. The unguided FFPI model consists of a single-mode fiber with a dielectric mirror of reflectance R_1 formed on the end-face of the fiber, a “cavity” filled with air, water, polymer, or any other transparent material, and a reflector with a mirror of reflectance R_2 on its front surface. The distance between the two mirrors is l , defined as the physical cavity length of the F-P interferometer. The reflector can be formed by the end-face of any flat surface including a diaphragm or a short piece of fiber. This model is a simplified representation of the EFPI [17] [39] [49], the in-line fiber etalon (ILFE) [99], the diaphragm-based Fabry-Perot interferometer (DFPI) [18] [100], or the MEMS-based Fabry-Perot interferometer [50], the thin film interferometer [101], and all other etalon type devices. The beauty of this FFPI analysis approach is that we can use a single transfer function for both the FFPI models. The transfer function is the starting point from which we can study the sensitivity, the fringe contrast, and the dynamic range of a FFPI sensor.

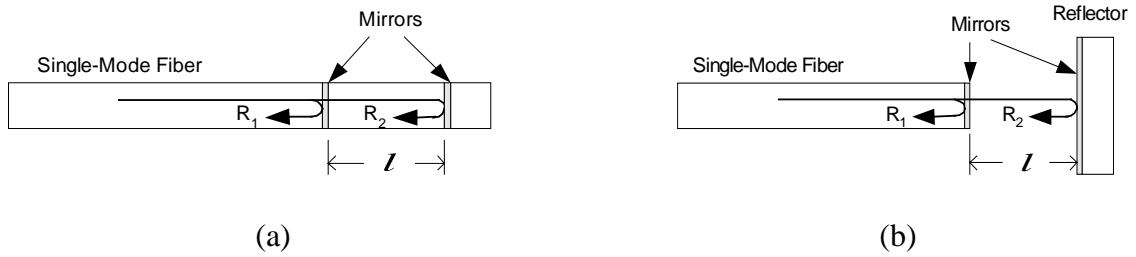


Fig. 3.1 Fiber F-P interferometer models. (a) Guided FFPI model; (b) Unguided FFPI model.

When the TOF is not considered, assuming normal incidence and zero mirror and medium absorption, the transfer function based on a multiple reflection model, in reflection, of a Fabry-Perot cavity at wavelength λ can be expressed as [18]

$$I_r(l, \lambda) = \alpha_0 \cdot I_0(\lambda) \cdot \frac{R_1 + \eta R_2 + 2\sqrt{\eta R_1 R_2} \cos \phi}{1 + \eta R_1 R_2 + 2\sqrt{\eta R_1 R_2} \cos \phi} \quad (3-1)$$

where l is the cavity length, $I_0(\lambda)$ is the input optical intensity at λ , α_0 is a constant describing the optical loss due to the lead-in/out fibers, optical couplers, connectors, etc. in the system, R_1 and R_2 are the reflectance of the two mirrors, ϕ is the optical phase given by

$$\phi = 4\pi nl/\lambda \quad (3-2)$$

where n is the refractive index of the medium in the Fabry-Perot cavity, and η is determined by the round trip loss in the cavity. η can be calculated by [17]

$$\eta = 10^{-\alpha/10} \quad (3-3)$$

where α is the loss coefficient inside the F-P cavity given by

$$\alpha(dB) = \alpha_l(dB) = 4.34(\pi n_c w_0(2\theta)/\lambda)^2 \quad (3-4a)$$

for the guided FFPI model, and

$$\alpha(dB) = \alpha_{II}(dB) = -10\log\left[\frac{1+4\zeta^2}{(1+2\zeta^2)^2+\zeta^2}\right] + 4.34\left\{\left[\frac{l \tan(2\theta)}{w_0}\right]^2 + \left(\frac{\pi n_c w_0(2\theta)}{\lambda}\right)^2\right\} \quad (3-4b)$$

for the unguided FFPI model, where w_0 is the mode field radius of the single mode fiber, n_c is the refractive index of the single-mode fiber cladding, θ is the misalignment angle between the two mirrors, and

$$\zeta = 2l\lambda/(2\pi n_c w_0^2) \quad (3-5)$$

The round trip loss inside a guided F-P cavity is mostly due to the parallel displacement of the two mirrors, and the propagation loss in the guided cavity is negligible because of the short cavity. On the other hand, the mechanisms that may contribute to the round trip loss inside an unguided F-P cavity are much more complex. The first term in Eq. (3-4b) describes the losses due to the beam divergence exiting a single-mode fiber and the cavity length l . The other two terms describe the losses due to the parallel displacement or angular misalignment of the two mirrors. The mirror quality, such as thin film uniformity, surface roughness and flatness, can also contribute to the round trip loss in both of the models, but this contribution can be described by the reduction of the reflectance of the mirrors. A more rigorous treatment of the coupling

efficiency of the front surface and the multilayer mirrors as fiber-end reflectors can be found in reference [102].

For a sensor system interrogated by a low-coherence light source, such as an LED or a SLD, the spectral distribution function of the source, $I_0(\lambda)$, may be approximated by a Gaussian profile

$$I_0(\lambda) = I_0 f(\lambda) = \frac{I_0}{(2\pi)^{1/2} \Delta\lambda} \cdot \exp\left[-\frac{(\lambda - \lambda_0)^2}{(2\Delta\lambda)^2}\right] \quad (3-6)$$

where I_0 is the total input optical intensity, $f(\lambda)$ is the distribution function, $\Delta\lambda = \delta\lambda_{FWHM} / (8\ln 2)^{1/2}$, where $\delta\lambda_{FWHM}$ is the 3-dB bandwidth of the light source, and λ_0 is the central wavelength of the low-coherence source.

The total reflection is a summation of the reflection contribution of each wavelength component. The total transfer function can, thus, be expressed by the integration of Eq. (3-1) over the whole spectrum range of the source BW

$$\frac{I(l)}{I_0} = \int_{\lambda_0 - BW/2}^{\lambda_0 + BW/2} \alpha_0 f(\lambda) \cdot \frac{R_1 + \eta R_2 + 2\sqrt{\eta R_1 R_2} \cos \phi}{1 + \eta R_1 R_2 + 2\sqrt{\eta R_1 R_2} \cos \phi} d\lambda \quad (3-7)$$

Eq. (7) is valid not only for a Gaussian light source, but also for any light source, as long as its spectral distribution function $f(\lambda)$ is known. When a bandpass optical filter is used to interrogate a white-light FFPI sensor, $f(\lambda) = f_s(\lambda) \cdot f_f(\lambda)$ should be used, where $f_s(\lambda)$ is the spectral distribution of the broadband source, while $f_f(\lambda)$ is the transmission spectrum of the filter. For the sake of simplicity, we assume that all the sources used for the following discussions have a Gaussian spectral-power density distribution. Starting from Eq. (7), we can derive formulas for the sensitivity, the fringe contrast, and the dynamic range if the linear operation region is used.

3.1.1 Sensitivity

The sensitivity of the sensor in response to the cavity length change is obtained by the derivative of $I(l)$

$$S(l) = \frac{dI(l)}{I_0 \cdot dl} = 8\pi m \cdot \int_{\lambda_0 - BW/2}^{\lambda_0 + BW/2} \alpha_0 f(\lambda) \cdot Z(l, \lambda) d\lambda \quad (3-8)$$

where

$$Z(l, \lambda) = -\frac{\sqrt{\eta R_1 R_2} \cdot (1 - R_1)(1 - \eta R_2) \cdot \sin(4\pi n l / \lambda)}{\lambda \cdot [1 + \eta R_1 R_2 + 2\sqrt{\eta R_1 R_2} \cos(4\pi n l / \lambda)]^2} \quad (3-8a)$$

In the derivation of Eq. (3-8), $d\eta/dl$ was assumed to be sufficiently small compared to cavity length dependence of sine and cosine terms in the equation so that it is negligible. This assumption is valid when the F-P cavity length is shorter than 100 μm and the angular displacement is less than 2.0° , which is true for most FFPI sensors. Eq. (3-8) can be used to calculate the sensitivity and Eq. (3-7) can be used to calculate the signal amplitude of an FFPI sensor with any mirror combination and at any physical cavity length l , provided that the distribution function of the light source is known. Fig. 3.2 shows an example of the intensity and the sensitivity as a function of the cavity length (nl/λ_0) for an IFPI sensor with 30% reflective films, zero misalignment, and $\delta\lambda_{\text{FWHM}}=35\text{nm}$ at 1300 nm wavelength.

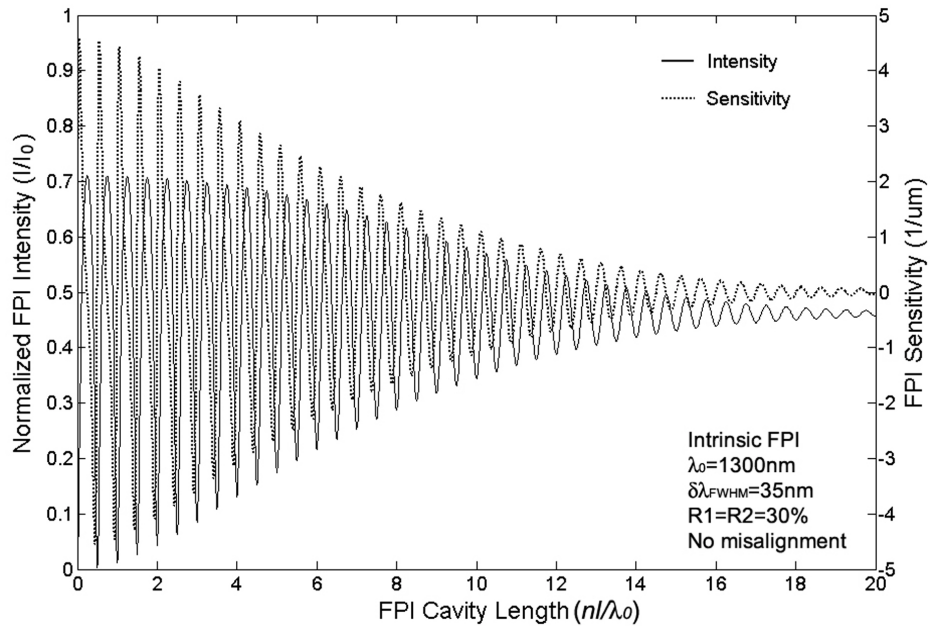


Fig. 3.2 Interference fringes and sensitivity as a function of optical path length of a typical low-finesse FFPI sensor.

Sometime it is of more interest to know the maximum sensitivity of an FFPI sensor designed for dynamic measurements of weak perturbations, such as acoustic waves and dynamic pressure

[4] [8] [13]. For a low-finesse FFPI, the maximum sensitivity usually occurs at the quadrature points of the transfer function when an LED or a SLED is used, which are

$$l_{SV}(m) = \frac{(2m+1/2)\lambda_0}{4n}, \text{ for the sensitivity valleys} \quad (3-9a)$$

$$l_{SP}(m) = \frac{(2m+3/2)\lambda_0}{4n}, \text{ for the sensitivity peaks} \quad (3-9b)$$

where $m=0, 1, 2, \dots$, is the interference fringe order number, and l_{SP} and l_{SV} are the cavity lengths corresponding to the sensitivity peaks and valleys, respectively.

Many researchers have proved this in the past. However, this conclusion is valid only for a low-finesse and a narrow source bandwidth. For example, the maximum sensitivity point in the transfer function will move to shorter cavity length as the finesse increases, and to longer cavity length as the source bandwidth increases. These short and long shifts cannot easily be observed directly from Eq. (3-8), but numerical calculation of Eq. (3-8) in the next section will prove this conclusion. For the sake of convenience, we name the positions of these maximum sensitivity points as “quasi-quadrature points” or “quasi-Q points”, though they do not occur at the real Q-points.

3.1.2 Fringe Contrast

The fringe contrast C of a F-P interferometer is defined as

$$C = [I(l_P) - I(l_V)]/[I(l_P) + I(l_V)] \quad (3-10)$$

where $I(l_P)$ and $I(l_V)$ are the fringe intensities at a peak and the valley next to the peak of the interference fringes, and l_P and l_V are the corresponding cavity lengths, respectively.

The peaks and valleys of the fringes occur at $dI/dl = S(l)=0$. By letting $S(l)=0$ in Eq. (3-8), the positions of the peaks and valleys may be computed. However, an analytical solution cannot be directly obtained from Eq. (3-8). When a narrow bandwidth Gaussian-type light source is used, which means $\delta\lambda_{FWHM} \ll \lambda$, the fringe valleys and peaks occur at

$$l_V(m) = 2m\lambda_0/4n, \text{ for the valleys} \quad (3-11a)$$

$$l_P(m) = (2m+1)\lambda_0/4n, \text{ for the peaks} \quad (3-11b)$$

However, this approximation becomes invalid when the source bandwidth is comparable with the wavelength. Numerical analysis has to be used to locate the peaks and valleys more accurately. This work is done in the next section.

3.1.3 Dynamic Range

The dynamic range of an FFPI sensor with linear operation is defined as the maximal magnitude of the measurand without significant distortion. Obviously, the maximal magnitude of the measurand is absolutely determined by the allowed maximal cavity length change. Here, for the sake of continuity, we define the dynamic range as the maximum cavity length change ΔL , in which the variation of the sensitivity $S(l)$ is within 3-dB from its peak, a common number used to define the response flatness of a sensor or a system, thus

$$\delta_s = \left| \frac{S(l) - S(l_{SP,SV})}{S(l_{SP,SV})} \right| \leq 50\% \quad (3-12)$$

and

$$\Delta L = 2 \times \left| l - l_{SP,SV} \right| \quad (3-13)$$

Other linearity bounds may be used for the definition of a linear region and dynamic range depending on the specific applications. In order to convert the dynamic range ΔL into that of the measurand, an equation relating the cavity length change and the measurand is required, which is different for different sensor configurations.

3.2 Numerical Analysis Results

Based on the analysis in the previous section, a numerical method can be employed to estimate the peak sensitivity using Eq. (3-8), the fringe contrast using Eqs. (3-7) and (3-10), and the dynamic range using Eqs. (3-8), (3-12) and (3-13), of an FFPI sensor of various configurations. In the first calculation, we model the characteristics, in terms of the peak sensitivity, the fringe contrast, and the dynamic range, of a guided FFPI sensor model with symmetric mirrors interrogated by a broadband source of $\delta\lambda_{FWHM}=35\text{nm}$. We consider two cases, in which the OPD is always a variable, while either finesse or angular misalignments will be treated as a parameter. This numerical analysis shows how a white-light interferometric sensor is

sensitive to OPD changes, the finesse, misalignments and environment changes. In a second calculation, we consider an optical bandpass filter of different 3-dB bandwidth $\delta\lambda_{FWHM}$. The results will show how a filter may improve a white-light interferometric sensor's performance.

In the following calculations, we assume that the central wavelength of a Gaussian-type light source is $\lambda_0=1300$ nm; the refractive index of the fiber core is $n=1.45$; and the lead-in/out optical path loss is not considered (i.e. $\alpha_0=1.0$). All the marked data points in the sensitivity and the dynamic range curves are taken at the positive sensitivity peaks, while all the marked data points in the fringe contrast curves are taken at the positive fringe peaks.

Sample Matlab programs used for the calculation of sensitivity, fringe contrast and dynamic range are given in Appendix A.

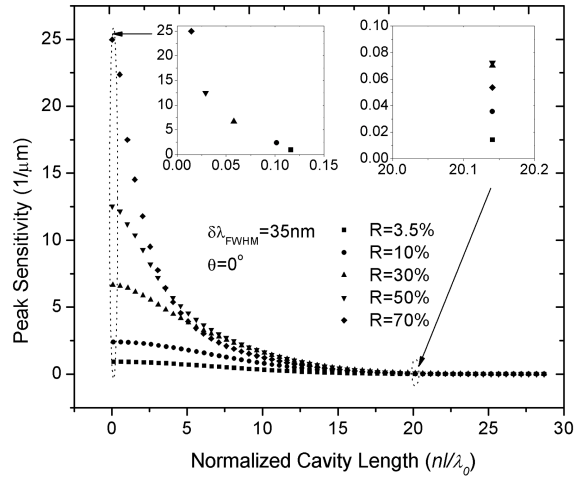
3.2.1 Guided FFPI Model with Symmetric Mirrors without Filter

In order to simplify the calculation, we consider a symmetric FFPI whose two mirrors of the F-P cavity have equal reflectivity, i.e. $R_1=R_2=R$. Also the source bandwidth is chosen as a constant $\delta\lambda_{FWHM}=35$ nm (Close to the smallest among all broadband sources).

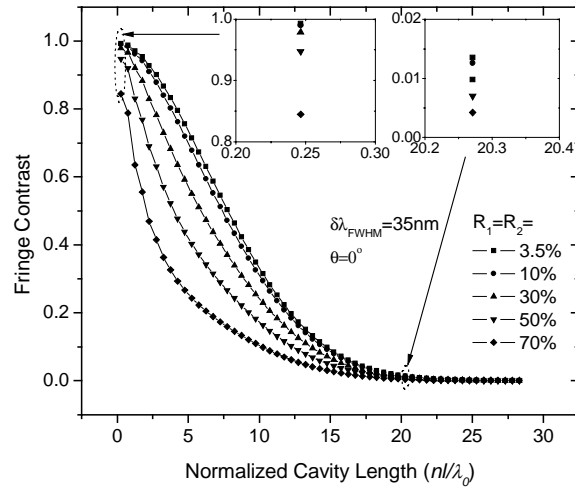
A. Finesse Effects

Assuming that there is no angular misalignment ($\theta=0^\circ$) in the sensor fabrication, then the cavity length dependence of peak sensitivity, fringe contrast and dynamic range are calculated at different mirror reflectance as shown in Fig. 3.3.

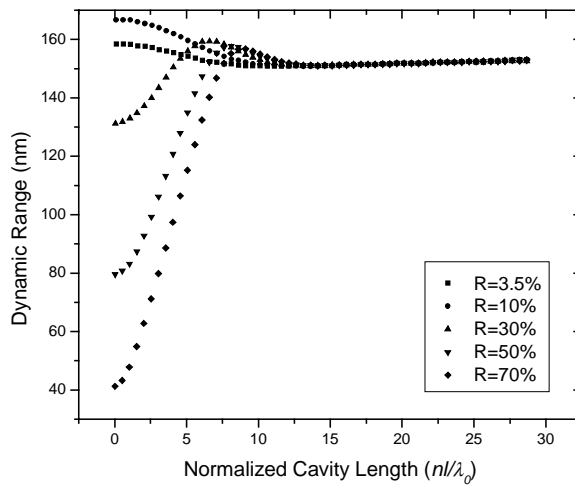
Fig. 3.3(a) indicates that the peak sensitivity increases drastically with the increase of mirror reflectance at a small cavity length. A factor of 27 times of the sensitivity can be obtained at the first sensitivity peak by using 70% reflective films compared with using a low-finesse FFPI ($R=3.5\%$). However, the peak sensitivity decreases faster for higher reflectance with the increase of the cavity length, and at a certain point there is an optimal reflectance for the maximum peak sensitivity as shown in the right inset of Fig. 3.3(a). As indicated in the insets of Fig. 3.3(a), there is a small shift of the peak positions to a shorter cavity length from the Q-points for a low-finesse FFPI when the cavity is short. We name these short-shifted peak positions as “quasi-quadrature points” or “quasi-Q points”. Both the increase of the peak sensitivity and the short-shifts of the quasi-Q points can be attributed to the many multiple-beam interferences at a high-finesse and a short cavity length, which makes the interference fringes much sharper than those of the two-beam interference.



(a)



(b)



(c)

Fig. 3.3 Performances of a guided FFPI model with symmetric mirrors at different finesses.

(a) Peak sensitivity; (b) Fringe contrast; (c) Dynamic range.

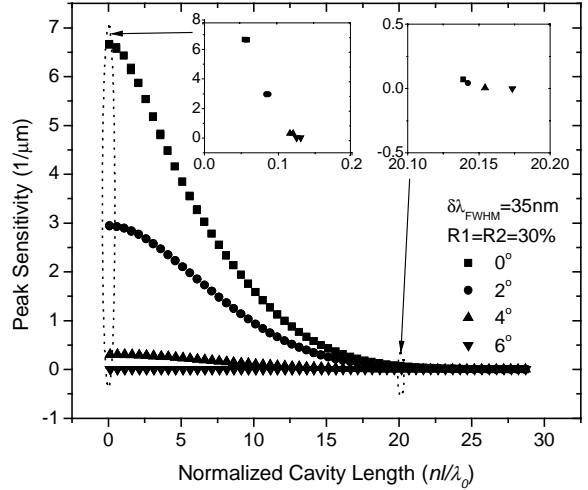
The fringe contrast versus the normalized cavity length for a guided FFPI with symmetric mirrors is shown in Fig. 3.3(b). Obviously, there is no noticeable change of the positions of the fringe peaks at any cavity length as indicated in both the insets. This can be readily deduced from Eq. (3-8) by letting $S(l)=0$. R_1 and R_2 have no effect on the position of the fringe peaks. Another important result is that the fringe contrast decreases as the finesse increases and the decrease rate becomes faster as the cavity length increases. This is due to the fact that when the finesse gets higher, the transmission bandwidth gets smaller, and therefore, less percentage of the total incident intensity is transmitted.

The cavity length dependence of the dynamic range at different mirror reflectivity when the FFPI sensor operates in the linear region is given in Fig. 3.3(c). It is not surprising that the dynamic range is smaller at a high-finesse than at a low-finesse at small OPD because of the sharper fringes for high-finesse cavities. All the curves converge at larger cavity lengths because the interference behaves closer to two-beam interference at larger OPD. What is interesting is that there is an optimal finesse, solely from the point of view of dynamic range, at very small OPD, which changes rapidly when the OPD increases. For example, when the normalized OPD is smaller than 5.5, the optimal mirror reflectance is around 10%, but this changes to 30% when the normalized OPD is between 5.5 and 7.5. It is not readily apparent why this transition occurs.

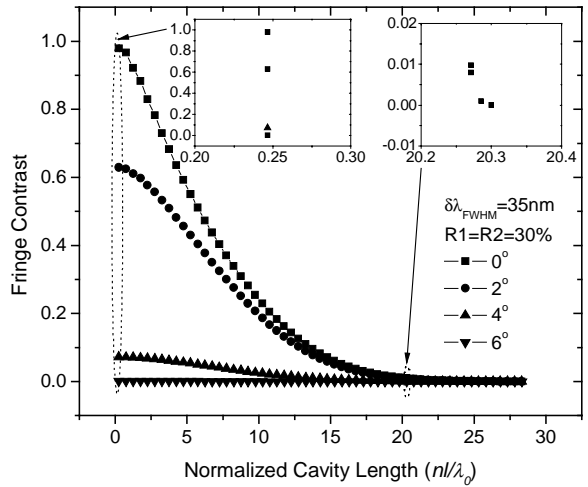
On the other hand, these results tell us that when medium- or high-finesse interferometers are used for higher sensitivity, the sensor becomes more sensitive to manufacture tolerance and environmental drifts, has a reduced fringe contrast and a smaller linear operation range. The increased sensitivity to environment drifts and a shorter linear range make it essential and more difficult to maintain the operating-point in a linear demodulation scheme, while the fringe contrast reduction may result in reduced signal to noise ratio. I will prove that the use of a TOF-based demodulation can solve the operating-point control issue and significantly improve the contrast.

B. Angular Misalignments

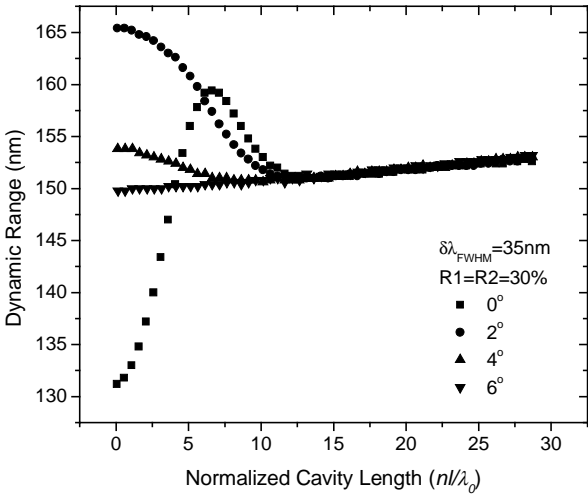
Angular misalignments inevitably occur in the fabrication of white-light interferometric sensors even if sophisticated control techniques are used. As indicated by Eqs. (3-3), (3-4a), (3-7) and (3-8), the round trip coupling efficiency η is a function of the angular misalignment θ , and



(a)



(b)



(c)

Fig. 3.4 Performance degradation of the guided FFPI model with symmetric mirrors caused by angular misalignment. (a) Peak sensitivity; (b) Fringe contrast; (c) Dynamic range.

is an important factor in the calculation of the peak sensitivity, and the contrast as well as the dynamic range of a guided FFPI sensor.

Assuming that the mirror reflectance is constant, 30%, the dependence of the performance of a guided FFPI sensor with symmetric mirrors on the cavity length and the angular misalignments are shown in Figs. 3.4(a), (b) and (c). Apparently, the peak sensitivity and contrast decrease rapidly with the increase of either the OPD or the angular misalignment. Actually, above 4° , the response of the sensor to any measurand becomes unacceptably small. A long-shift of the position of the sensitivity peaks occurs when the misalignment becomes larger, but becomes smaller when the OPD increases, as indicated by the insets of Fig. 3.4(a). This long-shift of the sensitivity peaks may be explained as a reverse process of the short-shift previously discussed in the finesse effects because the increase of the mirror angle can be equivalent to the decrease of the effective reflectance of the second mirror, and thus, the finesse of the F-P cavity. The angular misalignment does not make a noticeable difference on the position of the fringe peaks at small OPD, as shown in the left inset of Fig. 3.4(b). However, it does when the OPD increases, as shown in the right inset of Fig. 3.4(b). The peaks shift slightly to longer cavity lengths as the misalignment gets larger.

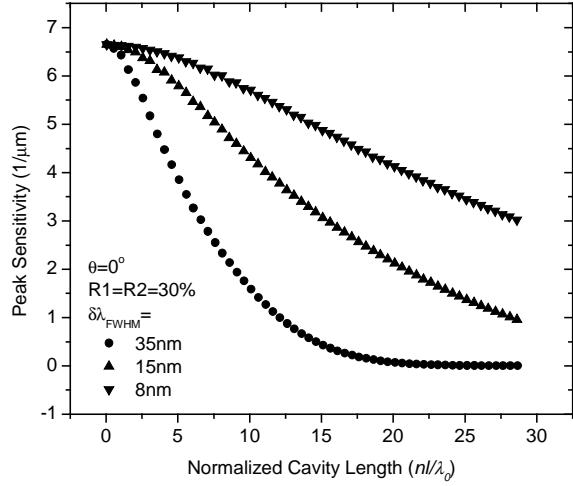
The effect of angular misalignment on the dynamic range is similar to that of the finesse. It will tend to converge when the OPD becomes large. The major difference is that the maximum of the dynamic range moves to a shorter cavity length as the misalignment increases.

Obviously, the shift of the “quasi-Q points” and the reduction of the linear operating range as well as the fringe contrast make it very necessary to find an efficient way to stabilize the operating-point and improve the fringe contrast.

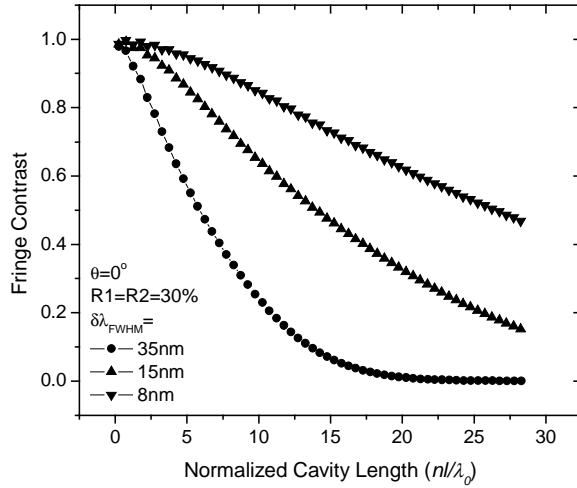
3.2.2 Filter Effects

In order to investigate the effects, in addition to the spectrum scanning and operating-point control, of using a tunable optical filter in the demodulation of a white-light interferometric sensor, filters of different passbands are simulated using different $\delta\lambda_{FWHM}$ in the calculation.

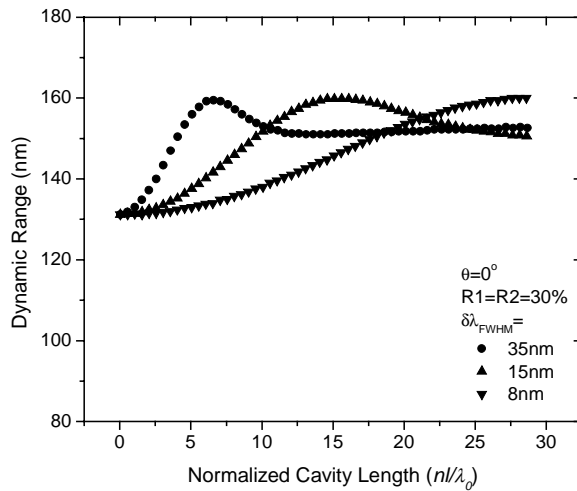
Fig. 3.5 shows the theoretical results of the peak sensitivity, fringe contrast and dynamic range for a guided FFPI sensor with symmetric mirrors having zero angular misalignment and 30% mirror reflectance, where $\delta\lambda_{FWHM}=35$ nm represents no filter, and $\delta\lambda_{FWHM}=15$ nm or 8nm



(a)



(b)



(c)

Fig. 3.5 Performance improvements due to an optical bandpass filter. (a) Peak sensitivity; (b) Fringe contrast; (c) Dynamic range.

means a filter of 15nm or 8nm 3-dB bandwidth is used.

At very small OPD values, the presence of a filter does not make significant difference on the sensitivity, the contrast and the linear range. However, as the OPD increases, the sensitivity and the contrast increases significantly with the decrease of the filter passband, as indicated in Fig. 3.5(a) and Fig. 3.5(b), while the peak of the dynamic range shifts to larger OPD, as shown in Fig. 3.5(c). The improvement on the sensitivity and contrast can be reasonably attributed to the longer coherence length at a narrower source bandwidth.

Unfortunately, it is very challenging to design white-light interferometric sensors of very small OPD and a majority of white-light interferometric sensors have an OPD from several to 100 microns. Therefore, the use of a tunable filter not only makes it easier to maintain the linear operation, but also significantly improve the sensitivity and fringe contrast.

3.3 Summary

In summary, a systematic analysis method has been developed to study the performance, including sensitivity, fringe contrast and dynamic range, of a white-light interferometric sensor. Numerical results on a guided FFPI sensor with symmetric mirrors show that a practical white-light interferometric sensor, especially those of high-finesse, are very sensitive to fabrication tolerances and environment changes, and it is challenging to maintain a linear operation or achieve high accuracy in the Spectrum-Domain demodulation. Numerical analysis also indicates that the use of a TOF may, in addition to the capability of stabilizing an operating-point for maximum sensitivity and linearity and scanning for output spectrum, significantly improve a white-light interferometric sensor's sensitivity and fringe contrast. The minimum bandwidth of the TOF is limited by the available source power, and therefore a tradeoff has to be made between for high sensitivity and contrast and for low insertion loss. To the best of our knowledge, similar theoretical analysis and numerical data have not been published by other researchers.

Chapter 4 Tunable Optical Filters: A Review

Tunable optical filters are now key components for wavelength or channel selection not only in optical communication systems using wavelength division multiplexing (WDM) techniques [103]-[105], but also in fiber optic video broadcast and select networks [106] [107], fiber optic sensing systems [68] [83] [84], as well as optical spectrometers [86] [109] [100]. However, different applications usually require different TOF characteristics, including bandwidth, tuning range, tuning speed, insertion loss, polarization dependence, stop band rejection ratio or sidelobe depression ratio, scalability, cost, repeatability and stability.

This chapter first introduces, in Section 4.1, the specifications and requirements of tunable optical filters for telecommunications, video distribution networks, optical fiber sensing applications and optical spectroscopy. Current tunable optical filter technologies that have received most interest are reviewed in detail in Section 4.2. Then, a summary of the current TOF techniques and a comparison of these techniques, from the point of view of sensing applications, are given in Section 4.3.

4.1 TOF Specifications

In telecommunication networks, TOFs can be used for amplified spontaneous emission (ASE) suppression of optical signals, for single channel demultiplexing from a multichannel WDM optical signal stream, and in flexible and dynamic wavelength add/drop applications. Tuning speed directly determines the switching speed between different circuits, and therefore, high speed is a fundamental requirement for tunable filters. For circuit-switched networks, tuning time of no more than a few milliseconds is essential. Very high-speed tunable filters, in the microsecond and nanosecond range, are a must in packet- and cell-switched networks [104]. Bandwidth and tuning range become more and more critical with the increased deployment of DWDM systems. Using filters of a very narrow bandwidth and a large tuning range is, so far, the most effective way to increase the channel capacity and to reduce the crosstalks in DWDM networks. Current optical communication systems are usually designed to work within the bandwidth of the erbium-doped fiber amplifier (EDFA), which has a gain bandwidth of about 30nm, and a channel separation of 0.5nm. Another critical parameter is the scalability of the

tunable filter, because in a large telecommunication network, tens or even hundreds of cascaded tunable filter or tunable filter arrays are often inevitable.

In fiber optic video broadcast and select networks, requirements on the bandwidth and tuning range are similar to those for DWDM communication networks in order to deliver as many channels as possible to subscribers, but cost is the most crucial factor. Fiber-to-the-home, to some extent, relies on the cost reduction of optical parts to an acceptable level for end users. Tunable optical filter is one of these parts. Channel selection by end users with a TOF has definite advantages over the solution of using high frequency and wideband electronics. On the other side, the tuning speed requirement for a video distribution system is much lower than that for communication systems. For selecting video channels in a subscriber television set, a tuning time, randomly between any channel pairs, up to 100 milliseconds is still acceptable.

TOFs are occasionally used in fiber optic sensing applications for wavelength demultiplexing of fiber Bragg grating sensors for wavelength shift and spectral scanning in interferometric sensors. Bandwidth is from sub-nanometer up to above ten nanometers, and tuning range from tens of nanometers to above 100 nm, varying from system to system. Tuning speed also varies, but generally slow. For example, a scanning time of a few second may be enough for the measurement of static and very slow signals, such as temperature, strain, and chemical or biomedical concentration. However, in most application areas, fiber-optic sensors have to face fierce competition from their electronic counterparts available extremely cheap in the market. Unfortunately, available TOFs in the market cost, in general, from \$2,000 up to above \$10,000 each.

Traditional optical spectrometers use dispersive devices, such as diffraction gratings. The wavelength scanning is realized either by rotating the grating or a mirror, or moving the position of the detector using a linear stage, and or using a photo-detector array. With the driving force for chemical and biomedical sensing, recent developments of spectrometers have been focused on the miniaturization using tunable optical filters. Obviously, a high resolution and a large tuning range are always favorable for the detection of a wide range of chemicals and biological agents. As for optic sensors, TOFs for spectrometers can sacrifice the tuning speed for a low cost in order to be mass-producible. Low speed is usually acceptable because most measurands change slowly or even do not change in a short period of time.

A large stop-band-rejection ratio (SBRR) or sidelobe-depression ratio (SDR) is always favorable for all applications. An ideal filter should have sharp band edges and infinite stop band rejection. In DWDM communication networks and fiber optic CAVT networks, larger SBRR means smaller crosstalks in an existing system or more channels in the available total bandwidth with a certain level of crosstalk. For optical sensors and spectrometers, small SBRR directly causes reduced measurement accuracy because of the intensity contributions of the out of band wavelengths.

Repeatability and stability are equally important parameters as those mentioned above in all applications. Highly repeatable and stable TOFs mean high resolution and accuracy in measurement instruments, and high reliability or low bit-error-rate (BER) in communications, and high quality in video distribution networks. Any survivable tunable filter technology must be highly repeatable and stable in long terms.

Insertion loss and polarization dependence are another two parameters that have to be considered in any optical systems. Low insertion loss and polarization dependence is mostly favorable in those systems which are sensitive to power budget, such as access networks, and to polarization, such as optical sensors.

4.2 Current Tunable Optical Filters

In the past decades, a great number of different tunable filter techniques have been proposed and developed. Some of them have been extensively studied and have achieved great success, at least in WDM telecommunication networks. These tunable filter techniques can be categorized, according to the core device being used, into Fabry-Perot TOF, mode coupling TOF, diffraction grating TOF, fiber grating TOF, and other tunable filters including Mach-Zehnder interferometers, ring or disk resonators, waveguide arrays, and photonic bandgap (PBG) filters. Among these types, Fabry-Perot filters have seen most wide research all over the world, and can be further classified as bulk F-P, fiber F-P, liquid crystal F-P, MEMS F-P, and thin film tunable filters.

In this section, I introduce the fundamental principles behind each technique and its characteristics, including bandwidth, tuning range, tuning speed, insertion loss, polarization dependence, stop band rejection, scalability, cost, repeatability and stability.

4.2.1 Fabry-Perot Type Tunable Filters

Fabry-Perot interferometers have been extensively studied for a very long time and a large number of different F-P filter structures have been developed. Although the physical forms are different, the theory of each of the various types of F-P filters is similar, which is based on multiple-beam interference [9]. Their common feature is that their interference fringes are much sharper than those in the two-beam interference, and therefore the width of the passband is reduced and the sidelobe depression is increased.

Fig. 4.1(a) shows the diagrammatic form of a symmetric F-P filter. Assuming that the cavity is loss free, the transmittance at wavelength λ for a plane wave incidence is given by [111]

$$T = \frac{1}{1 + F \sin^2 \delta} \quad (4-1)$$

where the phase term

$$\delta = 2\pi nL \cos \theta_0 / \lambda \quad (4-2)$$

where L is the F-P cavity length, n is the refractive index of the medium in the cavity, θ_0 is the angle of incidence, and

$$F = \frac{4R}{(1-R)^2} \quad (4-3)$$

where R is the reflectance of the mirrors. A plot of transmission coefficient T against optical phase δ is given in Fig. 4.1(b). Obviously, the peak transmission occurs at $\delta = m\pi$, where $m=0, \pm 1, \pm 2, \dots$, and m is known as the order of the fringe. When n, L and θ_0 are constants, the phase δ is determined solely by the wavelength λ . Thus, the transmission peaks occur at $\lambda = 2nL/m$. The distance between the two fringe peaks in the wavelength domain is called free spectral range (FSR), and the full width half maximum (FWHM), in terms of wavelength, of the fringes is termed the bandwidth of the transmission band. Consequently, the FSR is given by

$$FSR = \lambda^2 / 2nL \cos \theta_0 \quad (4-4a)$$

in terms of wavelength units, or

$$FSR = c / 2nL \cos \theta_0 \quad (4-4b)$$

in terms of frequency units, where c is the light speed in vacuum. As shown in Fig. 4.1(b), the BW becomes very much narrower as R increases. The ratio of the FSR to the BW is called the finesse (Γ) of the interferometer, i.e. [112],

$$\Gamma = FSR / FWHM = \frac{\pi\sqrt{R}}{(1-R)} \quad (4-5)$$

and

$$FWHM = \left(\frac{1-R}{\pi\sqrt{R}} \right) \cdot \left(\frac{\lambda^2}{2nL\cos\theta_0} \right) \quad (4-6)$$

Apparently, the BW depends not only on the reflectance of the mirrors, but also on the cavity length, and the refractive index of the cavity medium as well as the angle of incidence.

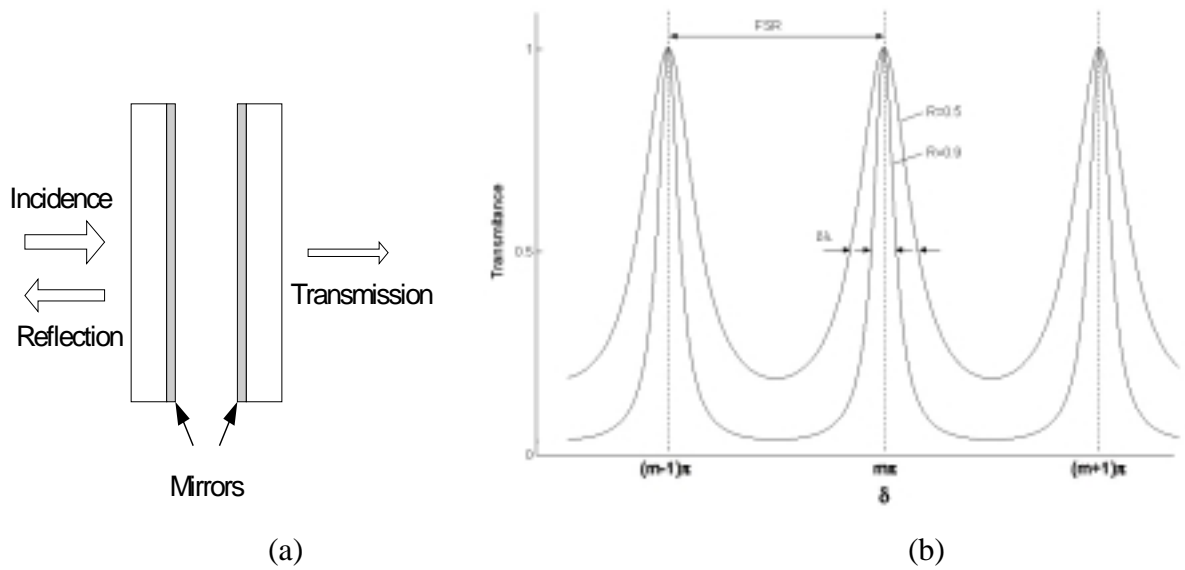


Fig.4.1 A Fabry-Perot filter. (a) Principle diagram; (b) Transmission bands.

In order to tune the Fabry-Perot filter from one wavelength to another, the resonant conditions of the F-P cavity have to be changed. As indicated by Eq. (4-2), this can be done by fine-adjusting the mirror separation, using a linear stage, piezoelectric controls [113] [114], electrostatic forces [83] [115]-[117], or thermal expansion [118], by changing the angle of incidence, known as an angle-tuning [119]-[121], or by modulating the refractive index of the medium in the F-P cavity using a voltage [122] [123] or heat [124]. As indicated by Fig.4.1(b),

the transmission profile of Fabry-Perot tunable filters (FP-TFs) is defined by Airy function which has high resolution capability.

The wavelength shift $\Delta\lambda$ can be derived directly from Eq. (4-2)

$$\Delta\lambda = \frac{\Delta L}{L} \cdot \lambda \quad ; \quad \text{if only cavity length is tuned.} \quad (4-7a)$$

or

$$\Delta\lambda = \frac{\Delta n}{n} \cdot \lambda \quad ; \quad \text{if only the refractive index is changed.} \quad (4-7b)$$

or

$$\Delta\lambda = -2\lambda \sin^2\left(\frac{\theta + \Delta\theta}{2}\right) \quad ; \quad \text{if only the angle of incidence is changed.} \quad (4-7c)$$

When the tunable filter operates within a small tuning range near the normal incidence ($\theta=0$), Eq. (4-7c) can be simplified as

$$\Delta\lambda = -\lambda \cdot \Delta\theta^2/2 \quad (4-7d)$$

The advantage of tuning the Fabry-Perot filter by changing the cavity length or the refractive index of the medium in the cavity is that the relationship between the wavelength shift and the change of the cavity length or the refractive index is linear, which makes a calibration unnecessary.

1) Bulk F-P Filters

A conventional F-P filter is simply made of two flat reflectors separated by a fixed spacer of some thickness. By adjusting the spacer thickness with a linear stage, or changing the angle of incidence with a rotary stage, one can adjust the wavelength of the filter. However, in spite of their superior optical resolution and large tuning range, bulk optic Fabry-Perot devices have several fundamental problems.

There is no way of guiding the light between the two mirrors, which results in extreme sensitivity to misalignment, temperature and vibration. With each bounce of the beam, some light walks off and is lost. Thus large insertion loss is not unusual.

Since the tuning is based on mechanical movement, there is no mechanism for moving the mirrors by the extremely small, atomic distances required to accurately tune or continuously scan the Fabry-Perot device. Repeatability and reliability can be an issue because of mechanical wear.

They are not compatible with fiber optic transmission systems and do not meet the miniaturization trend in optical systems. In bulk F-P filters, expensive optical stages and motion control systems have to be used, which significantly increase the system cost.

Therefore, volume F-P tunable filters are disappearing gradually from the industry and exist mostly in university laboratories.

2) Fiber Fabry-Perot Tunable Filters

Of all innovative tunable optical filter technologies pursued, fiber Fabry-Perot tunable filters (FFP-TFs) [113] [114] have become one of the most attractive TOF technologies, and been widely deployed in fields since the late 1990s [125]. Typical configuration of a FFP-TF is shown in Fig.4.2. The mirrors are directly deposited on to the polished fiber ends, which are aligned by a ferrule and two alignment fixtures. The tuning is usually achieved by changing the spacing of the gap between the mirror fibers using a piezoelectric element. Variations from this typical configuration are also available. For example, an internal waveguide may be used to eliminate extraneous cavity modes and ease mirror alignment required for high-finesse and low loss operation [113].

The best performances achieved by FFP-TFs include large tuning range ($>200\text{nm}$), high-finesse (>7000), high contrast ($>70\text{dB}$), and low insertion loss ($1.0\sim 2.0\text{dB}$) [125]. The tuning speed is determined by the resonant frequency of the PZT actuator. Resonant frequencies of industrial piezo actuators range from a few tens of kHz for actuators with total travel of a few microns to a few kHz for actuators with travel more than 100 microns. Other superb features of FFP-TFs are very compact in size, all fibers, thus, no in/out coupling is required compared to bulk or MEMS tunable filters, ease of alignment, and polarization independence.

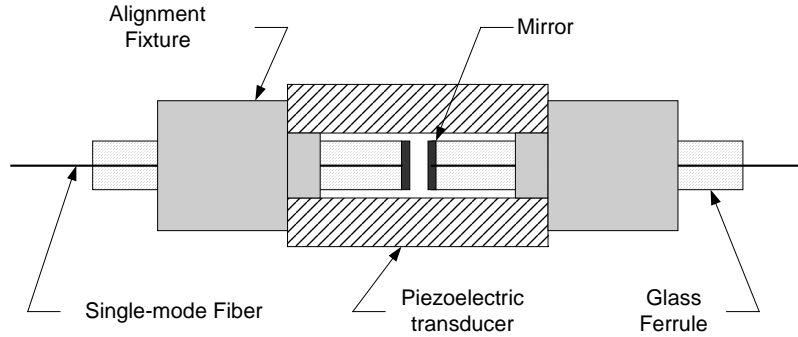


Fig. 4.2 Fiber Fabry-Perot tunable filter configuration [125].

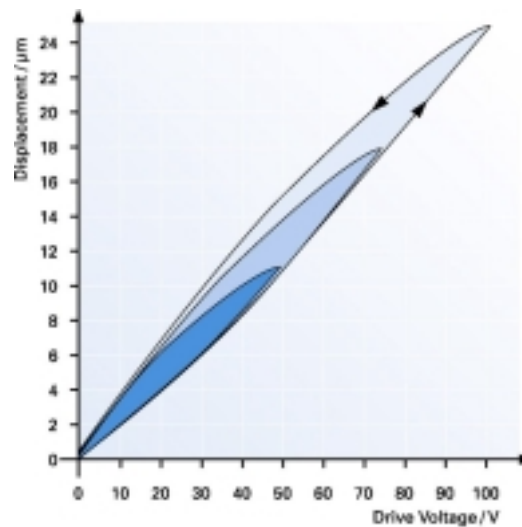


Fig. 4.3 Hysteresis curves of an open-loop piezo actuator for various peak voltages. The hysteresis is related to the distance moved [126].

However, FFP-TFs based on PZT do have their limitations, which are

- The glass ferrules, PZT transducers and alignment fixtures commonly used in the FFP-TF constructions have large thermal expansions. Compensation has to be considered during the design of the filters to reduce the temperature sensitivity and long-term drifts.
- Piezoelectric actuators generally have significant hysteresis and creep effects. Hysteresis is typically on the order of 10% to 15% of the commanded motion, as shown in Fig.4.3 [126]. A position sensor and a closed loop operation have to be used for good linearity, stability, repeatability and accuracy. The use of the position sensor and the closed loop operation significantly increases device cost and complexity.

- High voltage up to tens of volts is required to drive a piezoelectric actuator for the achieved tuning range.
- The achievable tuning speed of tens of KHz limits FFP-TFs to circuit-switched networks and other applications requiring lower speed.

3) Liquid Crystal Fabry-Perot Filters

Fabry-Perot tunable filters can also be fabricated by inserting a layer of liquid crystal (LC), whose refractive index is voltage controllable, between the two mirrors of an etalon. A Fabry-Perot tunable filter with a liquid crystal as cavity material is a combination of the F-P structure with LC technology, named a liquid crystal Fabry-Perot interferometer (LC-FPI). In this case, the physical thickness of the F-P cavity and the incident angle are usually fixed and the tuning can be achieved by modulating the refractive index of the liquid crystal with an applied voltage.

LC-FP-TFs have been fabricated by using both a bulk Fabry-Perot interferometer [127] and a fiber Fabry-Perot interferometer (LC-FFP-TF) [122]. A bandwidth of 0.2~0.5nm, a tuning range from 10 nm to 50 nm, a tuning speed of tens microseconds, and an insertion loss between 3dB to 5dB are typical for LC-FP-TFs, though a bandwidth as low as 0.07nm and a tuning range of 127nm were reported [123].

The first advantage of LC-FP-TFs is that the achievable minimal bandwidth is smaller than that of FFP-TFs because of the presence of the liquid crystal in the F-P cavity. The second advantage is that most LC-FP-TFs can be operated with a relatively low driving voltage (< 15V). However, LC-FP-TFs have a serious drawback which is the polarization-dependence. This polarization dependence can still be a problem when they are used for polarization sensitive systems, though it has been reduced to approximately 0.17 dB [128]. Another drawback of LC-FP-TFs is the limited tuning range compared to FFP-TFs and MEMS tunable filters. A high drive voltage has to be used for a large tuning range. As the bulk Fabry-Perot filters, LC-FP filters fabricated on substrates have the same difficulty to couple light between a single-mode filter and the filter. Although the LC-FFP-TFs suffer less from the coupling loss, fabricating electrodes and inserting liquid crystal inside the FFP is not an easy task.

4) MEMS Tunable Filters

In the last 10 years, tunable optical filters based on micromachining and microfabrication techniques developed for microelectromechanical systems (MEMS) have attracted the most attention and research interests among all tunable optical filter technologies. Although hundreds of MEMS-based tunable filters (MEMS-TFs) structures have been proposed, the fundamentals behind are the same – using lithography, etching or lift-up, bonding, and deposition processes to fabricate Fabry-Perot etalons on semiconductor wafers, such as glass, silicon, GaAs or InP substrates. Common MEMS F-P structures are cantilever-substrate pairs [115] [118], membrane-substrate pairs [116], or wafer-wafer pairs [83]. Mirrors are formed by the deposition of multi-layer dielectric films or distributed Bragg reflectors (DBRs) on to the inner surfaces of the MEMS F-P during the fabrication processes. Fig. 4.4 (a) gives a principle diagram of a MEMS Fabry-Perot etalon, while Fig. 4.4(b) shows the schematic of a micromachined vertical cavity filter with thermal strain control. Tuning is achieved by changing the air gap by either electrostatic force between the two mirrors or heat through the electrodes coated on the mirrors.

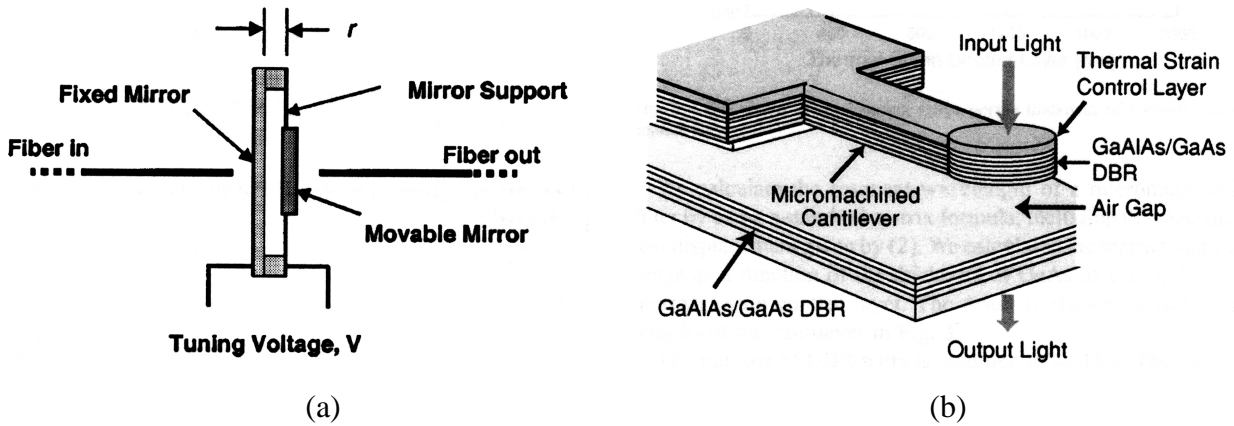


Fig. 4.4 MEMS-TFs. (a) Structure of MEMS Fabry-Perot etalon [31]; (b) Schematic structure of a micromachined vertical cavity filter with thermal strain control [118].

A linewidth of 2~8nm, a tuning range of 10~70nm and an insertion loss of 3~5 dB are very typical for MEMS-TFs, though a linewidth as low as 0.47nm and an insertion loss of less than 1 dB were reported by [117], and a tuning range of above 100nm may be obtainable [118]. The tuning speed of a MEMS-TF is on the order of tens of millisecond when the filter is tuned by

heat, and on the order of microseconds when it is tuned by electrostatic force, which is generally limited by the capacitance of the F-P.

In addition to the above-mentioned characteristics, MEMS-TFs have some unique features compared to other TOFs. First of all, the wafer-scale manufacturing results in very accurately controlled fabrication processes, thus, consistent performances in each batch as well as from batch to batch. Very compact in size and low power consumption is a second advantage of MEMS-TFs. Another important feature is the scalability potential because tens or even hundreds of filters can be fabricated on a single substrate with optical waveguides and other components. Finally, because of the micron scale F-P cavity length, the tuning voltage required can be as low as a few volts which can be supplied directly from a computer. All these features make MEMS-TFs an excellent candidate for telecommunication systems, video distribution networks and sensing applications. If an active lasing medium is chosen as the substrate, tunable lasers can be realized [129].

However, in addition to the obvious need of expensive cleanroom environment, complex semiconductor and microfabrication equipment, hazardous chemicals, and very fine characterization instruments, MEMS-TFs are also susceptible to thermal-mechanical perturbation and nonlinear optical properties [130]. In conventional Fabry-Perot etalons, thermal effects are not significant. However, in high-finesse devices, as the size and mass of the etalon mirrors and their support structures decrease, mechanical thermal noise causes random perturbation to the position of the mirrors, giving rise to random fluctuations of the center frequency of the filters. The nonlinearities are caused by small displacements of one or both of the etalon mirrors in response to changing optical power levels in the cavity. These effects are more significant in high-finesse F-Ps, where the stored optical power level can reach high levels. Another disadvantage is that higher drive voltage ($>50V$) may be required for large tuning range, resulting in possible breakdown of the filter because of high electric field inside the cavity. Last, but not trivial, accurate alignment is generally inevitable in order to couple light in and out of the MEMS-TFs. Large insertion loss from fiber to fiber is not unusual in MEMS tunable filters.

5) Thin Film Tunable Interferometer

For many decades, thin films filters have been the most widely deployed type of fixed optical filters, including edge filters and bandpass filters [111]. However, few dynamically tunable

filters have been designed purely based on thin film interferometers until mid 1990s, though thin films have been extensively used as the mirrors in most F-P tunable filters.

In general, a thin film tunable filter can be constructed by successive deposition of multilayer of quarter-wavelength high-index and low-index dielectric coatings, with a thick film sandwiched in the middle, on a thick substrate, for example, a quartz or silicon substrate. Fig. 4.5 shows the schematic of a typical single cavity thin film Fabry-Perot filter. Tuning of the wavelength can be achieved either by changing the angle of incidence using a rotary stage [121] or the position of the incidence beam using a linear stage [131], heating if thermo-optic material is used as the thick film [124] [132], or even both [119].

A typical thin film tunable interferometer has a bandwidth from 0.2 to several nanometers, a tuning range of 30~60nm, a tuning speed on the order of several milliseconds, and an insertion loss of 1-3 dB. A unique feature of thin film tunable filters is the capability of stacking multiple F-P cavities on a single substrate, thus a flat-topped passband with deep adjacent channel rejection can be obtained, which is particularly useful in DWDM networks [132].

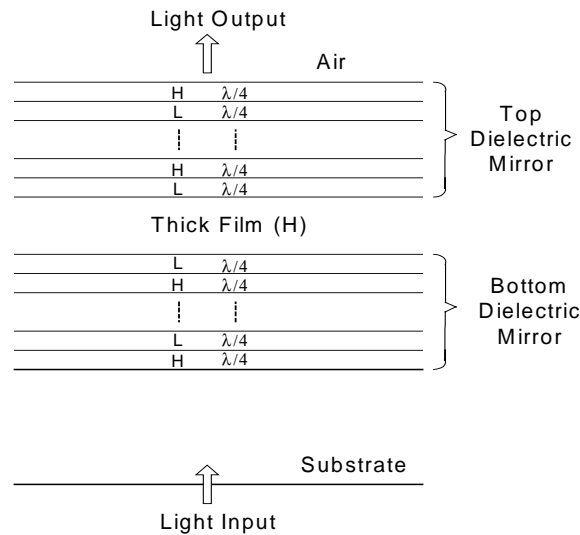


Fig. 4.5 Schematic of a typical thin film tunable interferometer.

Thin film tunable filters do have some drawbacks compared with other tunable filter techniques. As mentioned above, thin film filters are slow, no matter either angle-tuning or thermal tuning is used. The alignment between a single mode fiber and a thin film filter is also

not an easy task, which may result in large coupling loss. When an angle-tuning is used, polarization dependence increases with the increase of the angle.

4.2.2 Tunable Filters Based on Mode Coupling

Coupled mode theory is a method that can be used to describe the wave behavior in a perturbed waveguide system by means of the known normal modes of the unperturbed system [133] [134]. Based on the mode coupling theory, tunable filters can be constructed using acousto-optic, electro-optic or magneto-optic effects. The principle diagram of a typical structure of a mode coupling tunable filter is shown in Fig. 4.6 [107]. Acousto-optic tunable filters (AOTFs) are the most important mode coupling tunable filters. An AOTF consists of an input polarizer, an appropriate acoustic transducer, such as an x-cut LiNbO₃ substrate, and an output polarizer. By changing the frequency of the acoustic waves, a corresponding optical wavelength can be selected. Details on the operation principles of an AOTF can be found in Reference [135] and [136].

A typical AOTF has a bandwidth less than 1.0nm, a tuning range over 100nm, and a tuning speed on the order of microseconds. The distinguished characteristics of AOTFs are capability of selecting multiple arbitrary wavelengths simultaneously if multiple frequency acoustic waves are applied, low operation voltage and compatibility with integrated-optics. The multiple-wavelength selection capability is very useful in an optical add/drop (OAD) device of WDM networks. Major disadvantages in AOTFs are relatively low sidelobe rejection ratio, presence of Doppler frequency shifts, high polarization dependence, sensitivity to temperature change, relatively high power consumption and coupling issues with single mode fibers. The polarization dependence may be solved by more complex design as given in Reference [107].

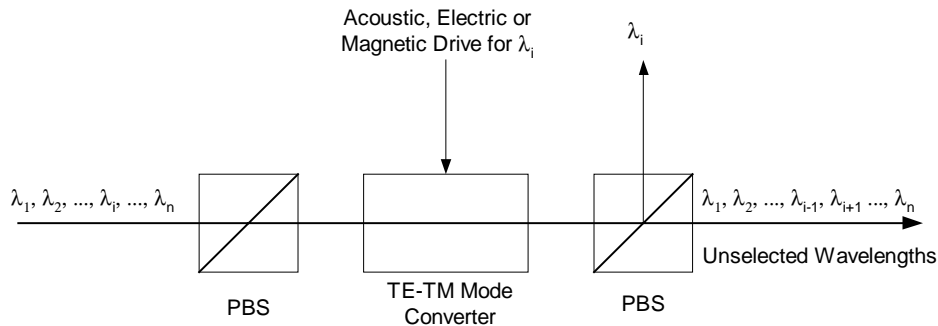


Fig. 4.6 Tunable filter based on mode coupling [107].

4.2.3 Grating Filters

Grating is periodic patterns, such as grooves or variations of refractive index, written in a substrate or an optical fiber. Most available gratings can be categorized into three groups: diffraction grating, fiber Bragg grating (FBG), and long period grating (LPG).

A diffraction grating is grooves formed on the surface of a substrate or periodic variations of refractive index formed inside a substrate. It has long history of being used to separate lights of different wavelengths with unsurpassed high accuracy and precision. Typical applications include spectroscopy, tunable filters, imaging, and optical signal-processing. Tunable filters based on diffraction gratings [137] generally have a much wider tuning range than any other tunable filters, an extremely high resolution, and the availability of a large variety of products for selection. Of course, the apparent drawbacks of volume grating tunable filters are bulk in size, slow in tuning because stages are used, large polarization dependence loss (PDL), and fiber incompatible. Recently, a MEMS tunable diffraction-grating filter with a 3-dB BW of 31.6 GHz was reported by Jill D. Berger and Doug Anthon from Iolon, Inc. [138]. The filter is a miniature monochromator based on a free-space Littrow diffraction-grating, a beam expander and silicon MEMS actuator. A polarization recovery module (PRM) was used to minimize the PDL to less than 0.2 dB. In order to tune the wavelength over 40 nm, ± 140 V has to be applied to the comb elements of the MEMS actuator.

A FBG can be directly written in the core of a photosensitive optical fiber using UV light and a phase mask. A FBG reflects a wavelength that satisfies the Bragg condition, and thus, can act as a band rejection filter. If strain from a stretcher or thermal change is applied to a FBG, the period or the refractive index of the FBG fiber changes accordingly which results in the shift of the Bragg wavelength. When strain ϵ_z is applied, the shift $\Delta\lambda$ of the Bragg wavelength λ is given by [139]

$$\frac{\Delta\lambda}{\lambda} \cong 0.78\epsilon_z \quad (4-8)$$

and when thermal tuning is employed, $\Delta\lambda$ is given by [140]

$$\frac{\Delta\lambda}{\lambda} = (\alpha + \zeta) \cdot \Delta T \quad (4-9)$$

where α is the effective thermal expansion coefficient of the FBG and ζ is the thermo-optic coefficient of the fiber.

The definite advantage of a FBG tunable filter is its single narrow reflection-band, ultra-low excess loss, and ease of fabrication. The disadvantages that limit the use of FBG tunable filters are band-stop filtering, very small tuning range (<15nm), relatively low speed (>2ms) [139], and very sensitive to temperature fluctuations.

LPGs have a similar structure as FBGs, but a much longer period. The fundamental mode guided by the core of the fiber can be coupled into different forward propagating modes guided by the cladding in a LPG. The phase matching condition between the guided mode and the cladding modes is given by [141]

$$\beta_{01} - \beta_{cl}^{(n)} = 2\pi/\Lambda \quad (4-10)$$

where Λ is the grating periodicity, and β_{01} and $\beta_{cl}^{(n)}$ are the propagation constants of the fundamental mode and the n^{th} -cladding mode, respectively. Obviously, the propagation constants are wavelength dependent and the matching condition, thus the wavelength can be tuned by changing the grating periodicity. Tunable band-rejection filters based on LPGs have been obtained mostly through heating [142] [143]. The best tuning range achieved with LPGs is 115.9nm. LPG tunable filters have similar disadvantages as FBG tunable filters.

4.2.4 Other Tunable Filters

In addition to the aforementioned tunable filter techniques, other mechanisms, such as Mach-Zehnder interferometers [144], ring or disk resonators [145], waveguide arrays [146], and photonic bandgap crystal (PBC) filters [147]-[149], are also good candidates for tunable filters. Each of these filters has its own unique features and is suitable for some specific applications, but has not been widely used because of its large insertion loss, small tuning range, slow speed, or not being fully understood yet.

What needs to be mentioned is that, among these techniques, photonic bandgap crystal is a recently emerging technology with great potential. PBCs are fabricated by arranging sub-wavelength alternating materials with high and low dielectric constants to produce a desired effective bandgap. Photons with energy within this bandgap cannot propagate through the

structure [149]. PBC research has grown tremendously in the last few years. The effective bandgap of a PBC can be shifted by mechanical stress, temperature change or other mechanisms, and therefore a PBC has great potential in tunable optical filters. The foreseeable benefits of using PBCs for TOFs are a low driving voltage and a large tuning range.

4.3 Summary

In conclusion, optical sensing applications require a TOF of bandwidth from sub-nanometer up to above ten nanometers, tuning range from tens of nanometers to above 100 nm, and high tolerance on the tuning speed. However, extremely low cost is the fundamental requirement for a TOF-WLI sensor system in order to compete with available WLI demodulation technologies and electronics sensors.

FFP-TFs and MEMS tunable filters are the two most successful Fabry-Perot type tunable filters. On one side, FFP-TFs have a large tuning range, a flexible bandwidth, a low insertion loss and polarization independence that can cover most sensing needs, but their relatively high temperature sensitivity, large hysteresis, and high operation voltage make them unsuitable for the TOF-WLI proposed in this dissertation. On the other side, cleanroom environment and semiconductor equipment are essential in the fabrication of MEMS tunable filters, which are susceptible to thermal-mechanical noises, nonlinearity and coupling misalignments. AOTF has found wide applications in WDM networks, but its low sidelobe-rejection-ratio, presence of Doppler-shift, highly polarization dependence, and large fiber-to-fiber loss hindered its applications in fiber-optic sensing. FBG and LPG filters are band-rejection filters. They have found some uses restricted in the demodulation of grating sensors.

A very important drawback common to all the aforementioned TOFs is their high cost due to expensive equipment or material requirement, or complex fabrication processes and filter designs. A TOF in the market generally costs thousands of US dollars. Therefore, TOFs particularly designed for sensing applications at extremely low cost (no more than hundreds of US dollars) are desirable to reduce the cost per sensor.

Chapter 5 Diffraction Grating Tunable Optical Filter (DG-TOF)

A diffraction grating is an array of reflecting or transmitting elements separated by a distance comparable to the wavelength of light under study, such as a pattern of transparent slits or apertures in an opaque plate, or an array of reflecting grooves on a substrate. A reflective grating consists of a grating superimposed on a reflective surface, whereas a transmissive grating consists of a grating superimposed on a transparent surface. A light beam incident on a grating will, upon diffraction, have its amplitude, or phase, or both, modulated in a predictable manner [150].

Since the first diffraction grating was made, by David Rittenhouse, in 1785, diffraction gratings have been widely used for spectroscopy – the study of wavelength composition of light – by the physicist, the astronomer, the chemist, the biologist, and the metallurgist due to its excellent ability to spread light of different wavelength into different directions [150] [151]. Recently, diffraction gratings also found applications in wavelength division multiplexing (WDM) networks as a channel-dropping component to increase the capacity of fiber-optic networks [152] [153]. Commonly used diffraction gratings include ruled gratings, holographic gratings and replicated gratings.

Ruled gratings can be mechanically ruled on the surface of a substrate, while holographic gratings are usually formed by the fringes of a two-beam interference whose standing wave pattern is exposed to a substrate coated with photoresist. Chemical development of the exposed photoresist results in a pattern of straight lines with a sinusoidal cross section. Replicated gratings are duplicates of their master gratings which can be either ruled or holographic gratings. Replication significantly reduces the cost of each grating compared with making a master grating.

Although holographic gratings have relatively lower diffraction efficiency, they are more suitable, compared with ruled gratings, for those applications where a high signal-to-noise ratio is desired, specifically, where a source of sufficient intensity is available and the scattered light or ghosts would interfere with the measured data.

In this chapter, a tunable optical bandpass filter based on a plane reflective holographic grating (DG-TOF) is designed for sensing application.

5.1 Principle of a DG-TOF

When a beam of monochromatic light is incident on to the grooves of a diffraction grating, it is diffracted into discrete directions, as shown in Fig. 5.1. The diffracted wavefront of the grating is a combination of all the diffractions from each groove. At a unique set of discrete directions determined by the grating period d , the diffracted light from each groove is in phase with those from any others, thus interfere with others constructively. Otherwise, the interference is partially constructively or even destructively. The grating equation that governs the angles of diffraction from such a grating is

$$\sin(\alpha) + \sin(\beta_m) = m\lambda / d \quad (5-1)$$

where α is the angle of incidence and β_m is the angle of the m^{th} order diffraction, $m=0, \pm 1, \pm 2, \dots$, m , and β_m are both positive on the same side of the incident beam, while they are negative on the other side. Gratings are usually optimized for a certain order, mostly the first order. For a grating optimized to the $+1^{\text{st}}$ order,

$$\sin(\alpha) + \sin(\beta) = \lambda / d \quad (5-2)$$

and the angle of the $+1^{\text{st}}$ diffraction can be obtained as

$$\beta = \arcsin(\lambda / d - \sin(\alpha)) \quad (5-3)$$

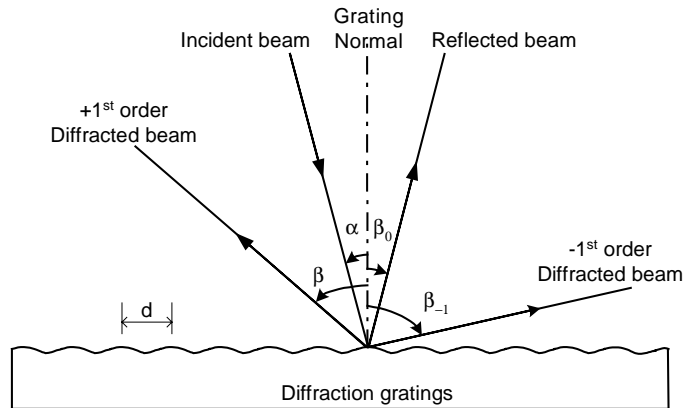


Fig. 5.1 Diffraction of a plane reflective holographic grating.

When a white-light source is used to illuminate the grating, according to Eq. (5-3), different wavelength components are diffracted to different angles. The wavelength components can, thus,

be separated by the grating, and a longer wavelength results in a larger diffraction angle. If a photodetector of finite area is put facing the output of the +1st order diffraction, a small fraction of the whole spectrum can be received by the detector. By changing the angle of incidence, or moving the detector along the perpendicular direction of the diffraction rays, and or rotating the grating about the axis coincident with its center ruling, one can easily change the passband continuously. This characteristic can definitely be used for the design of a tunable bandpass filter.

Fig. 5.2 shows the Schematic diagram of a grating-based tunable optical bandpass filter designed for the demodulation of white-light interferometric sensors. The filter consists of an input single-mode fiber, a first collimator (collimator I) which collimates the light from the single-mode fiber (SMF), a plane holographic grating mounted on a motorized rotary stage (with the center ruling at the center of the stage), a second collimator (collimator II) which collects the +1st order diffracted light and refocuses it into a receiving component which can be a single-mode fiber, a multimode fiber (MMF) or even a photodetector. In this design, multimode fibers of various core diameters will be used for different passband requirements. Using a receiving fiber is preferred than a photodetector because it provides more flexibility and the tremendous convenience of filter characterization later, for example using an optical spectrum analyzer. Single-mode fiber may be used if extremely narrow passband is necessary with the price of high insertion loss. The tuning is achieved by simply rotating the rotary stage about its axis. The rotation of the step motor is precisely controlled by a motor drive and a motion controller. The tuning resolution is mainly determined by the step size of the motor, the tuning speed depends on the speed of the motor, and the tuning range is limited by the travel range of the stage.

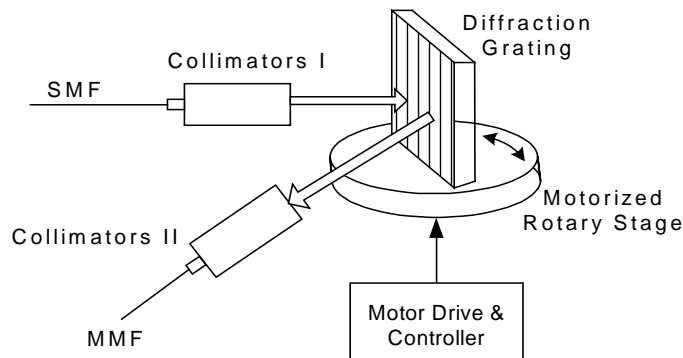


Fig. 5.2 Schematic diagram of a DG-TOF.

Starting from Eq. (5-2), we can derive the tuning range and the bandwidth of the tunable filter. Since the deviation angle $2K$ between the incidence and diffraction directions does not change during the tuning, it can be written as

$$2K = \alpha - \beta = \text{const} \tan t \quad (5-4)$$

Let's define a scan angle ϕ as

$$2\phi = \alpha + \beta \quad (5-5)$$

Combining Eqs. (5-2), (5-4) and (5-5), we have the central wavelength of a passband as

$$\lambda = 2d \cos(K) \cdot \sin(\phi) \quad (5-6)$$

Eq. (5-6) indicates that the central wavelength of the passband is solely determined by the angular position of the grating once the filter is constructed. The tuning range can, therefore, be estimated by

$$\Delta\lambda = 2d \cos(K) \cdot [\sin(\phi - \Delta\phi) - \sin(\phi)] \quad (5-7)$$

where $\Delta\phi$ represents the rotation of the stage from the scan angle ϕ which is positive when the normal goes counterclockwise, otherwise negative. Assuming that the focal length of the receiving collimator is f , the bandwidth of the bandpass filter can be expressed as [151]

$$\delta\lambda_{FWHM} = D \cdot P = \frac{dD \cos(\beta)}{f} \quad (5-8)$$

where P is the reciprocal linear dispersion of the grating system and D is the core diameter of the receiving MMF or the active area of the receiving photodetector.

Using Eqs. (5-5) - (5-8), and choosing a grating period $d = 1/750$ mm, $K = 55^\circ$, $D=0.2$ mm for a 200/230 μm MMF, and $f = 25$ mm, the relationships between the tuning angle, the center wavelength and the bandwidth of the filter are plotted in Fig. 5.3. Under this configuration, the 1300 nm passband occurs at $\phi=33.34^\circ$, and a tuning range of 100 nm in the 1300 nm band can be achieved with an angle change of less than 3.0° . In this small angle tuning range, the central wavelength is approximately proportional to the scan angle, thus the wavelength may be read out directly from the position or the travel distance of the stage. A bandwidth error of about $\pm 4.4\%$ occurs. This bandwidth error may induce optical intensity distribution error out of the original light source distribution, but can easily be compensated by scanning the whole spectrum range

and storing the new intensity distribution. Obviously, smaller bandwidth error is also obtainable by reducing the tuning range.

As indicated by Eq. (5-8), the bandwidth can be adjusted by changing the receiving area, once the grating, the collimators as well as the positions of the collimators are selected. For example, using a 100/140 μm MMF may result in a 2.6 nm bandpass filter, which is useful in a WLI using spectral domain demodulation. A bandwidth of 0.25 nm is achievable using a SMF with the same lens, however, the resulting high insertion loss may makes the filter not suitable for most sensing applications.

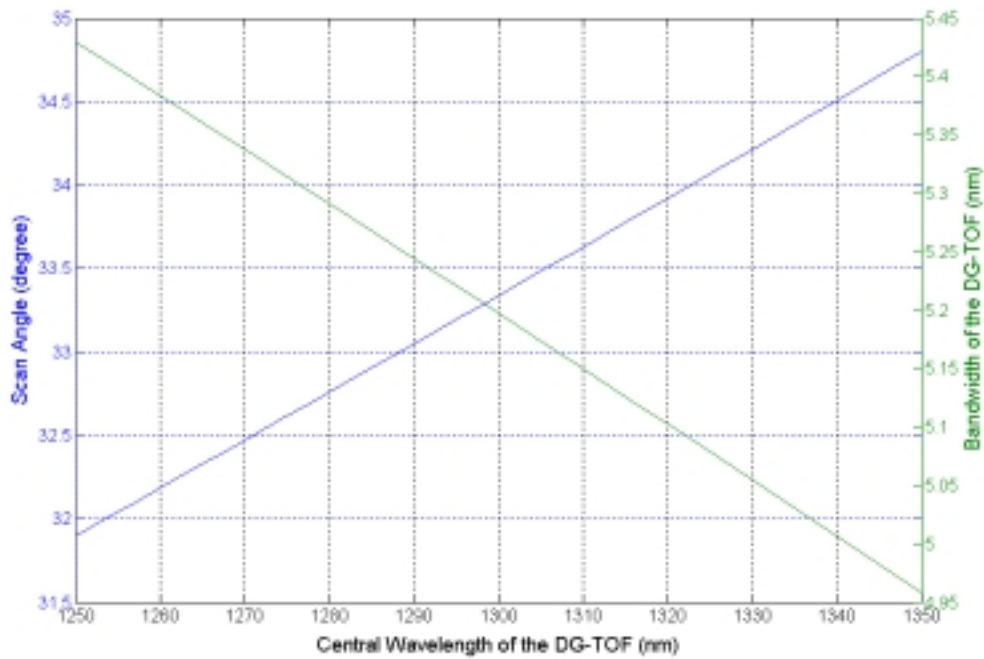


Fig.5.3 Wavelength dependence of the tuning angle and the DG-TOF bandwidth ($\Delta\lambda$).

5.2 Filter Fabrication

To physically construct a DG-TOF, a plane holographic reflectance grating of 750 grooves/mm, optimized for +1st order diffraction from Thermal RGL, Richardson Grating Laboratory, was selected. Its efficiency curve is given in Fig. 5.4. The grating has an efficiency of 95% for the s-plane polarization and 63% for the p-plane polarization at 1300 nm.

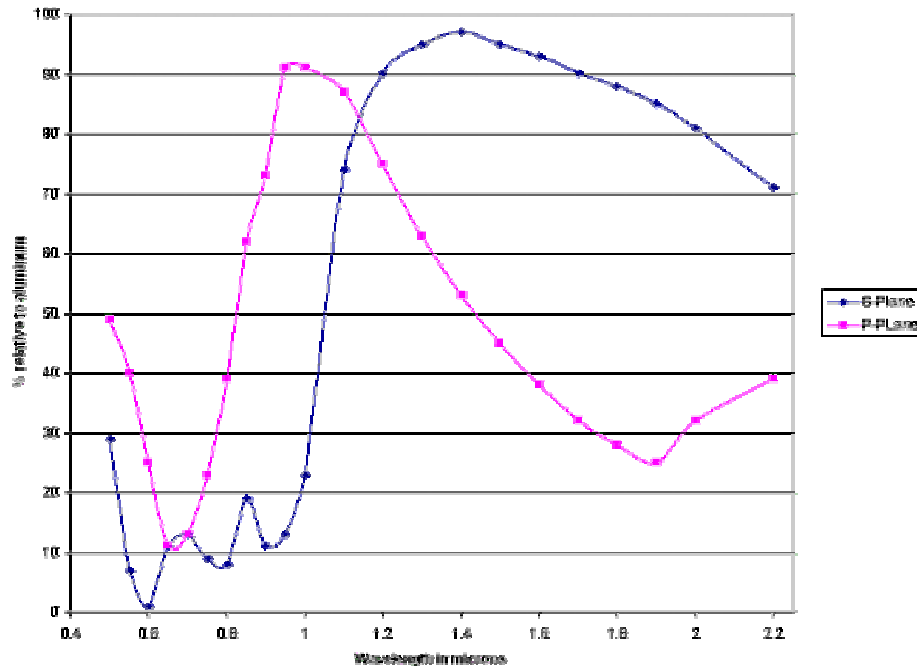


Fig. 5.4 Efficiency curves of the plane holographic grating (Thermal RGL, Richardson Grating Laboratory, 53004BK01-175H.).

A LC-22 collimator with a 40 mm focal length and a SMF pigtail and a LC-10 refocusing module with a 25 mm focal length from Multimode Fiber Optics, Inc., were selected as the Collimator I and II, respectively. The motorized rotary stage used is the Model 8401 rotary stage, and its driver is an 8801 Picomotor Driver, both from New Focus, Inc. The motor has a step resolution of 0.2-mrad and a rotation speed of 2 RPM, which means a central wavelength resolution of 0.38 nm and a tuning speed of 400 nm/s can be achieved. The grating was glued on to the stage with the center ruling on the axis of the stage. The input single-mode fiber is a SMF-28 fiber, while the output multimode fiber is a 200/230 μm MMF, but fibers of other diameters can be used.

A box was designed according to the above calculation to host all the parts. A photo of the finished DG-TOF is shown in Fig. 5.5. The position of the input collimator is fixed, but a 2-axis optical mirror mount was used for the receiving collimator to reduce the requirement on the machining tolerance and to finely adjust the alignment.

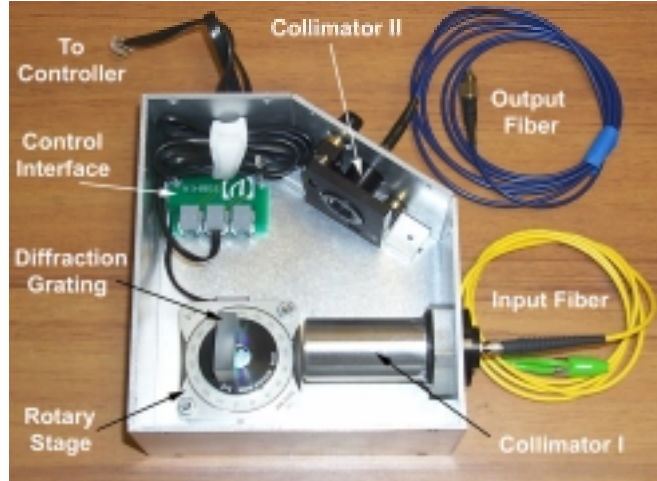
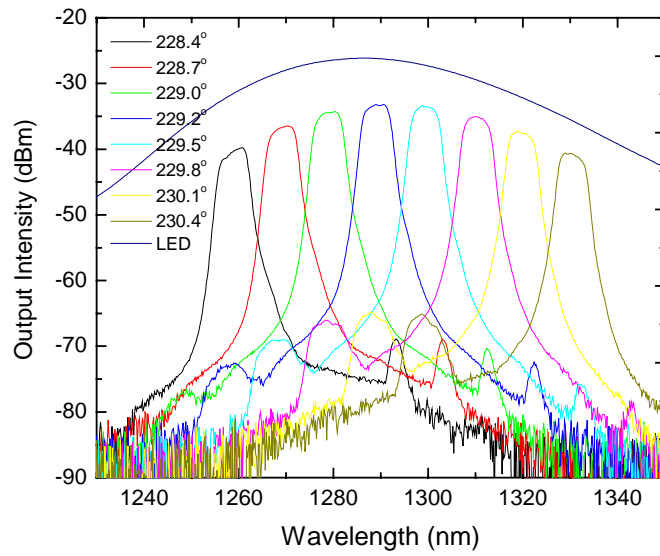


Fig. 5.5 A top view of the DG-TOF.

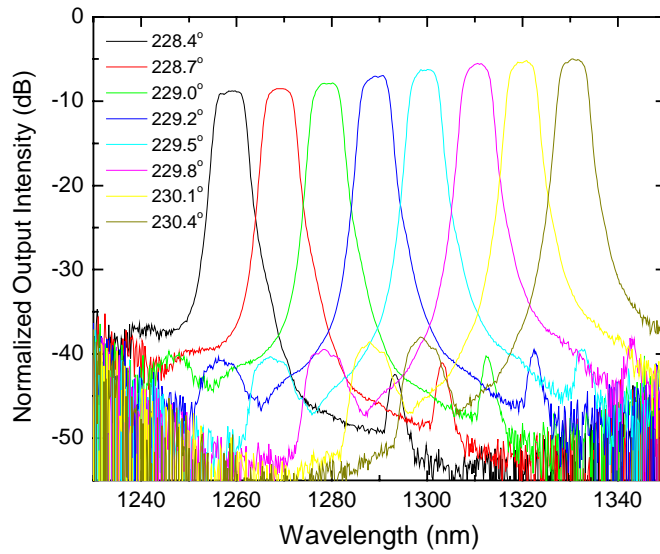
5.3 Filter Characterization

To characterize the DG-TOF, an MRED14C015-FC LED with a center wavelength of 1285.8 nm at 25 °C and a 3-dB bandwidth of 43 nm, from Luminent, Inc., was used as the source, and an AQ-6315A optical spectrum analyzer (OSA) was used to record the output spectrum of the bandpass filter. The position of the holographic grating can be roughly read from the scale on the rotary stage. Two types of MMFs, a 200/230 μm MMF and a 100/140 μm MMF have been tested as the receiving MMF fiber in Fig. 5.2, respectively. The multimode fiber was directly connected to the OSA.

Fig. 5.6(a) gives the original filter passband recorded by the OSA for the 200/230 μm MMF, while Fig. 5.6(b) shows the normalized filter output to the LED source, at a stage angle of 228.4°, 228.7°, 229.0°, 229.2°, 229.5°, 229.8°, 230.1°, and 230.4°. What needs to be mentioned is that the angle readout is not the same as the scan angle, but $\Delta\phi$ can be obtained from the rotation of the stage. The corresponding center wavelengths of the passbands are 1260 nm, 1269, 1279 nm, 1289 nm, 1300 nm, 1310 nm, 1320 nm, and 1331 nm, respectively. A tuning range of about 70 nm was reached with a tuning angle of 2°, which agrees well with the prediction by Fig. 5.3. Fig. 5.7 gives those results for the 100/140 μm MMF. Since the rotation speed of the stage is 2 RPM, a tuning speed up to 420 nm/s can be expected. A step size of 0.38 nm can be directly calculated from the 0.2 mrad resolution. Better resolution may be achieved with a finer motion controller and step motor.

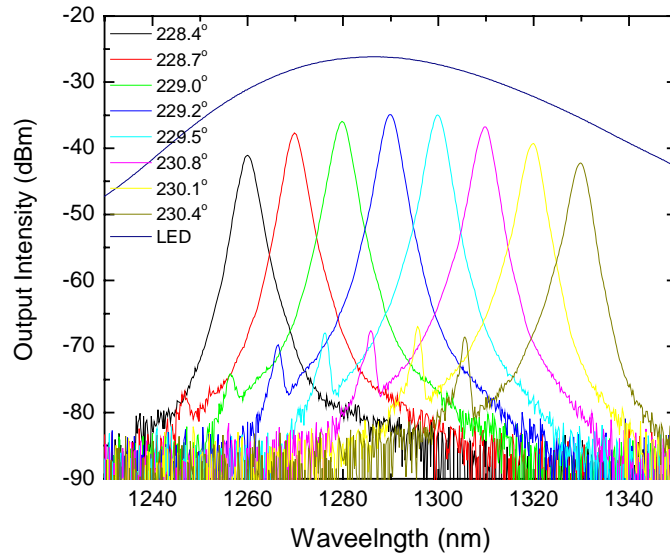


(a)

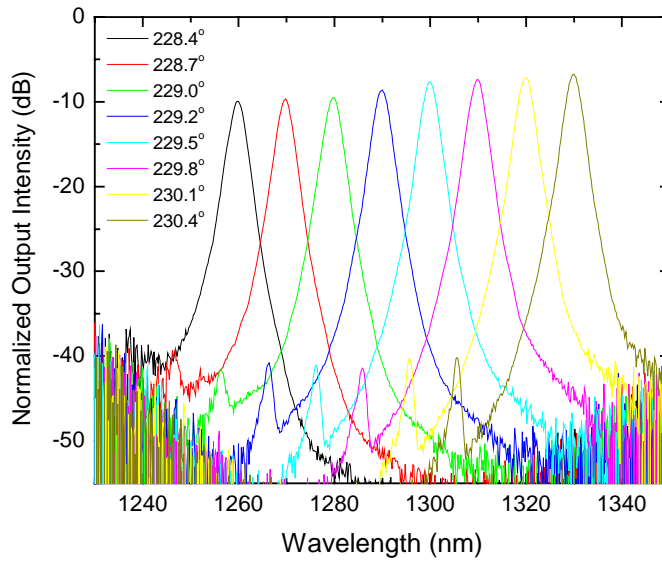


(b)

Fig. 5.6 Bandpass characteristics of the DG-TOF with a 200/230 μm MMF at different stage positions. (a) Original spectrum; (b) Normalized spectrum.



(a)



(b)

Fig.5.7 Bandpass characteristics of the DG-TOF with a 100/140 μm MMF at different stage positions. (a) Original spectrum; (b) Normalized spectrum.

Two interesting phenomena were observed on both cases. First, side lobes occur on both sides and about 30 nm from the main lobes. They are neither higher order diffractions nor ghost lights which exist only in ruled gratings. The reason is yet to be found. Fortunately, their intensity is more than 30 dB lower than their main lobes, and their effect on the filter

performance is negligible. Secondly, the transmission bands are not even in amplitude after normalization. A small increase in transmission or decrease in insertion loss from short to longer wavelengths can be easily observed. Misalignments could be one of the reasons. A peak transmission wavelength located at higher wavelength caused by the AR coatings on the lenses could be a second reason, and the wavelength dependence of the diffraction efficiency might be another cause. The insertion loss will be discussed later.

The bandwidth of the filter was measured after normalization, and the results are shown in Fig. 5.8 for both MMFs with the theoretical values. Obviously the measured numbers are always larger than the theoretical predictions. This is attributed to the offsets of the receiving fiber from the focus of the collimator II. The decrease trend of the BW for 200/230 μm MMF agrees with that of the prediction, but it does not for the 100/140 μm MMF. This is very likely caused by measurement accuracy limited by the resolution of the OSA. A better resolution may be used, but the SNR may decrease significantly, resulting in other errors unless a higher source power is used.

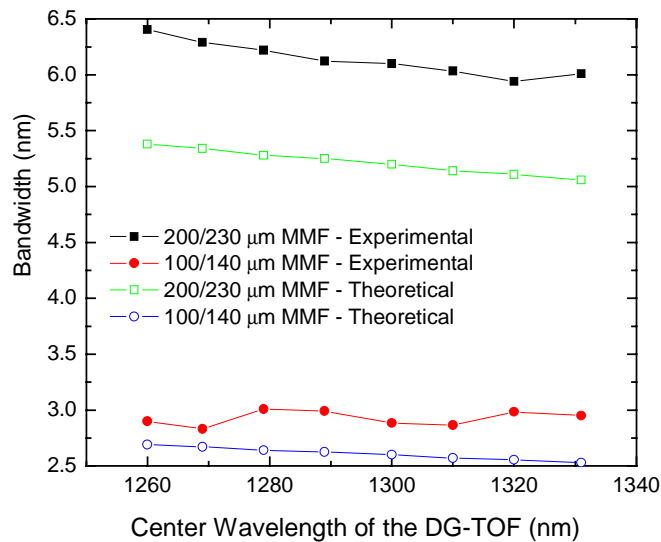


Fig. 5.8 Bandwidth of the DG-TOF passband.

5.4 Summary

The developed DG-TOF has several important advantages over other tunable filter technologies. First of all, it features a very wide tuning range, limited only by the operation range

of the grating. With a good selection of the diffraction grating, a several hundred nanometer tuning range can be easily achieved, which is sufficient to cover most sensing and spectroscopy applications using any whitelight source. Secondly, extremely high sidelobe suppression ratio and sharp edges are a unique characteristic of gratings, especially a blazed grating. It is very common to have a sidelobe suppression ratio above 50 dB. Another unique feature of the grating-based tunable filter is its superb wavelength resolution. A picometer resolution, which is almost unreachable by other filters, such as Fabry-Perot type filters, thin film type filters, and AOTFs, can be achieved with a moderate effort using a grating. Finally, diffraction gratings are available in the market with various specifications. One can easily select one for a specific application.

On the other hand, DG-TOFs do have some drawbacks. Plane diffraction gratings are generally bulky, though a concave grating makes the design more compact. Another concern of a diffraction grating is its polarization dependence, as shown in Fig. 5.4. For those applications sensitive to polarization, this TOF may not be applicable. Also, 100% diffraction efficiency is impossible, which means diffraction loss is inevitable. Finally, the cost of a DG-TOF is moderately high because of the stages and motion controller used.

In addition to those features discussed above, some other issues concerning the DG-TOF are also important. These include the misalignment, the multimode effects, the stability and the repeatability.

As shown in Fig. 5.6(b) and Fig. 5.7(b), an insertion loss from 5 to 10 dB was measured. The insertion losses are due to several sources, such as the diffraction loss, the reflection loss caused by the surfaces of the input and output fibers as well as the lenses, and various optical misalignments. The last one has the highest contribution in this design, and it includes the offsets of the input fiber from the focus of the collimator I, the misalignments among the incident plane, grating plane and output plane, the misalignments between the diffraction beam and the collimator II, and the offsets of the MMF from the focus of the collimator II. With more care in choosing the grating and collimators, and more accurate alignments, the total insertion loss may be reduced to ~3dB.

As a multimode fiber is used as the receiving fiber, interference between the modes guided in the fiber occurs. Modal interference may result in excess noise. In order to reduce modal noise, the length of the MMF should be as short as possible. In the DG-TOF, the length of the MMF is

less than 1.5 m, and an enlarged view of a passband for the 200/230 μm fiber is shown in Fig. 5.9. Because the photodetector used after the MMF has a smaller active area than the core of the MMF (for larger bandwidth and small dark current), the amplitude fluctuation of the passband top is believed to be caused by the modal noise. This modal noise may not be critical in some applications, for example operating-point control.

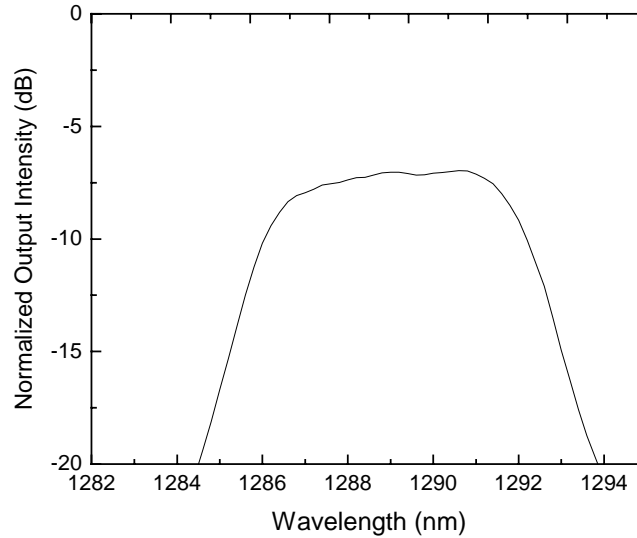


Fig. 5.9 Modal Noise.

Stability and repeatability are also very important parameters for a TOF. The current DG-TOF design has a good stability in laboratory environment, but may be sensitive to strong vibrations or shocks. More compact design and accurate machining to get rid of the adjustable stages may significantly improve its stability. Since the motor in the motorized rotary stage is a picomotor which moves by fraction and is not a real step motor, its repeatability is not very high. A real step motor or a similar rotary stage but operating in a close-loop mode will definitely make the filter more repeatable. Such motors or stages are available at higher prices.

Chapter 6 Extrinsic Fabry-Perot Tunable Filter (EFP-TF)

A variety of tunable optical filters have been proposed in the past decades, as discussed in Chapter 4, among which a significant number of filters are tuned either by thermal expansion or thermo-optical effects. Although slow compared with other tuning mechanisms, such as tuning by electrostatic force, electro-optic effects or acousto-optic effects, thermal tuning is straightforward and can be tailored for different filter structures, including MEMS F-P filters [118] [119] [124], fiber Bragg grating (FBG) filters [139] [140] [154], long period grating (LPG) filters [142] [143], arrayed-waveguide filters [155], and filters based on microcavity ring and disk resonators [145]. The highest tuning speed using thermal tuning is 2-60 ms for a tuning range of 20 nm with a thin film heater reported by Toyota, *et al* [155], and the highest thermal tuning efficiency achieved is 144.9 nm/°C by Shu, *et al* using a LPG [143].

The extrinsic fiber Fabry-Perot interferometer (EFPI) concept was originally proposed as a strain gauge by Murphy *et al* [46]. Since then, EFPIs have found tremendous applications in fiber-optic sensors for the measurement of strain [57] [69], temperature [39], pressure [39], acoustic waves [18] [156], vibration [17], etc. Similar structures have also been used for the construction of different tunable filters, such as fiber Fabry-Perot tunable filters (FFP-TFs) [113] [114], because of their structure simplicity, compact size and insensitivity to environment changes. In this chapter, we present an inherently inexpensive thermally tunable-optical-filter-based on an EFPI, which is named extrinsic Fabry-Perot tunable filter (EFP-TF).

6.1 Principle of Operation

The core of the device described here is basically a high-finesse EFPI that is formed by thermal fusion bonding of two mirror-coated single-mode optical fibers to a short piece of borosilicate capillary tubing, as shown in Fig. 6.1. For a Fabry-Perot interferometer, the resonant or transmission peaks occur when the optical phase difference $\delta=2\pi nL_a/\lambda$ is equal to multiples of π , where L_a is the distance between the two mirrors, and $n=1.0$ is the refractive index of the air in the cavity. For a given L_a , multiple wavelengths satisfy the resonant conditions, resulting in multiple transmission bands. Changing L_a results in the change of the resonant condition, and thus the shift of the transmission bands.

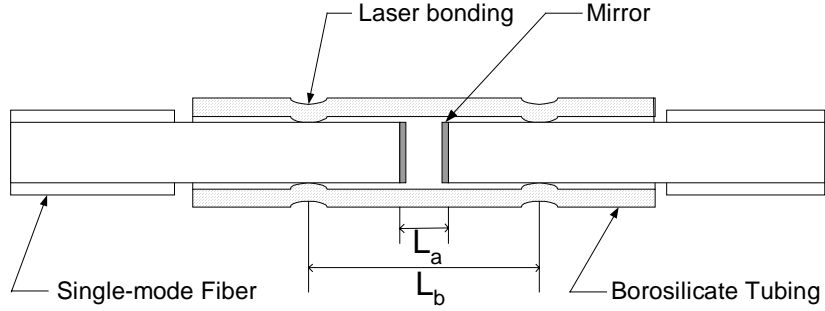


Fig. 6.1 Principle diagram of an EFPI filter.

The fundamentals of Fabry-Perot tunable filters are described in detail in Chapter 4, and the formulae for the filter parameters, including the transmission T , the bandwidth $FWHM$, the finesse \mathcal{F} , the free spectral range FSR , and the tuning range $\Delta\lambda$, are given by Eq. (4-1) - Eq. (4-7d). For the EFP-TF, only cavity length change is involved. Assuming that the central wavelength of the filter passband is λ_0 when the airgap is L_a , the shift of the central wavelength $\Delta\lambda$ caused by an airgap change ΔL can be expressed, according to Eq. (4-7a), as

$$\Delta\lambda = (\Delta L / L_a) \cdot \lambda_0 \quad (6-1)$$

The wavelength shift is proportional to the ratio $\Delta L/L_a$, which means a large tuning range may be obtainable with a small change of the airgap, if a short cavity is used. Taking advantage of the differential thermal expansions between the borosilicate tubing and the silica fiber, continuous tuning of the filter passband can be achieved by locally cooling or heating the EFPI. Assuming that a temperature change from T to $T+\Delta T$ is applied to an EFPI filter of gauge length L_b , corresponding to the distance between the two bonding points, resulting an airgap change from L_a to $L_a + \Delta L$, ΔL is given by

$$\Delta L = [\alpha_b L_b - \alpha_f (L_b - L_a)] \cdot \Delta T \quad (6-2)$$

where α_b and α_f are the coefficients of thermal expansion (CTE) of the borosilicate tubing and the fused silica fiber, respectively. α_b and α_f are constants from 0 to 300°C. Substituting Eq. (6-2) into Eq. (6-1) and assuming that $L_a \ll L_b$,

$$\Delta\lambda = (L_b / L_a) \cdot (\alpha_b - \alpha_f) \cdot \lambda_0 \cdot \Delta T \quad (6-3)$$

Eq. (6-3) indicates that the wavelength tuning is proportional to the temperature change. Since the borosilicate tubing has a CTE approximately 5~10 times higher than that of a silica fiber, a tuning range above 100 nm can easily be achieved within a temperature range of less than 80°C, which is within the normal operation range of a Peltier device.

As implied by Fig. 6.1, the alignment between the two mirrors is automatically achieved because of the tight matching between the inside diameter (I.D.) of the tubing and the diameter of a single-mode bare fiber. This self-alignment capability significantly reduces the coupling loss and eliminates the costly aligning process encountered by other tunable filter techniques. Furthermore high reliability can be expected because no motors or mechanical stages are used and therefore no mechanical wear is involved. The long time stability of the filter is determined by the temperature stability of the Peltier device and its controller, which can be as low as 0.001°C.

6.2 Filter Preparation

In preparation of prototype EFP-TFs operating in the 1550nm band, SMF-28 single-mode fibers with a CTE of $5.6 \times 10^{-7} / ^\circ\text{C}$, and Pyrex tubing with a CTE of $32.5 \times 10^{-7} / ^\circ\text{C}$, an inner diameter (I.D.) of $127 \pm 1.5 \mu\text{m}$ and an outer diameter (O.D.) of $290 \mu\text{m}$ were used. 120 pieces of one-meter-long SMF-28 fibers were cleaved at one end in the lab. To guarantee some degree of uniformity of the cleaved surfaces from fiber to fiber without going through the costly polishing process, a system including a broadband light source, a circulator, an optical receiver and a multimeter was set up to monitor the reflectance of the cleaved fiber-ends, as shown in Fig. 6.2.

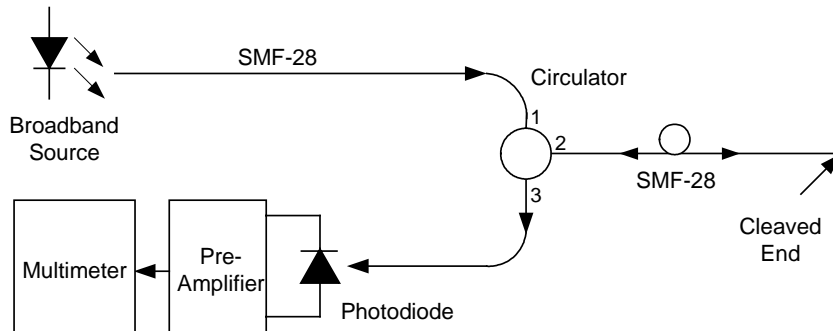


Fig. 6.2 Experimental setup for cleaved endface quality inspection.

Prepared fibers were bundled together with the cleaved endfaces protected. Coating of dielectric mirrors on the cleaved ends of the fibers were done by Evaporated Coating, Inc. Fig. 6.3 shows the design curve of the coating reflectivity. The mirrors have a peak reflectance of $R=87.5\%$ at 1565 nm, but down to 87.0% at 1529nm and 1602 nm. However, a 3% reflectivity reduction from the designed value and a variation about 4% from fiber to fiber were measured from the finished fibers, as a result of the imperfections of the cleaved fiber endfaces and coating thickness variations produced during the thin film deposition processes. Therefore, the setup in Fig. 6.2 was again used to measure the reflectivity of each mirror-coated fiber. Fibers were paired with close reflectivity to minimize the insertion loss and fringe contrast and finesse reduction due to mirror asymmetry.

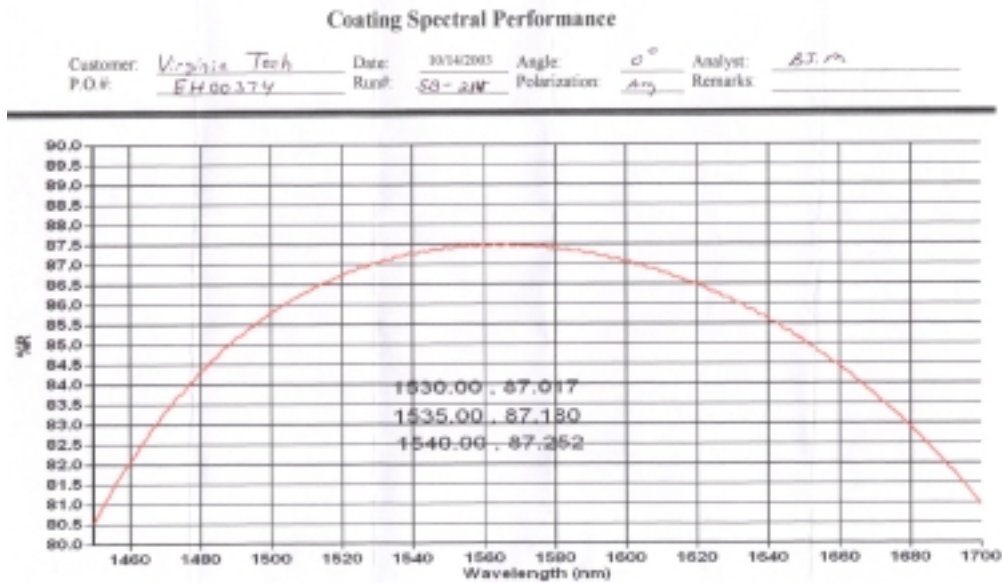


Fig. 6.3 Reflectivity of the dielectric mirrors.

The fibers of a fiber-pair were fusion bonded to a piece of 10~15mm long Pyrex tubing using the automated sensor fabrication stage system developed at the Center for Photonics Technology of Virginia Tech, shown in Fig. 6.4. The fabrication system consists of two XYZ stages mounted on a single base XY stage, a digital camera and a monitor to check the aligning and bonding processes, a pulsed 25W CO₂ laser integrated with a He-Ne laser for alignment, and a computer based white-light system for CO₂ laser control and airgap monitoring. In this experiment, the white-light system was not used. Instead, a simple system using an SLED with a central wavelength of 1557.6 nm and a bandwidth $\Delta\lambda_{FWHM}=61.7$ nm, and an AQ-6315A optical

spectrum analyzer (OSA), as show in Fig. 6.5, was employed to monitor the cavity length during the bonding process.



Fig. 6.4 Photograph of the sensor fabrication stage system.

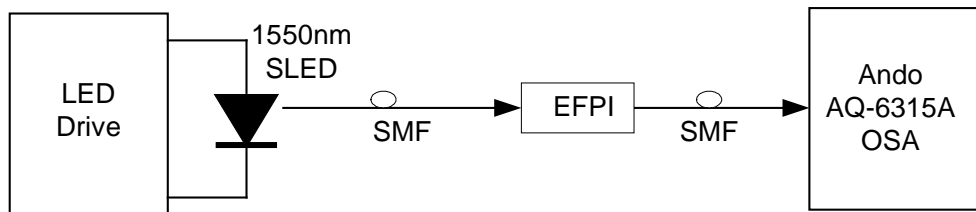


Fig. 6.5 Schematic diagram of the cavity length monitoring system.

The first fiber was bonded to the borosilicate tubing using a CO₂ laser power of 0.9 W and a pulse-duration of 1.0 second. The bonding point is about 2.0mm away from the mirror coated fiber end. Then, the second mirror-coated fiber was inserted into the tubing from the other end of the tubing. By adjusting the cavity length and the orientation of the second fiber, a main transmission peak was moved to around 1540nm with the adjacent peak(s) more than 110nm away from the main peak and the insertion loss the minimum, all at ambient temperature (~20°C). A CO₂ laser pulse of 0.9W and 1.0 second duration was applied to the second bonding point, which is about 4.0mm from the first bonded point. Multiple shots were required

sometimes, depending on the alignment of the laser beam. Fig. 6.6 is an optical micrograph showing a typical bonded point (the transparent area).

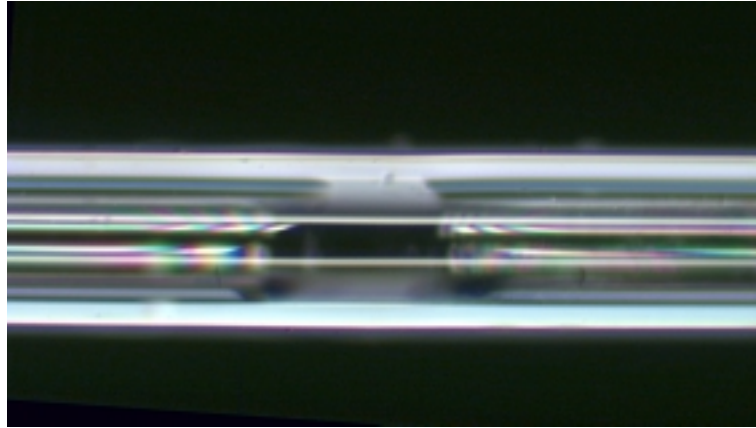


Fig. 6.6 Optical micrograph of a bonded point.

Obviously, the cavity length changes and the position of the peak transmission moves during the fusion-bonding process as a result of the thermal expansion of both the tubing and the optical fibers. Fine adjustment of the cavity length between the two mirrors was achieved with lower laser pulse power, mostly between 0.5~0.8W, and multiple shots on the same position were required for best peak position and FSR as well as lowest insertion loss. Fig. 6.7 shows the optical micrograph of a typical finished EFPI. The transmission spectrum of the prototype EFPI, which was used for subsequent investigation, was recorded right after the bonding processes, and is given in Fig. 6.8 with those of the SLED and the reflection from the input mirror.

The gauge length was measured as $L_b \approx 4.1\text{mm}$ using a microscope. From Fig. 6.8, the 3-dB bandwidth of the peak transmission, the FSR, and the insertion loss, were estimated as 6.9nm, 112nm, and 2.5dB, respectively. Accurate numbers for these parameters can be obtained only after normalization and are given in Section 6.3.

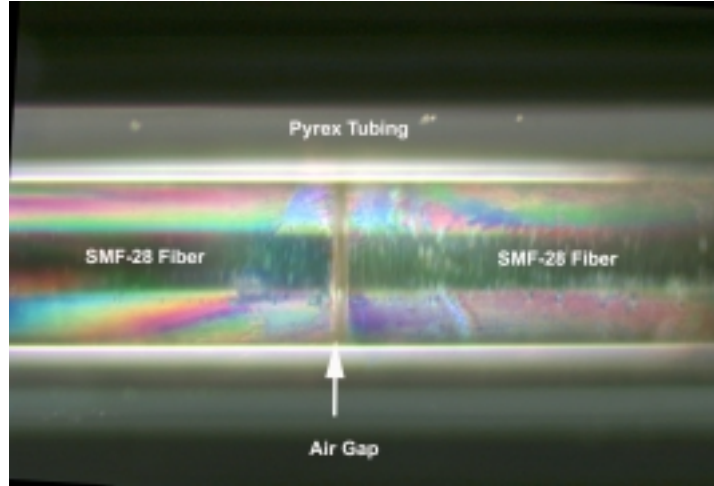


Fig. 6.7 Optical micrograph of an EFPI filter.

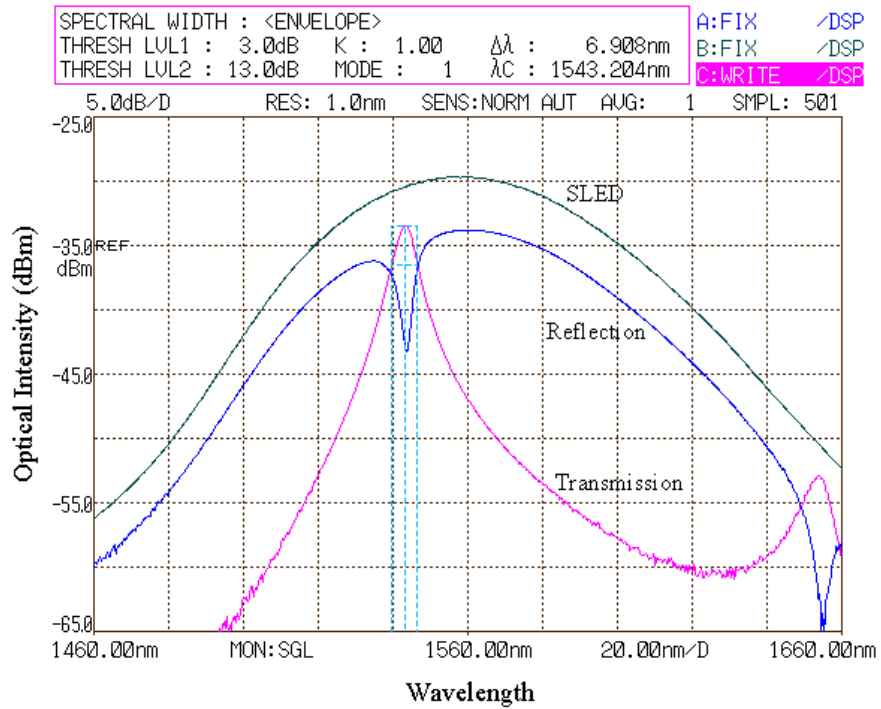


Fig. 6.8 Recorded spectrum of the prototype EFPI the bonding at ambient temperature.

To apply the thermal tuning function, the EFPI filter was then assembled into a 14-pin butterfly package with a thermoelectric cooling (TEC) module and a thermistor to form an EFP-TF, shown in Fig. 6.9. To achieve fast thermal response, the EFPI filter was brought in direct contact with the cold plate of the TEC and thermal compound was used to enhance thermal

coupling between the TEC and the EFPI filter. The input and output fibers were protected by 900 μ m plastic tubing. The top of the package was sealed with alumina tape to isolate the air inside from the ambient environment.

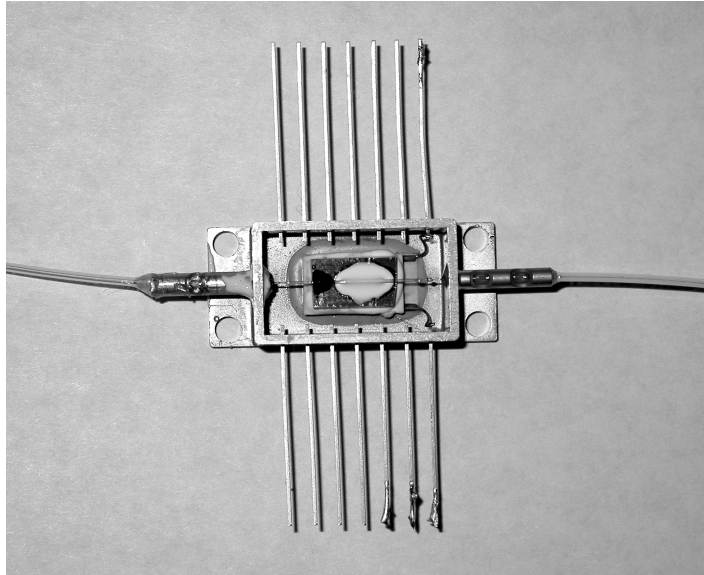


Fig. 6.9 Photo of a packaged prototype EFP-TF.

6.3 Filter Characterization

To characterize and operate the prototype EFP-TF, a TEC controller was constructed with a 24-hour temperature stability of 0.003 $^{\circ}$ C, using an HTC-3000 module from Wavelength Electronics, as shown in Fig. 6.10. The input of the controller is set by a laptop computer through a high-resolution 16-ch data acquisition card (DAQ) (MF236/I DAQ PC Card, 12-bit, 625Ksps, 16 channels, dual 12-bit DAC, 4 digital I/O, from Elan Digital Systems Ltd, Fareham, UK). Through the same DAQ, the actual temperature measured by the thermistor mounted beside the EFPI inside the butterfly package is also displayed on the laptop screen with the setting voltage. The detail circuits and computer programs will be discussed in Chapter 10. The same light source and OSA used for the filter fabrication in Section 6.2 were used for the performance evaluation. Fig. 6.11 gives a Schematic diagram of the experiment setup for filter characterization.

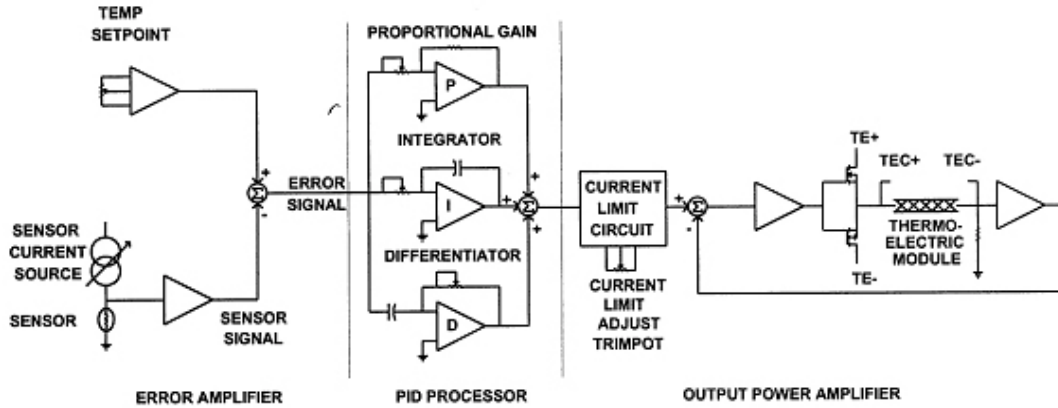


Fig. 6.10 Schematic diagram of the HTC-3000 from Wavelength Electronics.

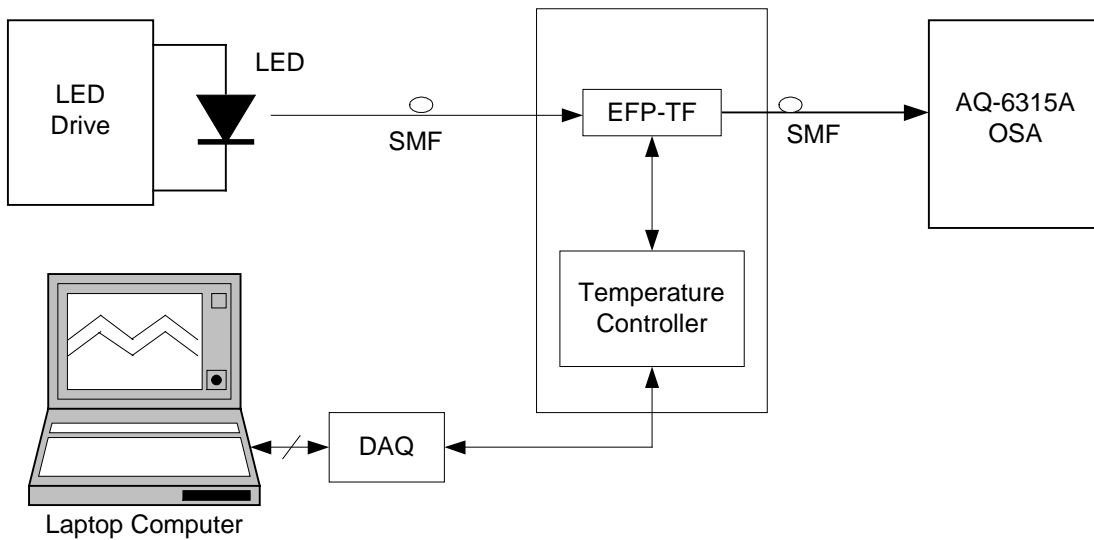


Fig. 6.11 Experimental setup for filter characterization.

Fig. 6.12 gives the output spectrum of the filter normalized to that of the source at a set voltage $V_{SET}=2.0V$, corresponding to a temperature $T=10.11\text{ }^{\circ}C$. A 3-dB bandwidth of 7.8 nm on the first passband and 8.0 on the second passband, a FSR of 110nm, and an insertion loss of 2.4 dB were measured at this temperature. From the positions of the two peaks, $\lambda_1=1519.4nm$ and $\lambda_2=1629.4nm$, the airgap can be readily calculated, using Eq. (2-9), as 11.253 μm . The FSR may be doubled by reducing the airgap to a few micrometers. A narrower passband as low as 0.5 nm may be obtained by using either mirrors of a much higher reflectivity or longer cavity length. The major sources of the insertion loss include misalignments between the two fibers, and

absorption and asymmetry of the two mirrors. The misalignments include the end separation, which is small in this case, and the tangential misalignment caused by the mismatch between the diameter of the fiber and the I.D. of the tubing. Insertion loss close to 1.0 dB can be expected by using tubing of smaller I.D. and higher quality thin films on polished fiber ends. Expanded core fibers may be necessary for even smaller bandwidth and coupling loss [157].

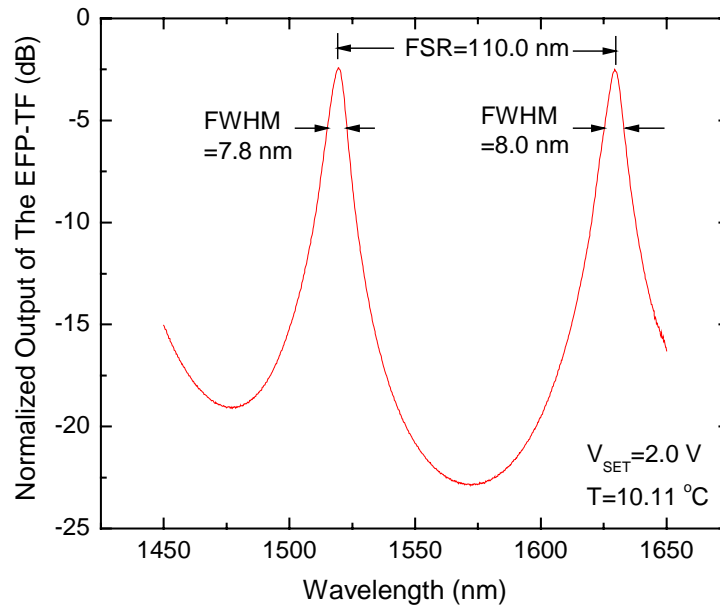


Fig. 6.12 Normalized spectrum at T=10.11°C.

Continuous tuning of the passband has been achieved by scanning the output voltage of the DAQ. Fig. 6.13 shows the dependence of the central wavelength of the filter on the control voltage with a 3rd order exponential curve fit. A tuning range of 91.7nm was obtained with a voltage change of 2.0~0.2 V, corresponding to a temperature change from 10.11°C to 68.32°C. This tuning range agrees well with the predicted value of 89.8 nm by Eq. (6-3), and the small discrepancy is believed to be caused by the gauge length measurement error. The 3rd order exponential dependence of the central wavelength on the control voltage can be explained by the similar dependence of the resistance of the thermistor on temperature. A maximal error of $\pm 1.0\text{nm}$ was observed around the mean of eight cycles. The three major sources of errors were the measurement error, the friction between the silica fiber and the borosilicate tubing, and the temperature control accuracy. The specified accuracy of the OSA is $\pm 0.5\text{nm}$, but it has not been calibrated in the last five years. The friction was mainly due to the tight fit between the fibers

and the tubing, which is essential for low misalignment. However, the contribution of the friction is very difficult to estimate at this time. The temperature control accuracy was limited by the noise of the analog output voltage of the DAC, and that of the PID temperature controller. The total noise is on the order of 0.2mV, causing a wavelength error about 0.05nm at the long wavelength side or 0.003nm at the short wavelength side.

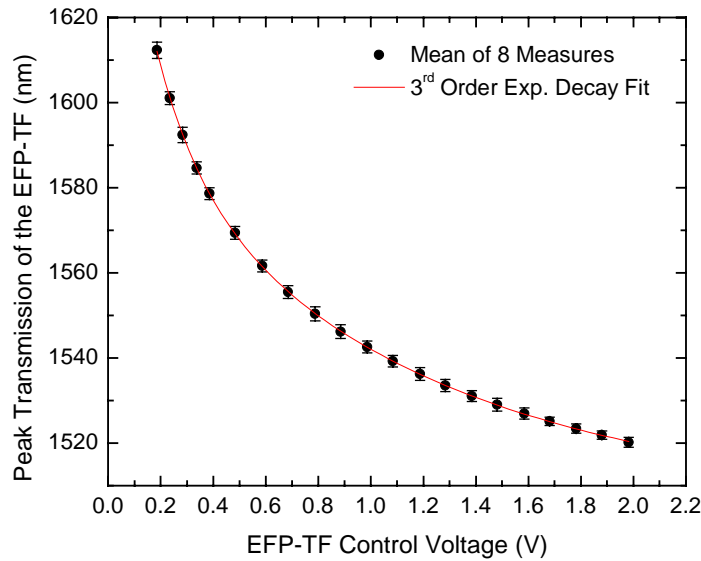


Fig. 6.13 Tuning curves of the prototype EFP-TF.

The hysteresis of the EFP-TF was measured by cycling the temperature up and down for eight times. Shown in Fig. 6.14 are the averaged tuning curves for the up and down cycles, respectively. A maximal hysteresis of 2% was found. The hysteresis may be due to the 3~4 mm distance between the EFPI filter and the thermistor. It could be significantly reduced by bringing the temperature sensor inside the butterfly package closer to the EFPI filter during the design of the package and using a thermistor of faster response.

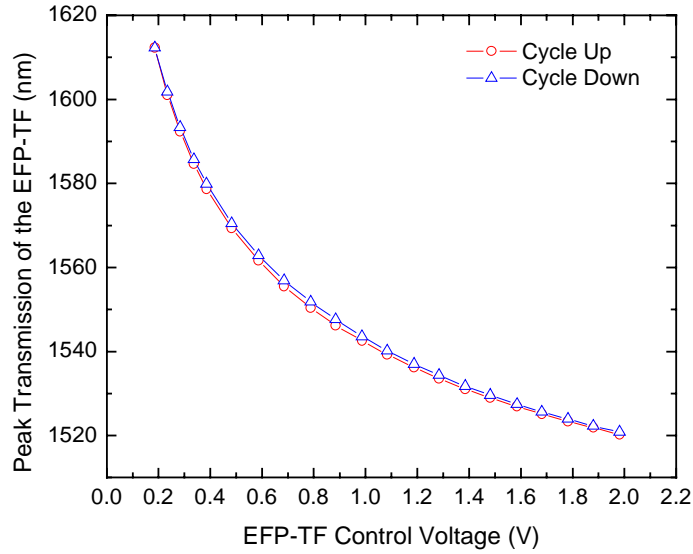


Fig. 6.14 Hysteresis of the prototype EFP-TF.

To convert the control voltage to the corresponding temperature, the following formula provided by the thermistor manufacturer was used.

$$V = I \cdot R_{25} \cdot \exp(A + B/k + C/k^2 + D/k^3) \quad (6-4)$$

where V – the control voltage (V)

k – the temperature (K)

I – the current through the thermistor

R_{25} – the thermistor resistance at 25 °C

A=-1.4141963e1;

B=4.4307830e3;

C=-3.4078983e4;

D=-8.8941929e6;

In this experiment, we chose $I=100\mu\text{A}$ and $R_{25}=10\text{k}\Omega$. The dependence of the temperature on the control voltage is plotted in Fig. 6.15.

When converting the control voltage to the corresponding temperature using the V-T curve given in Fig. 6.15, the tuning-curve in Fig. 6.13 is re-plotted in Fig. 6.16(a). Good linear dependence of the wavelength on temperature was observed. A temperature sensitivity of $1.58\text{nm}/^\circ\text{C}$ has been measured from the linear fit, which is the highest reported so far, to the best

of our knowledge. The discrepancy between the experimental data and the linear fit is very likely due to the limited accuracy of the V-T curve for the thermistor. In order to prove this judgment, a 3rd-order polynomial fit was performed and shown in Fig. 6.16(b). Obviously, the 3rd-order polynomial curve results in a better fit, which indicates that the nonlinearity is most likely resulted from the limited accuracy of the V-T curve in Fig. 6.15, or the tolerance of the resistance of the thermistor, or both. However, since a computer is used for data processing and the EFP-TF control, this nonlinearity can be easily calibrated and does not cause extra errors in a TOF-WLI system.

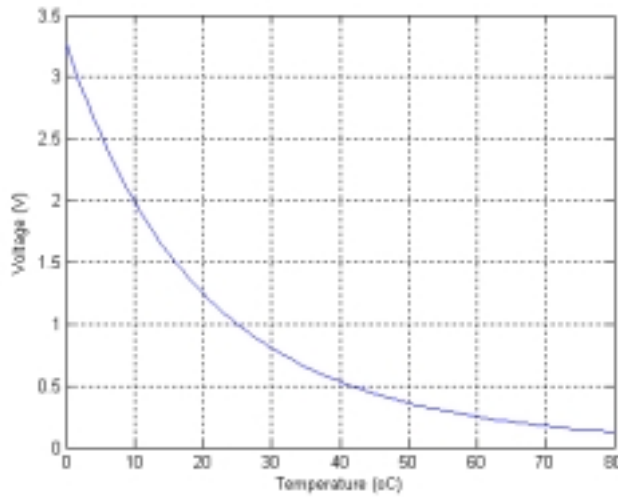


Fig. 6.15 Temperature – control voltage curve.

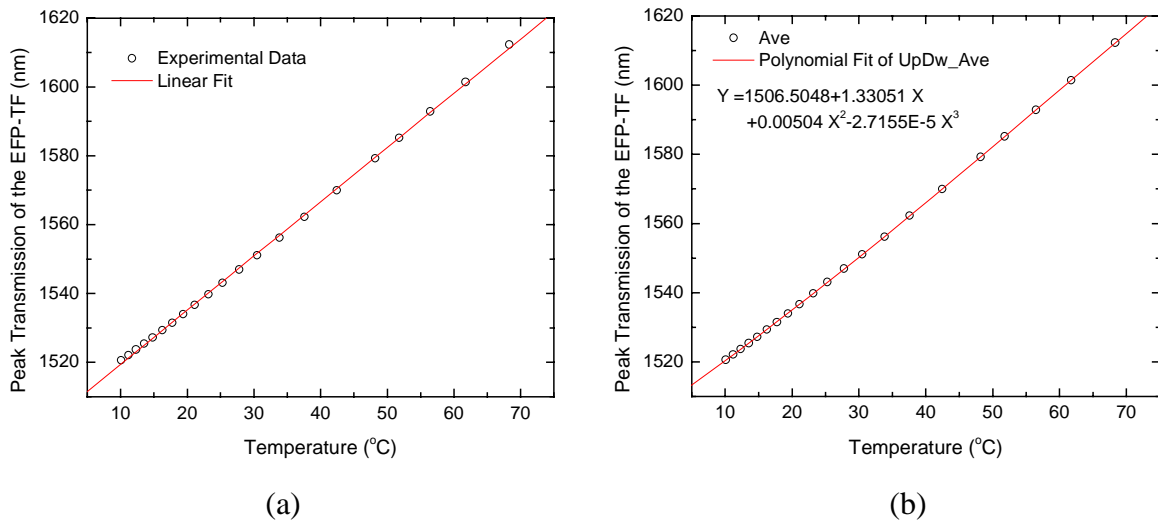


Fig. 6.16 Temperature sensitivity and linearity. (a) Linear fit; (b) 3rd-order polynomial fit.

A FSR change from 110nm at 10.11°C to 102.6nm at 68.32°C was observed which can be explained by $FSR=\lambda^2/2L_a$. A bandwidth of 7.8 nm at 1520.18 nm, 7.0nm around 1563.40 nm and 7.2 nm at 1612.3nm were measured on the main peaks. This bandwidth change is a combined effect of the airgap change with temperature and the non-flat reflectance spectrum of the mirrors, which has a peak at 1565nm. The bandwidth can be described by Eq. (4-6). It is inversely proportional to the airgap L_a , and thus to T . On the other hand, the reflectivity peak makes the filter have a smallest *FWHM* around 1565 nm than at other wavelengths.

The minimum of time needed to scan the whole tuning range is about 2 seconds. This relatively low speed can be attributed to the large package size and the associated thermal mass. Much higher scanning speeds can be expected by reducing the package size, for example, using a microheater, or by directly depositing a resistive coating onto the capillary tubing of the filter. Further thermal management on the package similar to those for microsystems [158] may be useful investigated in the future work in order to optimize the design for higher tuning speed.

6.4 Summary

In this chapter, we proposed and demonstrated an extrinsic Fabry-Perot tunable filter (EFP-TF) which can be tuned by using a Peltier device. The prototype EFP-TF has a tuning range of 91.7 nm, a 3-dB bandwidth from 7.0~7.8nm, an insertion loss of 2.4dB, and a temperature sensitivity of 1.58 nm/°C in the 1550 nm band. The filter features polarization independence, high repeatability, and inherently low drift and low insertion loss. EFP-TFs can be manufactured in extremely low cost, and therefore, can be used in a white-light interferometric sensing system as a demodulation component, or in the construction of a spectrometer for biomedical and chemical sensing.

Chapter 7 Fiber Fabry-Perot Interferometric Sensors

A series of laboratory experiments and field tests have been performed to demonstrate the feasibility of using a TOF-WLI as an effective means for the demodulation of various types of interferometric fiber optic sensors. In this dissertation work, two major types of interferometric sensors have been employed for the experiments. They are extrinsic Fabry-Perot interferometric (EFPI) sensors and diaphragm-based Fabry-Perot interferometric (DFPI) sensors. Because EFPI temperature sensors are simple in structure and extremely sensitive, they are perfect candidates for the evaluation of the performance of the TOF-WLI. All the experiments described in this dissertation with EFPI sensors have been done in the controlled laboratory environments. DFPI sensors described in this chapter were mainly designed for partial discharge (PD) detection and location in high voltage transformers, sponsored by the Electrical Power Research Institute (EPRI) and the National Science Foundation (NSF), and for turbine engine pressure measurement, sponsored by the Department of Energy (DOE). Both laboratory experiments and field demonstrations have been conducted on DFPI sensors. In this chapter, we briefly introduce the principles, the fabrication and packaging techniques, and the characterization of the EFPI temperature sensors, the DFPI-PD sensors, and the DFPI-Engine sensors.

7.1 EFPI Temperature Sensor

The geometry of the EFPI sensors was first described by Murphy et al. for the detection of the amplitude and the relative polarity of dynamically varying strain [46]. Because of their ease of construction, low fabrication cost, high reliability, high resolution, and avoidance of polarization problems [97], EFPI sensors are attractive and have found a lot of applications in the measurement of temperature [39] [159], micro-displacement [160], strain [69] [161] [162], acoustic emission [17] [156], biomechanics of tissues and cells [163], and chemical gasses [164]. In this section, we describe the principle of an EFPI sensor for temperature measurement, the fabrication processes of both low-finesse and high-finesse EFPI temperature sensors, and experimental setup for sensor characterization.

7.1.1 Principle of Operation

In general, an EFPI sensor head is formed by the two air-glass interfaces of two optical fibers inside an alignment tube, as shown in Fig. 7.1. Although transmission-type EFPIs have also been developed [12] [161], most EFPI sensors belong to the reflection-type. In either case, a majority of EFPIs are based on a low-finesse Fabry-Perot cavity formed by the endfaces of two cleaved fibers, but high-finesse EFPIs have sometimes been employed in specific applications [12]. In this research, a low-finesse reflection-type EFPI temperature sensor and a high-finesse transmission-type EFPI sensor were used for the evaluation of the proposed TOF-WLI.

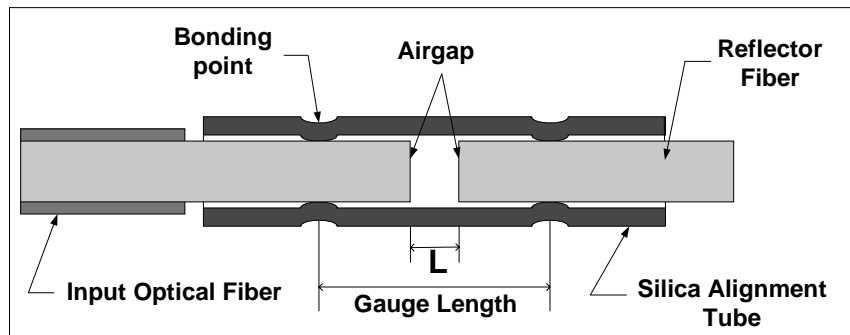


Fig. 7.1 Principle diagram of an EFPI sensor head.

For a reflection-type EFPI, the optical phase difference between the two reflections can be expressed as

$$\phi = \frac{4\pi nL}{\lambda} + \phi_0 \quad (7-1)$$

where n - refractive index of the medium in the F-P cavity, which is air in most EFPIs.

L - airgap length

λ - wavelength of the interrogation light source

ϕ_0 - initial phase difference

When a perturbation is applied directly on the sensor head or through any other mechanisms, a change of the gauge length is resulted from either expansion or compression, and therefore a length change of the airgap ΔL takes place. The optical phase difference change is given by

$$\Delta\phi = \frac{4\pi n \cdot \Delta L}{\lambda} \quad (7-2)$$

In the case of a temperature sensor used in this dissertation, a borosilicate glass tube was used. The change of the gauge length is caused mainly by the thermal expansion of the silica alignment tube in a temperature field, but the airgap change is determined by the difference between the expansion of the tube and that of the silica fiber, which is given by

$$\Delta L = [\alpha_b L_g - \alpha_f (L_g - L_a)] \cdot \Delta T \quad (7-3)$$

where $\Delta T = T - T_0$ is the temperature change from the initial temperature T_0 , L_g is the gauge length at T_0 , and α_b and α_f are the coefficients of thermal expansion (CTE) of the borosilicate tube and the fused silica fiber, respectively. α_b and α_f are constants from 0 to 300°C. Assuming that the gauge length, which is on the order of millimeters, is much larger than the airgap length, which is on the order of micrometers, so $L_b \gg L_a$, Eq. (7-3) is simplified as

$$\frac{\Delta L}{\Delta T} \approx (\alpha_b - \alpha_f) L_b \quad (7-4)$$

Obviously, the temperature sensitivity of the cavity length is proportional to the CTE difference and the gauge length. By using the TOF-WLI in either a scan-mode or a linear-mode to measure the airgap change ΔL , one can determine the temperature under test.

7.1.2 Sensor fabrication and characterization

In this work, Corning SMF-28 single-mode fibers with a CTE of $5.6 \times 10^{-7} \mu\text{m}/\mu\text{m}/^\circ\text{C}$ and Pyrex tubes with a CTE of $32.5 \times 10^{-7} \mu\text{m}/\mu\text{m}/^\circ\text{C}$, an I.D. of $127 \pm 1.5 \mu\text{m}$ and an O.D. of $290 \mu\text{m}$ were used. Although epoxies have been used for the fabrication of EFPI sensors by many researchers, our EFPIs were manufactured by using the well-developed CO₂ laser bonding technique and fabrication setup shown in Fig. 6-4. Comparing with epoxy bonding, the laser-bonding technique has better control on the initial airgap length and the gauge length, resulting in better sensor performance repeatability and much higher temperature capability.

For the low-finesse reflection-type EFPI sensor, a one-meter-long SMF-28 fiber was first cleaved, then the cleaved-end was inserted into a 20mm long Pyrex tube from one end, and finally the fiber and the tube were fusion-bonded together at a CO₂ output power around 0.9 W.

Another reflector fiber of 10~20mm in length was cleaved, inserted into the tube from the other end, and then fusion-bonded to the tube. All the bonding processes were completed on a bonding stage and the airgap length was monitored with a simple setup shown in Fig. 7.2. The reflection spectrum obtained for the low-finesse EFPI sensor and that obtained for a cleaved SMF are given in Fig. 7.3. An airgap length around 20 μm was estimated for this sensor. In Section 10.2, we will see that an EFPI sensor of this cavity length will show a very good fringe contrast and linear range when interrogated by the EFP-TF WLI system in a linear operation mode.

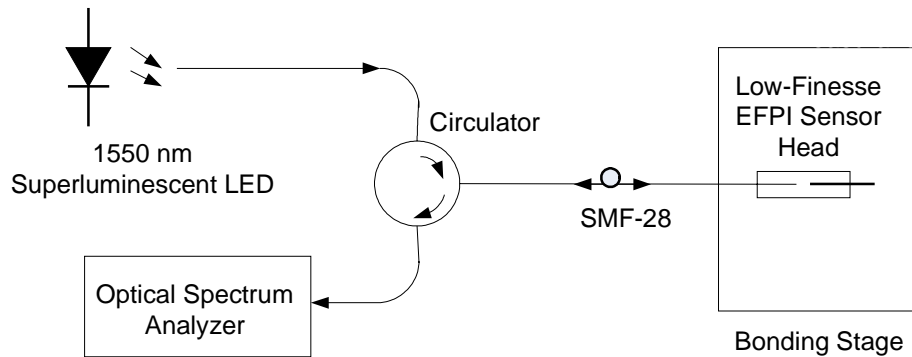


Fig. 7.2 Principle diagram of a low-finesse EFPI sensor fabrication monitoring system.

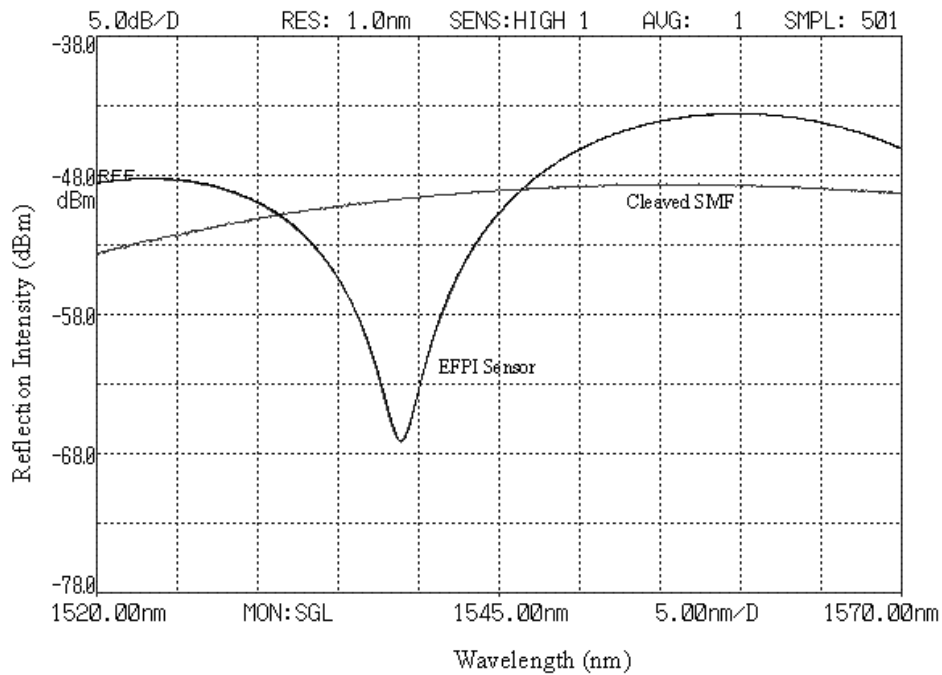


Fig. 7.3 Reflection spectrum of the low-finesse reflection-type EFPI sensor.

The high-finesse transmission-type EFPI sensor was fabricated in the same way and using the same material as in the EFP-TF, described in Chapter 6. The transmission spectrum of the sensor is given in Fig. 7.4. A passband width about 7~8 nm and a $FSR=119.6$ nm were measured. Using Eq. (2-9) and the two transmission peaks, the airgap length was calculated as 10.589 μm . We will see in Section 10.3 that this FSR range and passband match the EFP-TF pretty well when a scan-mode was used to demodulate the high-finesse EFPI sensor.

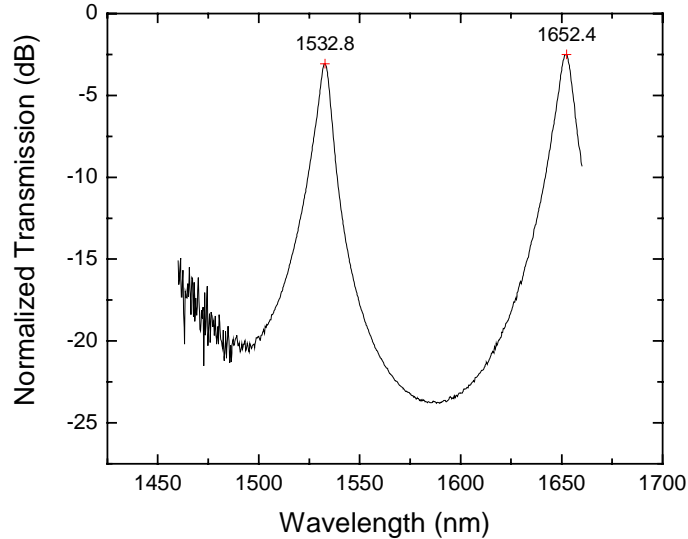


Fig. 7.4 Transmission spectrum of the high-finesse transmission-type EFPI temperature sensor at $T=20^{\circ}\text{C}$.

7.2 DFPI Sensors

Metal diaphragms, such as stainless steel and nickel alloys, have a long history of being used for pressure transducers [165]. Due to the advances in the last decades in microfabrication technology, silicon and silicon dioxide diaphragms have been extensively used in the fabrication of various types of piezoresistive sensors [166] [167] and capacitive sensors [168]. More recently, silicon and silicon dioxide diaphragms as well as polymer diaphragms have found increasing applications in Fabry-Perot type fiber-optic sensors [78] [169] [170] [171]. In the past five years, we have demonstrated a glass diaphragm based FPI (DFPI) sensor for both partial discharge detection in high voltage transformers and pressure measurement in gas turbine engines [18] [172] [173].

In this section, I will focus on the principles and fabrication techniques for DFPI-PD sensors only. The principles of the DFPI-Engine sensor is exactly the same as the DFPI-PD sensors. The major differences are that only one fused silica ferrule, instead of two in the PD sensors, laser-bonding, instead of glass powder or epoxy bonding in the PD sensors, and low-finesse, instead of medium-finesse Fabry-Perot in the PD sensors, have been used in the DFPI-Engine sensors. Detailed information about the DFPI-Engine sensors can be found in Reference [173].

7.2.1 Principle of Operation

As shown in Fig. 7.5, a DFPI-PD sensor head is fabricated by thermally bonding a single-mode fiber, a ferrule, a silica tube and a glass diaphragm together to form a sealed Fabry-Perot interferometer. The incident light from the lead-in/out single-mode fiber is first partially reflected (R_1) at the endface of the fiber. The remainder of the light propagates across the air gap to the inner surface of the diaphragm where it is once again partially reflected (R_2). In order to minimize or eliminate the effects of the parasitic interferences caused by the outer surface of the diaphragm, the thickness of the diaphragm is required to be larger than the air cavity length and the coherence length of the broadband light source. Another way to reduce the effects of the outer surface is to increase the reflectance of the inner surface. Both methods have been used in the design of our DFPI-PD sensors. The diaphragm vibrates at the presence of a pressure wave, such as an acoustic wave, which imposes a dynamic pressure on it. The DFPI-PD sensor converts pressure waves into a phase modulation of the lightwaves through the vibration of the diaphragm. In order to maximize the pressure sensitivity, the single-mode fiber has to be aligned to the center of the diaphragm. Theoretical analysis of the performance of a DFPI sensor using a low coherence light source is given in Chapter 3, which has been used as a guidance in the design of the sensors' parameters, including the cavity length, F-P finesse, reflectance and the source properties, etc.

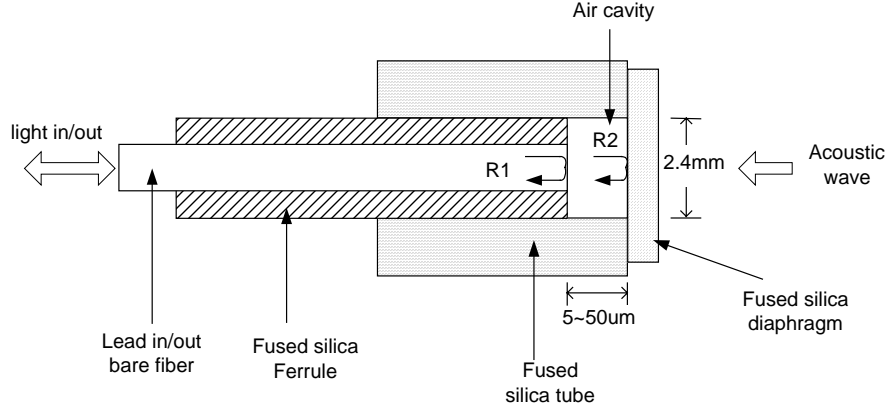


Fig. 7.5 Principle diagram of an DFPI-PD sensor.

For the detection of PD generated broadband acoustic waves, quadrature demodulation has to be used. To maintain a linear operation, the maximum airgap change is required not to exceed the linear region of a half fringe. The definition and calculation of a linear region is discussed in Chapter 3. By simplifying Eq. (2-13), the optical intensity arriving at the photodiode with a TOF-WLI interrogation system operating in linear mode can be expressed as

$$I(l, \lambda_0) = S_o(l_0, \lambda_0) \cdot l + C(l_0, \lambda_0) \quad (7-5)$$

where l – airgap length

λ_0 - TOF central wavelength

l_0 – airgap length at the Q-point

$S_o(l_0, \lambda_0)$ - fringe sensitivity of a sensor respect to the airgap change near its Q-point, given by Eq. (3-8).

$C(l_0, \lambda_0)$ – constant at the chosen Q-point.

The airgap length l can be expressed as

$$l = l_0 + y_0(P) \quad (7-6)$$

where $y_0(P)$ is the airgap change at the center of the diaphragm caused by the acoustic pressure P . Therefore, the AC component of the electrical output of the sensor $V(P)$ at the presence of acoustic waves is proportional to $y_0(P)$, and can be expressed as

$$V(P) = G \cdot \mathfrak{R} \cdot S_o(l_0, \lambda_0) \cdot y_0(P) = S_{oe}(l_0, \lambda_0) \cdot y_0(P) \quad (7-7)$$

where G – gain of the optical receiver.

\mathfrak{R} - responsivity of the InGaAs photodetector, ~ 0.9 at 1300 nm.

$S_{oe}(l_0, \lambda_0)$ – total optical and electrical sensitivity with respect to airgap change, given by

$$S_{oe}(l_0, \lambda_0) = G \cdot \mathfrak{R} \cdot S_o(l_0, \lambda_0) \quad (7-8)$$

7.2.2 Diaphragm Design Considerations

The diaphragm design is probably the most critical part in a DFPI-PD sensor for efficient pressure wave detection. The sensitivity, frequency response, linearity, temperature dependence, and the size of the sensor head are directly related to the diaphragm properties. For the sake of extremely low temperature dependence, fused silica, the same material as the silica fiber, has been chosen for the ferrule, the tube and the diaphragm. However, the shape and size of the diaphragm are yet to be determined by the sensitivity and bandwidth requirements of the system.

1) Sensitivity

The diaphragm will be deflected whenever there is a differential pressure P between the inside and outside of the sealed cavity. The out-of-plane deflection of the diaphragm y is a function of the pressure difference at any radial position r . With the assumption of a uniform diaphragm thickness, small deflection (required for linear operation), infinitely rigid clamping around the diaphragm periphery and perfectly elastic behavior [174] [165], which is true for the fused silica diaphragm and our bonding method, the deflection under the pressure difference P can be expressed as [165]

$$y(P) = \frac{3(1-\mu^2)}{16Eh^3}(a^2 - r^2)^2 P \quad (7-9)$$

where μ is the Poisson's ratio ($\mu = 0.16$ for fused silica glass 7940 at 25°C); E is the Young's modulus of the silica glass material ($E = 7.24 \times 10^{10}$ Pa or 73.5×10^8 kg/m² at 25°C); a is the radius of the diaphragm defined by the inner diameter of the fused silica tube; and h is the thickness of the diaphragm. In our sensor configuration, the fiber is positioned to the central part of the diaphragm so that only the center deflection $y_0(P)$ is of interest. The pressure sensitivity of a

fused silica diaphragm is given by

$$\delta = \frac{y_0(P)}{P} = 2.524 \times 10^{-6} \frac{a^4}{h^3} \text{ (nm / kPa)} \quad (7-10)$$

where $y_0(P)$ is in nm , a and h are in μm , and P is in kPa. Fig. 7.6 shows a typical sensor sensitivity curve at $a = 1.25 \text{ mm}$, calculated using Eq. (7-10).

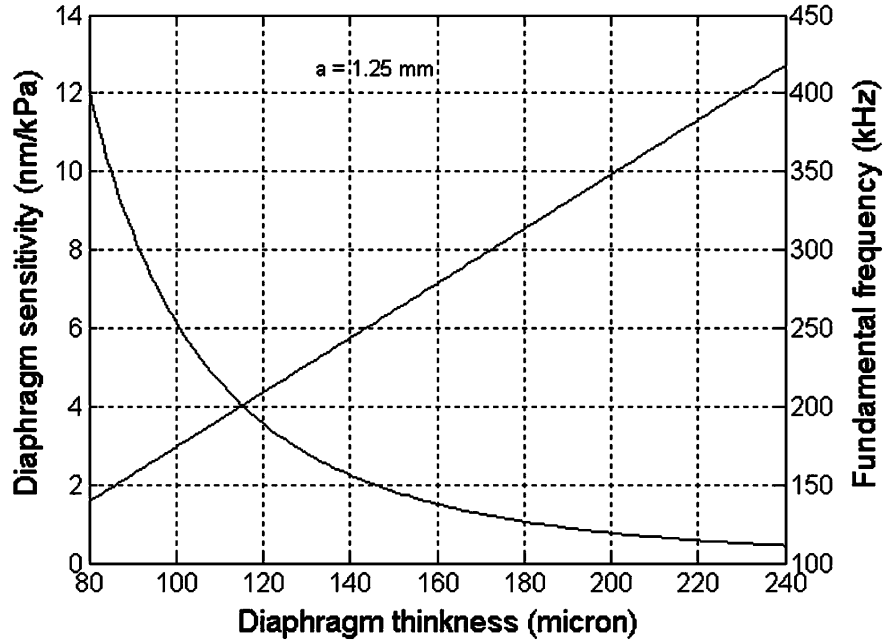


Fig. 7.6 Diaphragm sensitivity and frequency response.

Substituting Eq. (7-10) into Eq.(7-7) yields

$$V(P) = S_T(l_0, \lambda_0) \cdot P \quad (7-11)$$

where

$$S_T(l_0, \lambda_0) = 2.524 \times 10^{-9} \cdot G \cdot \mathfrak{R} \cdot S_o(l_0, \lambda_0) \cdot \frac{a^4}{h^3} \quad (7-11a)$$

is the total sensitivity of the TOF-WLI sensing system with a DFPI sensor.

Obviously, $V(P)$ is proportional to the applied dynamic pressure in the linear operation range. As indicated by Eq. (7-11a), the total sensitivity is determined by the dimensions of the diaphragm, the gain of the amplifier G , and the fringe sensitivity which is a function of the

airgap length l_0 , the finesse of the DFPI, the properties of the broadband source and the TOF. Higher amplifier gain increases the total sensitivity but the increase is limited by the bandwidth requirement, SNR and reduced dynamic range. Apparently, the sensitivity can be significantly increased by increasing the I.D. of the silica tube or by reducing the thickness of the diaphragm. However, the diaphragm dimensions are also related to the sensor's frequency response, which is discussed in the next subsection. Another effective way to increase the sensitivity is to use diaphragms with reflective coatings. Using coated diaphragm is that the parasitic interferences due to the outer surface of the diaphragm can be significantly reduced. However, when the reflectance is increased, the finesse of the F-P interferometer is also increased. This results in shorter linear regions and a reduced fringe contrast, as discussed in Section 3.2. Low to medium finesse DFPI sensors with asymmetric coatings were used in the fabrication of our DFPI-PD sensors.

2) Frequency Response

In partial discharge detection, the sensitive frequency of the sensor system is suggested to be in the range of 20 to 200 kHz [175]-[179]. This is basically due to the fact that magnetostriction-introduced noise of transformers usually exists in the low frequency range below 60 kHz, and the acoustic emission frequency of a PD is mostly around 150 kHz [177].

In order to faithfully respond to dynamic acoustic pressure, the resonant frequency of the diaphragm must be higher than the highest applied signal frequency. Based on the same assumptions used for the sensitivity calculation, the undamped n-order resonant frequency of a rigidly clamped diaphragm can be expressed as [165]

$$f_n = \frac{\alpha h}{2\pi a^2} \left[\frac{gE}{12w(1-\mu^2)} \right]^{1/2} \quad (7-12)$$

where α is a constant related to the vibrating modes of the diaphragm, and takes a value of 10.21 for the fundamental mode ($n=0$); $g=9.815 \text{ m/s}^2$ is the gravitational constant; w is the weight density of the diaphragm material, and for a fused silica glass diaphragm at 25 C° , w is $2.20 \times 10^3 \text{ kg/m}^3$. The frequency response of the diaphragm can thus be obtained

$$f_0 = 2.72 \times \frac{h}{a^2} \text{ (kHz)} \quad (7-13)$$

where h is in μm and a is in mm . As indicated by Eq.(7-13), the frequency response is proportional to the thickness of the diaphragm and inversely proportional to the square of the effective diaphragm radius. The fundamental natural frequency of a fused silica diaphragm with an effective diameter of 2.5 mm is given in Fig. 7.6 for various diaphragm thicknesses. In practice, Eq.(7-13) may not be accurate for a DFPI-PD sensor because of the presence of mineral oil. In a fluid, the natural frequency should be modified by a factor of $1/(1+\beta)^{1/2}$ [165], where $\beta=0.669w_1R/wh$, and $w_1 = 0.85 \times 10^3 \text{ kg/m}^3$ is the density of the transformer oil. For a 2.5 mm diameter and 150 μm diaphragm, the modification factor is about 0.56. However, considering that only one side of the diaphragm is in mineral oil, and in a condition where a small volume of air is trapped behind the diaphragm and the volume change caused by deflection is not insignificant compared with the total volume of the trapped air, a slight increase in the resonant frequency is possible as the trapped air might act as a stiffening spring as indicated by reference [165], the modification factor could be even close to 1. Therefore, Eq.(7-13) can still be used to estimate the fundamental natural frequency in the diaphragm design.

A trade-off must be made between a high sensitivity and a high frequency response of the sensor when selecting the geometric size of the diaphragm. However, if high sensitivity is more important, the diaphragm may operate in a resonant condition, similar to the operation of many PZT transducers.

7.2.3 DFPI Sensor Fabrication

In this subsection, we briefly introduce the fabrication of DFPI sensors. For a detail description of the sensor fabrication, please refer to the Reference [172].

Three major bonding methods, epoxy bonding, thermal-bonding with an inter-media layer and laser fusion bonding, have been investigated in DFPI sensor fabrication in order to achieve best air cavity length control, minimum misalignments between the endface of the single-mode fiber and the diaphragm, high reliability, and minimum temperature cross sensitivity.

In the epoxy bonding method, the fiber, the ferrule, the tubing and the diaphragm were bonded together using the Epoxy 907 Adhesive System from Miller-Stephenson Chemical Co.,

Inc. Epoxy 907 has a very good bonding strength after complete curing, thus DFPI sensors using Epoxy 907 have a very good reliability, even in mineral oil. Since epoxy bonding is a low temperature process, it is the easiest way to fabricate a DFPI sensor. However, due to the shrinking of the epoxy during curing, experience is required in control of the air cavity length. Because of the larger thermal expansion coefficient of the Epoxy 907 than that of fused silica, Q-point drifts due to environmental temperature fluctuations can be significant, and TOF-WLI has to be employed for dynamic drift compensation. Using the DG-TOF based WLI for DFPI sensor interrogation will be discussed in Chapter 9.

The thermal-bonding with an inter-media layer was developed by J. Deng at CPT [172]. In this method, borosilicate glass powders of $\sim 5 \mu\text{m}$ in size and a melting point around 700°C from Corning Corp. were used as an inter-media layer between the diaphragm and the silica tube, between the ferrule and the tube, and between the lead-in/out fiber and the ferrule. Fig. 7.7 is the schematic of the experimental setup used for the inter-media layer bonding. Heating was achieved using a homemade resistive heating coil. The same setup was also used for the epoxy bonding process. Fig. 7.8 is a photo of the real sensor fabrication setup.

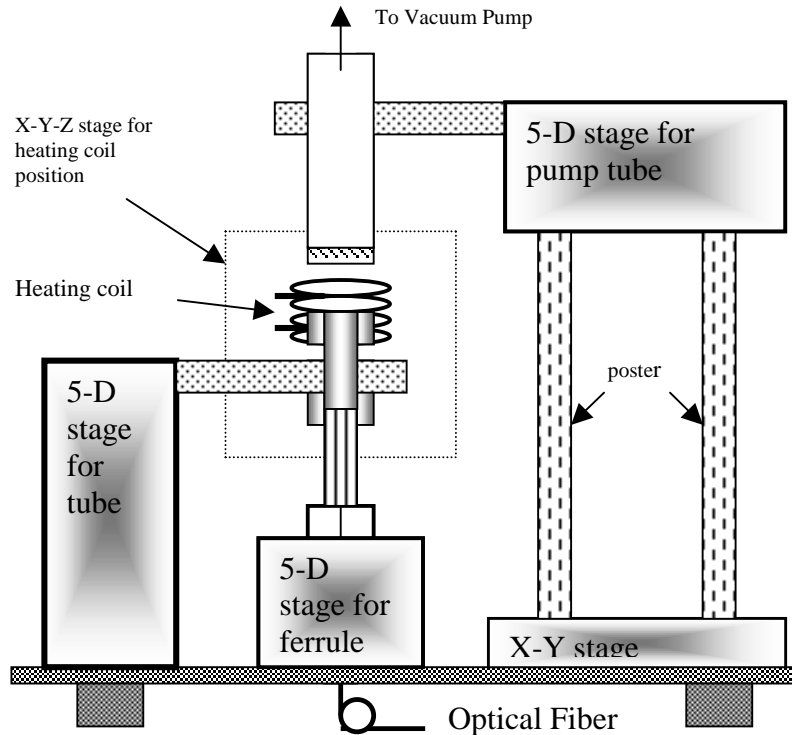


Fig. 7.7 Support system for the inter-media layer bonding method. [172]

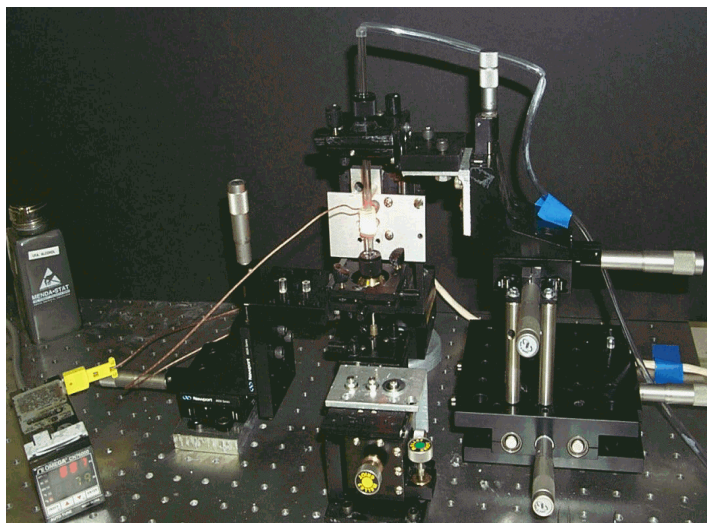


Fig. 7.8 Photo of the DFPI sensor bonding setup.

To reduce the thermal stress which occurs during any thermal process, therefore, increase the fabrication yield and the reliability of the sensor heads, the heating process was divided into three steps, including preheating (~15min), heating (750°C ~10min), and cooling (~2 hour), illustrated in Fig. 7.9.

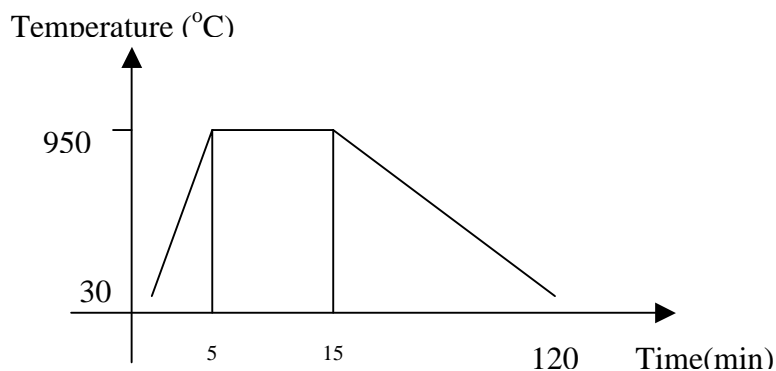


Fig. 7.9 Heating process during the thermal-bonding. [172]

An airgap length and interference fringe monitoring system, shown in Fig. 7.10, similar to the one in Fig. 7.2, but with a 1300 nm LED light source, was employed. Fig. 7.11 shows the typical interferogram of a medium-finesse DFPI-PD sensor, recorded by the OSA. The airgap length can be estimated from the positions of the fringe peaks or using Fourier transform, while the misalignments were minimized by fine-adjusting the alignment for best fringe contrast and highest peak intensity. The obvious advantage of the thermal-bonding with an inter-media layer,

over epoxy bonding, is that the temperature dependence of the DFPI cavity length was remarkably reduced due to the small difference between the thermal expansion coefficient of the fused silica and that of the borosilicate glass. However, due to the high temperature bonding process involved, precise control of the DFPI cavity length is a big challenge. Therefore, TOF-WLI still has played an important role in the interrogation of DFPI sensors fabricated by using this bonding method.

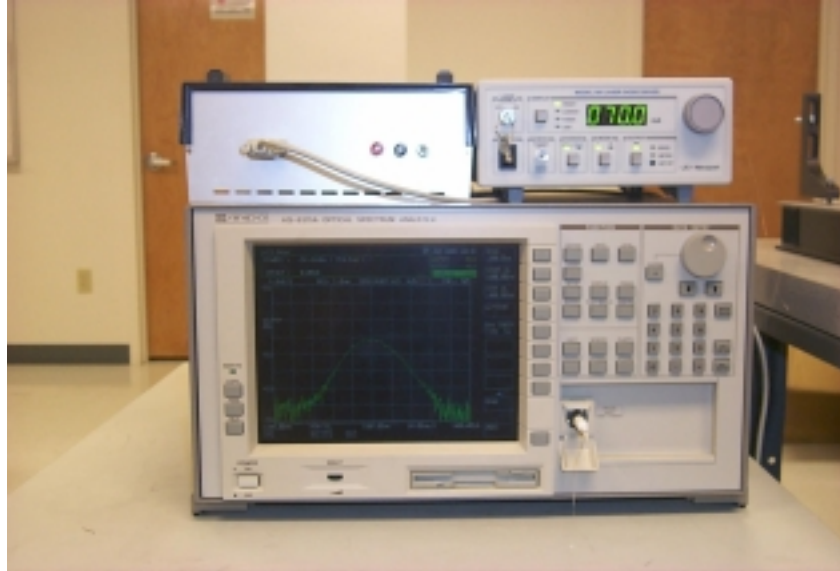


Fig. 7.10 Photo of the airgap length and interference fringe monitoring system.

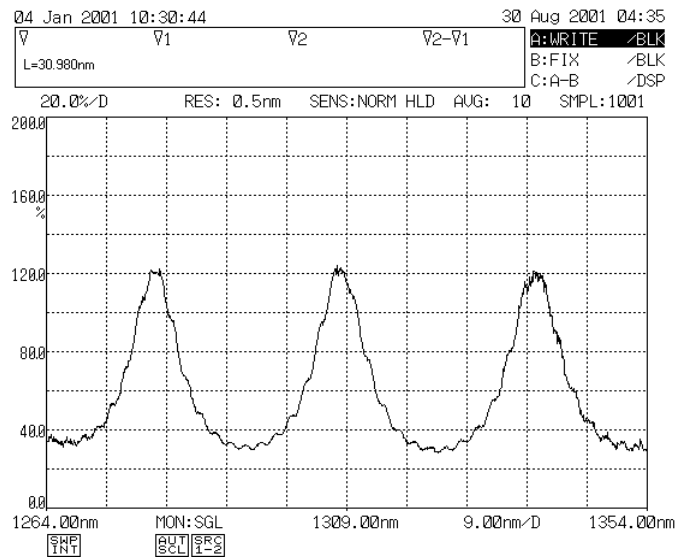


Fig. 7.11 Typical interferogram of a medium-finesse DFPI-PD sensor.

Laser fusion bonding is a technique in which the high intensity laser beam from a CO₂ laser is used to fuse the two glass components together at the bonding points or bonding areas. Using laser fusion bonding for the DFPI sensor fabrication was first proposed and tried by J. Deng [180], and improved by J. Xu [173]. A focused CO₂ laser beam provides very precise temperature control, and very small and localized bonding points, which are very important in sensor fabrication. DFPI sensors fabricated using this approach feature very accurate initial air cavity length and extremely small temperature dependence, and therefore, have been exploited for dynamic pressure measurements in gas turbine engines. For detail about the laser fusion bonding method, please refer to the Reference [173].

Due to the low environmental temperature in high voltage transformers (< 50 °C) and the success in the development of TOF-WLI with Q-point tuning capability, epoxy based technique was eventually chosen in the fabrication of DFPI-PD sensor heads. However, because of much higher temperature (above 800 °C) involved in turbine engine pressure measurements, laser fusion bonding was used in the fabrication of DFPI-Engine sensors.

Tens of DFPI-PD sensor heads have been fabricated by epoxy bonding for both laboratory test and field demonstrations. All the ferrules had an inner diameter of 130μm and an outer diameter of 2.5mm, and the tubes had an inner diameter of 2.52mm and an outer diameter of 6mm. The diaphragms used had three different thicknesses, 60~70μm (resonant sensors), 110~130μm and ~175μm with approximately 35% reflectance coatings. The end surfaces of the lead-in/out fibers were coated for about 20% reflectance. The silicon coatings were deposited using our AUTO 500 Sputtering system. A photograph of the two prototype PD sensors is shown in Fig. 7.12.

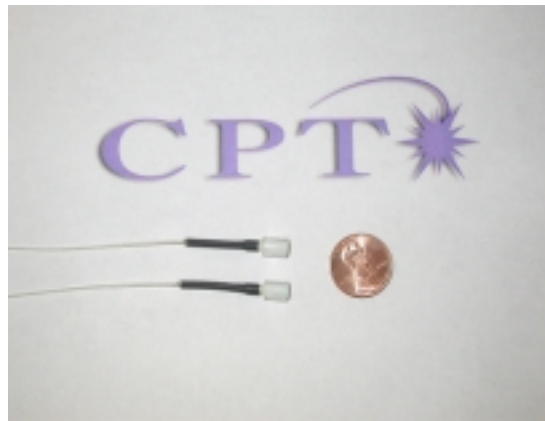


Fig. 7.12 Photograph of two DFPI-PD sensors.

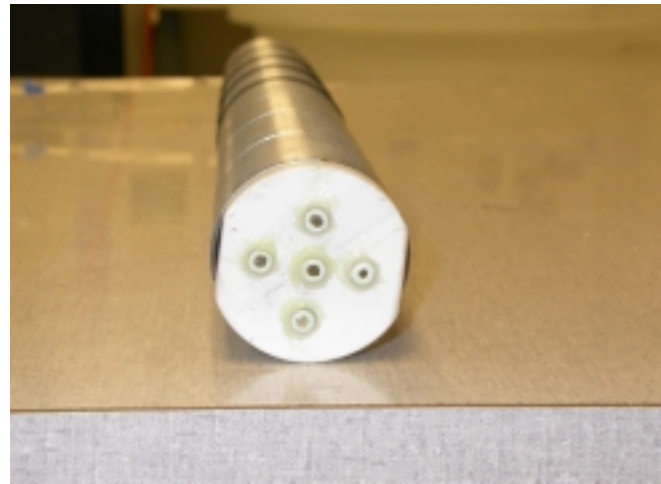
What needs to be emphasized is that no matter how well the epoxy bonding or laser bonding method is used, it is very hard, if not impossible, to obtain an initial cavity length with an accuracy on the order of nanometers. Although the temperature dependence of fusion-bonded sensors can be as small as $0.01\text{nm}/^\circ\text{C}$ for a cavity length of $20\ \mu\text{m}$, the high oil-pressure (up to $\sim 58\ \text{kPa}$ or $\sim 8.5\ \text{psi}$) in transformers and extremely high temperature in turbine engines may drive the operating point to a peak or a valley of an interference fringe. Therefore, a TOF-WLI system operating in linear mode has to be employed for the interrogation of both types of DFPI sensors.

7.2.4 DFPI sensor packaging

A DFPI-PD sensor holder was designed to provide easy and safe access to power transformers through a 2-inch or 3-inch drain valve. The holder consists of a flange, a tube, a link-bar, and accessories, as shown in Fig. 7.13. A special package with high temperature capability was also designed for DFPI-Engine sensors, as shown in Fig. 7.14.



(a)



(b)

Fig. 7.13 DFPI-PD sensor holder. (a) Side view of the holder, (b) DFPI-PD sensors mounted on the tube.

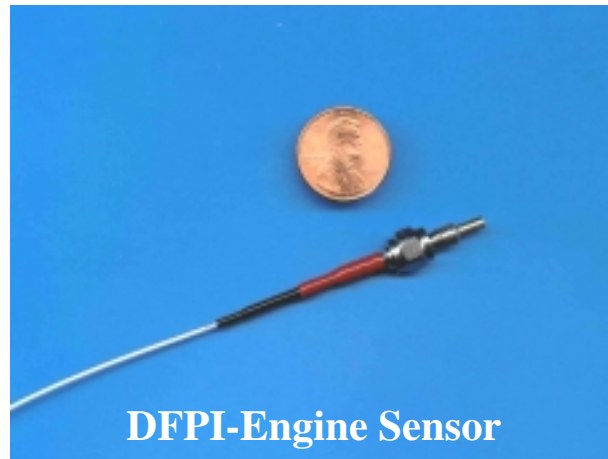


Fig. 7.14 A packaged DFPI-Engine sensor. (Provided by J. Xu)

7.3 Summary

This chapter first briefly introduced the principle of a low-finesse extrinsic Fabry-Perot interferometer (EFPI) and a high-finesse EFPI as temperature sensors, and then discussed the sensor fabrication techniques and the sensor characterization. These sensors were designed for best performance when interrogated by the TOF-WLI based on the EFP-TF.

For the DFPI sensors, we have described the operation principles, the diaphragm design for high sensitivity and large signal bandwidth, the sensor fabrication processes, especially the epoxy bonding, the inter-media layer bonding and the laser direct bonding methods, the airgap length control and alignment monitoring system, and the sensor packaging. The DFPI-PD sensors were optimized for partial discharge detection in high voltage power transformers, therefore, ultra-high sensitivity (with a resolution around a few Pa) and wide bandwidth (20~200kHz) were the fundamental requirements. The package for DFPI-PD sensors was specially designed for easy delivery of sensors into a power transformer through a drain valve. The DFPI-Engine sensors were less sensitive than the DFPI-PD sensors and had lower frequency response, but high temperature capability and large dynamic range were important. Laser bonding and high temperature packaging met these specifications.

Chapter 8 Low Noise Analog Optical Receiver

Analog optical receivers are one of the most critical components which partially determine the sensitivity, the resolution and the measurement range of a fiber-optic sensing system. This chapter introduces in detail the design of a low noise analog optical receiver for the engine pressure measurement. The focuses of the chapter are on the various types of noise sources present in an analog optical receiver, noise reduction strategies used, and some experimental results. The circuits of the optical receivers for PD detection are also given at the end of the chapter.

8.1 Introduction

In almost every area of measurement, the ultimate limit to the detectability of weak signals is set by noise - the unwanted signals that obscure the desired signal [181]. In an optical receiver, the signal-to-noise ratio is defined as [182]

$$SNR = \frac{\text{average_signal_power}}{\text{noise_power}} = \frac{i_p^2}{i_n^2} \quad (8-1)$$

where $i_p = \mathcal{R}P_{in}$ is the photocurrent generated by the incident optical power P_{in} on a photodiode, \mathcal{R} is the responsivity of the photodiode, and i_n is the total equivalent input noise current of the receiver. The resolution of a sensing system is reached when $SNR=1$, or $i_p = i_n$.

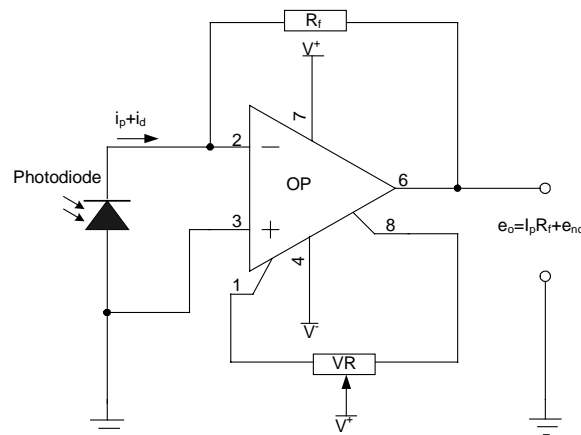


Fig. 8.1 Schematics of a basic transimpedance amplifier.

The most widely used preamplifier is a transimpedance amplifier, or called current-to-voltage converter [181]-[183], as shown in Fig.8.1. The preamplifier appears extremely simple, but its noise performance is much more complex. Particularly, when a transimpedance amplifier is used for fiber optic sensing, high gain (large feedback resistance R_f) is generally required for very low level of optical signals. Also photodiodes typically exhibit large shunt capacitance that rolls off the diode impedance. This combination produces noise gain peaking at higher frequencies and a complex response to the op amp's input noise voltage. In addition, the high R_f resistance increases the significances of the resistor's noise and the noise of the amplifier input current. [183]

Fig. 8.2 shows the noise model of the basic transimpedance amplifier, where R_D , C_D are the resistance and capacitance of the photodiode, C_{ia} , i_{ni} , e_{ni} are the input capacitance, noise current and noise voltage of the OP, and e_{nR} , C_S are the noise voltage and stray capacitance of R_f , respectively.

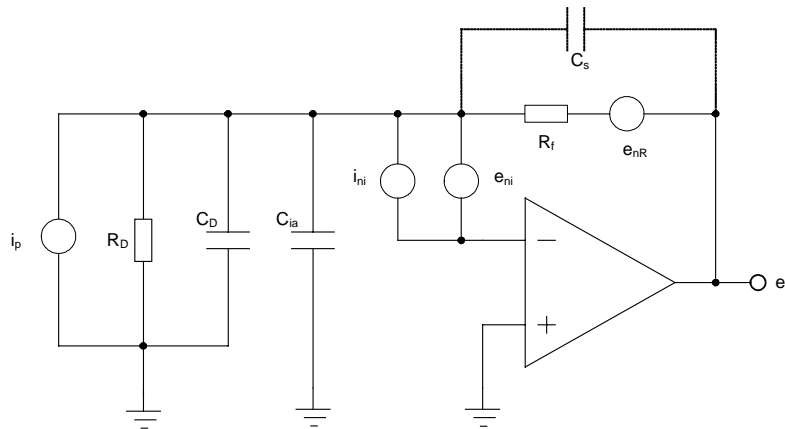


Fig. 8.2 Noise analysis model of the basic transimpedance amplifier.

8.2 Noise Sources

In general, the sources of noise can be classified into two types, intrinsic noise and external noise. The intrinsic noise is the noise generated by the electronic circuits itself, including detector noise, thermal noise and amplifier noise, while the external noise is induced or coupled into the circuits through various mechanisms, such as electromagnetic interference (EMI), power

supply, light source, and reflection due to unmatched load. This section introduces the mechanism behind each noise source.

8.2.1 Intrinsic Noise

1) Detector noise

Detector noise is also called shot noise. It is generated by random fluctuations of current (both dark current or photocurrent) flowing through the photodiode. The shot noise current can be expressed as [181]

$$i_{n(shot)} = \sqrt{2q(i_d + i_p)\Delta f} \quad (8-2)$$

where q - electron charge (1.6×10^{-19} coulombs)

i_d - dark current, leakage current generated by bias voltage applied to the photodiode.

i_p - photocurrent generated by the incident optical power

Δf - effective noise bandwidth of the receiver, determined by R_f and the shunt capacitance

2) Thermal noise

Thermal noise is caused by random thermal motion of electrons in the shunt or feedback resistor R_f . The random thermal motion of electronics manifests as a fluctuation current even in the absence of an applied voltage. [182] The equivalent input thermal noise can be written as [181]

$$i_{n(feedback)} = \sqrt{\frac{4k_B T \Delta f}{R_f / Shunt}} \quad (8-3)$$

where k_B is the Boltzmann's constant (1.38×10^{-23} J·K⁻¹), T is the temperature in Kelvin, and $R_{f/Shunt}$ is the feedback or shunt resistance, which is also a function of temperature for Silicon, InGaAs and Ge PIN photodiodes [181]. As temperature decreases, the shunt/feedback resistance increases, and thus the thermal noise decreases. However, the increase of the resistance is limited by the signal bandwidth and gain requirements.

3) Amplifier noise

The amplifier noise depends on the type of OP used and is also a function of the frequency f . The amplifier noise current is given by [181]

$$i_{n(amp)} = \sqrt{\langle i_{ni} \rangle^2 + \langle e_{ni} \omega C_T \rangle^2} \quad (8-4)$$

where i_{ni} - amplifier input noise current

e_{ni} - amplifier input noise voltage

$\omega = 2\pi f$

C_T - total input capacitance seen by the amplifier

The total intrinsic current noise:

$$i_{n(int\ intrinsic)} = \sqrt{\langle i_{n(shot)} \rangle^2 + \langle i_{n(feedback)} \rangle^2 + \langle i_{n(amp)} \rangle^2} \quad (8-5)$$

8.2.2 External Noise

External noise sources impose a background noise floor that requires attention to amplifier's environment rather than the amplifier itself and the peripheral components. This background noise typically results from the light source, and the parasitic noise coupling of external electrostatic and magnetic sources. These sources can dominate the noise performance, overriding any effort to further reduce the direct noise effects of the amplifier.

1) EMI noise

Electric field coupling, such as from the power line, supplies noise through mutual capacitances that exist between any two objects [183]. AC voltage difference between the two objects drives these mutual capacitances, coupling noise currents from one to the other. Fig. 8.3 illustrates an example of electrostatic noise coupling. Electrostatic noise source V_e represents any AC voltage source that creates an electric field in the vicinity of the amplifier. This source couples noise current i_{ne} through the mutual capacitances C_M to the amplifier's two inputs. The amplifier amplifies not only the photocurrent i_p , but also the noise current i_{ne} .

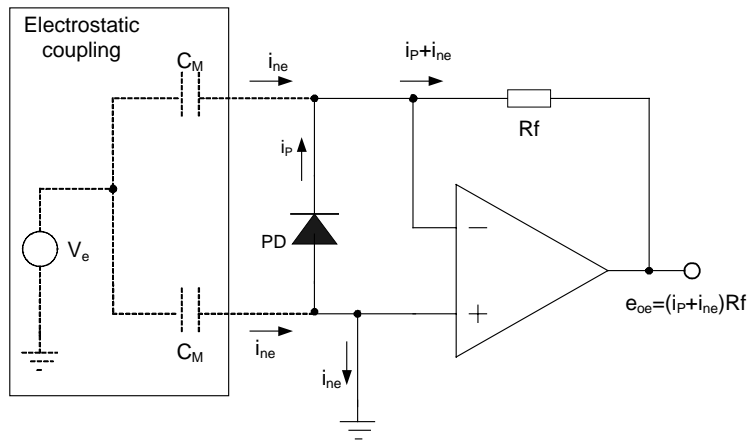


Fig. 8.3 Electrostatic noise coupling through mutual capacitances.

Magnetic noise coupling and radio-frequency interference (RFI) introduce circuit noise through a mutual inductance [183]. In this type of EMI coupling, the interference source acts like the primary of a transformer, and the loops in the preamplifier resemble secondary windings. Fig. 8.4 illustrates the loops exist in a basic transimpedance amplifier which may result in noise coupling. The preamplifier forms three magnetic receptor loops through the circuit connections of the photodiode, the feedback, and the load.

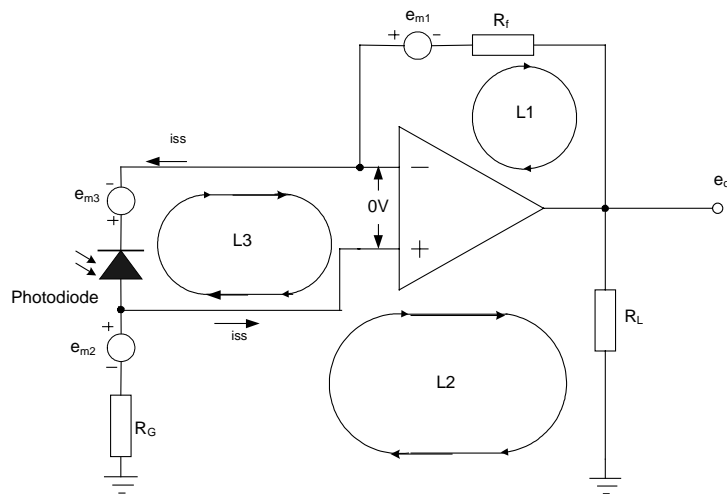


Fig. 8.4 Magnetic and RFI noise coupling through a mutual inductance.

2) Power supply

Noise on the power supply lines of the OP couples to the amplifier's output with a magnitude controlled by the supply line impedance, the amplifier's power supply rejection ratio (PSRR), and the circuit's noise gain [183]. In most cases, the supply-line impedance has the highest contribution to the noise coupling. Fig. 8.5 shows the mechanism how power noise can propagate to the amplifier output. Ideally, $V_P=V_+$ and $V_N=V_-$. But due to the existence of the line inductance L_P , the actual voltages applied to the OP react with the signal current i_S ,

$$V_P = V^+ - i_S Z_L \quad \text{and} \quad V_N = V^- + i_S Z_L \quad (8-6)$$

where $Z_L = L_P s$ is the resistance of the power-supply lines, producing a voltage error across the photodiode as

$$e_{error} = 2i_S Z_L / PSRR \quad (8-7)$$

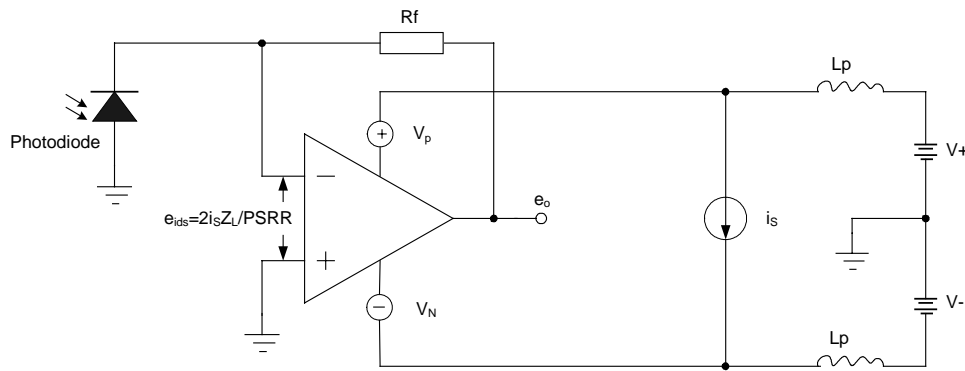


Fig. 8.5 Noise coupling from power-supply [183].

3) Light noise

Noise, such as EMI and power-supply noise, can also couple into the light source through the SLED driver. Random environmental temperature change may also cause the output power fluctuation and wavelength drift. Fig. 8.6 shows the noise performance of an optical receiver (with a 87kHz low pass filter) with and without a constant optical power input, respectively. The receiver had a total noise V_{rms} of 553 μ V in the absence of any optical power input, and a total noise V_{rms} of 752 μ V when a constant input power of 2.5 μ W was applied. Since the shot noise was negligible at this low level optical power, the increase of the noise level was attributed to the SLED driver.

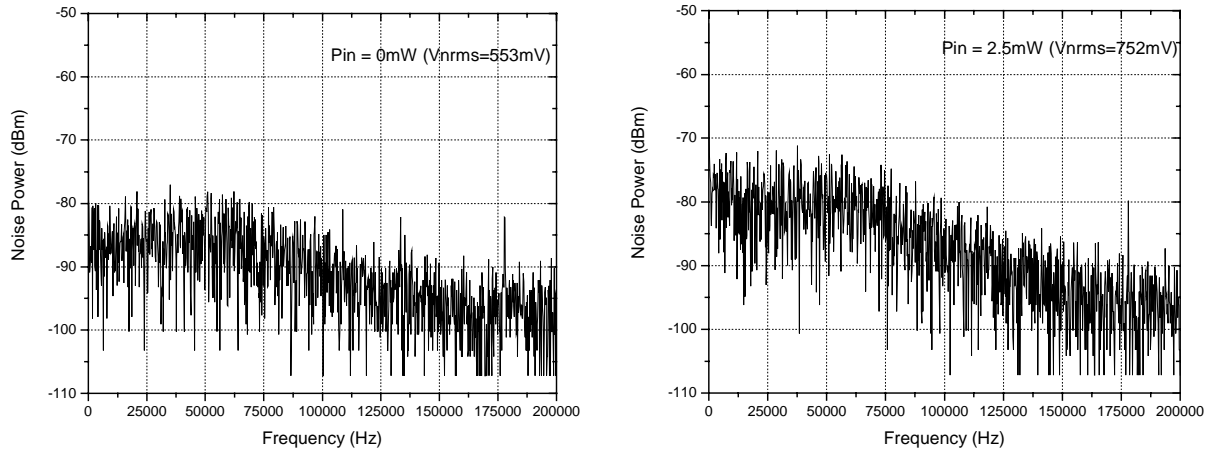


Fig. 8.6 Noise from the light source. (a) without optical input; (b) with $2.5\mu\text{W}$ optical input.

4) Reflection

Reflection may happen if there is any mismatch between the output resistance of the amplifier and its load. This reflection may directly add onto the total output noise, or cause an oscillation in the amplifier circuits. Reflection increases with the increase of signal frequency.

8.3 Noise Reduction Strategies

In order to achieve the best resolution or highest SNR in a TOF-WLI interrogation system, a variety of noise reduction strategies have been exploited in the design and construction of the sensing systems. This section describes each method briefly. Fig. 8.7 shows the setup used in noise measurements which includes a differential amplifier and a digital oscilloscope.

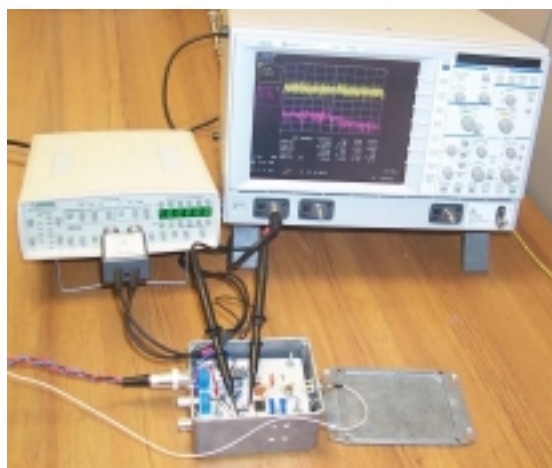


Fig. 8.7 Noise measurement setup.

1) Trace layout

Noise can be reduced by carefully placing the traces during the PCB design. There are several general rules which can be used for the optimization of the trace layout [184]:

- Minimizing the areas of the circuit's loops minimizes the mutual inductances that couple magnetic noise. Careful component layout achieves this by placing the amplifier's components, especially the photodiode, close to the OP amp.
- By matching loop areas and distances from a noise source, the amplifier's CMRR rejects the resulting equal noise coupling effects.
- Reducing the length of power-supply line can reduce the mutual inductance of the traces.
- Avoid unnecessary ground loops.

2) Low-pass filter

In order to remove or reduce the out of band noise, a second-order low pass filter was used after the preamp to limit the noise bandwidth to that of the signal. Fig 8.8(a) is the schematics of a second-order low pass filter. [185]

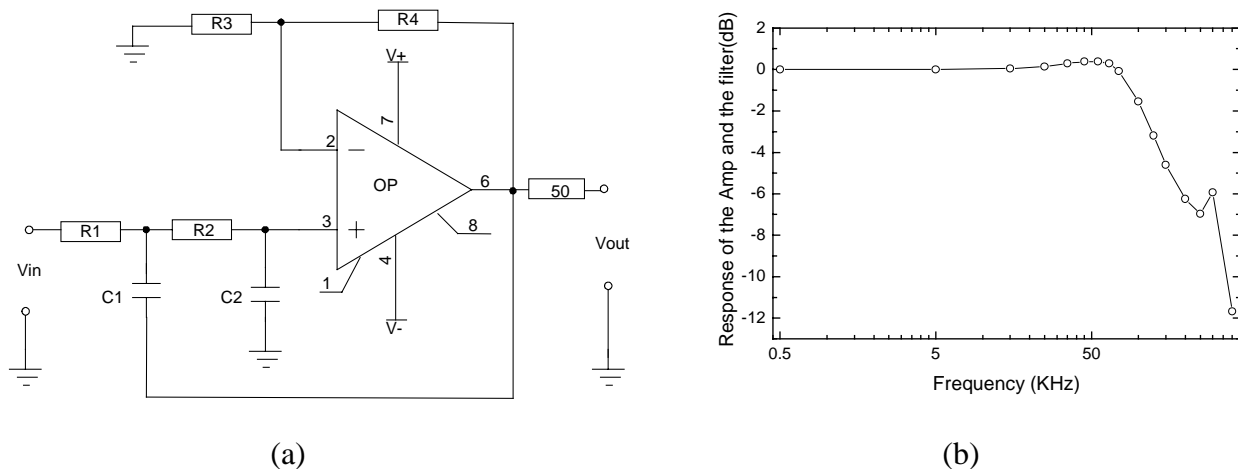


Fig. 8.8 Noise reduction using a low pass filter. (a) a second order low pass filter; (b) frequency response of the preamp with the low pass filter.

By selecting $R_1=R_2=R$, $C_1=C_2=C$, and $R_3=R_4$, the gain and the cutoff frequency of the filter can be calculated by

$$g = 1 + R_4 / R_3 = 2 \quad (8-8)$$

and

$$f = \frac{1}{2\pi\sqrt{R_1C_1R_2C_2}} = \frac{1}{2\pi RC} \quad (8-9)$$

Choosing R and C, a cutoff frequency about 87kHz for engine pressure measurements was easily realized. Fig. 8.8(b) is the experimental frequency response of the preamp and the low pass filter. The noise performances of the optical receiver for EFPI-Engine sensors before and after the filter are given in Fig. 8.9. The total noise was reduced to half while a gain of 2 was added. Apparently, an equivalent noise reduction of 12dB was readily obtained.

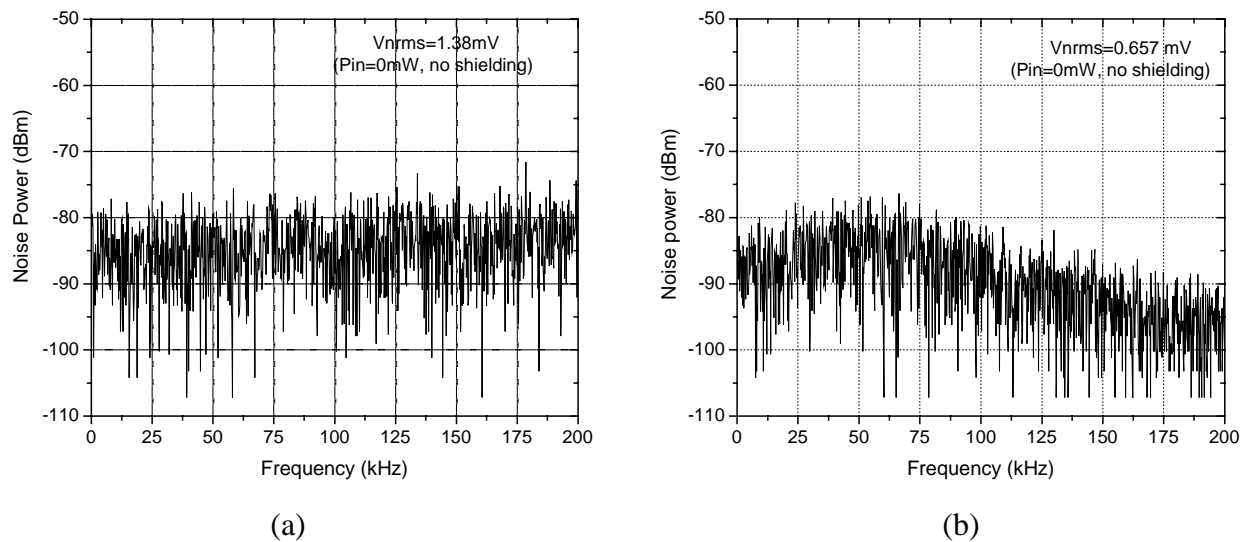


Fig. 8.9 Experimental results with a low pass filter. (a) Noise spectrum before the low-pass filter; (b) Noise spectrum after the low-pass filter (Gain =2).

3) Power-supply isolation

The light source and the optical receiver may be the two most noise sensitive components in a sensor system. However, the TEC may draw large current (>1A) from its power-supply in short time. Therefore a linear power supply was used for low noise circuits, including the optical receivers and the SLED driver, while a switching power-supply was used for high current parts and any digital parts in the system, as shown in Fig. 8.10.

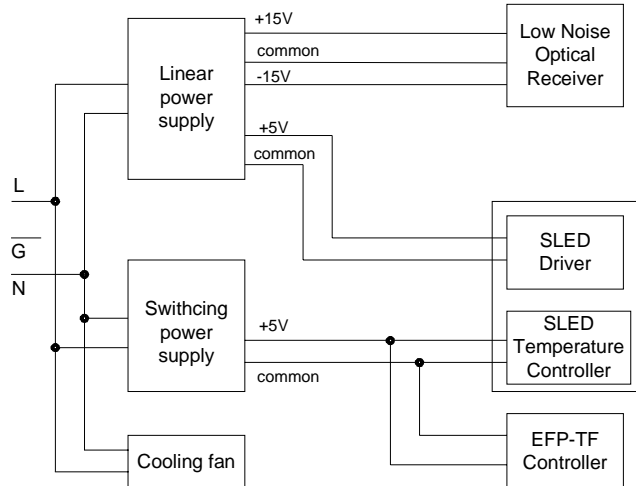
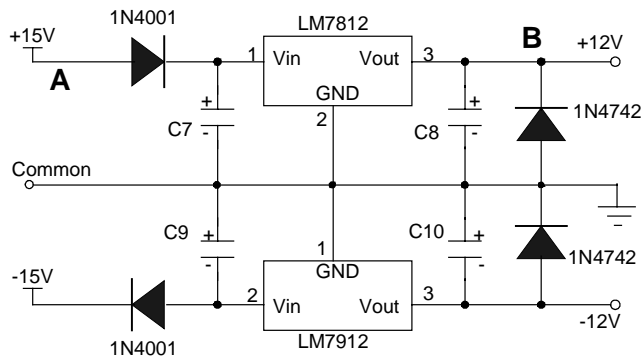


Fig. 8.10 Power-supply isolation.

4) Power-supply filtering

Since the linear power-supply is shared by the optical receivers, the SLED driver, and other circuits, the isolation of the preamplifier from others provides further protection from noise coupling through the power-supply lines. In this work, a power-supply filtering was applied using two voltage-regulator ICs, LM7812 and LM7912, as shown in Fig. 8.11(a), with the tested noise performances before (Point A) and after the filter (Point B) given in Fig. 8.11(b) and (c), respectively.

At Point A, the power-supply showed noise peaks at the 60Hz and its harmonic frequencies. Although the total noise power level was reduced less than 2dB at Point B, the noise amplitudes were remarkably attenuated at all major peaks.



(a)

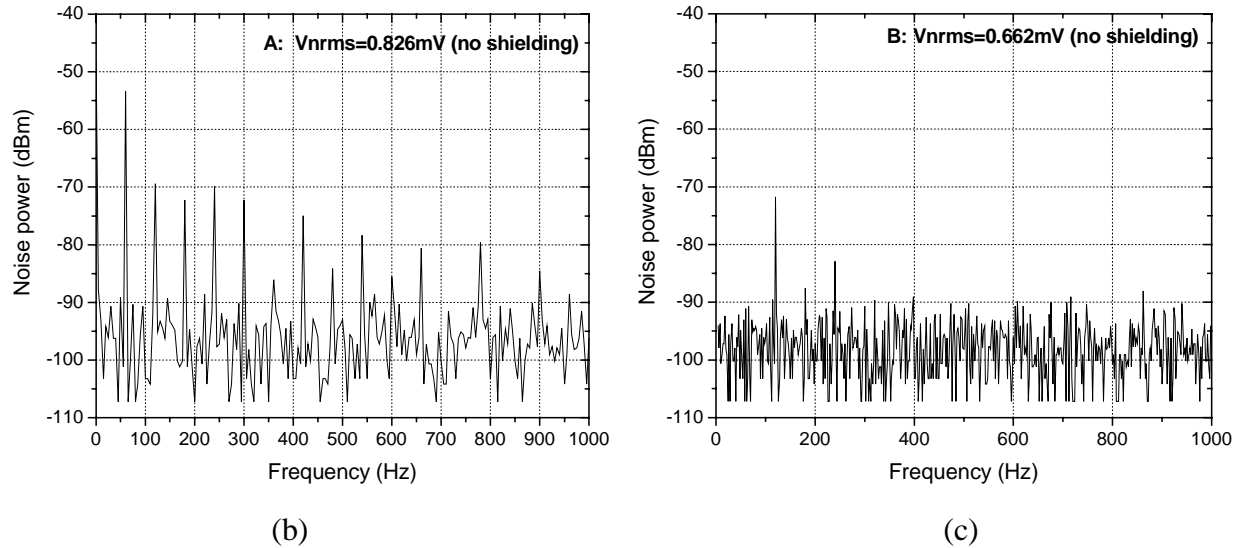


Fig. 8.11 Power-supply filtering. (a) Circuits; (b) Noise spectrum at Point A; (c) Noise spectrum at Point B.

5) Decoupling

Another effective way to reduce noise from the power-supply lines is decoupling by placing a bypass capacitor C_B between the component's power-supply pin and the ground pin. Fundamentally, adding the bypass capacitor shunts the line impedances to reduce the supply line voltage drops produced by i_S . From another perspective, the capacitors serve as local reservoirs for the immediate supply of high frequency current demands. [183] With the bypass capacitor, the error voltage in Eq. (8-7) is reduced due to the decrease of the Z_L

$$Z_L = \frac{L_p s}{1 + L_p C_B s^2} \quad (8-10)$$

6) Shielding, Grounding and Cabling

Physically shielding the amplifier from an EMI source offers the best protection for noise coupling. Making the shield with a material of high electrical conductivity and enough thickness ensures that the coupled currents produce little voltage drop across the shield. To be effective, the shield's ground must be earth ground. The shield should be connected to the system ground to minimize the effects of the parasitic capacitance induced. [183]

Fig. 8.12(a) illustrates the shielding, grounding and cabling used in the design of the EFP-TF WLI system. Shielded cables were used for interconnection between analog output and the DAQ card. Also, the power-supply cables were braided to reduce the loop area. Fig. 8.12(b) and (c) shows the noise spectrum before and after good shielding and grounding. Obviously, the low frequency noise was not noticeably affected, but the high frequency noise peaks were removed or attenuated.

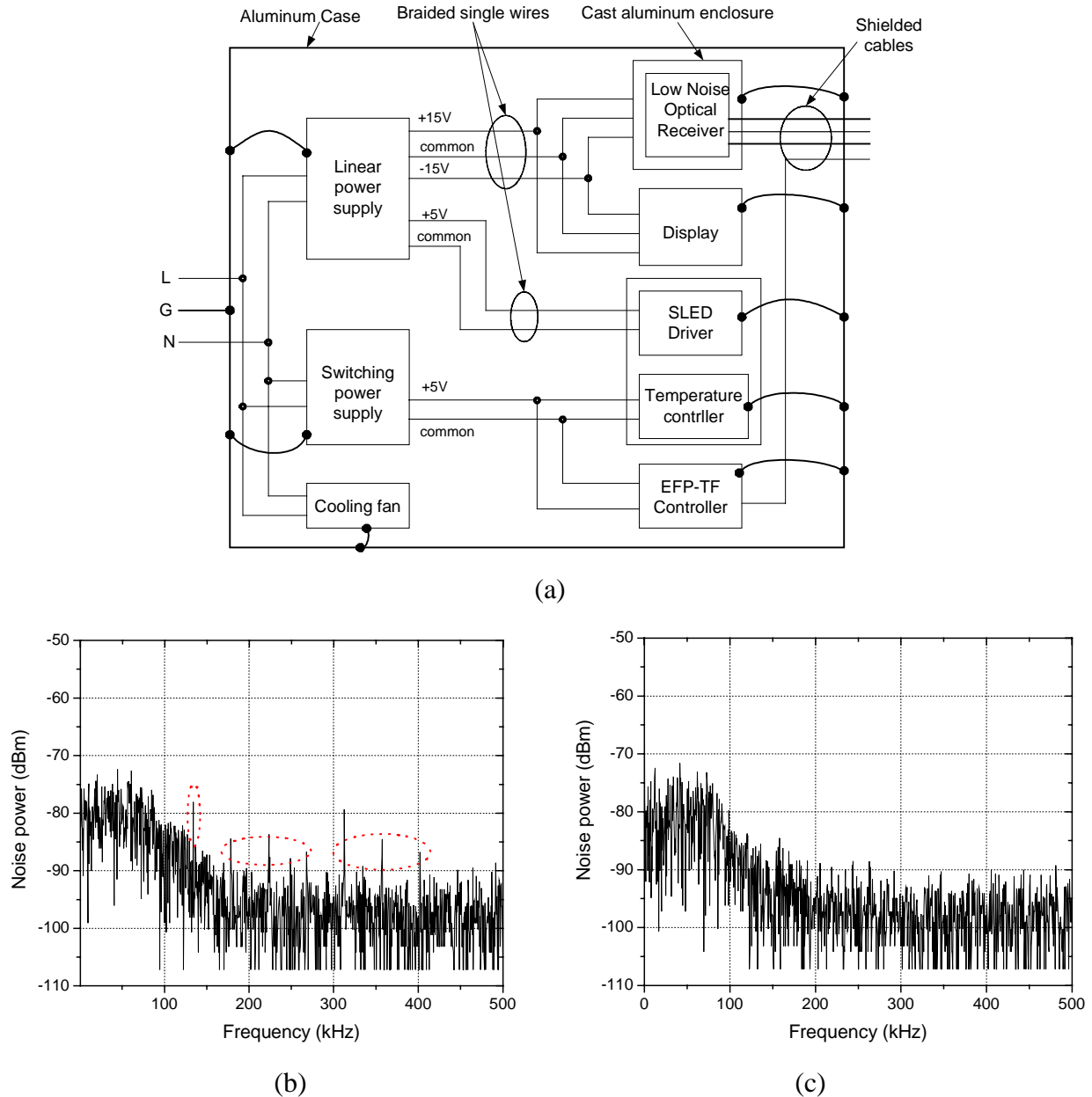


Fig. 8.12 Shielding, grounding and cabling. (a) Layout; (b) Noise w/o shielding and grounding; (c) Noise with shielding and grounding.

8.4 Optical Receiver for the EFP-TF WLI System

An InGaAs PIN (FD80FC) from Fermionics Opto-Technology was chosen as the photodiode. The FD80FC has an active area of $80\mu\text{m}$, a dark current of 0.04nA , a capacitance of 0.68pF , and a responsivity of 0.84A/W . The FC receptacle package makes it easy to be integrated into a preamplifier case.

Fig. 8.13 is the schematics of the narrowband channel in the optical receiver for the EFP-TF WLI system (refer to Fig. 10.1). OP37 was selected as the OP because of its large gain-bandwidth product (63MHz), relatively low current noise ($0.4\text{pA/Hz}^{1/2}$, @ 1kHz) and voltage noise ($3\text{ nV/Hz}^{1/2}$ @ 1kHz), excellent CMRR (126 dB), low drift ($0.2\text{ }\mu\text{V}/^\circ\text{C}$), low input offset voltage ($10\text{ }\mu\text{V}$). Potentiometer VR1 was used for offset adjustment, while VR2 for gain adjustment. The frequency response of the receiver is given in Fig. 8.8(b).

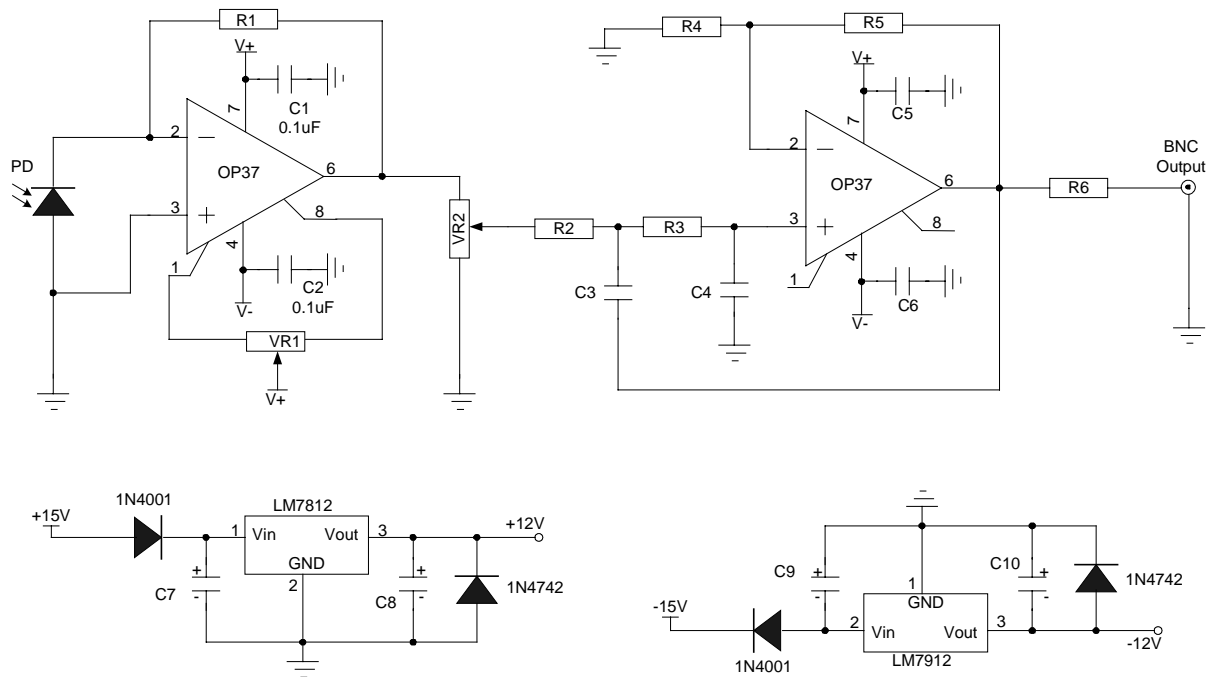


Fig. 8.13 Schematics of the optical receiver for the EFP-TF WLI system.

In addition to noise performance, the gain linearity of the optical receiver is also a very important parameter. Fig. 8.14 shows the relationship between the optical input power and the receiver output voltage when the gain was set to the maximum. A maximum gain of 1.8×10^6 and a linearity of $R = 0.99998$ were obtained.

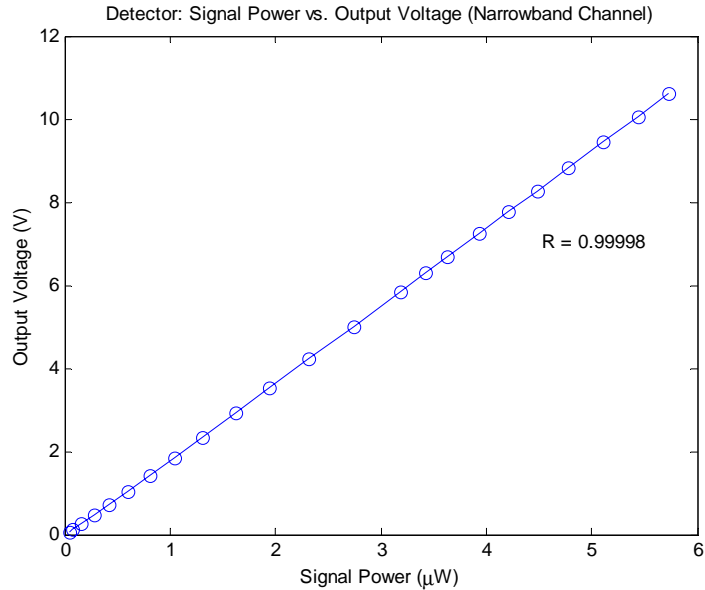


Fig. 8.14 Gain linearity.

8.5 Optical Receiver for the DG-TOF WLI System

Due to the different requirements on the power budget, the sensitivity, and the signal bandwidth by the PD detection, a bandpass low noise optical receiver was also built. Fig. 8.15 is the schematics of the optical receiver used in the DG-TOF WLI interrogation system for PD detection.

The receiver generally consists of FD150FC InGaAs PIN from Fermionics Opto-Technology, a transimpedance amplifier using an OP37, two first-order wideband bandpass filters [185] in the signal channel, and a low pass filter in the DC channel using AD795. The DC channel is for DG-TOF control.

The total gain of the receiver is up to several million. The bandwidth covers from 20kHz up to 400kHz, as shown in Fig. 8.16. In the DG-TOF WLI system, three identical optical receivers have been built into the system.

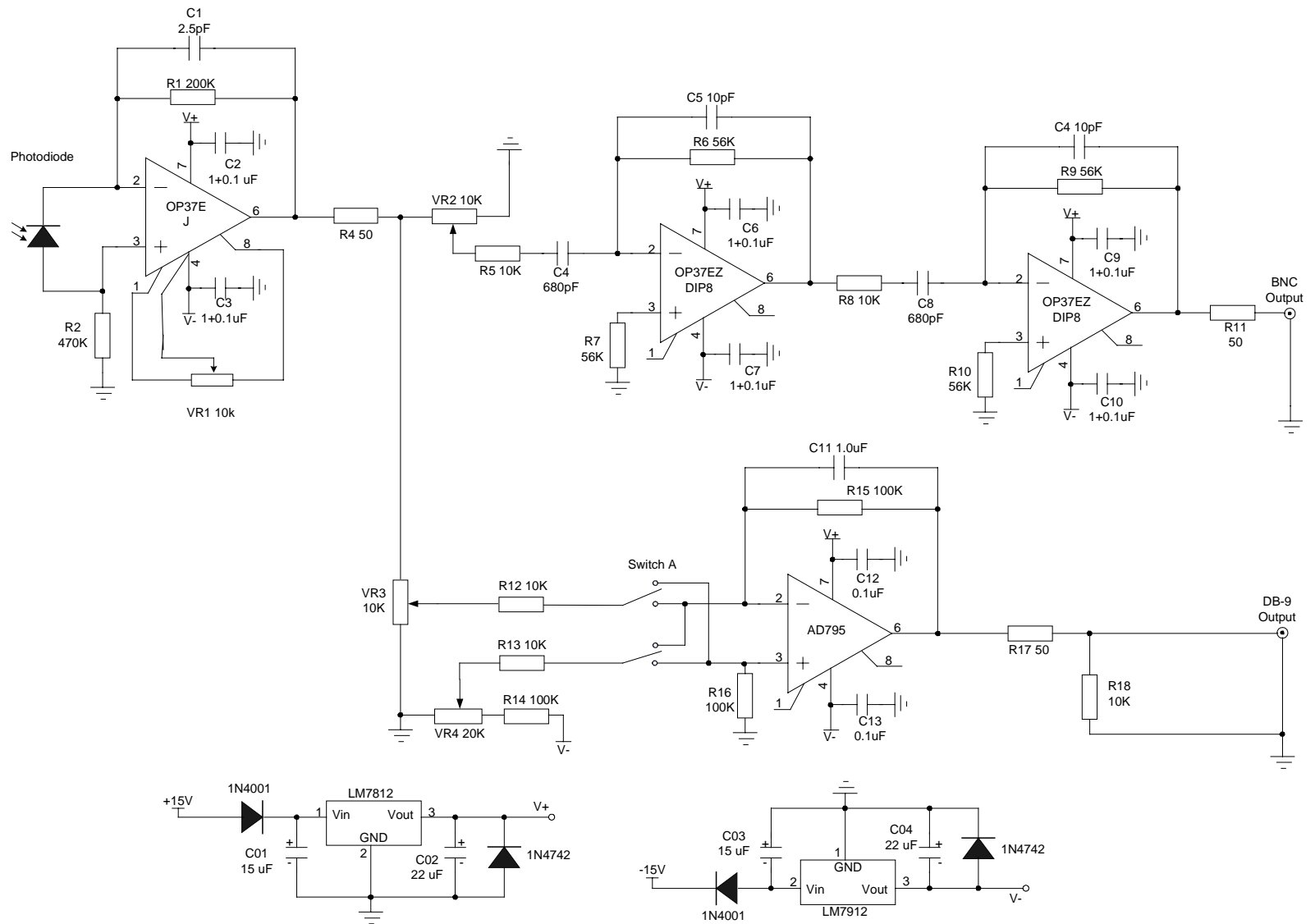


Fig. 8.15 Schematics of the optical receiver for the DG-TOF WLI system

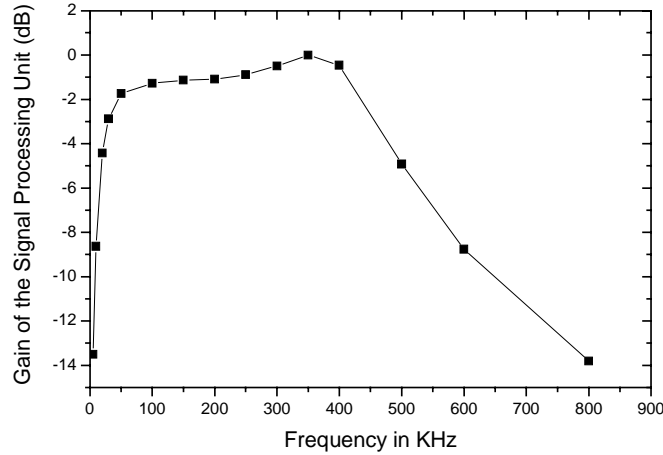


Fig. 8.16 Frequency response of the optical receiver for PD detection.

8.6 Summary

This chapter investigated the major noise sources in a high gain analog optical receiver for sensing applications. The noise sources are classified into two types, intrinsic and external noise sources.

Intrinsic noise, including shot noise, thermal noise and amplifier noise, has to be treated carefully during the circuit design and component selection, such as the photodiode and the OP amplifiers. The use of a low pass filter is an effective way to attenuate out of band noise.

External noise includes EMI, power-supply, SLED driver, and reflection. Power-supply filtering and isolation are essential in external noise reduction. Good shielding, grounding and cabling, as well as optimized trace layout also significantly reduce the external noise.

Two types of low-noise optical receivers have been developed for the EFP-TF WLI system and the DG-TOF WLI system, respectively. The use of these systems for laboratory experiments and field tests will be described in Chapter 9 and Chapter 10.

Chapter 9 DFPI Sensors for PD Detection Using DG-TOF WLI

This chapter describes the instrumentation of a DFPI-PD sensing system using the DG-TOF based WLI, the laboratory experiments, and the field demonstration of the developed system for on-line PD and thermal fault detection in high voltage power transformers.

9.1 Introduction

Power transformers are the most critical and expensive component in the power industry. When transformers fail, it is usually because of the electrical breakdown of the insulation system even when the primary cause is mechanical, chemical, or thermal. The cost of each failure can easily drive the total cost of a single transformer failure to more than \$10 million.

The most effective technique for signaling imminent failure in electrical apparatus is detecting and measuring PD [186]. During factory testing, PD measurements determine the dielectric integrity of the insulation system. Inception or increase in PD activity usually indicates insulation defects and is a precursor to incipient dielectric failure. Meeting factory PD test requirements usually means the transformer is ready for normal service and can be expected to last its design life. However, after installation and during their years of service, transformers are subjected to many extreme conditions that can create problems in the insulation system and eventually lead to failure. Most incipient dielectric failures generate PD prior to complete failure. It is, therefore, vital that the PD activities be monitored and studied in the field to detect incipient insulation problems, to prevent catastrophic failures, and to prevent extensive costs. Considerable research has been expended in developing field techniques for PD detection and measurement. To date, few commercially available systems are in existence, and research into new techniques continues.

The use of electrical, chemical, and acoustic measurements to detect PDs inside power transformers has been extensively studied. The electrical method may provide accurate recordings of PDs in laboratory conditions but is difficult to apply in the field for in-service transformers because of the high level of EMI and the impossibility of achieving accurate calibrations. Current chemical methods detect PDs in a transformer by taking gas or oil samples from the transformer. More-recent research includes the development of gas sensors and their

application for on-line gas monitoring [187]-[189]. One major problem associated with chemical methods is that there is a long delay between the initiation of a PD source and the accumulation of enough gas to be detectable. For electrical and chemical methods a further limitation is that it is generally not possible to determine the exact location of a detected PD source, information that is also important in PD study. In general, a PD results in a localized, nearly instantaneous release of energy. It produces ultrasonic waves that propagate through the insulation oil of a transformer. An acoustic sensor can detect ultrasonic waves and generate useful information relevant to the PD sources [175]-[177]. One obvious advantage of the acoustic methods is that by using them one can locate the position of a PD by studying the phase delay or the amplitude attenuation of the acoustic waves. Furthermore, acoustic methods have the potential advantage of better noise immunity in on-line PD detection applications.

One can achieve acoustic PD detection by mounting piezoelectric acoustic sensors externally on the walls of a power transformer, and often suitable acoustic couplant is used to enhance the acoustic wave's coupling to the sensors. An externally mounted piezoelectric acoustic sensor offers the advantages of easy installation and replacement. However, a piezoelectric sensor may suffer from degeneration of the SNR caused by environmental noises such as EMI and corona effects. Another possible disadvantage associated with an externally mounted piezoelectric sensor is that the multiple paths of acoustic wave transmission make locating the exact positions of PDs difficult [178] [179]. It is thus desirable to have sensors that can function reliably inside a transformer, even deep within the transformer windings, to pick up clean PD-induced acoustic signals. For the sake of safety and easy installation these sensors have to be chemically inert, electrically nonconductive, passive, and small in size.

Optical fiber based sensors have been shown to be attractive to measure a wide range of physical and chemical parameters because the sensors have a number of inherent advantages, including small size, light weight, high sensitivity, high frequency response, electrical nonconductivity, and immunity to EMI noise [190]. These advantages make optical fiber sensors excellent candidates for PD detection. Fiber optic acoustic sensors have been shown useful in many applications, such as underwater hydrophones [191] [192], material property analysis and civil structure nondestructive diagnosis [193] [194], vehicle detection and traffic monitoring [17], and partial-discharge detection [195] [196]. Early fiber optic sensors for acoustic signal

detection were based mostly on fiber optic intrinsic interferometers such as all-fiber Michelson interferometers and Mach–Zehnder interferometers.

These intrinsic fiber sensors usually use single-mode fiber and coherent sources, such as lasers. The light from a source is split into two fibers with equal intensity by a 3-dB fiber coupler. One fiber, referred to as the sensing arm, is exposed to the acoustic signal, and the other, referred to as the reference arm, is shielded from the impact of the acoustic wave. Either the reflections (Michelson) or the transmissions (Mach–Zehnder) of the light beams propagating in the two arms are recombined to generate interference signals that are modulated by the acoustic waves. The intrinsic fiber interferometric sensors have shown high sensitivity when a long fiber is used in the sensing arm. However, they suffer from the fringe fading problems resulting from random polarization rotation. They are also unstable because of drift in the source wavelength and temperature-induced path-length changes.

More recently, fiber optic extrinsic Fabry–Perot interferometric (EFPI) sensors have been under development for acoustic-signal detection [197]-[200]. EFPI sensors are fabricated with a small sensing element known as a Fabry–Perot cavity formed by two parallel reflecting surfaces. Compared to Michelson and Mach–Zehnder fiber sensors, EFPI sensors are compact in size and therefore achieve virtually single-point measurement. More importantly, those random polarization rotation and phase changes that are environmentally induced in the fiber connecting the optical source, the sensor head, and the detectors are common mode and therefore do not affect the signal phases.

In the past 5 years, supported by the Electrical Power Research Institute (EPRI) and NSF, the Center for Photonics Technology at Virginia Tech has demonstrated a DFPI-PD prototype sensor system for on-line detection and location of PDs in high voltage power transformers. The technique is particularly suited for field measurement since the sensors are mounted inside the transformer tank, thus eliminating much of the external acoustic noise. The principle of the DFPI-PD sensors, the sensor head fabrication techniques, and the sensor packaging are described in Section 7.2 of Chapter 7. This chapter will describe in detail the instrumentation of a DFPI-PD sensing system using the DG-TOF WLI, the laboratory experiments, and the field demonstrations of the developed system for on-line PD detection.

9.2 Instrumentation

A TOF-WLI system based on the DG-TOF presented in Chapter 5 was built to interrogate the DFPI-PD sensors described in Section 7.2. The system operated in the 1300nm wavelength band, and could simultaneously interrogate three DFPI-PD sensors. This section describes the system design and the instrument.

9.2.1 System design

A schematic illustration of a single-channel TOF-WLI system based on a DG-TOF is shown in Fig. 9.1. The system consists of a broadband light source, a wideband 3-dB coupler, a DFPI-PD sensor, two collimators, a diffraction grating mounted on the top of a motorized rotary stage, a short piece of 200/230 μm MMF, a photodiode, a preamplifier, a computer with a data acquisition card, and a motorized rotary stage and its driver.

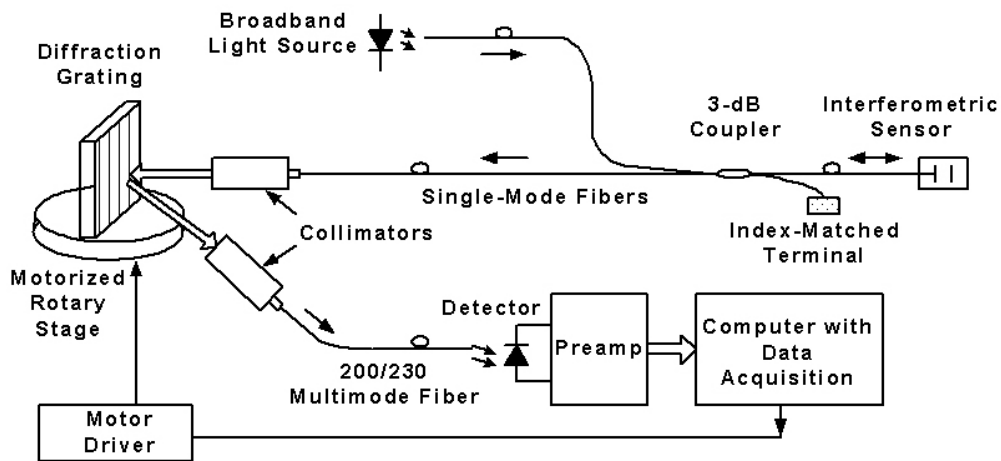


Fig. 9.1 Principle diagram of a FFPI sensor system based on DG-TOF.

The light from the broadband source is launched into a single-mode fiber, propagates through a 3-dB coupler, and arrives at the DFPI-PD sensor, where it is modulated by the PD-generated acoustic waves. The phase-modulated light propagates back through the same 3-dB coupler and reaches the input collimator. The collimated light beam illuminates a diffraction grating, which can be rotated by a motorized rotary stage with high resolution (~ 0.2 mrad). The $+1^{\text{st}}$ diffractions collected by a second collimator are focused into a 200/230 μm multimode fiber (MMF), and only part of the total spectrum ($\lambda_0 \pm \Delta\lambda$) can be collected by the MMF. The MMF can be

removed and the photodetector can be placed on the focal point of the receiving collimator with the penalty of less flexibility. The collimators, the diffraction grating, the motorized rotary stage and the MMF compose a DG-TOF described in Chapter 5. The bandpass characteristics of the DG-TOF are given in Figs. 5.6 and 5.8. The transimpedance preamplifier (shown in Fig. 8.15) converts the photocurrent from the photodiode into a voltage, and a subsequent divider separates the signal into a DC component and an AC component which are amplified and filtered further. A computer with a data acquisition card is used to record and to calibrate the DC and AC signals. The calibration reference, a representation of the original optical intensity distribution, is an output-position curve obtained by scanning the whole wavelength range with a cleaved fiber, instead of a sensor, connected. The calibrated AC signals directly represent the absolute value of the acoustic waves, and the frequency response is limited only by the sensor-head and the bandwidth of the electronics. On the other hand, the calibrated DC signals represent the current operation-point on the transfer function. Ideally, this DC voltage (V) should be equal to the setting-point (V_0), most likely the Q-point. However, any manufacturing tolerances and environment changes may cause undesired changes in the OPD of the sensor, thereby drift of the DC voltage V . The difference ΔV between the DC output and the setting-point is the control signal that can be used to adjust the position of the grating through the motorized rotary stage, and therefore the central wavelength of the interrogation light. By this feedback control, the optimal operation-point can be dynamically maintained, and the DC pressure signal may also be recovered from the position of the grating if environmental effects can be determined. Obviously, the tuning range is limited only by the available source spectrum and the tuning range of the DF-TOF, and the DC accuracy is limited by the resolution and repeatability of the rotary stage.

9.2.2 Instrument

Fig. 9.2 shows the schematic of the DG-TOF WLI interrogation system for PD detection. A superluminescent light emitting diode (SLED) SLED1300D20A, from Optospeed (now Exalos), with a peak wavelength around 1296 nm, an output power of 20 mW (output of the SMF pigtail), and a 3-dB bandwidth of 35 nm, was selected as the broadband light source. The output spectrum of the SLED is given in Fig. 9.3. The high output power is necessary in order to support three

channels simultaneously, which is required for PD source location. However, large driving current (up to 500 mA), good heat dissipation and temperature control are required to operate this SLED. A laser diode driver module PLD500 with 500 mA maximal output current and an Evaluation PCB, both from Wavelength Electronics, Inc., were chosen to drive the SLED. An HTC3000 temperature controller module and an evaluation PCB board from Wavelength Electronics, Inc. were used for temperature control. For best heat dissipation, the SLED was mounted into an LDM-4980 Series laser diode mount from ILX Lightwave.

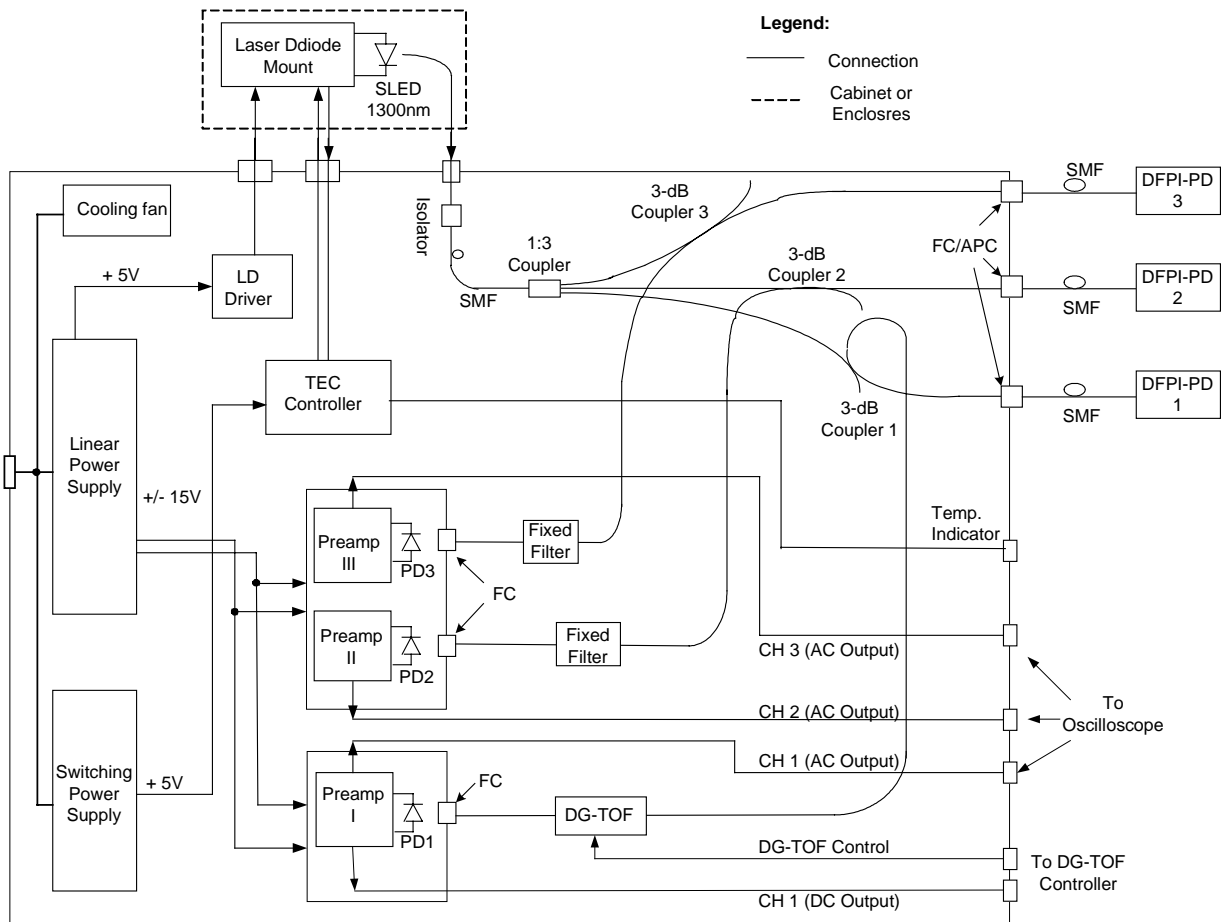


Fig. 9.2 Schematic of the DG-TOF WLI interrogation system for PD detection.

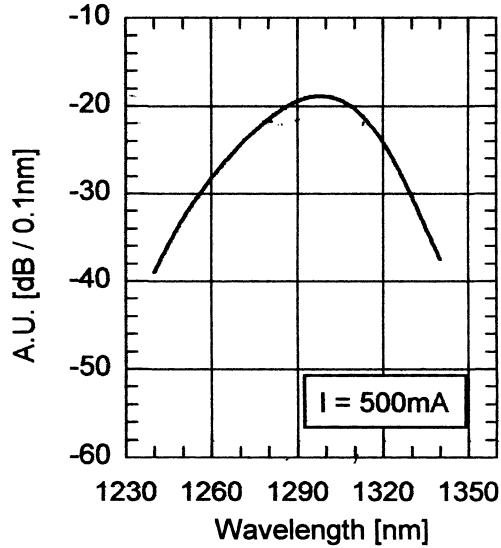


Fig. 9.3 Spontaneous emission spectrum of the SLED1300D20A.

The output of the SLED propagates through an optical isolator, and is then equally divided into three channels by a 1:3 optical splitter. In each channel, light propagates to a DFPI-PD sensor through a 3-dB optical coupler and an FC/APC connector on the front panel of the cabinet. The reflection from each DFPI-PD sensor propagates backward to the same 3-dB coupler and reaches the corresponding photodiode (PD1~3) through an optical filter. Three low-noise optical receivers described in Section 8.5 were used for signal detection, amplification and filtering. The AC outputs of the optical receivers (20 kHz~400 kHz) were monitored using a digital oscilloscope.

It is noticed that only one DG-TOF was actually used in CH1, while two fixed optical filters were used in CH2 and CH3, due to the relatively high cost of a prototype DG-TOF. Another reason was because the system was modified from a previous prototype system without a TOF and therefore had limited space available. Fixed optical filters, with central wavelengths reasonably distributed within the 35 nm 3-dB bandwidth of the SLED, were made with a similar structure to that of the EFPI filter in an EFP-TF. The major difference is that a fused silica tube was used instead of a borosilicate tube for minimal temperature sensitivity. For each DFPI-PD sensor connected to CH2 or CH3, a fixed filter was selected for the best SNR.

As mentioned in Chapter 8, a switching power supply was employed only for the TEC controller as a low reduction strategy. Fig. 9.4 is a photograph of the finished DG-TOF WLI interrogation system.



Fig. 9.4 Photograph of the DFPI-PD sensor interrogation system.

9.3 Laboratory Experiments

To verify the feasibility of linear demodulation of DFPI-PD sensors, the instrument was tested in the laboratory with an acoustic wave test setup, as shown in Fig. 9.5. A DFPI-PD sensor was installed in water at one end of a polyvinyl chloride (PVC) tube facing a piezoelectric (PZT) transducer (Physical Acoustic Corporation) at the other end of the PVC tube. The transducer has an acoustic bandwidth of 100 kHz–1 MHz. The perturbed angular correlation C-101_HV pulser (Physical Acoustic Corporation) has an output pulse rise time of 20 ns and a pulse width of 100–500 ns. We can adjust the static water pressure by varying the height of the water column from 0.1 to 2.2 m, simulating the static oil pressure of a power transformer. The distance from the PD sensor to the PZT transducer is about 18 cm. As a reference, another PZT transducer was attached to the outside of the PVC tube as an acoustic sensor. Because the signal coupling is not efficient, the PZT sensor was mounted closer to the source than the fiber sensor. This arrangement was chosen because it represents many practical PD test situations in which PZT sensors are attached to the sidewalls of a transformer tank whereas fiber sensors can be inserted into the transformer tank. A LeCroy two-channel digital oscilloscope was used to display and store the acoustic signals captured by the sensors.

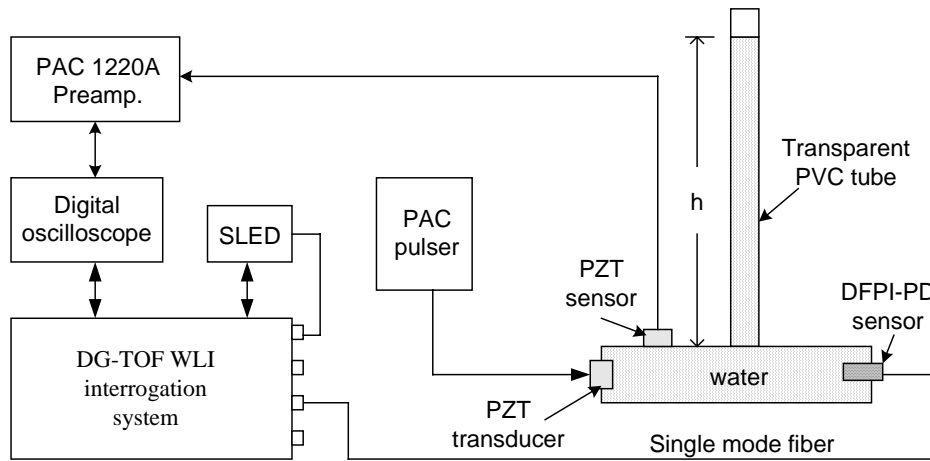


Fig. 9.5 Acoustic wave test setup for PD sensor evaluation.

The wavelength-scan outputs (CH1 DC Output) of a DFPI-PD sensor in the acoustic wave setup and the theoretical results in atmospheric pressure are shown in Fig. 9.6. The peak amplitudes were un-equal because of the non-flat spectral distribution of the SLED source. The peak position difference between the experimental results and the theoretical calculation were caused by a cavity-length measurement error, whereas the amplitude differences are believed to be caused by the offset of the spectrum distribution from the ideal Gaussian distribution used for the calculation and by misalignments of the DG-TOF and the sensor's F-P cavity.

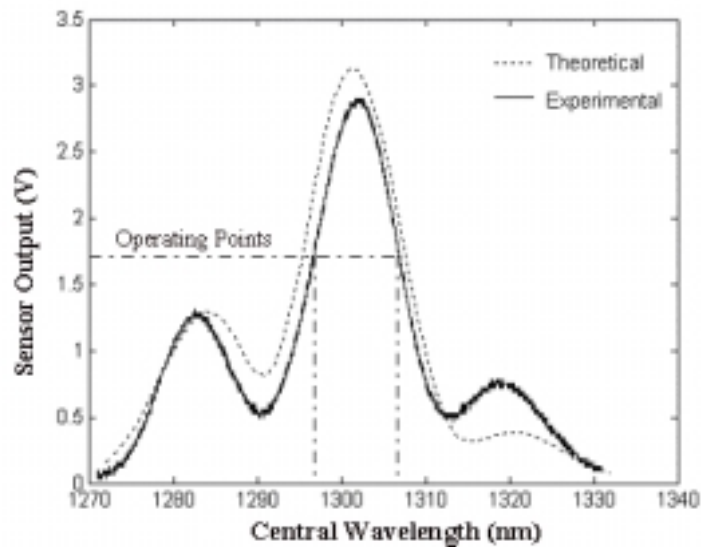


Fig. 9.6 Scan output of a DFPI-PD sensor in atmospheric pressure.

Fig 9.7 gives the scan-outputs (CH1 DC Output) of the DFPI-PD sensor in atmospheric environment and under 50 cm of water normalized to the source spectrum. A Q-point drift of ~ 3 nm resulted from the 50-cm static water pressure. Obviously there is more than one Q-point on the fringes, but only those two Q-points on the highest fringe have the best SNR and thereby are suitable as optimal operation-points.

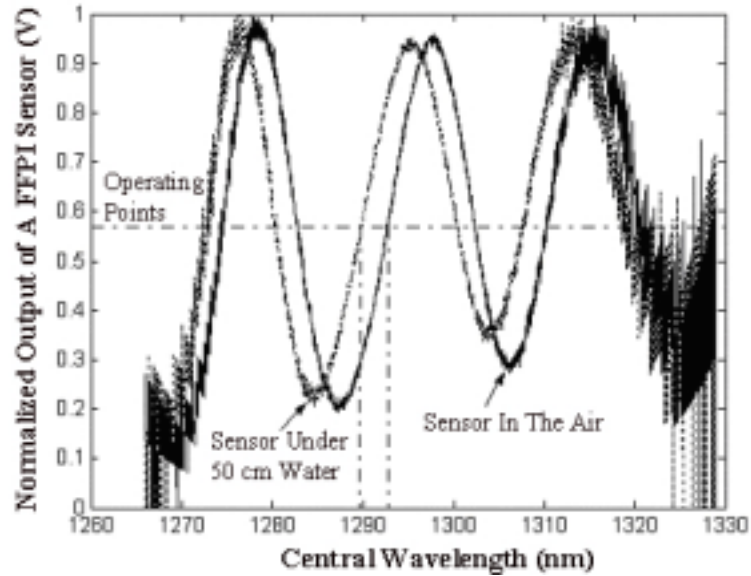


Fig. 9.7 Normalized outputs of the sensor in atmospheric pressure and under 50cm water.

Fig. 9.8 shows the scan-output (CH1 DC Output) of the same DFPI-PD sensor in the acoustic wave test setup under 20 cm water, with the sensor's outputs at the marked points A, B C, D and E given in Fig. 9.9. Also shown in Fig. 9.9 is the output of the same sensor under the same experimental condition, but without a DG-TOF.

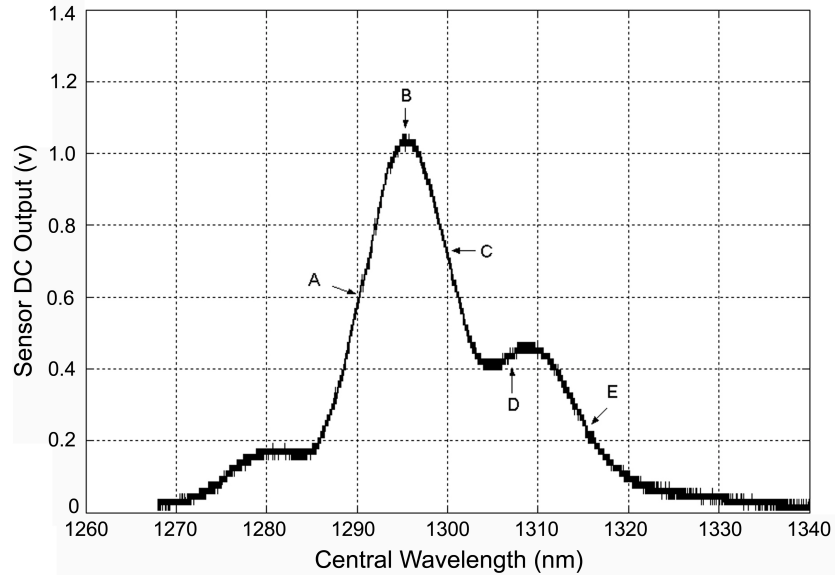


Fig. 9.8 Scanning the DG-TOF for Q-points of the DFPI-PD sensor.

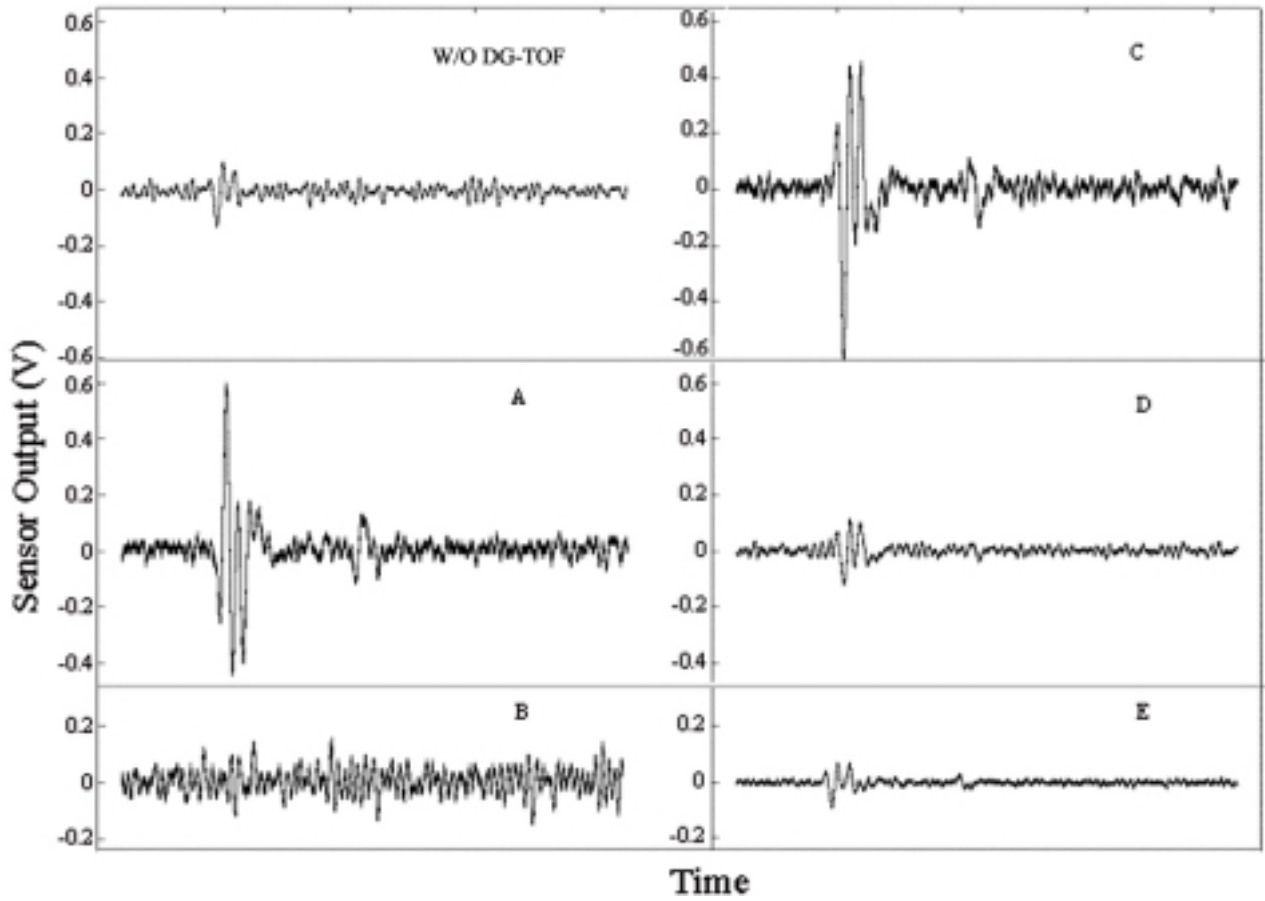


Fig.9.9 Acoustic wave outputs without and with a DG-TOF at different operation-points.

Obviously, the system had a very low SNR without a DG-TOF due to the unknown Q-point and low fringe contrast. The best SNR occurred at points A and C, which were the Q-points of the interference fringes. A SNR improvement of about 15 dB was easily obtained, comparing with that of the system without a DG-TOF. We also observed that the output polarities at points A and C were reversed. The reverse polarities were resulted from the different slope signs on the different sides of the main fringe. Apparently, the sensor had zero sensitivity at the fringe peak – point B, though the source power density was the highest (thereby the noise level was the highest). Point D and E were also Q-points, but the signal amplitudes were low due to the much smaller source power density.

Once the operation-point is determined, a signal-processing system based on a computer makes the tracking of the Q-point, the data recording and calibration easy and fast.

9.4 Field Demonstrations Without DG-TOF WLI

In the absence of any TOF, a field test had been done in a NGC SGT3A 400KV/275KV transformer at the Northfleet West Substation, London, UK, between May 13 ~ 19, 2002, to estimate the performance and deployability of the developed PD sensors. This section describes the sensor selection in the laboratory, the installation and the equipment setup, and the test results.

9.4.1 Sensor selection

From all the DFPI-PD sensors we have made, nine were selected for this field test. Due to the lack of tunable filters and Q-point control capability, we did have had many difficulties in precise control of the initial DFPI cavity length and the sensor fabrication yield was very low. A simulated test had been done in the laboratory to better understand the performances and to roughly locate the Q-points of each sensor in the transformer oil. These sensors were tested one by one under water from 0.1m to 2.2 meters using the test setup shown in Fig. 9.5. The Q-point location was so important in the PD detection as an offset from the Q-point not only results a sensitivity reduction, but also distortion. A DFPI sensor recorded the acoustic wave with good fidelity at a water depth of 1.0 m (Fig. 9.10(a)), but distorted signals at 2.0 m (Fig. 9.10(b)).

The sensors' peak-to-peak amplitudes of the acoustic outputs versus the water depth are given in Fig. 9.11. Because transformer oil is lighter than water, the static pressure on the DFPI-PD sensors from 2 meters of oil is approximately corresponding to that of 1.5 meters of water. The sensors with a good sensitivity under 1.5 m water were selected for the top drain valve, which was 2 m from the oil surface. The bottom drain valve was about 6 meters from the oil surface, which was difficult to simulate at this even higher liquid pressure in the laboratory test setup.

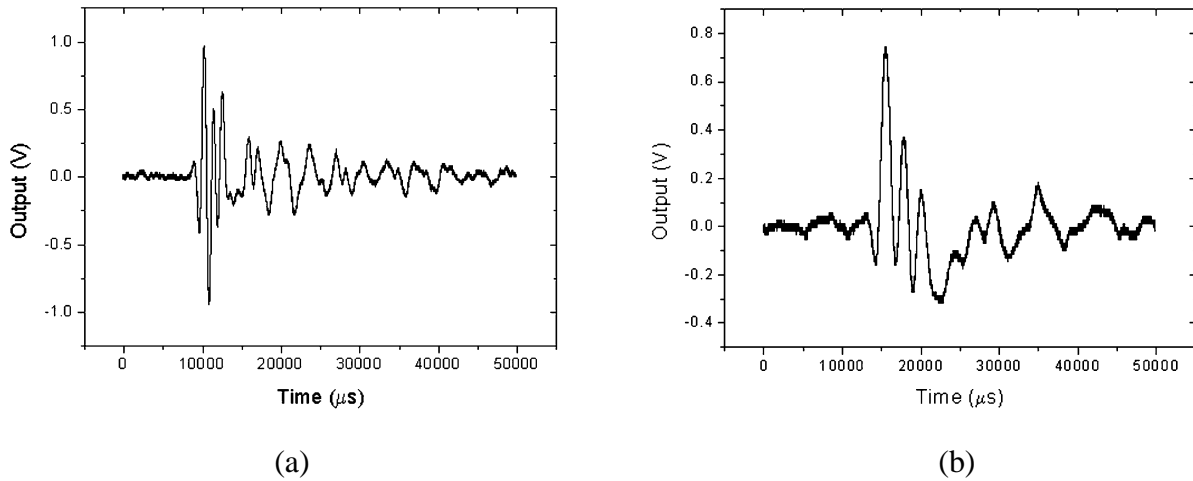


Fig. 9.10 Laboratory simulation of acoustic wave detection. (a) $h=1.0\text{m}$. (b) $h=2.0\text{m}$.

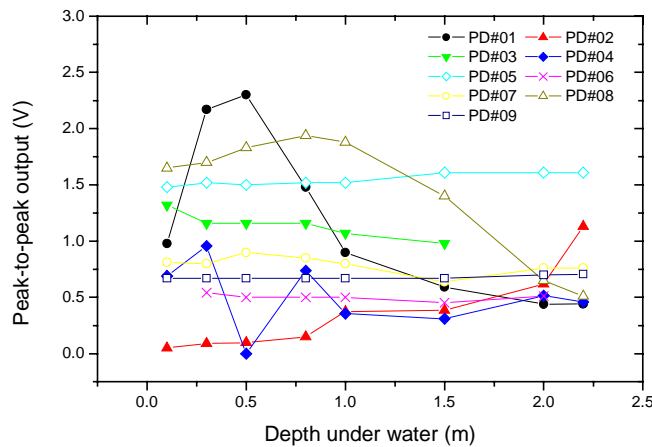


Fig. 9.11 Static-pressure sensitivity test results in the laboratory.

Fig. 9.12 shows the typical acoustic signals captured by a DFPI-PD sensor and those by the PZT sensor attached to the PVC tube. Also shown in the figure is the FFT of the signals from the DFPI sensor. The acoustic spectrum spreads out from very low frequency up to about 400 kHz

with a peak around 180 kHz. The peak frequency matches well with the peak emission of the PZT acoustic transducer, while the high frequency components, much lower than the emitted power density, which are defined by the 400 kHz cutoff frequency of the optical receiver. The nine DFPI sensors were packaged into two groups with sensor PD#1, PD#5, PD#8 and PD#9 into Group 1, and all other five into Group 2.

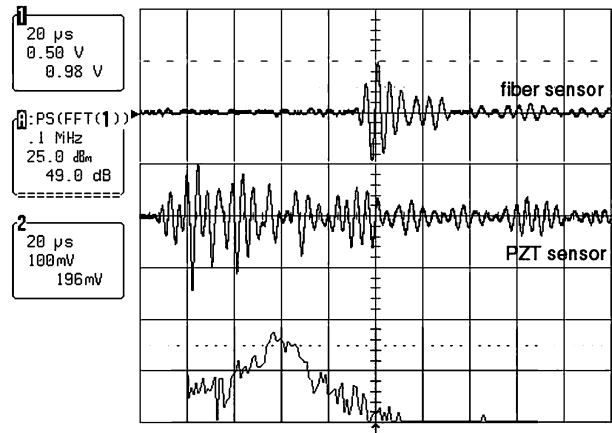


Fig. 9.12 Typical acoustic signals recorded by a DFPI-PD sensor and a PZT sensor in the Lab.

9.4.2 Sensor installation

During the same week of test, six companies and universities had tested various types of PD sensors. Our DFPI-PD sensors were the only one allowed to be installed inside the transformer tank. Fig. 9.13 is a photo of the transformer under test. This transformer had the history of PD activities and was taken out of service during sensor installation.



Fig. 9.13 The NGC SGT3A 400KV/275KV transformer.

Three drain valves of the SGT3A 400KV transformer were assigned for the DFPI-PD detection sensors, including a 2” valve at the top, a 2” valve at the bottom and a 3” valve at back side of the bottom. Fig. 9.14 shows the layout of the drain valves, DFPI-PD sensors and PZT reference sensors on the transformer. DFPI sensor Group #1 was installed into the top 2” drain valve which was about 2 meters below the surface of the oil and the sensors were assigned a name FT1~4. In the meantime, Group #2 was mounted into the bottom 3” drain valve and the sensors were assigned a name of FB1~5.

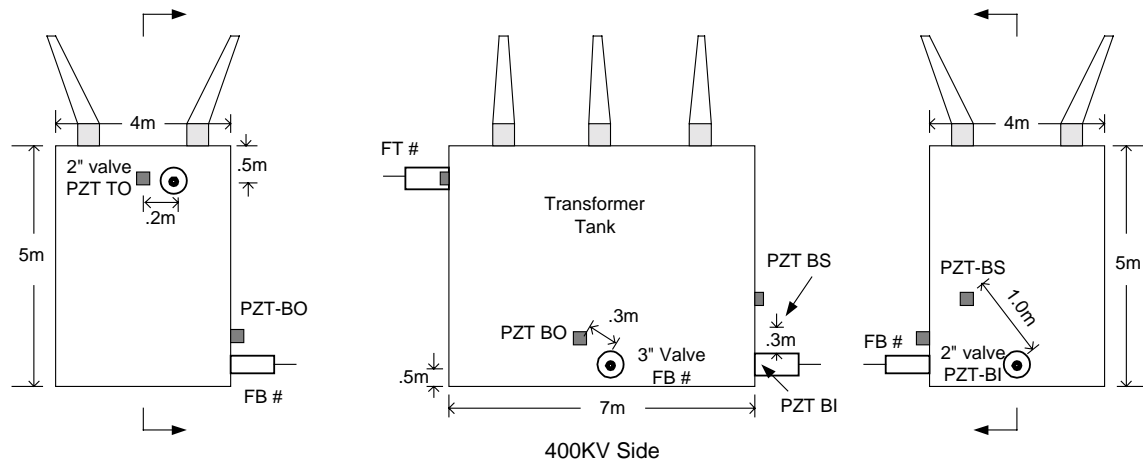


Fig. 9.14 Layout of the drain valves and sensor positions (Approximate dimensions, not to scale). (FT1~4 - DFPI-PD sensors in the top valve, FB1~5 - DFPI-PD sensors in the bottom drain valve, PZT TO -PZT sensor attached on the tank close to the top 2” drain valve, PZT BO – PZT sensor attached on the tank close to the bottom 3” drain valve, PZT BI – PZT sensor in the bottom 2” drain valve.)

Fig. 9.15 is an illustration of DFPI-PD sensors installed inside the transformer tank through a drain valve. However, considering the high oil pressure in the bottom drain valves and the potential leaks, PD sensors FB1~5 were not allowed to go beyond the drain valve shut. In urgent situations, the drain valve can be easily closed without removing the sensors. Eventually, only two of the Group #2 sensors were spliced to a transmission fiber cable because of limited time for installation. In this test, the sensor holders are different from the one in Fig. 7.13. Fig. 9.16 is a photo of five DFPI-PD sensors mounted on the holder, facing different directions.

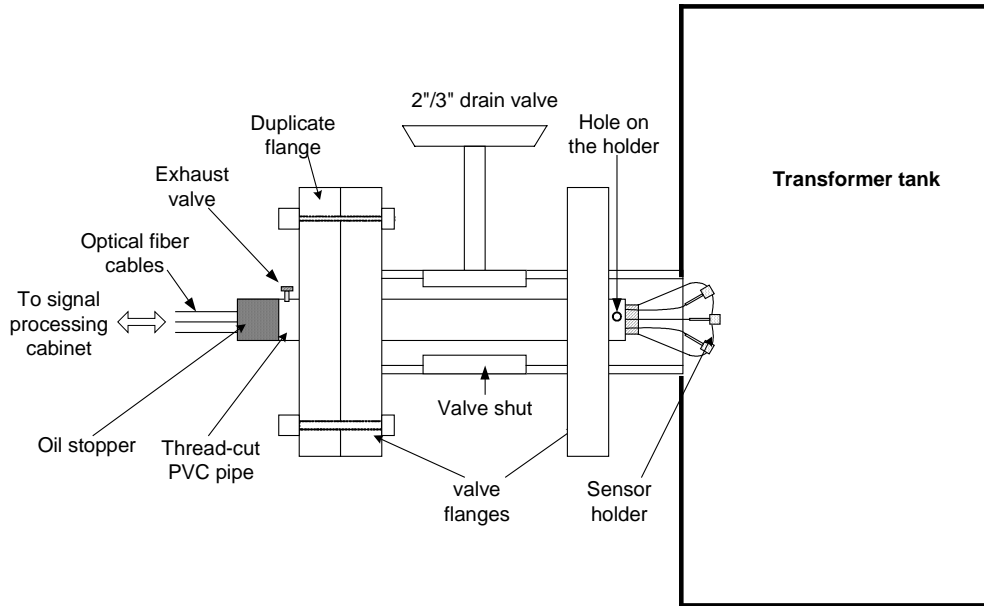


Fig. 9.15 Illustration of PD sensors installed inside the transformer tank through a drain valve.



Fig. 9.16 Packaged DFPI-PD sensors in a sensor holder.

Fig. 9.17 is a photo of the transformer showing the Group #1 sensors installed inside the top 2” drain valve and the optical fiber cables connecting the sensors to the control cabin. As a reference, a PZT sensor was tapped on to the tank beside the top drain valve and silicon couplant was applied in between the sensor and the tank to enhance acoustic coupling.

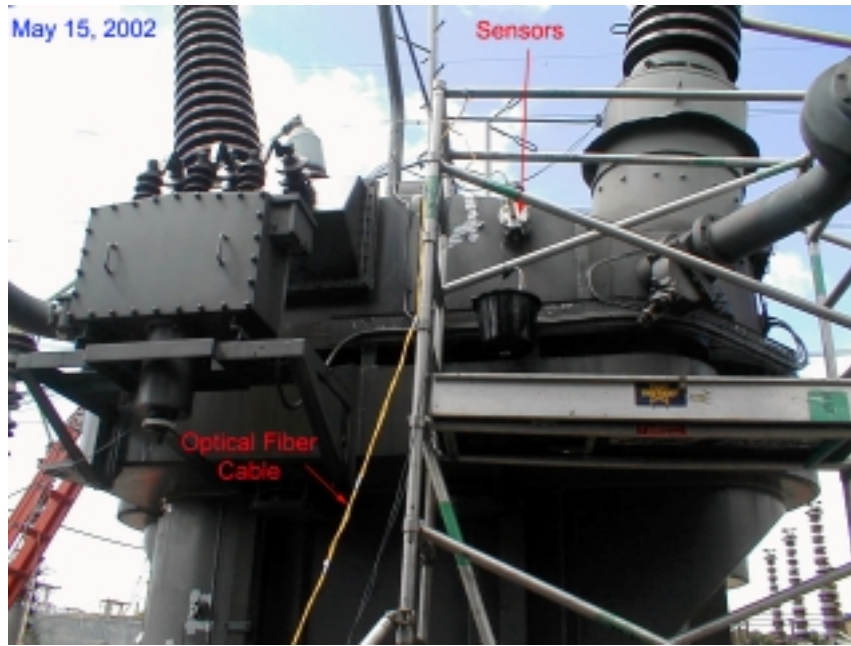


Fig. 9.17 Picture of the Group 1 sensors inside the tank.

After the sensor packages were successfully installed, fibers were laid following the assigned routes to the control cabin about 25 m from the drain valves. Then, APC connectors with pigtail fibers were spliced (in the control cabin) to the fibers from the deployed sensors. At this moment, only six sensors were successfully deployed and connected to the WLI interrogation system. After a quick check of all the six sensors, we found that five of them were still alive while one malfunctioned. The damage to one of the FT sensors might happen during the installation of the sensors into the threaded pipe. Therefore, the sensors were numbered as FT1, FT2, FT3, FB1 and FB2, respectively.

The WLI system shown in Fig. 9.2, but without any DG-TOF or fixed filters, was then employed to measure the optical signals back from all the DFPI-PD sensors. Fig. 9.18 shows the test equipment setup in the control cabin. As mentioned before, the interrogation system could simultaneously support three DFPI sensors. A 4-channel digital oscilloscope with a 512 MB hard disk was exploited for PD signal monitoring. The 4th channel of the oscilloscope was assigned to a PZT reference sensor. Backup data were stored in the laptop computer.



Fig. 9.18 Test equipment setup in the control cabin.

In addition to major test equipment setup, a redundant system was also set up in the control cabin (not shown in the picture), which consists of a Velocity Tunable Laser (1509 -1583 nm) from New Focus, Inc, a Stanford SR570 current amplifier, and a 80 μm InGaAs PIN from Fermonics. The redundant system could support only one channel. However, since a tunable laser was used, the operation point of the fiber sensors can be moved back and forth to find an optimal point by scanning the optical wavelength. Although most sensors used have a wide operation range, this function was still useful because the sensors were installed several feet below the tank oil surface and a static pressure might have shifted the operation-points from their Q-point positions.

9.4.3 Test results

The test lasted four days from May 15 to May 18, 2002. Measurements were carried out under the following conditions:

- Transformer was power off;
- Transformer was Power on;
- Drain valves were close;
- Drain valves were open;

- Fiber sensors only (to isolate possible interference from PZT sensors);
- Fiber sensors with PZT sensors;
- The combinations of some of the above conditions;

Due to the very weak PD activities during the one-week test, we did have had some trouble to distinguish the PD like waveforms from background noise and a trigger level was set to capture the PD spikes. Fig. 9.19 shows a sample of measured signals from DFPI-PD sensor FB-1 and FT-3. Typically, signals from bottom valve have the dominant spike at the triggered time (=0 sec), whereas signals from the top valve indicate only noise present. Obviously, the SNR was very low, which was believed being caused by the low PD energy, relatively high background noise and the lack of Q-point control.

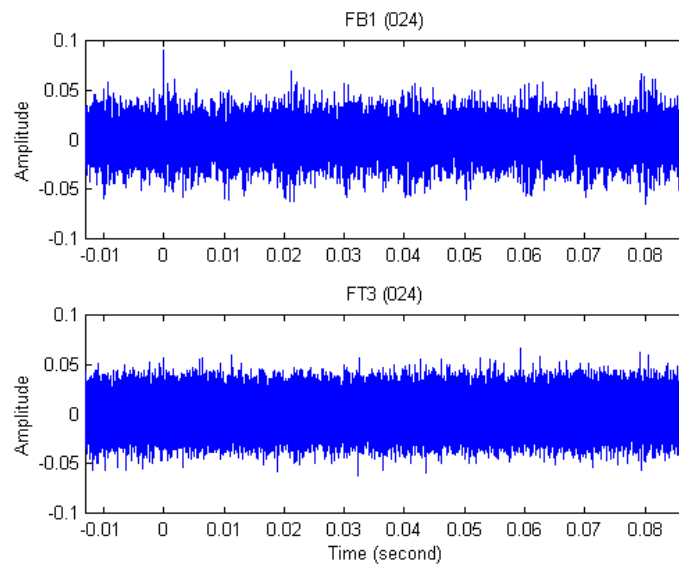


Fig. 9.19 A sample of measured signal from DFPI-PD sensor FB-1 and FT-3.

The reason we believed that the PD energy was low was because only two out of the six groups, including us, observed very weak PD activities during the one week test. Since the sensor heads and the transmission cables between the sensors and the control cabin are non-conductive and didn't pick up any EMI noises, the low SNR can be attributed to three sources: optical noise, electronics noise, and vibrations. Electronics noise was caused by the wide bandwidth (20~300 kHz) and very high transimpedance ($\sim 4.0 \times 10^6 \Omega$) of the preamplifiers. Optical noise might be from the noisy high power SLED and low fringe visibility. A low fringe visibility represents a large DC optical power, thereby small AC optical power. When modulated

optical signals arrived at the optical receiver, only the AC part contained real acoustic signals, while the DC part contributed only to total noise. A very large transimpedance had to be used to amplify the small AC signal. Strong vibration was always present during the test. This vibration generated pressure on the diaphragm of a DFPI-PD sensor and detected by the WLI system. However, the low fringe visibility was the dominating factor in the total background noise.

The PD signals were analyzed through the discrete wavelet transform (DWT) decomposition, thresholding of wavelet coefficients, and signal recovery by the inverse discrete wavelet transform [201]. By applying DWT, detected signals were decomposed into various frequency sub-bands. Several approaches were compared to determine the optimal mother wavelet using correlation, energy, and inspection. The threshold limit was determined based on the maximum Gaussian noise removal for each decomposition level. The results indicated that this method could extract the PD spike from the noisy measurement effectively. As an example, Fig. 9.20 shows the original signals and the de-noised signals from sensor FB1. The frequency of the PD pulse was also analyzed. It is shown that the frequencies lie in the range of 70 kHz to 250 kHz. In addition, with the assumed acoustic wave propagation delay between the PD source and the sensors, it was found that all PD activities occurred in the first and third quadrants in reference to the applied sinusoidal transformer voltage. For details about the de-noising and PD signal analysis, please refer to Reference [201].

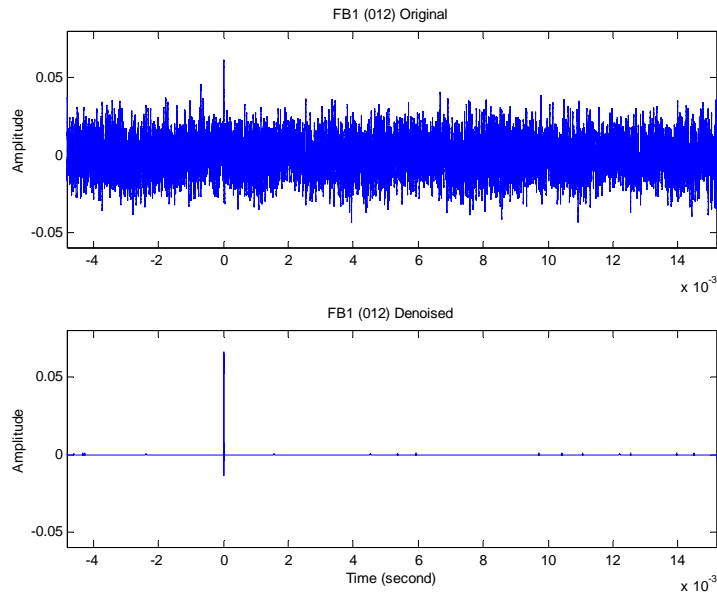


Fig. 9.20 Original signals and denoised signals of FB1.

9.5 Field Tests with DG-TOF WLI

Upon successful completion of the DG-TOF WLI interrogation system and the laboratory demonstration, a second test for electrical fault and thermal fault detection was performed with a simulated power transformer environment in the Transformer Lab at the Rensselaer Polytechnic Institute in July 2003. This section focuses on the test setup, sensor installation and equipment setup, electrical fault detection and thermal fault detection.

9.5.1 Corona and thermal fault generation system

The test setup was a simulated power transformer environment with a corona and thermal fault generation system. Fig. 9.21 is a schematic of the corona and thermal fault generation system. It consists of an iron tube connected to an oil tank (12 gallons of insulating oil), a corona generator mounted in the middle of the iron tube (but isolated from the iron tube by isolation materials), a resistive heater and a thermocouple in the center of the oil tank, an oil pump system, and a gas and vacuum system. A DC and an AC high voltage source were also used to support the system.

The corona device was used to generate controllable corona or PDs inside the oil system. It was simply made of razor blade electrodes, as shown in Fig. 9.22. The ground flanges were directly mounted on the insulating part of the tube. DC or AC high voltages were applied between the blades and the ground flanges. Before the experiments, mineral oil used in the test (Shell Diala AX) was degassed and de-moisturized to ensure the PDs occur normally. The heating wire was employed to quickly heat the oil in the tank to generate thermal faults or bubbles. The bubbling process generates weak acoustic waves which propagate in the transformer oil. The thermocouple was used as a temperature sensor, while the oil pump system was used to cool or change the oil in the tank. The mechanisms for the generation of corona and electrical discharges as well as thermal faults in insulating liquids can be found in Reference [202].

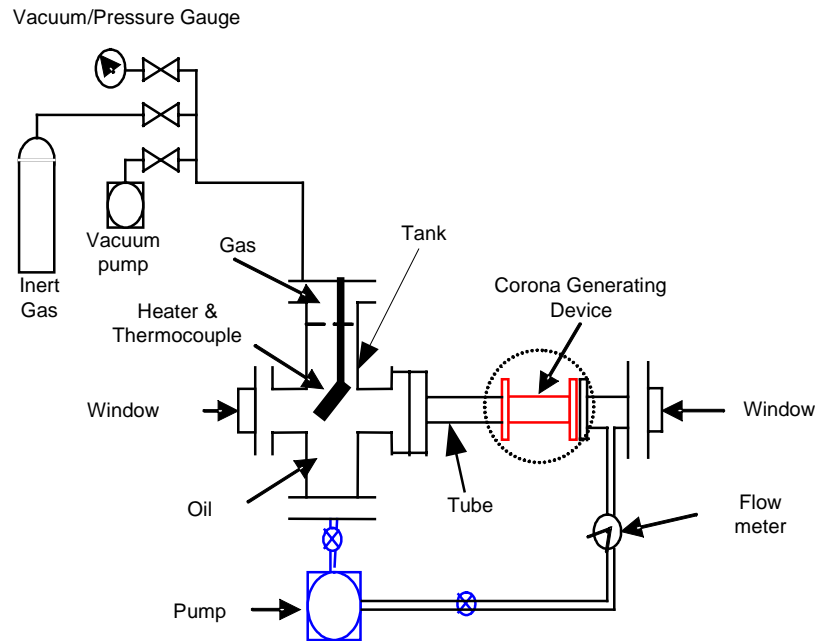


Fig. 9.21 Schematic of the corona and thermal fault generation system. (Provided by A. Shamsiah)

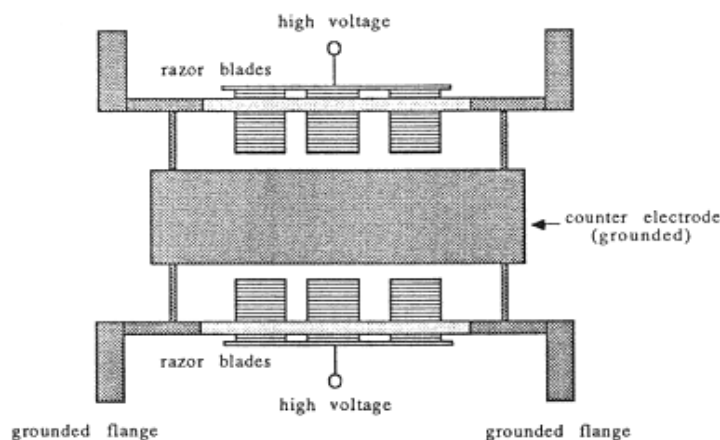


Fig. 9.22 Schematic of the corona generator.

9.5.2 Sensor installation and equipment setup

There were two windows on the test setup for sensor installation. One is at the end of the tube and the other on the tank side. Five DFPI-PD sensors were mounted into the tube through the window on the tube side for electrical fault detection. The sensor holder used on this side was the one shown in Fig. 7.13. Fig. 9.23(a) shows the five sensors installed. The sensor heads were about 15~20 cm from the corona generator. Three DFPI-PD sensors were mounted into the oil tank through the window on the tank side for thermal fault detection, as shown in Fig. 9.23(b). The sensor holder used for the three sensors was the one used for the London test (Fig. 9.16). In general, the sensors for electrical faults had higher sensitivity than the sensors for thermal faults. However, the three sensors were replaced later by the more sensitive sensors used for PD detection. It is noticed that there was a 45° between the normal of the diaphragms of the PD sensors and the heating wire in the tank. For easy comparison, two PZT acoustic sensors from Physical Acoustic Corporation (PAC) were used. One was attached to the outer surface of the test tube near the corona generator for electrical fault test, and the other was tapped on the tank for thermal fault test. For safety reasons, the corona generator was shielded by a high-voltage cage, as appearing in both photos of Fig. 9.23.



(a)



(b)

Fig. 9.23 Test setup and PD sensor installation. (a) DFPI-PD sensors for electrical faults (corona, PD and breakdown); (b) DFPI-PD sensors for thermal faults.

The DG-TOF WLI interrogation system was set up about 2 m away from the high-voltage cage, sharing the same power-supply with the high-voltage systems, which was proved later being a bad idea. Fig. 9.24 shows the WLI interrogation system in the field. It consisted of the 1300 nm SLED in a laser diode mount, a backup 1300 nm LED (250 μ W output power and 55 nm 3-dB bandwidth) source, a main box (including all the SLED drivers, three low-noise optical receivers, an isolator, optical couplers, and power-supplies.), a DG-TOF with its controller, two fixed optical bandpass filters, and a 4-channel digital oscilloscope. In the test, three DFPI sensors were monitored simultaneously, but only the sensor in CH1 was connected to the DG-TOF, while the other two were connected to the fixed bandpass filters which were carefully selected for the best SNRs. All three channels were operated in a linear demodulation mode.

The two reference PZT sensors were connected, using coaxial cables, to a computer based data processing system, as shown in Fig. 9.24. Also shown in Fig. 9.25 are the DC and AC high-voltage sources used in the test.



Fig. 9.24 Signal conditioner and data recording system.



Fig. 9.25 Signal conditioner for the PZT sensors and the DC and AC high-voltage sources.

9.5.3 Test results

During the test, three groups of experiments had been performed. In the first group, PDs were

generated by applying DC voltages to the electrodes of the corona generator. In the second one, AC voltages were applied to the electrodes. The reason that both DC and AC high voltage experiments had been conducted was because PDs from DC and AC voltages were believed to have different characteristics. In the last group of experiments, we investigated thermal fault detection using the DFPI-PD sensors. Each group of experiments is described in detail in this subsection.

1) PD detection under DC condition

To perform the PD detection test under DC condition, A DC voltage was applied to the corona generator. The DC voltage was slowly increased until a PD occurred. During the test, a 4-channel oscilloscope was used to monitor and record the outputs of the three DFPI sensors and the PZT sensor. Channels 1-3 of the oscilloscope were connected to the DFPI sensors, while channel 4 was used for the PZT sensor.

During the DC test, the DC voltage was increased slowly up to 20kV, and sounds of partial discharges occurred randomly inside the corona generator. When the first PD happened, the oscilloscope was triggered and the acoustic emission (AE) signals were captured, as shown in Fig. 9.26. All DFPI sensors recorded very consistent signals, which were formed by two major peaks followed by some small peaks. The first peak was the real PD signals, but the others are believed to be the reflections from the generator tank. However, the signal picked up by the PZT sensor is slightly different from those by the DFPI sensors. The decrease of the main peak takes longer for the PZT sensor and the amplitudes of the minor peaks are also smaller than those for the DFPI sensors. The reason was due to the effect of the dimension of the tube. In general, all these acoustic waves are similar in shape, which should lead to similar monitoring result.

Before a PD event, there were some sizzling sounds heard in air which were generated by the blades exposed to outside. It is well known that corona initiation voltage in air is always lower than that in oil. Therefore, experts attending the test were wondering if the PZT sensor actually picked up these sizzling sounds. To answer this doubt, the PZT sensor was turned over and the sensing side of the sensor faced up in air. No signal was picked up during the raising of voltage. However, this method still could not answer the doubt. If the PZT sensor is detached from the iron tube, it will miss the signal transmitted from the tube, which may be the path for these

coronas generated nearby the blades and transmitted to the iron tube. When the PZT sensor was turned over, the PD signal might be missed.

The DC test was run for the second time by using the same method as in the first one. The only change was to use a new PZT sensor with an integrated preamplifier. The signals are shown in Fig. 9.27. Obviously, the strong signals indicated that a total breakdown happened, instead of a PD. The high frequency oscillation was present in the PZT sensor output due to the breakdown. However, high-frequency components were filtered out by the built-in bandpass filters in the optical receivers of the DG-TOF WLI system.

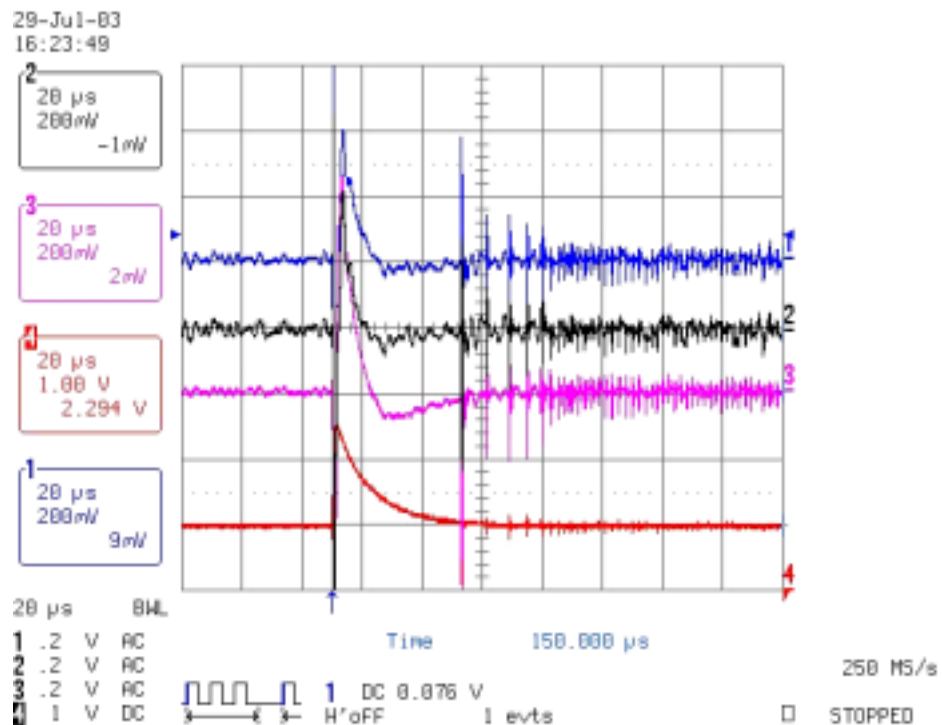


Fig. 9.26 Oscillogram of the 1st DC test. (CH 1~3 for the DFPI sensor and CH 4 for the PZT sensor w/o an integrated preamp)

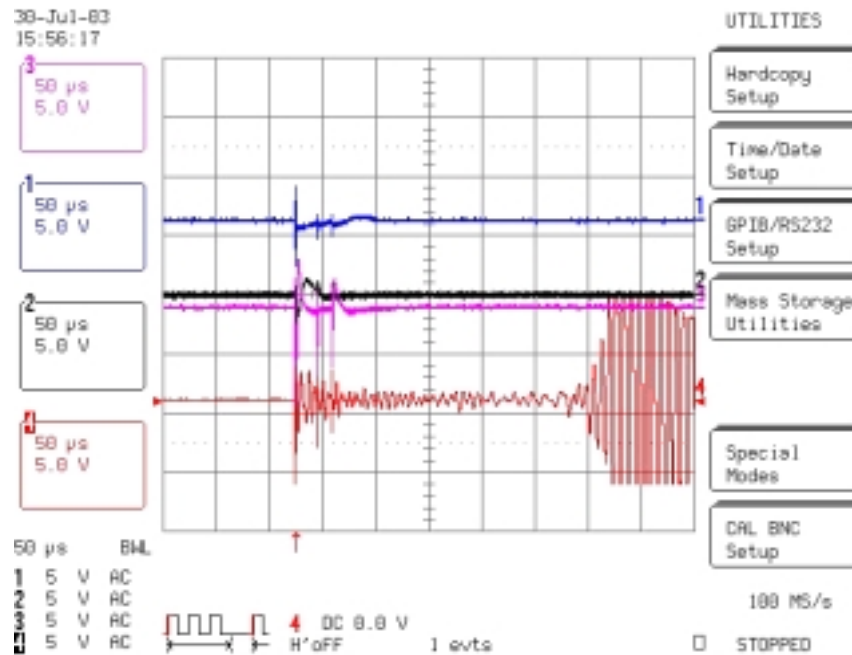


Fig 9.27 Oscillogram of the 2nd DC test. (CH1-3 for the DFPI sensors, CH 4 for the PZT sensor with an integrated preamp)

2) PD detection under AC condition

PDs under the AC condition are different from those under the DC condition. The number of PD events in a certain time interval will be much larger for AC voltage than for DC voltage [203]. PDs at different locations near the energized blades can occur in a very short interval or even at the same time. According to the previous field test in UK, the estimated frequencies of the PD acoustic signals fall in the range of 70 kHz to 250 kHz. The system was designed with a bandwidth between 20 kHz and 400 kHz. Therefore, the acoustic signal under the AC condition may not be as clear and apparent as under the DC condition. The experiment results verified this point.

The AC tests were done by following similar steps as under the DC condition. The AC voltage applied to the blades was increased slowly until a PD occurred inside the transformer oil. The results of the first AC test are given in Fig. 9.28. Multiple peaks in a very short time interval were observed, and the peaks in the middle of the waveforms had the highest energy. The reason was that the breakdowns in air cavities inside the oil occurred more and more frequently as the applied voltage reached a certain level and the breakdown frequency decreased when the AC

source was triggered out. This was actually a total breakdown between the blades and the ground electrode. The total breakdown might be caused by the fast increase of the AC voltage.

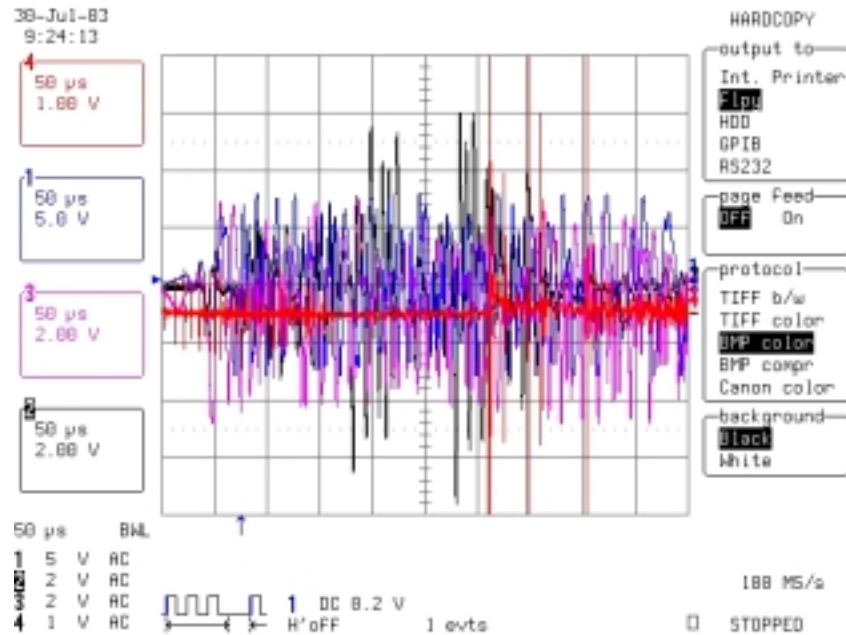


Fig. 9.28 Oscillogram for the 1st AC test. (CH 1~3 for the DFPI sensor and CH 4 for the PZT sensor w/o an integrated preamp)

A second AC test was done by using the same method, but the AC voltage was applied more slowly than in the first experiment. Unfortunately, our high power SLED was shocked down just before this test due to the bad grounding of the electrical power supply, and the backup 1300nm LED of a much lower power was used, as mentioned in the last section. Therefore, only one DFPI sensor and a PZT sensor could be monitored at the same time. The best DFPI-PD sensor was used in this test.

The sensor's outputs are shown in Fig. 9.29. The first separated peak of the outputs from the DFPI sensor was an indication of a PD, while the following peaks were multiple breakdowns in the oil, which might have lead to total breakdown between the electrodes. When the AC power supply was triggered out, the number of breakdown decreased. From the acoustic waves captured by the PZT sensor, we confirmed the judgment in spite of the amplified minor noises by the preamplifier.

Although this time we increased the AC voltage in a slower speed, the AC supply was again triggered out. This might be caused by the limited capacity of the AC supply or mismatched relay. As an unexpected benefit, we tested our sensor for picking up and telling the difference of PDs and total breakdowns, in addition to just showing the different wave shapes for AC and DC voltages.

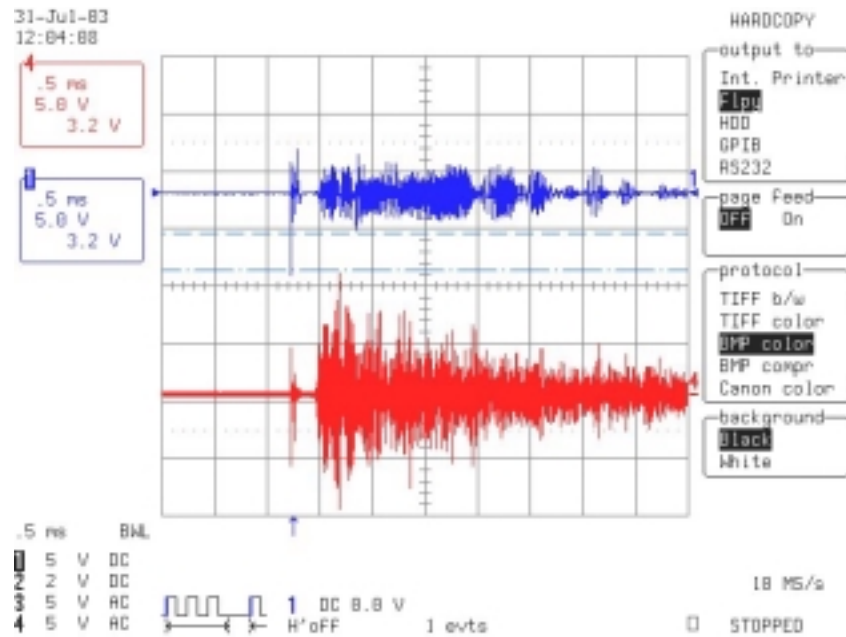


Fig. 9.29 Oscilloscope for the 2nd AC test. (CH 1 for a DFPI sensor, and CH 4 for new PZT sensor with an integrated preamp)

3) Thermal fault test

In order to prove the capability of thermal fault detection inside a transformer using fiber optic sensors designed for PD measurements, thermal fault tests were also performed using the same experiment setup. The thermal tests were done using the backup light source. Unfortunately, the best DFPI sensor out of the three sensors for thermal test was broken during the installation and the other two sensors did not pick up any thermal activities during the first few trial experiments. We decided to move the five DFPI sensors for electrical faults to the tank side for thermal tests. Fig. 9.30 shows the five DFPI sensors installed into the tank through the tank window. However, only the best DFPI sensor was tested during all the thermal tests.



Fig. 9.30 DFPI-PD sensors installed for thermal tests.

During the tests, the temperature of the mineral oil was cycled from 50 °C up to 240 °C in a very short time. Fig. 9.31 shows the acoustic waveforms captured by the DFPI sensor and the PZT sensor. CH2 in the figure represents the DC output of the DFPI sensor which was used to monitor and control the operation-point. Obviously, the fiber sensor has different frequency response from the PZT sensor. Although the PZT transducer has a higher signal amplitude, the SNR of the DFPI sensor is still a little better. The FFT of the acoustic signals recorded by the DFPI sensor indicates that the acoustic waves had a central frequency around 25 kHz.

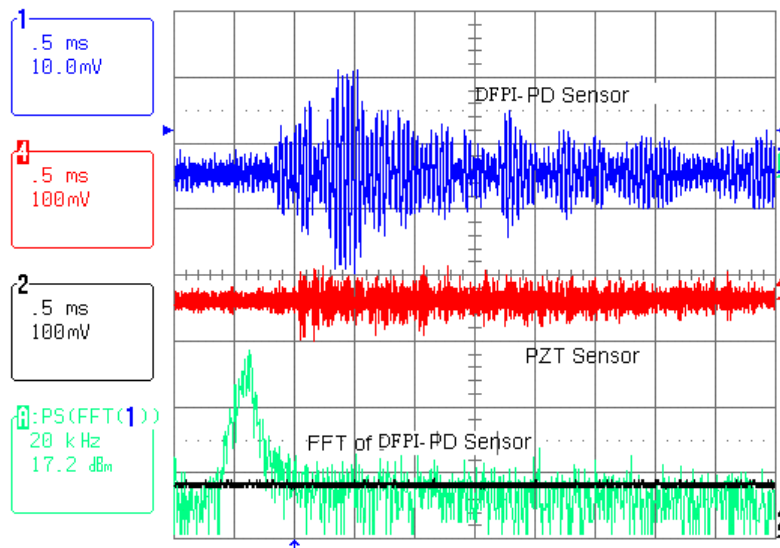


Fig. 9.31. The thermal test results. (CH 1 - DFPI sensor, CH 2 - DC output of DFPI sensor, and CH 4 - PZT sensor with an integrated preamp)

What should be mentioned is that the light source used in this experiment is a backup source with a much lower output optical power. Since the noise of the fiber sensor was dominated by electronics, its SNR can be significantly improved by the use of a higher power LED or SLED.

9.6 Summary

A 1300 nm DG-TOF WLI interrogation system specially designed for partial discharge and thermal fault detection in high voltage transformers have been constructed. By scanning the DG-TOF, the best Q-point of a DFPI sensor can be found. Once the system is locked to a Q-point, linear demodulation of a DFPI-PD sensor becomes feasible and reliable, even with the presence of large fabrication tolerances or/and random environmental fluctuations. The system can be used to interrogate three DFPI-PD sensors simultaneously.

Laboratory experiments indicated that a SNR improvement of 15 dB was easily achieved using a DG-TOF comparing with the same system without a TOF. The real linear operation makes signal distortion the minimum. In addition to the SNR improvement, the requirement on the sensor's temperature-cross-sensitivity was significantly relaxed and the sensor fabrication yield was also remarkably increased.

Two field tests have been successfully performed. In the UK test, nine DFPI-PD sensors were deployed into a SGT3A 400KV/275KV transformer. The 1300 nm WLI system without a TOF was employed for sensor interrogation. Although our team was one of the only two groups, out of the six companies and universities attending the one-week test, who observed very weak PD activities, the low SNR made it essential to use wavelet transform for de-noising and signal analysis.

The second test was performed in the RPI Transformer Lab with a simulated power transformer environment. During the test, three groups of experiments had been performed. In first two groups, PDs were generated by applying DC or AC voltages to the electrodes of the corona generator. The experiments confirmed that PDs from DC and AC voltages have clearly different characteristics. In the last group, we investigated thermal fault detection using the DFPI-PD sensors. In the DC and AC experiments, the PZT sensor showed higher signal amplitudes than the DFPI sensors because the PZT sensor was closer to the corona generator (5~10 cm). However, the DFPI sensor showed better SNR than the PZT sensor for thermal fault detection. The last experiment better represents the real situations in the field, where PZT sensors

are tapped on the wall of a transformer tank, while a DFPI sensor can be installed inside the tank and therefore can be much closer to a PD source than the PZT sensor.

Although the DG-TOF WLI has a flexible bandwidth and a large tuning range, and have achieved great success in PD and thermal fault detection, it is generally bulky, still polarization dependent, and not cheap because of the use of stages and motors. Recently, miniature rotary stages, especially MEMS based DG-TOFs are available in the market [Berger, 2003]. The introduction of such a MEM DG-TOF into a WLI system may remarkably improve the performance while reducing the cost of a DG-TOF WLI system. Of course, the EFP-TF WLI is another alternative solution. The experiments on using the EFP-TF WLI for interferometric sensor interrogation will be discussed in the next chapter.

Chapter 10 EFP-TF WLI for EFPI and DFPI Sensor Interrogation

As mentioned in the summary of Chapter 9, the DG-TOF WLI system works reasonably good for PD and thermal fault detection, but has some limitations which prevent it from being used as a general tool in the interrogation of various types of interferometric sensors.

To further investigate the feasibility and effectiveness of TOF-WLI for sensing, this chapter describes the instrumentation of a TOF-WLI interrogation system using the EFP-TF, the laboratory investigation using the system for the interrogation of low-finesse and high-finesse EFPI temperature sensors, and the field demonstration using the system, with DFPI-Engine sensors, for dynamic pressure measurement in a gas turbine engine.

10.1 Instrumentation

A 1550 nm TOF-WLI system was built using the developed EFP-TF. The layout schematic of the system is shown in Fig. 10.1.

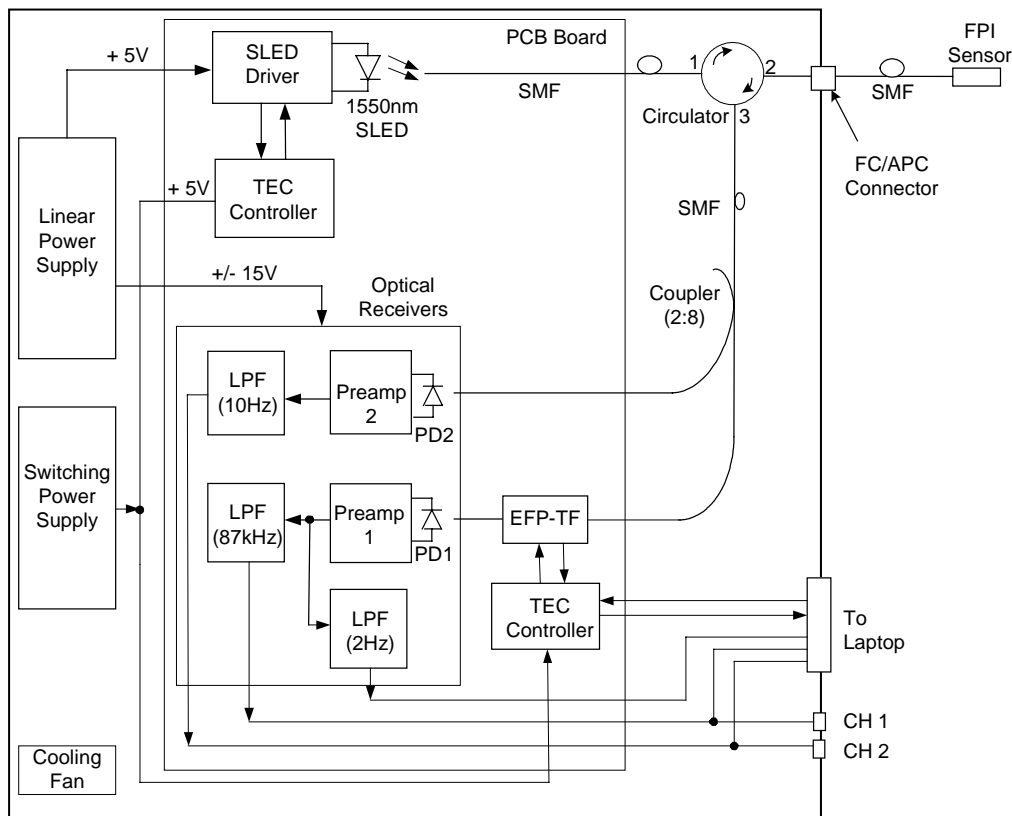


Fig. 10.1 Layout schematic of the EFP-TF WLI interrogation system.

The system is generally composed of a linear power-supply, a switching power supply, a 1550nm SLED and its driver and temperature controller, a 1550nm wideband circulator, a 2:8 optical coupler (optical power split ratio 20:80), an EFP-TF and its temperature controller, a two-channel low noise optical receiver, a cooling fan, a laptop computer with a data acquisition card and Labview programs for EFP-TF control and low frequency signal recording, and a two-channel digital oscilloscope for high frequency signal (above 10 kHz) monitoring. Two receiver channels, including a narrowband channel (the one with an EFP-TF) and a broadband channel, were built into the system for the purpose of self-calibration as described in Reference [39]. The broadband channel responds only to source power fluctuations, fiber bending and other factors common to both the broadband channel and the narrowband channel, but not to the measurand signal due to the low coherence length of the broadband light source. When the narrowband signal is divided by the broadband output, any common-mode fluctuations can be removed from the former one. For this reason, the bandwidth of the broadband optical receiver was designed to be very low for best SNR, but high enough for most fluctuations. The signal bandwidth of the narrowband channel is determined by the frequency response requirement of the perturbation to be measured. For static or quasi-static measurements, such as temperature and strain, a bandwidth from DC to a few Hz is usually sufficient. For dynamic signals, such as vibration and pressure fluctuations, a bandwidth from DC up to hundreds of kHz may be required. In acoustic applications, such as hydrophone and PD detection, a bandpass filter can be used to remove both low frequency and high frequency noises.

10.1.1 Light source

A 1550 nm SLED from Exalos ESL1505 with 2.5 mW Power in SMF (at 180 mA maximum operating current) and 60 nm Bandwidth in FWHM was selected as the light source due to its both large bandwidth and good output power. The high output power eases the power budget and increases the SNR in a sensing system. The large bandwidth is also important because it takes advantage of the large tuning range of the EFP-TF and provides a large dynamic range for both the signal amplitude and the compensatable drifts. Fig. 10.2 shows the output spectrum of the SLED at the maximum operating current.

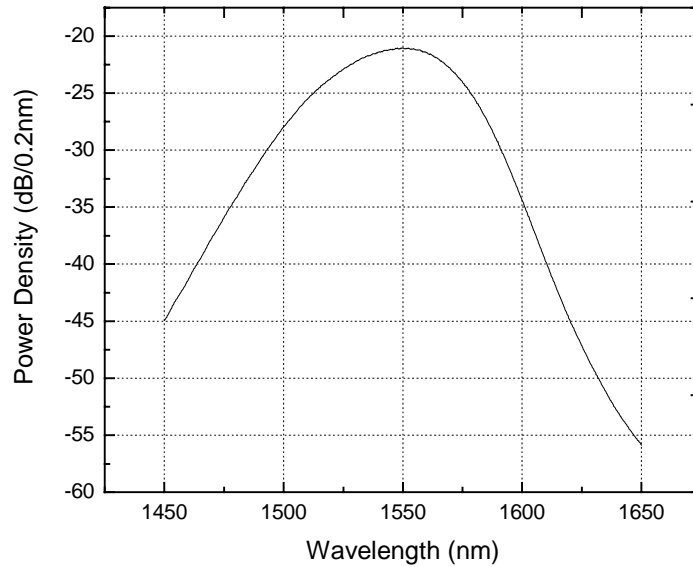


Fig. 10.2 Output spectrum of the SLED at 180 mA and 20 °C.

Since the SLED's output power and spectrum are temperature dependent, temperature control is very necessary to reduce the temperature effects. Also because of the high output power of the SLED, temperature control is very important to protect the SLED from being damaged.

The SLED comes with a thermistor and an embedded TEC. The absolute rating for the TEC current at 25 °C is 0.8A. A laser diode driver module PLD500 with 500 mA maximum output current was used to drive the SLED, and an HTC1500 temperature controller module for temperature control from Wavelength Electronics, Inc.

10.1.2 Electronics

To make the system portable, all the electronic components were integrated onto a single PCB board, as shown in Fig. 10.3. The board hosted the following subsystems: the 1550 nm SLED, the SLED driver, the temperature controller for the SLED, the EFP-TF and its controller, two low-noise optical receivers described in Section 8.4, and a computer interface. The advantage of integrating all these components onto a single PCB board significantly reduces the system size and the cost, while improving the reliability. The major drawback is that shielding of the optical receivers becomes very challenging due to the heat dissipation requirement, and

therefore the EMI noise is slightly increased. Heat dissipation is very important because both the TEC for the SLED and the one for the EFP-TF give off heat that has to be removed out of the system box. The cooling fan in Fig. 10.1 and the net openings on the main box force air-exchange and maintain the environmental temperature inside the box a little bit above the room temperature.



Fig. 10.3 Interrogation system on a single PCB board.

10.1.3 EFP-TF controller and computer interface

As indicated in Chapter 6, the EFP-TF is controlled by a laptop computer through a data acquisition card (DAQ). For Q-point stabilization in the linear operation mode, a feedback control has to be used. In the prototype system, a MF236/I DAQ PC Card with 12-bit, 625Ksps, 16 A/D channels, and dual 12-bit D/A converters, from Elan Digital Systems Ltd, was employed. The dual analog output channels make it possible to control two EFP-TFs simultaneously using only one laptop computer.

The A/D channels of the DAQ card are used to convert the outputs of the optical receivers into digital signals, which are then processed by software. The results from the DC channel of

CH 1 can be used to obtain the interference fringes during the scanning of the EFP-TF and to lock the Q-point during the linear operation mode. The outputs from the signal channel of CH1 and those from CH 2 can be used to recover the real measurand signals.

Labview was chosen for the EFP-TF control, data acquisition and signal processing. Fig. 10.4 is a flow chart of the programs used. The program is composed of three modules, a scan mode, a manual mode and an auto mode. In the scan mode, the interference fringes are obtained by scanning the EFP-TF from the Start Voltage to the Stop Voltage, and then saved in the hard disk. By simple data processing, the best Q-point and the sign of the fringe slope can be found and the linear operation range can be determined. The information about the Q-point is displayed on the front panel of the programs. The manual mode can be used to manually enter and modify the Q-point when the system is running in a linear mode. The outputs of the sensor are saved in the hard disk for further signal processing. Once the Q-point and the linear range, as well as the sign of the fringe slope on the Q-point side are determined, the auto mode may be used to dynamically lock the system to the Q-point using a feedback control loop in the program.

The front panel of the programs is shown in Fig. 10.5. The Labview codes can be found in Appendix B.

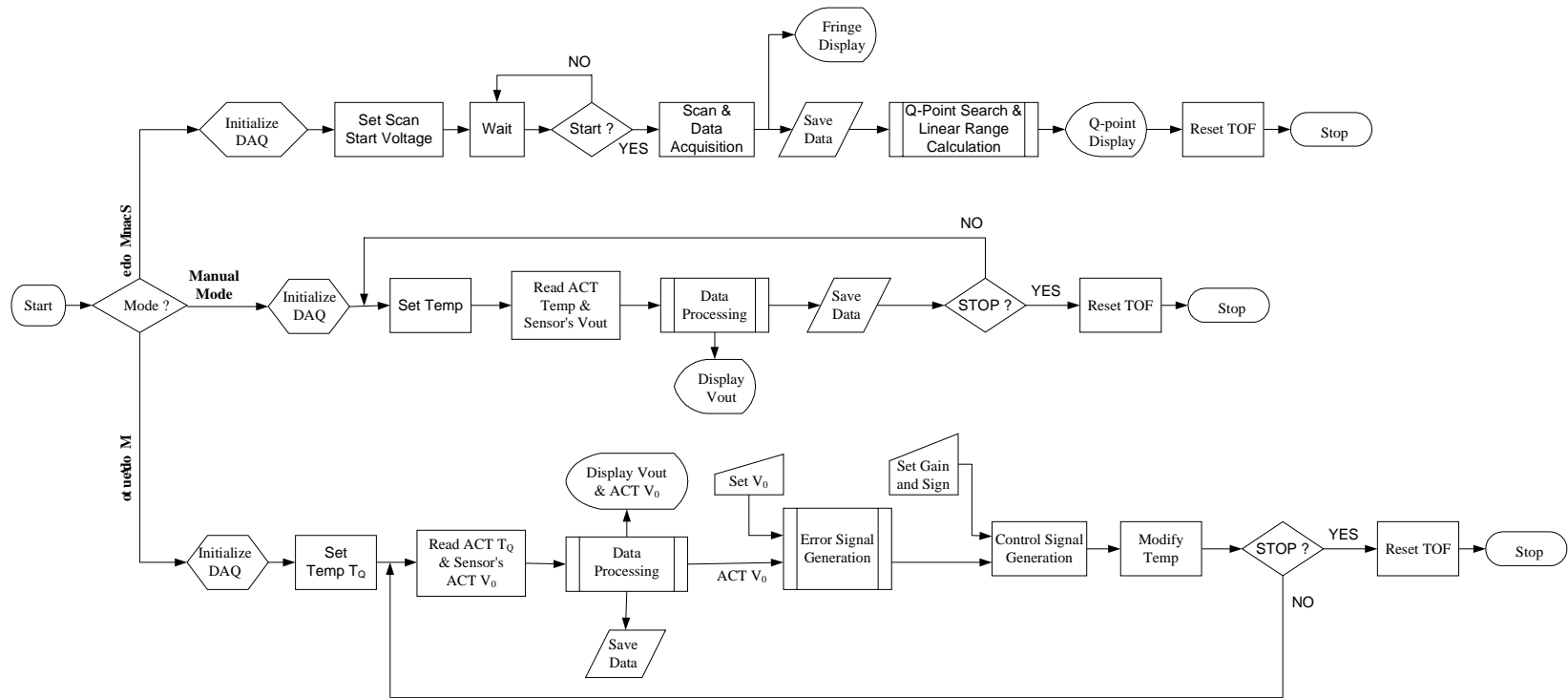


Fig. 10.4 Flow chart of the Labview programs for EFP-TF control and data acquisition.

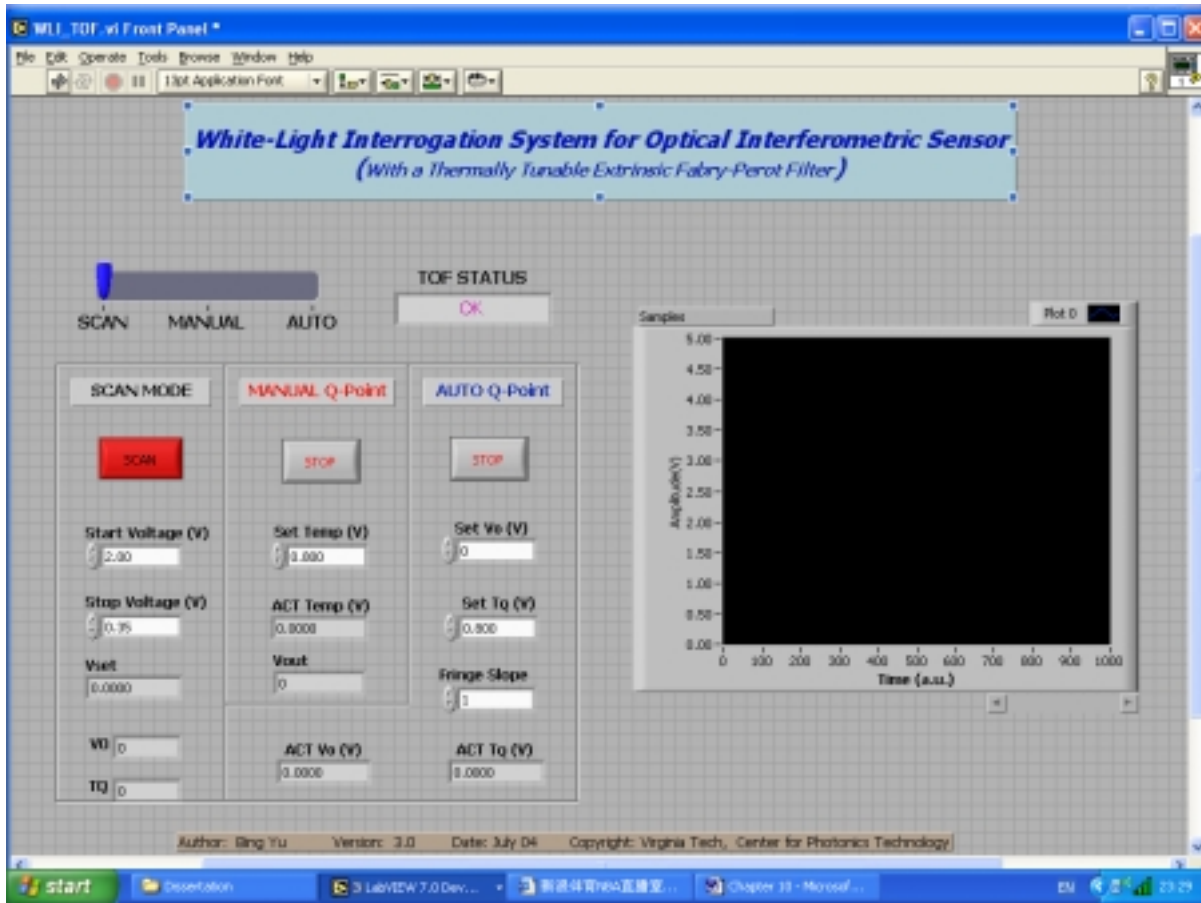


Fig. 10.5 The front panel of the Labview programs.

10.1.4 Instrument

Fig. 10.6 is a photo of the whole system, including a main box, a circulator box on top of the main box, a laptop computer with Labview programs for EFP-TF control and data acquisition, and an oscilloscope for high frequency signal monitoring. The system may operate either in a scan-mode or a linear demodulation mode. A sensor can be directly plugged into the circulator box through a FC/APC connector. Fig. 10.7 is a top view of the main box.



Fig. 10.6 Photo of the 1550nm EFP-TF WLI interrogation system.

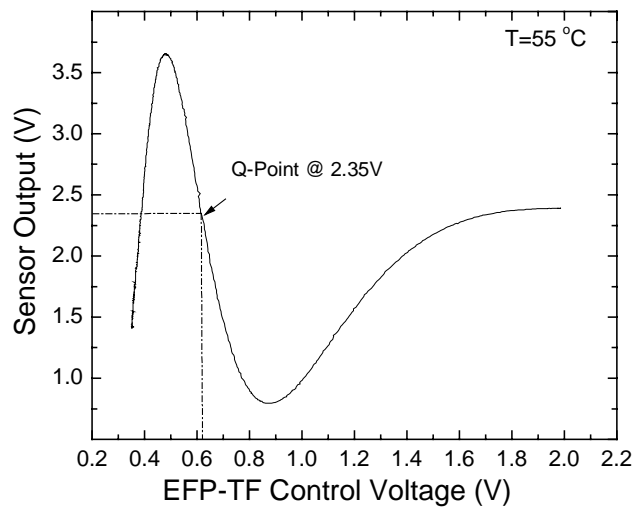


Fig. 10.7 A top view of the main box.

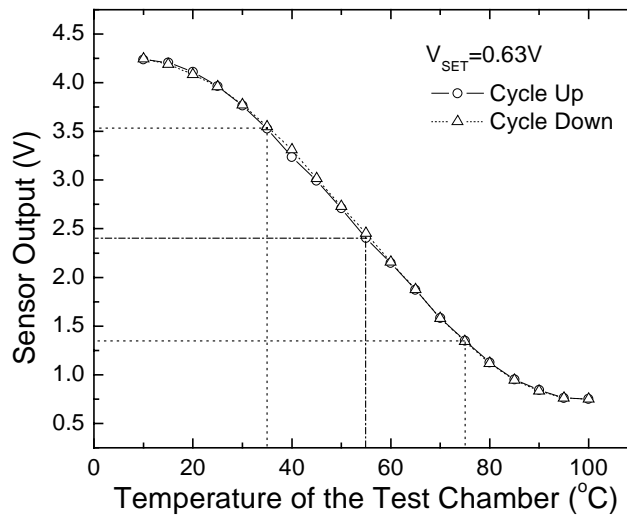
10.2 Low-finesse EFPI temperature sensor

In the first experiment, the low-finesse EFPI temperature sensor with a borosilicate tube, as described in Section 7.1, was used in a linear operation mode. The sensor was tested inside a TESTEQUITY 1000 Series Temperature Chamber in the laboratory environment. The resolution of the chamber temperature controller is $0.1\text{ }^{\circ}\text{C}$, and the short-term stability of the temperature inside the chamber is around $\pm 0.2\text{ }^{\circ}\text{C}$.

By scanning the TOF at a chamber temperature of 55 °C, the Q-point of the sensor was found at a control voltage of 0.63 V, as shown in Fig. 10.8(a). Locking the control voltage to this point, but cycling the temperature chamber from 10 to 100 °C, and then back to 10 °C, the sensor's output was recorded and shown in Fig. 10.8(b). Obviously, this EFPI sensor has a linear operation range from 35 to 75 °C with an output voltage change from 1.35 to 3.54 V. Beyond this range, the linearity becomes poor and distortion becomes significant. The linear temperature range can be easily increased by either reducing the gauge length of the EFPI sensor or the thermal expansion difference between the tubing and the silica fibers using a different tubing



(a)



(b)

Fig. 10.8 Low-finesse EFPI temperature sensor. (a) Q-point searching, (b) Lock-mode.

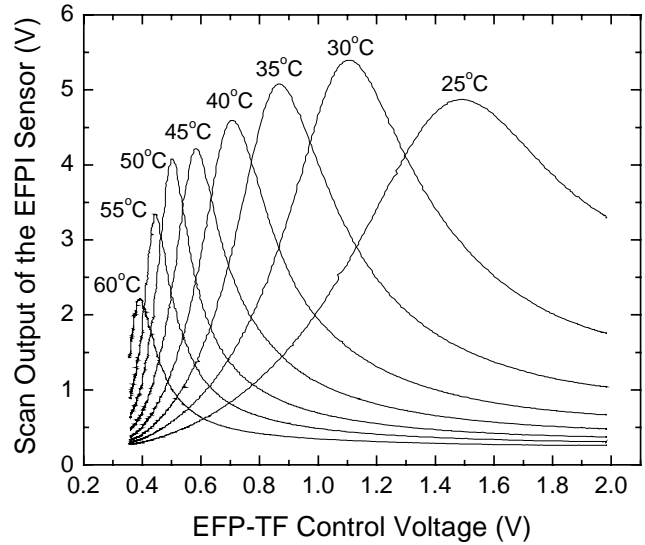
material, for example fused silica tubing. A sensitivity of $54.8 \text{ mV}/^\circ\text{C}$ was calculated from Fig. 10.8(b). Since the low frequency noise of the system in DC channel of CH1 is around 0.45 mV , a dynamic range to resolution ratio of about 5000:1 was obtained.

Because of the long time needed for a single cycle of test, only one cycle test was performed. The small discrepancy between the cycle-up and the cycle-down processes was believed mainly due to the hysteresis of the chamber temperature. The waiting time at each temperature before taking the data was 5~10 minutes. Considering the large chamber size ($24'' \text{ W} \times 21'' \text{ H} \times 24'' \text{ D}$), better repeatability can be expected if longer time interval were used for each data point.

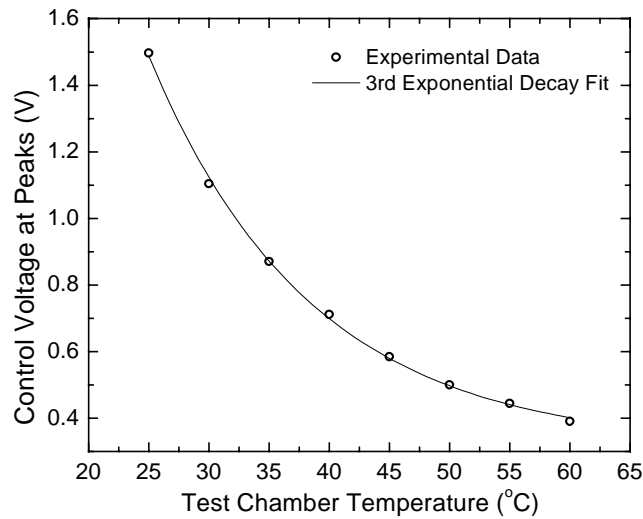
10.3 High-finesse EFPI temperature sensor

In the second experiment, the high-finesse EFPI temperature sensor, as described in Section 7.1, was tested in the same chamber. The major difference from the previous experiment is that a transmission mode, instead of a reflection mode, and fringe peak tracking, instead of linear-mode, were used. Fig. 10.9(a) shows the scan outputs of the sensor at chamber temperatures from 25 to $60 \text{ }^\circ\text{C}$ with a $5 \text{ }^\circ\text{C}$ interval. The peak intensity variations from scan to scan were caused by the source power distribution, while the changes of the fringe width were mainly due to the non-linear response of the EFP-TF to its control voltage.

By plotting the control voltages at the peaks against the chamber temperature, we obtained a temperature-voltage curve with a 3rd order exponential decay fit, as shown in Fig. 10.9(b). The 3rd order exponential decay was, once again, due to the same relationship between the EFP-TF and its control voltage, as shown in Fig. 6.15. In this approach, a dynamic range to resolution ratio of about 2200:1 was obtained, which was limited by the free spectral range (*FSR*) of the sensor, the tuning range and the low frequency noise of the DC channel of CH1, as well as the available SLED bandwidth. Therefore, a higher dynamic-range-to-resolution ratio could be obtained by using an EFPI with a smaller cavity length, an EFP-TF sensor with a smaller cavity length, and a light source with a larger FWHM. The ratio may also be increased by a better electronic circuits design, for example using balanced detection, and shielding to further reduce the background noise.



(a)



(b)

Fig. 10.9 High-finesse EFPI sensor. (a) Scan outputs; (b) Temperature-voltage curve.

10.4 DFPI-Engine Sensors

In the last experiment, a field test of the DFPI-Engine sensors [173] and miniature fiber optic sensors [204] [205] for dynamic pressure measurements at the inlet of a F109 turbine engine at the Virginia Tech Airport was performed. Fig. 10.10 shows three DFPI-Engine sensors with a diaphragm of 60 μm in thickness and 1.5 mm in effective diameter were mounted on the engine along with a Kulite pressure sensor XT-190-300A (the one in white) as a reference. The Kulite

sensor had a sensitivity of 0.33 mV/psi, a dynamic range of 300 psi, a resolution of 0.1% of the dynamic range or 0.3 psi, and a natural frequency of 650 kHz. In order to increase its sensitivity and reduce out of band noise, an 1822 Differential Amplifier from Preamble Instruments, Inc., was exploited in a low pass mode (DC~100 kHz). The Kulite sensor with the Differential Amplifier has a total sensitivity of 33.3 mV/psi and a slightly better resolution.



Fig. 10.10 Gas turbine engine under test.

The TOF-WLI system operating in a linear-mode was employed. Fig. 10.11 shows the test equipment setup in the control room which was about 30 m from the turbine engine. Since the frequency components of the pressure waves in the engine were higher than the speed of the DAQ card, the outputs of the pressure signals were displayed and recorded by a two-channel Lecroy oscilloscope, and data were saved into a computer for further signal processing.

What should be mentioned is that the interrogation system used in this test was an earlier version of the EFP-TF WLI system operating in the 1300 nm band. In the 1300 nm EFP-TF WLI system, the light source was a 1300 nm LED with 250 μ W power in SMF, the EFP-TF had a 3-dB bandwidth about 14 nm and an insertion loss above 4 dB, and the base noise of the optical receivers was about 1.3 mV. Laboratory static pressure tests with the 1300 nm system indicated that the DFPI-Engine sensors generally had a sensitivity of 87 mV/psi, a resolution of 0.023 psi (159 Pa), and a natural frequency about 250 kHz [173]. The 1550 nm system is superior to the earlier version due to its four times higher source power, 7~8 nm 3-dB bandwidth, and one-third

noise level, of the 1300 nm EFP-TF WLI system. All these factors result in much better SNR and therefore higher resolution.



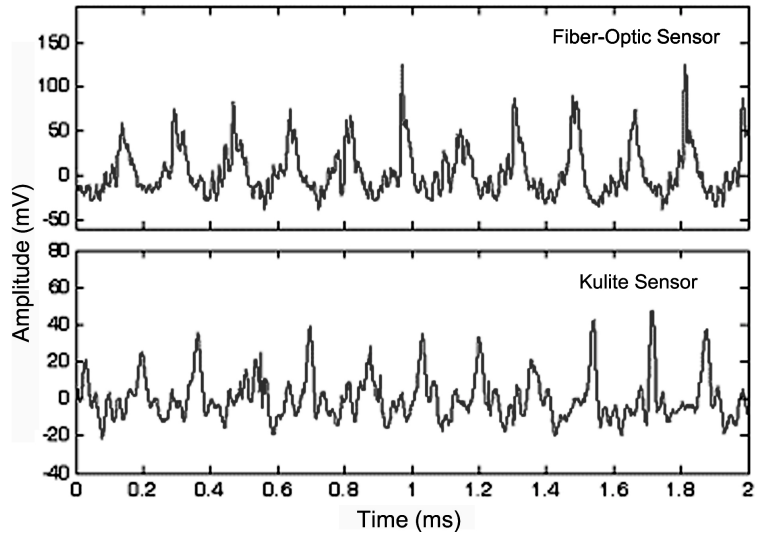
Fig. 10.11 Test equipment setup in the control room.

Since the WLI system supports only a single sensor, all the DFPI sensors were numbered and spliced to a single-mode fiber cable with an APC connector at the instrument end. The signals of the three sensors were checked in sequence. During the test of each sensor, the sensor was first plugged into the FC/APC connector on the instrument front panel. The interference fringes, and thus the best Q-point, were obtained by scanning the EFP-TF. The EFP-TF was then locked to the selected Q-point. The dynamic pressure signals were recorded using the oscilloscope.

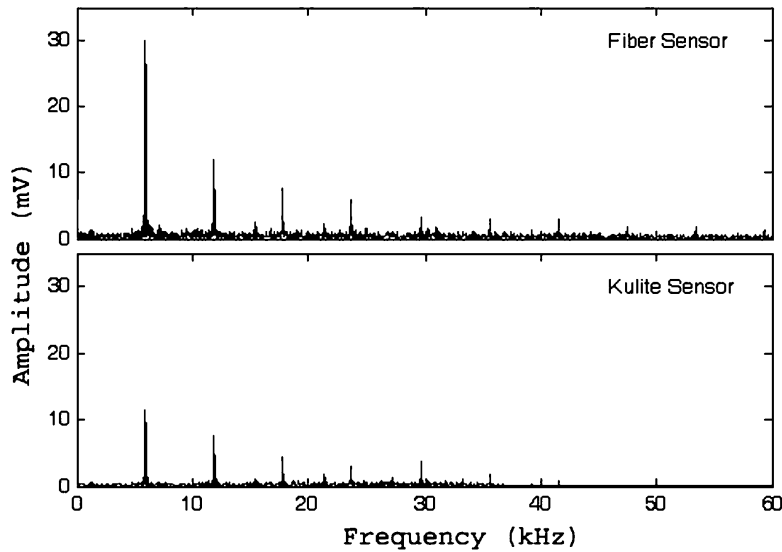
The pressure fluctuation at the inlet of a turbine engine is mainly caused by the rotation of the fan blades. The typical time domain pressure signals recorded by one of the three DFPI sensors with those by the Kulite sensor, when the engine was operated at 90% of its maximum power (estimated fan speed 1200 rpm), are shown in Fig. 10.12(a). The signal from the fiber sensor had about 2.5 times higher amplitude than that from the Kulite sensor. The 0.058ms time delay between the two signals was due to the spatial distance between the sensor DFPI sensor and the Kulite sensor.

Fig. 10.12(b) shows the same signals but in the frequency domain. Apparently, they matched well at all major frequency components. The major frequency components and the signal amplitude at each frequency are listed in Table 10.1. A fundamental frequency of 5.93 kHz was

measured by both the DFPI sensors and the Kulite sensor. This frequency component was resulted by the rotation of the fan with 30 fan blades. Other components are the harmonic frequencies. It is also clear from Fig. 10.12(b) that the DFPI sensors have better SNR than the Kulite sensor with an 1822 Differential Amplifier. A further increase in the SNR can be expected when the 1550nm EFP-TF WLI system is used.



(a)



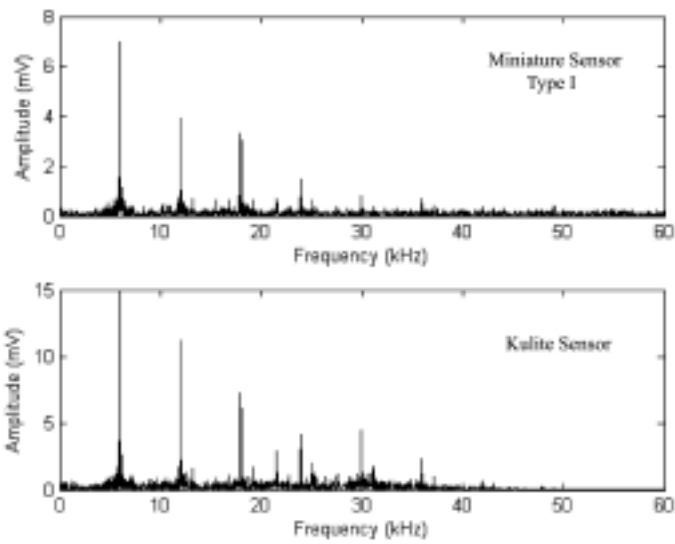
(b)

Fig. 10.12 Typical test results from DFPI-Engine sensors and the reference sensor. (a) Time-domain signals; (b) Frequency-domain signals.

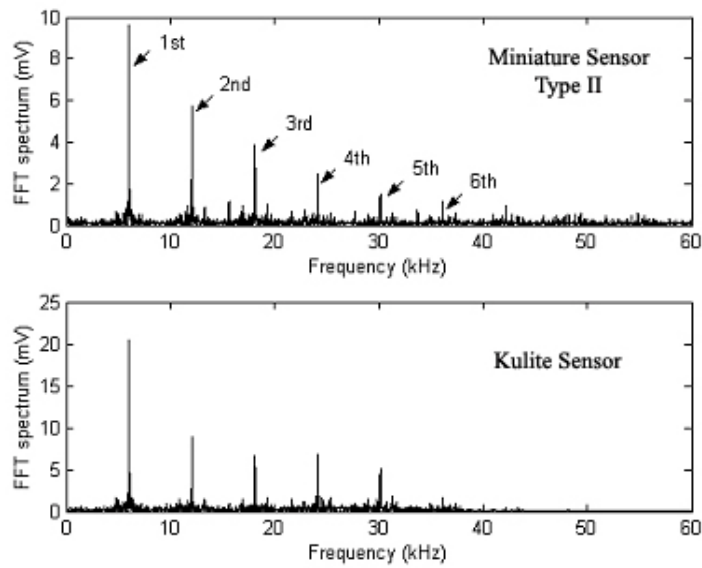
Table 10.1 Main frequencies measured by the Kulite and the DFPI-Engine sensor. (Table provided by J. Xu)

	Frequency (KHz)		Amplitude (mV)	
	DFPI-Engine Sensor	Kulite Sensor	DFPI-Engine Sensor	Kulite Sensor
1	5.930	5.930	30.0634	11.3772
2	11.860	11.865	12.1294	7.4924
3	17.795	17.800	7.7381	4.5748
4	23.725	23.720	6.0433	2.9771
5	29.660	29.660	3.2610	3.7025
6	35.590	35.595	2.9957	1.8222

The 1300nm EFP-TF WLI system was also exploited for the interrogation of two types of miniature fiber optic sensors during the same field test. These sensors were fabricated, using two different processes, directly on the tip of a single-mode fiber [204] [205]. Similar results were obtained with both types of miniature sensors. Fig. 10.13 shows the typical frequency domain signals captured by the miniature sensors. Obviously, the signals from the miniature sensors matched those from the reference sensor very good at all major frequency components. The lower sensitivities for all the miniature sensors tested than those of the DFPI-Engine sensors and the Kulite sensor were mainly due to the much smaller diaphragm diameters.



(a)



(b)

Fig. 10.13 Frequency-domain dynamic pressure signals recorded by the miniature sensors and the Kulite reference sensor. (a) Type I miniature fiber optic sensor; (b) Type II miniature fiber optic sensor.

10.5 Summary

A TOF-WLI interrogation system was constructed using the EFP-TF. Three major experiments have been performed to investigate the feasibility and effectiveness of the TOF-WLI for the interrogation of various types of interferometric sensors.

In the first experiment, a low-finesse reflection type EFPI temperature sensor was tested inside a temperature chamber with the TOF-WLI system operating in a linear mode. A dynamic range to resolution ratio of about 5000:1 was achieved with a high degree of linearity.

The experiment with the high-finesse transmission type EFPI temperature sensor demonstrated the feasibility of demodulating an interferometric sensor by fringe peak tracking. In this approach, a dynamic range to resolution ratio of about 2200:1 was obtained, which was limited by the *FSR* of the sensor, the tuning range and the amplifier noise as well as the available SLED bandwidth.

The field demonstration of using the system, with DFPI-Engine sensors and miniature fiber optic sensors, for dynamic pressure measurements in a gas turbine engine proved the high sensitivity and SNR of the system in the real field. In general, the DFPI-Engine sensor system has a sensitivity 263 times higher, a resolution 13 times better, and a dynamic range 3 time and a frequency response 2.6 time lower (but sufficient for pressure measurements in gas turbine engines), than those of the Kulite reference sensor.

Chapter 11 Conclusions

11.1 Conclusions

Interferometric fiber-optic sensors represent the most sensitive sensor type which has attracted more and more laboratory research and industrial deployment in the last two decades, attributing to its ultra-high sensitivity to many physical, chemical and biomedical parameters, immunity to EMI interference, high survivability in very harsh environments, potential for multiplexing, ease of fabrication, and miniaturization. In the past five years, various types of Fabry-Perot interferometric fiber-optic sensors, including EFPI / IFPI temperature sensors, DFPI-PD acoustic sensors, DFPI-Engine pressure sensors, and miniature sensors, have been developed in the Center for Photonics Technology at Virginia Tech. These sensors were specially designed for harsh environments, such as oil-wells, high voltage power transformers, and gas turbine engines.

Interrogation of interferometric sensors with a high accuracy and a high speed at a low cost has been a challenge to researchers for decades. Taking advantage of the powerful white light interferometry (WLI) or low coherence interferometry (LCI), I have proposed and studied a tunable optical filter based white light interferometry (TOF-WLI) as an effective but low cost solution. Comparing with the available scanning white light interferometry (SWLI) which has been widely used in optical coherence tomography, surface profiling, and optical sensors, the TOF-WLI is simpler in structure, applicable to most types of interferometers, more reliable, and more compact in size. The TOF-WLI is also compatible in signal processing with the accurate, but expensive, spectral-domain white light interferometry (SD-WLI) and the tunable laser based white light interferometry (TL-WLI). A unique feature of the TOF-WLI is that it adds a linear operation capability to the already powerful WLI technique, which is extremely useful in the detection of very weak or dynamic perturbations.

The formulae for the evaluation of the sensitivity, fringe contrast and dynamic range of a white light interferometric sensor have been derived. Numerical methods have been exploited to study the effects of the FP finesse, the mirror misalignments and the band-pass filter or TOF on the performances of a FPI sensor. This theoretical study and numerical analysis may be used as a

tool in the design of various types of white light interferometric sensors, especially those interrogated by a TOF-WLI system.

The key component to the success of the TOF-WLI is the TOF which must be cheap and specially designed for sensing applications. Commercially available TOFs are generally designed for telecommunications, and are not suitable for sensing systems also due to the high price. In this dissertation, a DG-TOF was proposed and constructed using a holographic diffraction grating. The DG-TOF has a large tuning range, flexible bandwidth, and high speed. The drawbacks are large component size, polarization dependence, large insertion loss and relatively high cost. It could be made more compact by using miniature stages and lenses, the insertion loss could possibly be significantly reduced by using concave gratings and finer stages, and the polarization dependence can be minimized by choosing a diffraction grating with equal efficiency for both polarizations. However, the cost of each DG-TOF may limit it to some specific applications. Therefore, a second novel TOF, named EFP-TF was proposed and studied. The core of the EFP-TF is a high-finesse EFPI, and tuning is achieved by heating or cooling the EFPI using a Peltier device or a micro-heater. The EFP-TF features a large tuning range, polarization independence, a low insertion loss, easy fabrication and control, and thus, extremely low cost, suitable for sensing and spectroscopy.

The effectiveness of using the TOF-WLI as a low-cost solution for the interrogation of various types of interferometric sensors has been validated both in the laboratory and in the fields with DFPI-PD sensors, DFPI-Engine sensors and EFPI temperature sensors. A 1300nm DG-TOF WLI system was built and employed in the study of DFPI-PD sensors for electrical fault and thermal fault detection. In addition to the 15 dB SNR improvement achieved, the use of the DG-TOF provided dynamic compensation of Q-point drifts and remarkable increase in the DFPI-PD sensor fabrication yield. Better SNR of the DFPI-PD sensor system than that of the PZT acoustic sensor system from PAC was observed during the thermal fault experiments. The 1550nm EFP-TF WLI system has been successfully used with the low-finesse EFPI temperature sensors in linear demodulation mode, the high-finesse EFPI temperature sensors in a peak tracking mode (SD-WLI), and the DFPI-Engine sensors and miniature sensors in a linear operation mode. The most important advantage of the EFP-TF WLI is its extremely low cost and high adaptability to various applications.

11.2 Summary of Contributions

This section outlines the major contributions of this dissertation and related work as follows:

Most important contributions

- Proposing and validating the tunable-optical-filter-based white-light interferometry (TOF-WLI) as a low cost, but efficient solution to the interrogation of various types of interferometric optical sensor.
- Proposing and demonstrating a novel extrinsic Fabry-Perot tunable filter (EFP-TF) for optical sensing, spectroscopy and wavelength-division multiplexing (WDM) networks.
- Introducing and demonstrating a diffraction grating tunable optical filter (DG-TOF).
- Leading the design and fabrication of DFPI-PD sensors for the detection and location of partial discharges (PDs) and thermal faults inside high voltage power transformers and transmission cables.
- Participating as a key researcher in the development of high temperature (0~800°C) DFPI-Engine sensors for pressure measurements inside gas turbine engines with full responsibility for system level design and instrumentation.
- Introducing a systematic analysis method for the calculation of the sensitivity, the fringe contrast and the linear operation range of white-light interferometric sensors.
- Developing a 1300nm DG-TOF WLI sensor interrogation system, a 1300nm EFP-TF WLI interrogation system, and a 1550nm EFP-TF WLI interrogation system.
- Leading the field test of DFPI-PD sensors for PD detection in the NGC SGT3A 400KV/275KV transformer at the Northfleet West Substation, London, UK, in May 2002, and the test of DFPI-PD sensors for both PD and thermal fault detection in a simulated power transformer in the RPI Transformer Lab in July 2003.
- Participating in the field test of DFPI-Engine sensors and DFPI-Tip sensors for dynamic pressure measurements in a gas turbine engine at the Virginia Tech Airport in July 2004.

Other significant contributions

- Developing low noise analog optical receivers for PD detection and engine pressure measurements.

- Designing, purchasing, installing, maintaining of a Class 1000 modular cleanroom at CPT, which houses an RF Magnetron sputtering system, a wet processing station, a surface profiler, an ellipsometer, and some other facilities.
- Participating the study of miniature sensors for material characterization.
- Serving on the CPT Research Committee, which manages and supervises all the ongoing research projects and equipment needs at CPT.
- Co-authoring four research proposals.
- Reviewing proposals for the US Department of State for the Science Centers.
- Mentoring of two undergraduates and three graduate students.
- Developing a course project for the ECE course “Design in Power Engineering”.
- Preparing various types of thin films for CPT students and staff.

11.3 Suggestions for Future Research

This dissertation lays the groundwork for the new areas of research in white light interferometry and in tunable optical filters. Suggestions for future work springing from this research are as follows:

- Investigate techniques to increase the tuning speed of the EFP-TF.
- Investigate the use of other languages, such as Matlab or C, which are faster and have better signal processing functions than Labview, in the EFP-TF control, data acquisition and real-time signal processing.
- Minimize the power consumption by the EFP-TF controller.
- Investigate different EFP-TF bandwidths for applications requiring different source bandwidths.
- Study the signal processing techniques based on TOF-WLI for sensor multiplexing networks.
- Investigate the feasibility of using TOF-WLI for other applications, such as surface profiling, biomedical imaging, and spectroscopy.

Appendix A: Matlab Programs for the Calculation Sensitivity, Fringe Contrast and Dynamic Range

1) Guided F-P: Intensity & Sensitivity

```

n0=1.45;    % Rrefractive index inside the FPI cavity
nc=n0*(1-0.005); % Cladding index of the SMF
w0=1300;    % Central wavelength
W0=5000;    % Mode field radius of a SMF-28
alpha0=1.0; % Coupling efficiency
BW=200;     % Total source spectral width
FWHM=35;    % 3-dB bandwidth of the source
dBW=FWHM/sqrt(8*log(2));
R1=0.30;
R2=0.30;

%C=1.0;     % Round trip coupling efficiency
Angle=0;    % Mirror angular misalignment in degree
An=Angle*pi/180; % Mirror angular misalignment in rad

M=20;      % Maximal cavity length over wavelength (l/w0)
m=M*100+1; % Data points in cavity length
k=BW*100+1; % Data points in wavelength

S=zeros(m,2); % Sensitivity array
I=zeros(m,2); % Intensity array
for i=1:m     % Cavity length

    l=w0*(i-1)/((m-1)/M);

    x=0;
    y=0;
    for j=1:k % Wavelength integration
        dw=1/((k-1)/BW);
        w=w0-BW/2+(j-1)*dw;
        f=(1/(sqrt(2*pi)*dBW))*exp(-(w-w0)^2/(2*dBW^2)); % Source spectrum - Gaussian type

        alpha=4.34*(pi*nc*W0*(2*An)/w)^2;
        C=10^(-alpha/10);

        %Sensitivity calculation
        x1=sqrt(C*R1*R2)*(1-R1)*(1-C*R2)*sin(4*pi*n0*l/w);
    end
end

```

```

x2=w*(1+C*R1*R2-2*sqrt(C*R1*R2)*cos(4*pi*n0*l/w))^2;
x=x+8*pi*n0*alpha0*f*(x1/x2)*dw;

% Intensity calculation
y1=R1+C*R2-2*sqrt(C*R1*R2)*cos(4*pi*n0*l/w);
y2=1+C*R1*R2-2*sqrt(C*R1*R2)*cos(4*pi*n0*l/w);
y=y+alpha0*f*(y1/y2)*dw;

end
S(i,1)=n0*l/w0;
S(i,2)=x*1000;      % Sensitivity. The factor 1000 is to convert the 1/nm to 1/um

I(i,1)=n0*l/w0;
I(i,2)=y;          % Intensity of the FPI output

end

[AX,H1,H2]=plotyy(I(:,1),I(:,2),S(:,1),S(:,2),'plot');
xlabel('F-P Cavity Length (n0*l/w0)')
set(get(AX(1),'Ylabel'),'String','Normalized FPI Intensity (I/I0)')
set(get(AX(2),'Ylabel'),'String','FPI Sensitivity (1/um)')
title('Guided Model')

```

2) Guided F-P: Fringe Contrast

```

w0=1300; % Central wavelength (nm)
BW=200; % Integration limit (nm)
FWHM=60; % Spectrum (Gaussian distribution)
delta=FWHM/sqrt(8*log(2)); % Spectrum width (1/e)
R1=0.4; % Reflectance of the fiber endface
R2=0.4; % Reflectance of the second mirror
n0=1.0; % Medium RI in the cavity
c=1.0; % Round trip coupling efficiency

airgap=zeros(0,31);
peak=zeros(0,31);
valley=zeros(0,31);
y=0;

for i=1:1:31
    airgap(i)=(2*i-1)*w0/4;

    for j=1:1:(10*BW+1)
        d=1/10;

```

```

    x=w0-BW/2+(j-1)*d;
    f=(1/(sqrt(2*pi)*delta))*exp(-(x-w0)^2/(2*delta^2));
    y1=R1+c*R2-2*sqrt(c*R1*R2)*cos(4*pi*n0*airgap(i)/x);
    y2=1+c*R1*R2-2*sqrt(c*R1*R2)*cos(4*pi*n0*airgap(i)/x);
    y=y+f*(y1/y2)*d;
end

    peak(i)=y;
    y=0;
end

y=0;
for i=1:1:31
    airgap(i)=(2*i-2)*w0/4;

    for j=1:1:(10*BW+1)
        d=1/10;
        x=w0-BW/2+(j-1)*d;
        f=(1/(sqrt(2*pi)*delta))*exp(-(x-w0)^2/(2*delta^2));
        y1=R1+c*R2-2*sqrt(c*R1*R2)*cos(4*pi*n0*airgap(i)/x);
        y2=1+c*R1*R2-2*sqrt(c*R1*R2)*cos(4*pi*n0*airgap(i)/x);
        y=y+f*(y1/y2)*d;
    end

    valley(i)=y;
    y=0;
end

contrast=(peak-valley)./(peak+valley);

%plot(airgap/1000,peak,'-r',airgap/1000,valley,'--b',airgap/1000,contrast,'-k')
plot(airgap/1000,contrast,'--k')
xlabel('F-P cavity length (micrometer)')
ylabel('Fringe contrast')
hold on

```

3) Guided F-P: Dynamic Range

```

n=1.45;    % Rrefractive index inside the FPI cavity
nc=n*(1-0.005); %Cladding index of the SMF
w0=1300;   % Central wavelength
W0=5000;   % Mode field radius of a SMF-28
alpha0=1.0; % Coupling efficiency
BW=200;    % Total source spectral width

```

```

FWHM=35;    % 3-dB bandwidth of the source
dBW=FWHM/sqrt(8*log(2));

Angle=6;    % Mirror angular misalignment in degree
An=Angle*pi/180; % Mirror angular misalignment in rad

R1=0.3;
R2=0.3;
K=BW*100+1; % Data points in wavelength
M=2000;    % Calculation points nearby the (Lmax,Smax) points in nm
N=58;     % Peak points

DL=zeros(N,2);
DeltaL=zeros(N,1); % Initialize the Dynamic Range matrix
for i=1:N
    L0=Lmax(i)*w0/n; % Lmax in nm
    S0=Smax(i);

    for j=1:M % Sensitivity calculation
        l=L0+j/10;

        x=0;
        for m=1:K
            dw=1/((K-1)/BW);
            w=w0-BW/2+(m-1)*dw;
            f=(1/(sqrt(2*pi)*dBW))*exp(-(w-w0)^2/(2*dBW^2)); % Source spectrum - Gaussian
type

            alpha=4.34*(pi*nc*W0*(2*An)/w)^2;
            C=10^(-alpha/10); % Round trip coupling efficiency

            %Sensitivity calculation
            x1=sqrt(C*R1*R2)*(1-R1)*(1-C*R2)*sin(4*pi*n*l/w);
            x2=w*(1+C*R1*R2-2*sqrt(C*R1*R2)*cos(4*pi*n*l/w))^2;
            x=x+8*pi*n*alpha0*f*(x1/x2)*dw;

        end
        S=x*1000; % Sensitivity. The factor 1000 is to convert the 1/nm to 1/um
        Error=abs((S-S0)/S0);
        if Error > 0.5
            DeltaL(i,1)=2*j/10; % Dynamic range in nm
            break
        end
    end
end
end
end

```

```
DL(:,1)=Lmax;
DL(:,2)=DeltaL;
```

```
plot(Lmax,DeltaL(:,1))
```

4) Un-guided F-P: Intensity & Sensitivity

```
n=1.0; % Rrefractive index inside the FPI cavity
nc=1.45; %Cladding index of the SMF
w0=1300; % Central wavelength
W0=5000; % Mode field radius of a SMF-28
alpha0=1.0; % Coupling efficiency
BW=200; % Total source spectral width
FWHM=35; % 3-dB bandwidth of the source
dBW=FWHM/sqrt(8*log(2));
```

```
R1=0.3;
dR=0;
R2=R1*(1+dR); % Calculation of R2
Angle=0; % Mirror angular misalignment in degree
An=Angle*pi/180; % Mirror angular misalignment in rad
```

```
M=20; % Maximal cavity length over wavelength (l/w0)
m=M*13000+1; % Data points in cavity length
k=BW*10+1; % Data points in wavelength
```

```
S=zeros(m,2); % Sensitivity array
I=zeros(m,2); % Intensity array
for i=1:m % Cavity length
```

```
l=w0*(i-1)/((m-1)/M);
```

```
x=0;
y=0;
```

```
for j=1:k % Wavelength integration
```

```
dw=1/((k-1)/BW);
```

```
w=w0-BW/2+(j-1)*dw;
```

```
f=(1/(sqrt(2*pi)*dBW))*exp(-(w-w0)^2/(2*dBW^2)); % Source spectrum - Gaussian type
```

```
% Calculate Coupling Efficiency.
```

```
Z=2*I*w/(2*pi*nc*W0^2);
```

```
alpha=-
```

```
10*log10((1+4*Z^2)/((1+2*Z^2)^2+Z^2))+4.34*(I*tan(2*An)/W0)^2+4.34*(pi*nc*W0*(2*An)/w)^2;
```

```

C=10^(-alpha/10);

%Sensitivity calculation
x1=sqrt(C*R1*R2)*(1-R1)*(1-C*R2)*sin(4*pi*n*l/w);
x2=w*(1+C*R1*R2-2*sqrt(C*R1*R2)*cos(4*pi*n*l/w))^2;
x=x+8*pi*n*alpha0*f*(x1/x2)*dw;

%Intensity calculation
y1=R1+C*R2-2*sqrt(C*R1*R2)*cos(4*pi*n*l/w);
y2=1+C*R1*R2-2*sqrt(C*R1*R2)*cos(4*pi*n*l/w);
y=y+alpha0*f*(y1/y2)*dw;

end
S(i,1)=n*l/w0;
S(i,2)=x*1000;      % Sensitivity. The factor 1000 is to convert the 1/nm to 1/um

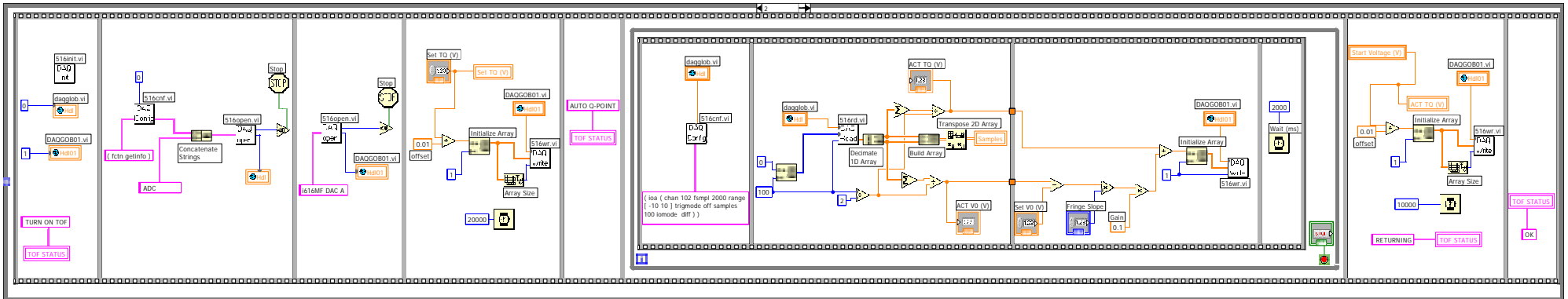
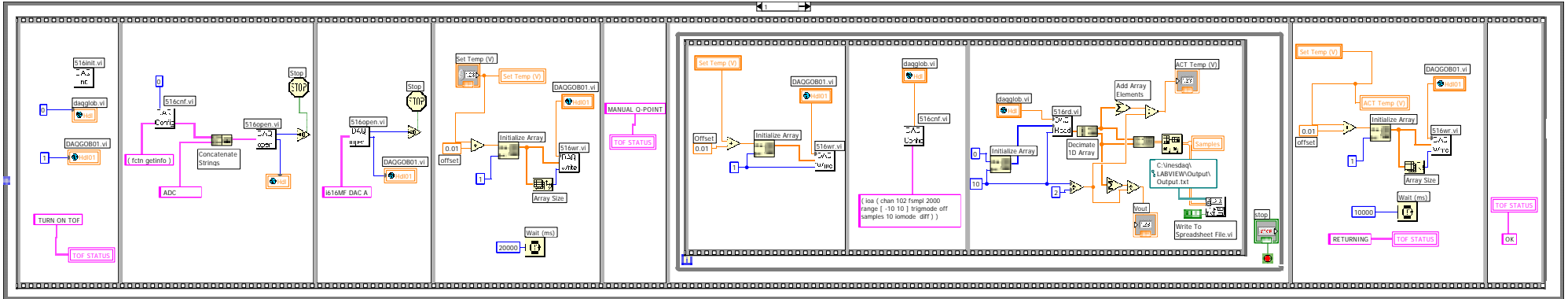
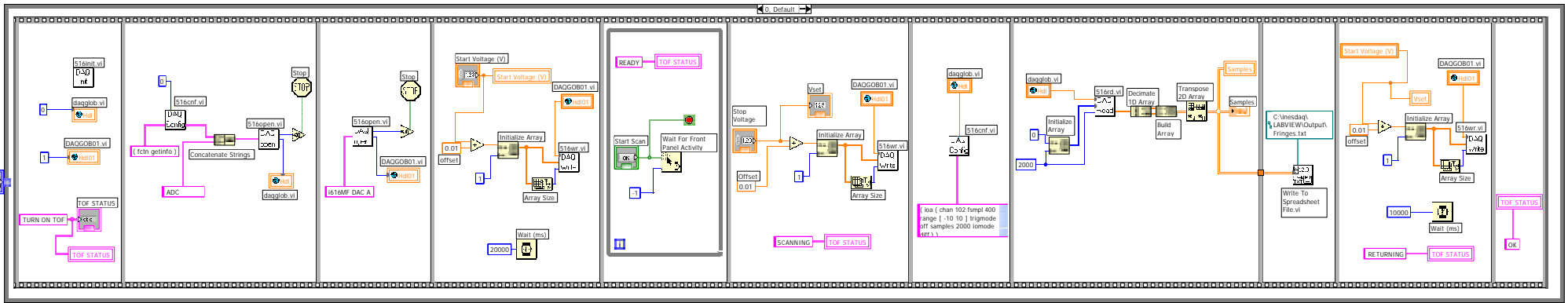
I(i,1)=n*l/w0;
I(i,2)=y;          % Intensity of the FPI output

end

[AX,H1,H2]=plotyy(I(:,1),I(:,2),S(:,1),S(:,2),'plot');
xlabel('F-P Cavity Length (n*l/w0)')
set(get(AX(1),'Ylabel'),'String','Normalized FPI Intensity (I/I0)')
set(get(AX(2),'Ylabel'),'String','FPI Sensitivity (1/um)')
title('UnGuided Model')

```

Appendix B: Labview Programs for EFP-TF Control and Data Acquisition



Appendix B: Labview Programs for EFP-TF Control and Data Acquisition (Continue)

Notes: LabVIEW Function Reference

1. 516init.vi - DAQ init

Application

First operation before use of all DAQ functions. Performs detection of all available cards and sets internal data structures.

Parameters - No parameters required

Return values - Errors

Return value: ERR_INIT_NOCARD, (No card inserted)
means that no supported card was found. This occurs if a wrong or no card is inserted at initialisation time.

Return value: ERR_INIT_REG, (Registry information not available)
The most common reason might be that the installation process was interrupted. In that case, restart the installation.

Return value: ERR_INIT_IOADR, (I/O address out of range or IRQ level out of range)

These messages indicate that something is wrong with the information stored in the registry database.

Return value: ERR_INIT_IRQ, (IRQ level out of range)
These messages indicate that something is wrong with the information stored in the registry database.

Return value: ERR_INIT, (Not initialised error)
The IRQ redirection to the ines VXD driver failed. This may be caused by an interrupt conflict. Review the resources settings of the PCMCIA drive and the PCMCIA card.

2. 516cnf.vi - DAQ config

Application

Sets configuration of data acquisition card.

Parameters - Hdl

Device Handle obtained from DAQopen function.

Cfg

The parameter is a string (type TEXT). The hardware-dependent settings of the card are defined with this string. The goal is: if you install another ines card and if you use the same card features, you may have to change only this string, but no other parts of your LabVIEW-Program.

An easy example is the initialisation string that must be sent prior to any other action:

(fctn init)

An example configuration string:

```
(
  fctn setcfg
  ioa (
    timeout 60000
    chan 1
    fsmpl 44100
    unit v
    range [ -2.5 2.5 ]
    iomode single
    dir input
    coeff [ 0 1.0 ]
    trigmode off
    triglevel 0.0
    pretrigger 0
    samples 1
  )
)
```

The key names

ioa and
iod

control the settings of a specific device. The subkeys (timeout, chan, fsmpl...) identify a property of a device. The parentheses are needed to attach the subkeys to the keys. Braces enclose array values (subkeys 'range' and 'coeff'). New lines, tabs and multiple spaces are not significant in the configuration string. At least a space is required between two items for recognition purposes. If you use a string constant in LabVIEW, a configuration string looks like:

```
( fctn setcfg ioa ( timeout 60000 chan 1 fsmpl 44100 unit v range [ -2.5 2.5 ] iomode single coeff [ 0 1.0 ] trigmode off triglevel 0.0 pretrigger 0 samples 1 ) )
```

This string shows a full configuration of the A/D converter device with all available keys and subkeys. Most of these items are optional. You need only to create a string with your desired

options. The phrase 'fctn setcfg' is not necessary too. 'setcfg' is the default value for 'fctn' if 'fctn' is omitted.

Every item left will be set to default value. Default values are printed underlined in the table.

Return values - Error

Device not initialised

Invalid argument type
occurs if configuration string is not present.

Invalid handle
occurs if the device was not opened correctly and, for that reason, no valid handle was created.

Device not available/undefined
occurs if the card has no such device.

Parameter out of range <parameter's name>In the configuration phase, error messages relate most often to parameters being out of range. Note that some parameter combinations cause errors, e.g. if

iomode diff and
chan 8
was set, then chan is out of range because of the differential input mode.

Timeoutoccurs if the card does not respond to commands in the specified time limit.

CfgRet

The string that was passed in Cfg is returned. This is only of use if a text representation of an error value is generated (with '(fctn geterr)'). Exactly this is performed in DAQ error.

3. 516open.vi - DAQ open

Application

Opens a device for further use. This requires that the device was closed before.

Parameters - Device

Depending on the cards type, following device strings are predefined:

Card types	Device string for opening specified device
A/D converter	FirstD/A converter
SecondD/A converter	Digital I/O port

```

DAQ i108: 'i108 ADC' - - 'i108 DIO'
DAQ i116: 'i116 ADC' - - 'i116 DIO'
DAQ i250: 'i250 ADC' - - 'i250 DIO'
DAQ i508: 'i508 ADC' - - 'i508 DIO'
DAQ i516: 'i516 ADC' - - 'i516 DIO'
DAQ i608: 'i608 ADC' - - 'i608 DIO'
DAQ i616: 'i616 ADC' - - 'i616 DIO'
DAQ i108MF: 'i108MF ADC' 'i108MF DAC A' 'i108MF DAC B' 'i108MF DIO'
DAQ i116MF: 'i116MF ADC' 'i116MF DAC A' 'i116MF DAC B' 'i116MF DIO'
DAQ i250MF: 'i250MF ADC' 'i250MF DAC A' 'i250MF DAC B' 'i250MF DIO'
DAQ i508MF: 'i508MF ADC' 'i508MF DAC A' 'i508MF DAC B' 'i508MF DIO'
DAQ i516MF: 'i516MF ADC' 'i516MF DAC A' 'i516MF DAC B' 'i516MF DIO'
DAQ i608MF: 'i608MF ADC' 'i608MF DAC A' 'i608MF DAC B' 'i608MF DIO'
DAQ i616MF: 'i616MF ADC' 'i616MF DAC A' 'i616MF DAC B' 'i616MF DIO'

```

Device strings are case-insensitive. If multiple cards are used, a card index can be concatenated. The number of the first card is '0', the second card is '1' and so on.

Example:

'i508 ADC 0' refers to the A/D converter of the first card.

'i508MF DAC B 1' refers to the second D/A converter of the second card.

Mode

Integer parameter. The mode defines in which manner the card is written to and read from. Mode 0 sets the 'normal' mode that returns scaled results in double format from the read function. Mode 1 is a binary (raw data) mode that is intended for streaming data to disk with maximum speed. Then the read integer function must be used in order to pass integer arrays (instead of double, as defined above). Post processing is necessary because the data format from converter output is not changed.

Mode is used only for the A/D converter device and is not used while operating the digital I/O or DAC port.

Return values - Error

An error (if negative) or an integer handle (value ≥ 0) is returned. This handle is a necessary argument for all following operations like configuration, reading or writing. Finally the device should be closed. The handle is unique for each card and logical device.

ERR_UNDEF (-1), Undefined function means that the string contents is not equal to any of the predefined device strings and that no device could be opened.

ERR_LOCK (-2), Device in use means that the device was already open.

4. 516rd.vi /516rdi.vi - DAQ read / DAQ readI

DAQ read (for transferring arrays of double): 516rd

DAQ readI (for transferring arrays of INT32): 516rdi

Application

Read results from the device identified by handle.

For detailed information how read works, see `i_read()`.

Parameters - HdI

An integer handle identifies the device to read from.

Value

Value that holds the result. The value type depends on the device (here a DAQ i508 is taken):

i508 ADC eMode=0 : pVal is a pointer to double. An array of double will be initialised with successive readings, with a speed according to the sampling rate.

eMode=1 : pVal is a pointer to an unsigned 32 bit integer (unsigned long), one integer holds 2 readings (16 bit each). The demangle function is used for converting raw data into scaled readings.

i508 DIO eMode= any value A single integer argument is required (pVal is int *). The first 8 bits affect the digital I/O port. For an input port a bit set means TTL level high.

Return values

>0:

The number of elements read is returned.

The real or integer argument is filled with the read values. In case of the A/D converter, either a single real reading or an array of readings is returned.

<=0:

Nothing was read. An error is returned.

Value

The real or integer argument is filled with the read values. In case of the A/D converter device an array of readings is returned. The digital I/O device can return only a single element.

Error & status messages

Error messages:

ERR_RANGE (-3), Parameter out of range

ERR_UNDEF (-1), Undefined function

ERR_TIMEOUT (-2), Timeout

ERR_HANDLE, Invalid handle

ERR_HALT, Card halted during acquisition

ERR_IRQ_OVERRUN, Interrupt overrun

ERR_FIFO_OVERRUN, Shared memory FIFO overrun

Status messages:

ERR_FIFO_EMPTY, Shared memory FIFO empty

ERR_FIFO_FULL, Shared memory FIFO full

ERR_COMPLETE, Acquisition is complete

5. 516wr.vi / 516wri.vi - DAQ write / DAQ writeI

DAQ write (for transferring arrays of double): 516wr

DAQ writeI (for transferring arrays of INT32): 516wri

Application

Write data to device. The VI DAQ writeI is used for writing to the I/O port device (i.e. 'i508 DIO'). DAQ write is used for the MF (multifunction) cards.

Parameters - Hdl

Integer Handle identifies device , i.e. "i508 DIO" (MF cards: "i508MF DAC A" or "i508MF DAC B" also).

Value

Standard cards:

Pointer to integer value that holds data that is sent to port data register Only the first 8 bit (range 0 to 255) affect the port value. For a pin defined output a set bit means TTL level high.

MF (Multifunction) cards, in case of digital I/O port device:

Pointer to integer value that holds data that is sent to port data register Only the first 4 bit (range 0 to 15) affect the port value. For a pin defined output a set bit means TTL level high.

MF (Multifunction) cards, in case of D/A converter device:

Pointer to a single value of type double. The value is directly the voltage in +/-10V range. If the +2.5V output (and U2.5) is used, the voltage to be set U10 must be calculated using:

$$U10 = U2.5 * 8.0 - 10.0$$

Return values

Error

ERR_RANGE (-3), Parameter out of range

ERR_UNDEF (-1), Undefined function

6. 516close.vi - DAQclose

Application

Makes a device available for further use by other processes/programs. Undoes the open operation. The card's state is retained (e.g. configuration of digital I/O-port, port levels, current sources).

Parameters - Hdl

The integer handle of the open device is required.

Return value

Error

ERR_HANDLE (-55), Invalid handle

occurs if the device was not opened correctly and, for that reason, no valid handle was created.

Bibliography

- [1] B. Culshaw, "Optical Fiber Sensor Technology: Opportunities and-Perhaps-Pitfalls," *J. Lightwave Technol.*, vol. **22**, no. **1**, pp.39-50, 2004.
- [2] J. M. López-Higuera, *Handbook of Optical Fibre Sensing Technology*, John Wiley & Sons, LTD, 2002.
- [3] A. D. Kersey, "A Review of Recent Developments in Fiber Optic Sensor Technology," *Optical Fiber Technol.* **2**, pp. 291-317, 1996.
- [4] C. E. Lee, "Review of the present status of optical fiber sensors," *Optical Fiber Technology* **9**, pp. 57-79, 2003.
- [5] C. Delisle and P. Cielo, "Application de la modulation spectrale a la transmission de l'information," *Canadian J. of Physics* **53**, 1047-53, 1975.
- [6] S. A. Al-Chalabi, B. Culshaw and D. E. N. David, "Partially coherent sources in interferometer sensors", *Proc. 1st Int. Conf. on Optical Fibre Sensors*, pp. 132-135, London, 1983.
- [7] T. Bosselmann and R. Ulrich, "High-accuracy position-sensing with fibre-coupled white-light interferometers," *Pro. 2nd Int. Conf. on Optical Fibre Sensors*, pp. 361-364, Berlin: VBE, 1984.
- [8] Y.-J. Rao and D. A. Jackson, "Recent progress in fibre optic low-coherence interferometry," *Meas. Sci. Technol.* **7**, pp. 981-999, 1996.
- [9] M. Born and E. Wolf, *Principle of Optics*, 6th Ed., New York: Pergamon Press, 1986.
- [10] Y.-J. Rao, D.A. Jackson, "Long-distance fibre-optic white light displacement sensing system using a source-synthesizing technique," *Electron. Lett.*, vol. **31**, no. **4**, 1995, pp.310 – 312.
- [11] C. E. Lee and H. F. Taylor, "Fiber-Optic Fabry-Perot Temperature Sensor Using a Low-Coherence Source," *J. Lightwave Technol.*, vol. **9**, no. **1**, pp. 129-134, 1991.
- [12] V. Bhatia, M. B. Sen, K. A. Murphy, R. O. Claus, "Wavelength-tracked white light interferometry for highly sensitive strain and temperature measurements," *Electron. Lett.*, vol. **32**, no. **3**, 1996, pp. 247 – 249.
- [13] P. G. Sinha, T. Yoshino, "Absolute strain demodulation with acoustooptic scanning low-coherence fiber interferometry," *IEEE Photon. Technol. Lett.*, vol. **9**, no. **8**, 1997, pp. 1137 – 39.

- [14] Bock, W.J.; Urbanczyk, W.; Wojcik, J.; Beaulieu, M.; “White-light interferometric fiber-optic pressure sensor,” *IEEE Transactions on Instrumentation and Measurement*, vol. **44**, no. **3**, 1995, pp. 694 – 697.
- [15] Totsu, K.; Haga, Y.; Esashi, M.; “Vacuum sealed ultra miniature fiber-optic pressure sensor using white light interferometry,” *12th International Conference on TRANSDUCERS, Solid-State Sensors, Actuators and Microsystems*, 2003, Vol. 1, 2003, pp. 931 – 934.
- [16] Weir, K.; Boyle, W.J.O.; Palmer, A.W.; Grattan, K.T.V.; Meggitt, B.T.; “Low coherence, interferometric fibre optic vibrometer using novel optical signal processing scheme,” *Electron. Lett.*, Vol. 27, no. 18, 1991, pp. 1658 – 60.
- [17] N. Fürstenau, M. Schmidt, H. Horack, W. Goetze, and W. Schmidt, “Extrinsic Fabry-Perot interferometer vibration and acoustic sensor systems for airport ground traffic monitoring”, *IEE Proc. Optoelectronics*, Vol. 144, No.3, pp. 134-144, 1997.
- [18] B. Yu, D. W. Kim, J. Deng, H. Xiao, and A. Wang, “Fiber Fabry-Perot Sensors for Partial Discharge Detection in Power Transformers”, *Applied Optics*, Vol.42, No. 16, pp. 3241-50, 2003.
- [19] Santos, J.C.; Hidaka, K.; Cortes, A.L.; Da Silva, L.P.C.; “Improved optical sensor for high voltage measurement using white light interferometry,” IMOC 2003. Proceedings of the 2003 SBMO/IEEE MTT-S International Microwave and Optoelectronics Conf., vol. 2, 20-23 Sept. 2003, pp. 615 – 619.
- [20] Fischer, K.W.; “High spectral resolution, low-coherence technique for daytime Doppler wind measurements with lidar,” Geoscience and Remote Sensing Symposium, 1996. IGARSS '96. 'Remote Sensing for a Sustainable Future.' International, Vol. 1, 27-31 May 1996, pp. 694 – 696.
- [21] Imai, Y.; Tanaka, K.; “Vector velocimetry by using fiber-optic low coherence interferometers,” 15th Optical Fiber Sensors Conf. Tech. Digest, 2002. OFS 2002, vol.1, pp. 387 – 390, 6-10 May 2002.
- [22] McMurtry, S.; Wright, J.D.; Jackson, D.A.; Keddie, J.L.; “Humidity sensing using PMMA-PMTGA-PMMA polymer in low coherence interferometric system,” *Electron. Lett.*, vol. 36, no. 1, 2000, pp. 73 – 74.
- [23] Rao, Y.-J.; Jackson, D.A.; “Universal fiber-optic point sensor system for quasi-static absolute measurements of multiparameters exploiting low coherence interrogation,” *J. Lightwave Technol.*, Vol. 14, no. 4, 1996, pp. 592 – 600.
- [24] H. C. Lefevre, “White light interferometry in optical fibre sensors,” *Proc. 7th Int. Conf. on Optical Fibre Sensors*, pp. 345 – 51, 1990.
- [25] K. T. Grattan and B. T. Meggitt, *Optical Fiber Sensor Technology*, London: Chapman & Hall, pp. 269-310, 1995.

- [26] S. Capone, A. Forleo, L. Francioso, R. Rella, P. Siciliano, J. Spadavecchia, DS Presicce, AM Taurino, "Solid State Gas Sensors: State of the Art and Future Activities," *J. of Optoelectronics and Advanced Materials*, vol. 5, No. 5, 2003, p. 1335 – 48.
- [27] Podoleanu, A.G.; Dobre, G.M.; Webb, D.J.; Jackson, D.A.; "Fiberized setup for en-face imaging of the retina with use of low coherence interferometry," *Lasers and Electro-Optics, 1997. CLEO '97.*, Summaries of Papers Presented at the Conference on, Vol. 11, May 18-23, 1997, pp. 168 – 168.
- [28] Ohmi, M.; Ohnishi, Y.; Yoden, K.; Haruna, M.; "In vitro simultaneous measurement of refractive index and thickness of biological tissue by the low coherence interferometry", *IEEE Transactions on Biomedical Engineering*, vol. 47, no. 9, Sept. 2000, pp.1266 – 70.
- [29] Schmitt, J.M.; "Optical coherence tomography (OCT): a review," *IEEE Journal of Selected Topics in Quantum Electronics*, vol. 5, no. 4, 1999, pp. 1205 – 1215.
- [30] Rao, Y.J.; Henderson, P.J.; Jackson, D.A.; Zhang, L.; Bennion, I.; "Simultaneous strain, temperature and vibration measurement using a multiplexed in-fibre-Bragg-grating/fibre-Fabry-Perot sensor system," *Electron. Lett.*, Vol. 33, no. 24, 1997, pp. 2063 – 64.
- [31] L. Yuan; W. Jin; L. Zhou; Hoo, Y.L.; Demokan, M.S.; "Enhancement of multiplexing capability of low-coherence interferometric fiber sensor array by use of a loop topology," *J. Lightwave Technol.*, Vol. 21, no. 5, May 2003, pp. 1313 – 1319
- [32] Volanthen, M.; Geiger, H.; Dakin, J.P.; "Distributed grating sensors using low-coherence reflectometry," *J. Lightwave Technol.*, Vol. 15, no. 11, 1997, pp. 2076 – 2082.
- [33] Engin, D.; "Complex Optical Low Coherence Reflectometry (OLCR) With Tunable Source," *IEEE Photon. Technol. Lett.*, Vol. 16, no. 5, May 2004, pp.1346 – 48.
- [34] K. P. Chan; Umetsu, E.; Tanno, N.; "Real-time optical coherence-domain reflectometry with an angular dispersion imaging scheme," *Lasers and Electro-Optics Europe, 2000. Conference Digest. 2000 Conference on*, 10-15 Sept 2000, Pages:1 pp.
- [35] Dyer, S.D.; Espejo, R.J.; "Fast and accurate characterization of optical components using low-coherence interferometry," *Lasers and Electro-Optics, 2001. CLEO/Pacific Rim 2001. The 4th Pacific Rim Conference on*, Vol. 1, 15-19 July 2001, pp. I-478 - I-479.
- [36] Imran, T.; Kyung-Han Hong; Tae Jun Yu; Chang Hee Nam; "Measurement of the group-delay dispersion of optical elements using white-light interferometry," *CLEO/Pacific Rim 2003 - The 5th Pacific Rim Conference on Lasers and Electro-Optics*, Vol. 1, Dec. 15-19, 2003, pp. 264 – 264.
- [37] Salzenstein, F.; Montgomery, P.; Renatpazane, A.; Boudraa, A.; "2D discrete high order energy operators for surface profiling using white light interferometry," *Proc. 7th Int. Symposium on Signal Processing and Its Applications*, vol. 1, July 1-4, 2003, pp. 601 – 604.

- [38] D. A. Jackson, "Recent progress in monomode fibre-optic sensors", *Meas. Sci. Technol.* **5**, 621-638, 1994.
- [39] A. Wang, H. Xiao, J. Wang, Z. Wang, W. Zhao, and R. G. May, "Self-Calibrated Interferometric-Intensity-Based Optical Fiber Sensors," *J. Lightwave Technol.*, vol. **19**, no. **10**, pp. 1495-1501, 2001.
- [40] P. Gysel and R. K. Staubli, "Statistical properties of Raleigh backscattering in single-mode fibers", *J. Lightwave Technol.*, vol. **8**, no. **4**, pp. 561-567, 1990.
- [41] Koch and R. Ulrich, "Fiber-optic displacement sensor with 0.02 μm resolution by white-light interferometry," vol. 25, no. 1-3, pp. 201-207, 1990.
- [42] S. Chen, B. T. Meggitt, A. J. Roggers, "Electronically-scanned white light interferometry with enhanced dynamic range," *Electronics Letters*, vol. 26, no. 20, 1990, pp. 1663 – 65.
- [43] L. Deck, P. D. Groot, "High-speed noncontact profiler based on scanning white-light interferometry," *Appl. Opt.* **33**, 7334 (1994).
- [44] S. A. Egorov, A. N. Mamaev, A. S. Polyantsev, "Spectrum signal processing in intrinsic interferometric sensors based on birefringent polarization-maintaining optical fibers," *J. Lightwave Technol.*, vol. 13, no. 7, pp. 1231-36, 1995.
- [45] T. G. Giallorenzi, J. A. Bucaro, A. Drandidge, G. H. Sigel, JR., J. H. Cole, S. C. Rashleigh, and R. G. Priest, "Optical Fiber Sensor Technology," *IEEE J. of Quantum Electron.*, vol. QE-18, no. 4, pp. 626-665, 1982.
- [46] K. Murphy, M. F. Gunther, A. M. Vengsakar, and R. O. Claus, "Quadrature phase-shifted, extrinsic Fabry-Perot optical fiber sensors," *Optics Letters*, vol. 16, No. 4, pp. 273-275, Feb. 1991.
- [47] J. F. Dorigi, S. Krishnaswamy, and J. Achenbach, "Stabilization of an embedded fiber optic Fabry-Perot sensor for ultrasound detection," *IEEE Trans. on Ultrasonics, Ferroelectrics, and Frequency Control*, vol. **42**, 820 (1995).
- [48] C. E. Lee, W. N. Gibler, R. A. Atkins, and H. F. Taylor, "In-line fiber Fabry-Perot Interferometer with high-reflectivity internal mirrors", *J. Lightwave Technol.*, vol. **10**, no. **10**, 1376-79, 1992.
- [49] K. A. Murphy, M. F. Gunther, A. Wang, R. O. Claus, A. M. Vengsarkar, "Extrinsic Fabry-Perot Optical Fiber Sensor," *8th Optical Fiber Sensors Conference*, Jan. 29-31, 1992, pp. 193 – 196.
- [50] M. A. Chan, S. D. Collins and R. L. Smith, "A micromachined pressure sensor with fiber-optic interferometric readout," *Sensors and Actuators A*, **43**, pp. 196-201, 1994.
- [51] D. A. Krohn, *Fiber Optic Sensors: Fundamentals and Applications*, 2nd Edition, Instrument Society of America, 1992, pp. 49-65.

- [52] J. L. Santos and D. A. Jackson, "Optical fiber sensing with a low-finesse Fabry-Perot cavity", *Appl. Opt.*, vol. **31**, no. **34**, 7361-66, 1992.
- [53] Dandridge, A. B. Tveten, and T. G. Giallorenzi, "Homodyne demodulation scheme for fiber optic sensors using phase generated carrier," *Quantum Electron.*, vol. **QE-18**, no. **10**, pp. 1647-53, 1982.
- [54] B. Yu, A. Wang, and G. Pickrell, "Analysis of Fiber Fabry-Perot Interferometric Sensors Using Low-Coherence Light Sources", submitted to *J. Lightwave Technol.*, March 2004.
- [55] Smartec product information, "SOFO Fiber Optic Monitoring System," from www.smartec.ch/index.html.
- [56] R. H. Marshall, Y. N. Ning, X. Jiang, A. W. Palmer, B. T. Meggitt, and K. T. V. Grattan, "A novel electronically scanned white-light interferometer using a Mach-Zehnder approach," *J. Lightwave Technol.*, vol. **14**, no. **3**, 397-402, 1996.
- [57] C. Belleville, G. Duplain, "White-light interferometric multimode fiber-optic strain sensor," *Opt. Lett.*, **18**(1), pp. 78-80, 1993.
- [58] Y. J. Rao and A. D. Jackson, "Improved synthesized source for white light interferometry," *Electron. Lett.*, vol. **30**, no. **17**, 1440-41, 1994.
- [59] D. N. Wang, Y. N. Ning, K. T. V. Grattan, A. W. Palmer, and K. Weir, "Three-wavelength combination source for white-light interferometry," *IEEE Photon. Technol. Lett.*, vol. **5**, no. **11**, 1350-52, 1993.
- [60] S. Chen, A. W. Palmer, K. T. V. Grattan and B. T. Meggitt, "Fringe order identification in optical fibre white-light interferometry using centroid algorithm method," *Electron. Lett.*, vol. **28**, no. **6**, pp. 553-555, 1992.
- [61] M. S. Rizk, D. Romare, K. T. V. Grattan, and A. W. Palmer, "Adaptive filtering of white-light interferometry fringe patterns," *IEEE Trans. On Instrumentation and Measurement*, vol. **47**, no. **3**, pp. 782-788, 1998.
- [62] D. N. Wang, Y. N. Ning, A. W. Palmer, K. T. V. Grattan and K. Weir, "Scanning in a white light interferometer using a tunable laser," 10th Optical Fiber Sensors Conference, 592-595, Jan. 1994.
- [63] S.H. Yun, G. J. Tearney, B.E. Bouma, B.H. Park, and J.F. de Boer, "High-speed spectral-domain optical coherence tomography at 1.3 μ m wavelength," *Opt. Express* **11**, 3598 (2003).
- [64] A. F. Fercher, C. K. Hitzenberger, G. Kamp, and S. Y. El-Zaiat, "Measurements of intraocular distances by backscattering spectral interferometry," *Opt. Comm.* **117**, 43-48, 1995.
- [65] G. Hausler and M. W. Lindner, "Coherence radar and spectral radar – new tools for dermatological diagnosis," *J. Biomed. Opt.* **3**, 21-31, 1998.

- [66] T. Liu, M. Wu, Y. Rao, D. A. Jackson, and G. F. Fernando, "A multiplexed optical fibre-based extrinsic Fabry-Perot sensor system for *in-situ* strain monitoring in composites," *Smart Mater. Struct.* **7**, pp. 550-556, 1998.
- [67] K. BlØtekjaer, "Theoretical concepts of a novel Vernier-based fringe-counting fibre optic sensor," *IEE Proc. Optoelectron.* vol. **144**, no. **3**, pp. 126-129, June 1997.
- [68] M. G. Xu, H. Geiger, and J. P. Dakin, "Interrogation of fibre-optic interferometric sensors using acousto-optic tunable filter," *Electron. Lett.*, vol. **31**, no. **17**, pp. 1487-88, 1995.
- [69] H. Xiao, J. D. Deng, G. Pickrell, R. G. May and A. Wang, "Single-crystal sapphire fiber-based strain sensor for high-temperature applications," *J. Lightwave Technol.*, vol. **21**, no. **10**, pp. 2276-83, 2003.
- [70] S. A. Egorov, Y. A. Ershov, I. G. Likhachiev, A. N. Mamaev, "Spectrally encoded fiber-optic sensors based on Fabry-Perot interferometer," *SPIE Proc.*, vol. **1972**, pp. 362-369, 1993.
- [71] S. A. Egorov, A. N. Mamaev, I. G. Likhachiev, Y. A. Ershov, A. S. Voloshin, and E. Nir, "Advanced signal processing method for interferometric fiber-optic sensors with straightforward spectral detection," *SPIE Proc.*, vol. **3201**, pp. 44-48, 1997.
- [72] J. Tapia-Mercado, A. V. Khomenko, and A. Garcia-Weidner, "Precision and sensitivity optimization for white-light interferometric fiber-optic sensors," *J. Lightwave Technol.*, vol. **19**, no. **1**, pp. 70-74, 2001.
- [73] New Focus publications, "How Can a Tunable Laser Help You with Your Application?" http://www.newfocus.com/Online_Catalog/literature/LaserEvangelical_3.0.pdf.
- [74] Mark Wippich and Kathy Li Dessau, "Tunable lasers and fiber-Bragg-grating sensors," *The Industrial Physicist* by American Institute of Physics, June/July 2003, pp. 24-27.
- [75] Intune Technologies product datasheet, AltoWave5500™ Sensor Interrogator, <http://www.intune-technologies.com/pdf/altow5500ps.pdf>.
- [76] Blue Road Research product datasheet, "Fiber Optic Sensor Readout Systems & Components," <http://www.bluerr.com/pdf/catalog.pdf>.
- [77] Micron Optics product data sheet, "Optical sensing analyzer si720", <http://www.micronoptics.com/pdfs/si720.pdf>.
- [78] P. C. Beard and T. N. Mills, "Miniature optical fibre ultrasonic hydrophone using a Fabry-Perot polymer film interferometer," *Electron. Lett.*, vol. **33**, no. **9**, pp. 801-803, 1997.
- [79] F. Lexer, C. K. Hitzenberger, A. F. Fercher, and M. Kulhavy, "Wavelength-tuning interferometry of intraocular distances," *Applied Optics*, vol. **36**, no. **25**, 6548-53, 1997.

- [80] L. L. Deck, "Fourier-transform phase-shifting interferometry," *Appl. Opt.* **42**, no. 13, 2354-65, 2003.
- [81] S. R. Chinn, E. Swanson, J. G. Fujimoto, "Optical coherence tomography using a frequency-tunable optical source," *Opt. Lett.* **22**, 340-342 (1997).
- [82] S.H. Yun, G. J. Tearney, J.F. de Boer, N. Iftimia and B.E. Bouma, "High-speed optical frequency-domain imaging," *Opt. Express* **11**, no. 22, 2953-63 (2003).
- [83] H. Alause, J. P. Malzac, F. Grasdepot, V. Nouaze, J. Hermann, W. Knap, "Micromachined optical tunable filter for long term stability gas sensors," *IEE Proc.-Optoelectron.*, vol. **144**, no. **5**, 350-354, Oct. 1997.
- [84] C. Boulet, D. J. Webb, M. Douay, and P. Niay, "Simultaneous interrogation of fiber Bragg grating sensors using an acousto-optic tunable filter," *IEEE Photon. Technol. Lett.*, vol. **13**, no. **11**, 1215-17, 2001.
- [85] H. Geiger, M. G. Xu, N. C. Eaton and J. P. Dakin, "Electronic tracking system for multiplexed fibre grating sensors," *Electron. Lett.*, vol. **31**, no. **12**, pp. 1006-07, 1995.
- [86] G. Lammel, S. Schweizer, S. Schiesser, and P. Renaud, "Tunable optical filter of porous silicon as key component for a MEMS spectrometer," *J. Microelectromechanical Systems*, vol. **11**, no. **6**, 815-827, 2002.
- [87] T. Yoshino, K. Kurosawa, K. Itoh, and T. Ose, "Fiber-Optic Fabry-Perot Interferometer and Its Sensor Application," *IEEE Trans. on Microwave Theory and Techniques*, vol. **MTT-30**, no. **10**, pp. 1612-1620, Oct. 1982.
- [88] K. D. Oh, J. Ranade, V. Arya, A. Wang, and R. Claus, "Optical fiber Fabry-Perot interferometric sensor for magnetic field measurement," *IEEE Photon. Technol. Lett.*, vol. **9**, no. **6**, pp. 797-799, 1997.
- [89] W. Pulliam, P. Russler, R. Mlcak, K. Murphy, C. Kozikowski, "Micromachined, SiC fiber optic pressure sensors for high temperature aerospace applications," *SPIE Proc.: Industrial Sensing Systems*, SPIE vol. **4202**, pp. 21-30, 2000.
- [90] E. L. Green and P. G. Cable, "Passive Demodulation of Optical Interferometric Sensors," *IEEE Trans. On Microwave Theory and Techniques*, vol. **MTT-30**, no. **10**, pp. 1627-32, Oct. 1982.
- [91] S. Gerges, F. Farahi, T. P. Newson, J. D. C. Jones, D. A. Jackson, "Fibre-optic interferometric sensor utilising low coherence length sources: Resolution enhancement," *Electron. Lett.*, vol. **24**, no. **8**, 472-474, 1988.
- [92] Y.-L. Lo and C.-H. Chuang, "New synthetic-heterodyne demodulator for an optical fiber interferometer," *IEEE J. of Quantum Electron.*, vol. **37**, no. **5**, pp. 658-663, 2001.

- [93] D. W. Stowe and T.-Y. Hsu, "Demodulation of interferometric sensors using a fiber-optic passive quadrature demodulator," *J. Lightwave Technol.*, vol. **LT-1**, no. **3**, pp. 519-523, 1983.
- [94] A. Ezbiri and R. P. Tatam, "Passive signal processing for a miniature Fabry-Perot interferometric sensor with a multimode laser-diode source," *Opt. Lett.* **20**, no. 17, pp. 1818-20, 1995.
- [95] M. Schmidt and N. Fürstenau, "Fiber-optic extrinsic Fabry-Perot interferometer sensors with three-wavelength digital phase demodulation," *Opt. Lett.*, vol. **24**, no. **9**, pp. 599-601, May 1999.
- [96] Murphy, K.A.; Miller, M.S.; Vengsarkar, A.M.; Claus, R.O.; "Elliptical-core two mode optical-fiber sensor implementation methods," *J. Lightwave Technology*, vol. **8**, no. **11**, 1990, pp. 1688 – 1696.
- [97] V. Arya, M. D. Vries, K. A. Murphy, A. Wang, and R. O. Claus, "Exact Analysis of the Extrinsic Fabry-Perot Interferometric Optical Fiber Sensor Using Kirchhoff's Diffraction Formalism," *Optical Fiber Technology* **1**, 380-384, 1995.
- [98] M. N. Inci, S. R. Kidd, J. S. Barton, and J. D. C. Jones, "Fabrication of single-mode fibre optic Fabry-Perot interferometers using fusion spliced titanium dioxide optical coatings," *Meas. Sci. Technol.* **3**, 678-684, 1992.
- [99] J. Sirkis et al., "In-line fiber etalon (ILFE) fiber optic strain sensors," *J. Lightwave Technol.*, vol. **13**, no. **7**, pp. 1256-63, 1995.
- [100] R. A. Wolthuis, G. L. Mitchell, E. Saaski, J. C. Hartl, and M. A. Afromowitz, "Development of Medical Pressure and Temperature Sensors Employing Optical Spectrum Modulation," *IEEE Trans. on Biomedical Engineering*, vol. 38, No. 10, pp.974-981, Oct. 1991.
- [101] P. C. Beard and T. N. Mills, "Extrinsic optical-fiber ultrasound sensor using a thin polymer film as a low-finesse Fabry-Perot interferometer," *Appl. Opt.*, vol. **35**, no.4, pp. 663-675, 1996.
- [102] Dietrich Marcuse and J. Stone, "Coupling Efficiency of Front Surface and Multilayer Mirrors as Fiber-End Reflectors", *J. Lightwave Technol.*, vol. **LT-4**, no.4, pp. 377-381, 1986.
- [103] D. A. Smith, "Tunable Optical Filters for Lightwave Networks," LEOS 1992 Summer Topical Meeting Digest on Broadband Analog and Digital Optoelectronics, Optical Multiple Access Networks, Integrated Optoelectronics, Smart Pixels, 29 July-12 Aug. 1992, Pages:A19 - A20.
- [104] D. Sadot and E. Boimovich, "Tunable Optical Filters for Dense WDM Networks," *IEEE Communication Magazine*, Dec. 1998, 50-55.
- [105] D. A. M. Khalil, "Advances in Optical Filters," Second Workshop on Teaching Photonics at Egyptian Engineering Faculties and Institutes, 2000, 24 Oct. 2000, pp. 1 – 27.

- [106] D. W. Faulkner, D. M. Russ, J. C. Regnault, and A. Lord, "Optical samplers for gigabit cable TV receiver," *Electronics Letters*, vol. 24, no. 23, 1430-31, 1988.
- [107] H. Kobrinski and Kwok-Wai Cheung, "Wavelength-Tunable Optical Filters: Applications and Technologies," *IEEE Communications Magazine*, Oct. 1989, 53-63.
- [108] T. H. Chao, J. Yu, G. Reyes, D. Rider, and L. J. Cheng, "Acousto-optic tunable filter imaging spectrometer," *IEEE*, 585-588, 1991.
- [109] T. H. Chao, J. Yu, G. Reyes, D. Rider, and L. J. Cheng, "Acousto-optic tunable filter imaging spectrometer," *Geoscience and Remote Sensing Symposium, 1991. IGARSS '91. 'Remote Sensing: Global Monitoring for Earth Management'.*, International, vol. 2, June 3-6, 1991, pp. 585 - 588.
- [110] N. Mortensen, S. A. Dyer, R. M. Hammaker, and W. G. Fateley, "A Hadamard-Multiplexed spectrometer based on an acousto-optic tunable filter," *IEEE Trans. On Instrumentation and Measurement*, vol. 45, no. 2, 394-398, 1996.
- [111] H. A. Macleod, "Thin-Film Optical Filters," 2nd Edition, McGraw-Hill Publishing Company, 1989, New York.
- [112] B.E.A. Saleh and M.C. Teich, "Fundamentals of Photonics", Wiley Series, 1991.
- [113] J. Stone and L. W. Stulz, "Pigtailed high-finesse tunable fibre Fabry-Perot interferometers with large, medium and small free spectral ranges," *Electronics Letters*, vol. 23, no. 15, 781-782, Jul. 1987.
- [114] M. Miller and F. J. Janniello, "Fiber Fabry-Perot filter with passive temperature compensation and its application in a wavelength-division multiple-access computer network," *OFC91 Technical Digest*, **45**.
- [115] E. C. Vail, M. S. Wu, G. S. Li, L. Eng and C. J. Chang-Hasnain, "GaAs micromachined widely tunable Fabry-Perot filters," *Electron. Lett.*, vol. **31**, no. **3**, pp. 228-229, 1995.
- [116] T. T. D. Tran, Y. H. Lo, Z. H. Zhu, D. Haronian, and E. Mozdy, "Surface micromachined Fabry-Perot tunable filter," *IEEE Photon. Technol. Lett.*, vol. 8, no. 3, pp. 393-395, 1996.
- [117] P. Tayebati, P. Wang, D. Vakhshoori, and R. N. Sacks, "Microelectromechanical tunable filters with 0.47nm linewidth and 70nm tuning range," *Electron. Lett.*, vol. 34, no. 1, 76-78, 1998.
- [118] T. Amano, F. Koyama, T. Hino, M. Arai, and A. Mastutani, "Design and Fabrication of GaAs-GaAlAs Micromachined Tunable Filter with Thermal Strain Control," *J. Lightwave Technology*, vol. **21**, no. **3**, pp. 596-601, 2003.
- [119] Y. C. Chung, "Temperature-tuned ZnS etalon filters for WDM systems," *IEEE Photonics Technology Letters*, vol. 4, no. 6, 600-602, Jun. 1992.

- [120] M. Ogusu, Y. Shimomura, and S. Ohshima, "A Thermally Stable Fabry-Perot Tunable Filter for 1 Å-Spaced High-Density WDM Systems," *IEEE Photonics Technology Letters*, vol. 5, no. 10, Oct. 1993, 1222-24.
- [121] Y. Suemura, A. Tajima, N. Henmi, H. Morimura, and H. Takahashi, "An Adaptive Wavelength Tunable Optical Filter Employing an Angle-Tuned Interference Filter and an Intelligent Digital Controller," *J. Lightwave Technol.*, vol. 14, no. 6, 1048-55, June 1996.
- [122] Sneh, K. M. Johnson, and J.-Y. Liu, "High-speed wavelength tunable liquid crystal filter," *IEEE Photon. Technol. Lett.*, vol. 7, no. 4, pp. 379-381, 1995.
- [123] K. Hirabayashi, H. Tsuda, and T. Kurokawa, "Tunable wavelength selective liquid crystal filters for 600 channel FDM systems," *IEEE Photon. Technol. Lett.*, vol. 4, no. 6, pp. 597-599, 1992.
- [124] D. Hohlfield and H. Zappe, "A silicon-based tunable optical filter designed for low power consumption and fast thermal modulation," *Optical MEMS 2002. Conference Digest. 2002 IEEE/LEOS International Conference on, 20-23 Aug. 2002*, pp. 171 – 172.
- [125] K. Hsu, and R. Cormack, "Tunable optical filters for dynamic networks," *Proceedings of 53rd Electronic Component and Technology Conference*, pp. 776 – 781, May 27-30, 2003.
- [126] <http://www.physikinstrumente.com/tutorial/>, "Theory and Applications of Piezo Actuators and PZT NanoPositioning Systems," Provided by Physik Instrument (PI), GmbH & Co. KG.
- [127] K. Hirabayashi, H. Tsuda, and T. Kurokawa, "Tunable liquid-crystal Fabry-Perot interferometer filter for wavelength-division multiplexing communication systems," *J. Lightwave Technol.*, vol. 11, no. 12, pp. 2033-43, 1993.
- [128] S. Matsumoto, K. Hirabayashi, S. Sakata, and T. Hayashi, "Tunable wavelength filter using nano-sized droplets of liquid crystal," *IEEE Photon. Technol. Lett.*, vol. 11, no.4, pp. 442-444, 1999.
- [129] F. Sugihwo, M. C. Larson, J. S. Harris, "Micromachined widely tunable vertical cavity laser diodes," *J. of Microelectromechanical Systems*, vol. 7, no. 1, pp. 48 – 55, March 1998.
- [130] R. S. Tucker, D. M. Baney, W. V. Sorin, C. A. Flory, "Thermal noise and radiation pressure in MEMS Fabry-Perot tunable filters and lasers," *IEEE J. Selected Topics in Quantum Electronics*, vol. 8, no. 1, pp. 88-97, 2002.
- [131] Santec product data sheet, "Optical Tunable Filters OTF-610," from www.santec.com.
- [132] L. Domash, M. Wu, N. Nemchuk, and E. Ma, "Tunable and switchable multiple-cavity thin film filters," *J. Lightwave Technol.*, vol. 22, no. 1, pp. 126-135, 2004.
- [133] A. Yariv, "Coupled-mode theory for guided-wave optics," *IEEE J. Quantum Electron.*, QE-9(9), pp. 919, Sept. 1973.

- [134] H. Nishihara, M. Haruna, and T. Suhara, *Optical Integrated Circuits*, McGraw-Hill Book Company, New York, 1985, pp. 46-61.
- [135] D. A. Smith, Zhuoyu Bao, "Technology and applications of the integrated acousto-optic filter," Electrotechnical Conference, 1996. MELECON '96., 8th Mediterranean , vol. 1, 100 – 107, 13-16 May 1996.
- [136] E. Tony and S. K. Chaudhuri, "Acousto-optic filters," *IEEE Potentials*, October/November 1994, pp. 19-22.
- [137] Bing Yu and Anbo Wang, "Grating-assisted demodulation of interferometric optical sensors," *Applied Optics*, vol. 42, no. 34, 2003, 6824-29.
- [138] Jill D. Berger and Doug Anthon, "Tunable MEMS Devices for Optical Networks," *Optics & Photonics News*, March 2003, pp. 42-49.
- [139] Iocco, H. G. Limberger, R. P. Salathe, "Bragg grating fast tunable filter," *Electronics Letters*, vol. 33, no. 25, pp. 2147 – 2148, 1997.
- [140] N. H. Ky; Limberger, H.G.; Costantini, D.M.; Salathe, R.P.; Muller, C.A.P.; Fox, G.R.; "High performance wavelength-tunable filter based on in-fiber Bragg grating and electrically resistive coating," *CLEO '97, Summaries of Papers Presented at the Conference on*, vol. 11, pp. 310 – 310, May 18-23, 1997.
- [141] M. Vengsakar, P. J. Lemaire, J. B. Judkins, V. Bhatia, T. Erdogan, and J. E. Sipe, "Long-Period Fiber Gratings as Band-Rejection Filters," *J. Lightwave Technol.*, vol. 14, no. 1, 58-65, 1996.
- [142] A. Abramov, B. J. Eggleton, J. A. Rogers, R. P. Espindola, A. Hale, R. S. Windeler, and T. A. Strasser, "Electrically Tunable Efficient Broad-Band Fiber Filter," *IEEE Photonics Technol. Lett.*, vol. 11, no. 4, 445-447, Apr. 1999.
- [143] X. Shu, T. Allsop, B. Gwandu, L. Zhang, I. Bennion, "Thermally tunable optical fiber loss filter with wide tuning range," *CLEO 2001*, CTuF4, 126-127, 2001.
- [144] E. L. Wooten, R. L. Stone, E. W. Miles, and E. M. Bradley, "Rapidly tunable narrowband wavelength filter using LiNbO₃ unbalanced Mach-Zehnder interferometers," *J. Lightwave Technol.*, vol. 14, no. 11, pp. 2530-36, 1996.
- [145] D. Rafizadeh, J. P. Zhang, S. C. Hagness, A. Taflove, K. A. Stair, and S. T. Ho, "Temperature tuning of microcavity ring and disk resonators at 1.5- μm ," *Lasers and Electro-Optics Society Annual Meeting, 1997. LEOS '97 10th Annual Meeting. Conference Proceedings, IEEE* , vol. 2 , 10-13 Nov. 1997, pp. 162 - 163.
- [146] S. Toyoda, N. Ooba, A. Kaneko, T. Kitoh, M. Hikita, T. Kurihara, T. Maruno, "Wide-band thermo-optic wavelength tunable filter using polymer arrayed-waveguide grating phase-shifter," *Lasers and Electro-Optics Society 2000 Annual Meeting. LEOS 2000. 13th Annual Meeting. IEEE*, Vol. 2, 13-16 Nov. 2000, pp. 834 - 835 vol.2.

- [147] Yasha Yi, Peter Bermel, Kazumi Wada, Xiaoman Duan, J. D. Joannopoulos, and L. C. Kimerling, "Tunable multichannel optical filter based on silicon photonic band gap materials actuation," *Appl. Phys. Lett.* **81**(22), pp. 4112-14, 25 Nov. 2002.
- [148] T. T. Larsen and A. Bjarklev, "Optical devices based on liquid crystal Photonics bandgap fibres," *Optics Express*, vol.11, no. 20, pp. 2589-96, Oct. 2003.
- [149] S. Rajic, J. L. Corbeil, and P. G. Datskos, "Feasibility of tunable MEMS photonic crystal devices," *Ultramicroscopy* 97, pp. 473-479, 2003.
- [150] E. G. Loewen and E. Popov, *Diffraction Gratings and Applications*, MerceL Dekker, New York, 1997.
- [151] Christopher Palmer, *Diffraction Grating Handbook*, 5th Edition, Richardson Grating Laboratory, New York, 2002.
- [152] Raisi, M.; Ahderom, S.; Alameh, K.E.; Eshraghian, K.; "Opto-VLSI multiband tunable optical filter," *Electron. Lett.*, vol. 39, no. 21, 2003, pp. 1533-35.
- [153] Griffiths, D.C.; Preston, K.R.; "Space and wavelength filter for use in WDM-based optical switching networks," *Electron. Lett.*, vol. 28, no. 18, 1992, pp. 1729-30.
- [154] Y. Tachikawa, S. Nagakao, and Y. Suzuki, "Compact fiber Bragg grating tunable filter: Microheater loading type," *Lasers and Electro-Optics, 1997. CLEO/Pacific Rim '97*, Pacific Rim Conference on, 14-18 July 1997, pp. 72 - 73.
- [155] S. Toyoda, N. Ooba, A. Kancko, M. Iikita, T. Kurihara and T. Maruno, "Wideband polymer thermo-optic wavelength tunable filter with fast response for WDM systems," *Electron. Lett.*, vol. 36, no. 7, pp. 658-660, 2000.
- [156] K. A. Murphy, M. F. Gunther, A. Wang, and R. O. Claus, "Detection of acoustic emission using optical fiber sensors," *Proc. of SPIE*, vol. 2191, pp. 282-291, 1994.
- [157] J. Stone, L. W. Stulz, D. Marcuse, C. A. Burrus, and J. C. Centanni, "Narrow-Band FiEnd Etalon Filters Using Expanded-Core Fibers," *J. Lightwave Technol.*, vol. 10, no. 12, 1851-54, 1992.
- [158] Rao R. Tummala, *Fundamentals of Microsystems Packaging*, McGraw-Hill, pp. 212-263, 2001.
- [159] Degamber, B.; Fernando, G.F., "Remote process monitoring using optical fibre sensors," *Sensors*, 2002, Proceedings of IEEE, vol. 2, pp. 1537 - 1542, 12-14 June 2002.
- [160] Tianchu Li, Russell G. May, Anbo Wang, Richard O. Claus, "Optical scanning extrinsic Fabry Perot interferometer for absolute microdisplacement measurement," *Applied Optics*, vol. 36, no. 34, pp. 8858, December 1997.

- [161] Sang-Hoon Kim; Jung-Ju Lee; Dong-Chun Lee; Il-Bum Kwon; “A study on the development of transmission-type extrinsic Fabry-Perot interferometric optical fiber sensor,” *J. Lightwave Technology*, vol. **17**, no. 10, Oct. 1999, pp. 1869 – 1874.
- [162] Zetterlind, V.E., III; Watkins, S.E.; Spoltman, M.W.; “Fatigue testing of a composite propeller blade using fiber-optic strain sensors,” *Sensors Journal, IEEE*, vol. **3**, no. 4, Aug. 2003, pp. 393 – 399.
- [163] Barrett, M.D.; Peterson, E.H.; Grant, J.W.; “Extrinsic Fabry-Perot interferometer for measuring the stiffness of ciliary bundles on hair cells,” *Biomedical Engineering, IEEE Transactions on*, vol. **46**, no. 3, March 1999, pp. 331 – 339.
- [164] Zeakes, J.S.; Murphy, K.A.; Elshabini-Riad, A.; Claus, R.O.; “Modified extrinsic Fabry-Perot interferometric hydrogen gas sensor,” *LEOS '94 Conference Proceedings. IEEE*, vol. **2**, 31 Oct.-3 Nov. 1994, pp. 235 – 236.
- [165] Mario Di Giovanni, *Flat and Corrugated Diaphragm Design Handbook*, (Marcel Dekker, New York, 1982).
- [166] Chung, G.S.; Kawahito, S.; Ishida, M.; Nakamura, T.; “High-resolution pressure sensors fabricated by silicon wafer direct bonding,” *Electronics Letters*, Volume: 27, Issue: 12, 6 June 1991, Pages:1098 – 1100.
- [167] Singh, R.; Low Lee Ngo; Ho Soon Seng; Mok, F.N.C.; “A silicon piezoresistive pressure sensor,” *Electronic Design, Test and Applications, 2002. Proceedings. The First IEEE International Workshop on*, 29-31 Jan. 2002, Pages:181 – 184.
- [168] Park, J.-S.; Gianchandani, Y.B.; “A low cost batch-sealed capacitive pressure sensor,” *Micro Electro Mechanical Systems, 1999. MEMS '99. Twelfth IEEE International Conference on*, 17-21 Jan. 1999, Pages:82 – 87.
- [169] Gander, M.J.; MacPherson, W.N.; Barton, J.S.; Reuben, R.L.; Jones, J.D.C.; Stevens, R.; Chana, K.S.; Anderson, S.J.; Jones, T.V.; “Embedded micromachined fiber-optic Fabry-Perot pressure sensors in aerodynamics applications,” *Sensors Journal, IEEE*, vol. 3, Issue: 1, Feb. 2003, pp. 102 – 107.
- [170] Toshima, K.; Watanabe, T.; Kaneko, Y.; Maesako, T.; Takahashi, K.; “Diaphragm-type optical fiber pressure sensor with a sleeve for fiber insertion,” *Micromechatronics and Human Science, 2003. MHS 2003. Proceedings of 2003 International Symposium on*, 19-22 Oct. 2003, Pages:171 – 174.
- [171] Cibula, E.; Donlagic, D.; Stropnik, C.; “Miniature fiber optic pressure sensor for medical applications,” *Sensors, 2002. Proceedings of IEEE*, Volume: 1, 12-14 June 2002, Pages:711 – 714.
- [172] J.D. Deng, “Development of Novel Optical Fiber Interferometric Sensors with High Sensitivity for Acoustic Emission Detection,” Ph.D. Dissertation, *Virginia Polytechnic Institute and State University*, 2004.

- [173] J. Xu, G. R. Pickrell, B. Yu, M. Han, Y. Zhu, X. Wang, K. L. Cooper, and A. Wang, "Epoxy-free high temperature fiber optic pressure sensors for gas turbine engine applications," *Proc. of SPIE* 5590, 2004.
- [174] VISHAY Tech Notes, "Design Considerations For Diaphragm Pressure Transducers," http://www.vishay.com/brands/measurements_group/guide/tn/tn510/510index.htm.
- [175] L.E. Lundgaard, "Partial Discharge - Part XIII: Acoustic Partial Discharge Detection - Fundamental Considerations", *IEEE Electrical Insulation Magazine*, Vol. 8, No. 4, pp.25-31, July/August 1992.
- [176] L.E. Lundgaard, "Partial Discharge - Part XIV: Acoustic Partial Discharge Detection - Practical Application", *IEEE Electrical Insulation Magazine*, Vol. 8, No. 5, pp. 34-43, September/October 1992
- [177] H. Kawada, M. Honda, T. Inoue, T. Amemiya, "Partial Discharge Automatic Monitor for Oil-Filled Power Transformer", *IEEE Transactions on Power Apparatus and Systems*, Vol. PAS-103, No. 3, 422-428 (1984).
- [178] E. Howells, E.T. Norton, "Location of Partial Discharge Sites in On-Line Transformers", *IEEE Transactions on Power Apparatus and Systems*, Vol. PAS-100, No. 1, pp. 158-161, 1981.
- [179] P.M. Eleftherion, "Partial Discharge XXI: Acoustic Emission-Based PD source Location in Transformers", *IEEE Electrical Insulation Magazine*, Vol. 11, No. 6, pp. 22-26, Nov/Dec 1995.
- [180] Anbo Wang, Yilu, Liu, and J. D. Deng, "Further Investigation of Partial Discharge Detection Using Fiber Optic SCIIB Acoustic Sensor," 2000 Annual Report submitted to the Electrical Power Research Institute, December 18, 2000.
- [181] Nick Bertone and Paul Webb, "Noise and Stability in PIN Detectors," posted at <http://optoelectronics.perkinelmer.com/content/whitepapers/NoiseandStabilityPINDetectors.pdf>.
- [182] Govind P. Agrawal, *Fiber-Optic Communication Systems*, 2nd Edition, John Wiley & Sons, Inc., 1997.
- [183] Jerald G. Graeme, *Photodiode Amplifiers*, McGraw-Hill Companies, Inc., New York, 1995.
- [184] D. Y. Chen, Virginia Tech course ECE5234 (EMI Noise) notes, 2002.
- [185] Sergio Franco, *Design with Operational Amplifiers and Analog Integrated Circuits*, 2nd Edition, McGraw-Hill Companies, Inc., Boston, 1998.
- [186] B. Ward, "Prototype Fiber-Optic Acoustic Partial Discharge Sensor – Lessons Learned Documentation and Field Test," EPRI Internal Report 1001768, 2002.

- [187] Yasuo Inoue, Kimio Suganuma, Massaru Kamba, Masanari Kikkawa, "Development of Oil-Dissolved Hydrogen Gas Detector for Diagnosis of Transformers", *IEEE Transactions on Power Delivery*, Vol.5, No.1, 226-232, (1990)
- [188] W.A. Pledger, S.C. Pyke, "Gas Monitor Update: Review of Progress in the Development of a Microelectronic In-Situ Transformer Fault Gas Analyzer", Proceedings: *EPRI Substation Equipment Diagnostics Conference*, Electrical Power Research Institute (New Orleans, Louisiana, July 1994).
- [189] J.W. Abbott, Don Chu, A.E. Diamond, H.A. ElBadaly, C.S. Slemon, "Development of an Automated Transformer Oil Monitor (ATOM)", Proceedings: *EPRI Substation Equipment Diagnostics Conference*, Electrical Power Research Institute (New Orleans, Louisiana, July 1994).
- [190] B. Culshaw, "Basic Concepts of Optical Fiber Sensors", Chapter 2 in *Optical Fiber sensors: principles and components*, Edited by J. Dakin and B. Culshaw (Artech House, Boston, 1988).
- [191] J.A. Bucaro, H.D. Dardy, and E. Carome, "Fiber Optic Hydrophone", *Journal of Acoustic Society of America*. Vol. **62**, pp. 1302-1304 (1977).
- [192] A. Dandridge and A.D. Kersey, "Overview of Mach-Zehnder Sensor Technology and Applications", in *Selected Papers on Fiber Optic Sensors*, edited by Reinhardt Willsch and Ralf Th. Kersten, SPIE Milestone vol. MS 108, pp. 216-234, (Society of Photo-optical Instrumentation Engineers, 1995).
- [193] M. F. Gunther, A. Wang, B. R. Fogg, K. A. Murphy, and R. O. Claus, "Fiber optic impact detection and location system embedded in a composite material," in *Fiber Optic Smart Structures and Skins V*, edited by R.O. Claus and R.S. Rogowski, Proc. SPIE **1798**, (Boston, Sept., 1992), pp. 262-269.
- [194] J. A. Greene, T. A. Tran, V. Bhatia, M. F. Gunther, A. Wang, K. A. Wang, and R. O. Claus, "Optical fiber sensing technique for impact detection and location in composites and metal specimens," *J. of Smart Materials and Structures*, **4**, pp. 93-99 (1995).
- [195] J. Teunissen, C. Helmig, R. Merte, D. Peier, "Fiber Optical On-Line Monitoring for High-Voltage Transformers", in *SPIE International Symposium on Environmental and Industrial Sensing: Fiber Optic Sensor Technology II*, edited by Michael A. Marcus, Brian Culshaw, Mohammed Saad and James A. Harrington, SPIE Proc., vol. 4204, pp. 198-205, 2001. (5-8 Nov. 2000, Boston, USA).
- [196] Zhao Zhiqiang, Mark MacAlpine, and M. Süleyman Demokan, "The Directionality of an Optical Fiber High-Frequency Acoustic Sensor for Partial Discharge Detection and Location", *J Lightwave Tech.*, Vol. **18**, No. **6**, 795-805 (2000).
- [197] R. O. Claus, M. F. Gunther, A. Wang, and K. A. Murphy, "Extrinsic Fabry-Perot sensor for strain and crack opening displacement measurement from -200 to 900°C," *J. of Smart Materials and Structures*, vol. **1**, 237-242 (1992).

- [198] K. A. Murphy, Michael F. Gunther, A. Wang, and R. O. Claus, "Detection of acoustic emission location using optical fiber sensors," in *Proc. Smart Structures and Materials 1994: Smart Sensing, Processing, and Instrumentation*, edited by James S. Sirkis, *SPIE Vol. 2191*, pp. 282-290 (1994).
- [199] A. Wang, M. S. Miller, A. J. Plante, M. F. Gunther, K. A. Murphy, and R. O. Claus, "Split-spectrum intensity-based optical fiber sensors for measurement of microdisplacement, strain and pressure", *Applied Optics*, Vol. **35**, 2595-2601 (1996).
- [200] J. Wang, W. Zhao, H. Xiao, and A. Wang, "Self-calibrated interferometric/intensity-based optical fiber sensors," in *Proc. Sensors and Controls for Advanced Manufacturing*, edited by Nnaji, Bartholomew O. and Wang, Anbo, *Proc. SPIE vol. 3201*, pp. 20-26, 1998. (Pittsburgh, PA, 14-15 Oct. 1997).
- [201] Shu-Jen Steven Tsai, Bing Yu, Ling Chen, Anbo Wang, Yilu Liu, Barry Ward, "Analysis of On-site Transformer Partial Discharge Measurement from Fiber Optic Acoustic Sensors" *EPRI Substation Equipment Diagnostics Conference*, New Orleans, LA. Feb 2003.
- [202] D. W. Kim, B. Yu, A. Wang, Y. Liu, S. Yang, S. Ahmad, D. Robert and B. Ward, "Partial Discharges and Thermal Faults Monitoring using Fiber Optic Acoustic Sensors," *EPRI Substation Equipment Diagnostics Conference*, New Orleans, LA. Feb 2004.
- [203] E. Kuffel, W.S. Zaengl, J. Kuffel, "High Voltage Engineering", second edition. July 17, 2000.
- [204] Y. Zhu, G. R. Pickrell, X. Wang, J. Xu, **B. Yu**, M. Han, K. L. Cooper, A. Wang, A. Ringshia, W. Ng, "Miniature fiber-optic pressure sensor for turbine engine," *Proc. of SPIE, Sensors for Harsh Environments*, Edited by Anbo Wang, Vol. 5590, 2004.
- [205] X. Wang, J. Xu, Y. Zhu, **B. Yu**, M. Han, K. L. Cooper, G. Pickrell, and A. Wang, "An Optical Fiber Tip Sensor for Pressure Measurement in High Temperature Environment", 2004 Optics in the Southeast, November 4 - 5, 2004, Charlotte, North Carolina.

Vita

Bing Yu was born in Sichuan, China, in 1968. He received the B.S. and M.S. degrees in Electrical Engineering from University of Electronic Science and Technology of China in 1989 and 1994, respectively. He is expecting his Ph.D. degree in Electrical Engineering, in May 2005, from the Virginia Polytechnic Institute and State University (Virginia Tech).

He joined the Chinese Academy of Engineering and Physics in 1989, and carried out research in high speed X-ray recording system. From 1995 to 1999, he was a telecommunication engineer at Chang Tong Mobile Telecommunication Engineering, Co. Ltd., and Alcatel (Chengdu) Telecommunication System Co., Ltd., Chengdu, China. After one year of study in Singapore, he joined the Center for Photonics Technology at Virginia Tech in 2000 as a graduate research assistant. He has authored or co-authored more than 25 journal and conference papers. His current research interests are in the area of fiber optic sensors, tunable optical filters, white light interferometry, biomedical sensing and bioimaging with white-light interferometry, and optoelectronic instrumentations.

Mr. Yu is a member of the OSA and the SPIE.